Missouri S&T Library and Learning Resources

Scholars' Mine

Masters Theses

Student Theses and Dissertations

Spring 2019

A study on end-anchorage and bond behavior of steel-fiber reinforced cementitious matrix composites externally bonded to a concrete substrate

Christopher Michael Moore

Follow this and additional works at: https://scholarsmine.mst.edu/masters_theses

 Part of the Civil Engineering Commons

Department:

Recommended Citation

Moore, Christopher Michael, "A study on end-anchorage and bond behavior of steel-fiber reinforced cementitious matrix composites externally bonded to a concrete substrate" (2019). *Masters Theses*. 7888.
https://scholarsmine.mst.edu/masters_theses/7888

This thesis is brought to you by Scholars' Mine, a service of the Missouri S&T Library and Learning Resources. This work is protected by U. S. Copyright Law. Unauthorized use including reproduction for redistribution requires the permission of the copyright holder. For more information, please contact scholarsmine@mst.edu.

www.manaraa.com

A STUDY ON END-ANCHORAGE AND BOND BEHAVIOR OF STEEL-FIBER REINFORCED CEMENTITIOUS MATRIX COMPOSITES EXTERNALLY BONDED TO A CONCRETE SUBSTRATE

by

CHRISTOPHER MICHAEL MOORE

A THESIS

Presented to the Faculty of the Graduate School of the

MISSOURI UNIVERSITY OF SCIENCE AND TECHNOLOGY

In Partial Fulfillment of the Requirements for the Degree

MASTER OF SCIENCE IN CIVIL ENGINEERING

2019

Approved by

Dr. Lesley H. Sneed, Advisor
Dr. John Myers
Dr. Guirong Yan

www.manaraa.com

© 2019

Christopher Michael Moore

All Rights Reserved

www.manaraa.com

ABSTRACT

Fiber reinforced cementitious matrix (FRCM) composites are a strengthening material consisting of continuous fibers embedded in an inorganic matrix that have the potential to provide additional flexural and shear strength to concrete and masonry members. When used for external strengthening, however, debonding of the material is often observed due to slippage of the fiber with respect to the matrix, causing loss of composite action and a reduction in load carrying capacity. The composite utilized in this study consisted of continuous steel fibers embedded in an inorganic cementitious matrix bonded to a concrete prism. Additionally, an end-anchorage system was implemented with the goal of limiting or preventing fiber slip by anchoring the free end of the steel fibers into a pre-drilled hole in the concrete prism. A total of 33 single lap direct shear specimens were tested with varying composite bonded length, anchor depth, and anchor material to study the effectiveness of an end anchorage system on bond performance. Also, strain data was collected from 12 of the 33 specimens to better observe the bond behavior of anchored and unanchored specimens. The results from the experimental analysis found minimal contribution of the end-anchorage system for specimens with a bonded length longer than the assumed effective bond length. However, the end-anchorage did have a considerable effect on the bond behavior (both peak load and absorbed energy) for specimens with a relatively short composite bonded length. Finally, based on the results of a strain distribution analysis, a preliminary bond-slip model for steel-FRCM composites was determined from nonlinear regression analysis of the steel fiber strain at debonding.

www.manaraa.com

ACKNOWLEDGMENTS

First, I would like to thank my advisor Dr. Lesley Sneed. She is the primary reason I decided to pursue an advanced degree, taking me on as one of her first Greenberg Scholars. Her guidance and expertise helped bring success to my research, undergraduate, and graduate careers. I am very grateful for her dedication to my work and this project over the last three years. I would also like to thank my committee members, Dr. John Myers and Dr. Guirong Yan, for their support throughout the program.

Next, I would like to thank my family. My parents John and Lori Moore, from a young age, instilled in me the importance of education. It is because of their commitment to my success that I was able to reach this point in my academic career. I would also like to thank my wife, Haley, for her constant encouragement.

My experimental work would not have been possible without the Missouri S&T high-bay laboratory staff, specifically Gary Abbott and John Bullock. Their technical knowledge of the laboratory testing equipment made the experimental portion of my research significantly easier, and they were always wonderful to work with.

Lastly, I would like to thank my colleagues, friends, and fellow advisees of Dr. Sneed, especially Sarah Jemison and Xingxing Zou. Sarah and I began our FRCM research projects around the same time, and she was always willing to assist with my work. Xingxing spent many hours in the lab with me preparing specimens and many more hours in the office helping with data analysis. He was an extremely valuable resource during my research program, and I am very grateful for his help.

www.manaraa.com

TABLE OF CONTENTS

Page

www.manaraa.com

www.manaraa.com

www.manaraa.com

www.manaraa.com

www.manaraa.com

LIST OF ILLUSTRATIONS

Page

www.manaraa.com

www.manaraa.com

www.manaraa.com

www.manaraa.com

www.manaraa.com

www.manaraa.com

www.manaraa.com

LIST OF TABLES

Page

www.manaraa.com

1. INTRODUCTION

1.1. PROBLEM DEFINITION

Fiber reinforced cementitious matrix (FRCM) composites have become an increasingly popular alternative to fiber reinforced polymer (FRP) composites for the retrofit and rehabilitation of concrete and masonry structural elements. FRCM composites provide a number of benefits over FRP composites, namely: 1) the cementitious material poses less of a toxicity concern compared to the epoxy resins required in FRP systems; 2) the cementitious material also provides better performance under extreme heat conditions such as fire exposure; and 3) cementitious material is not adversely affected by the presence of excess water. For these reasons, as well as others, FRCM composites have shown promise as an externally bonded strengthening system for concrete and masonry structures.

Numerous studies (which are discussed in Section 2) have investigated FRCM composites in various strengthening configurations. The composite system has shown to provide additional strength in flexural, shear, confinement, and torsional applications. In addition, research has been conducted to study the bond behavior of the composite, including the debonding failure mode. The results of those studies have concluded that one of the most commonly observed debonding failure modes of FRCM composites results from slippage of the fiber relative to the matrix material between the internal and external matrix layers. This fiber slippage results in a loss of composite action and ultimately leads to debonding of the fibers with or without the external matrix layer.

www.manaraa.com

It is well known that debonding of FRP composites can be delayed or even mitigated by anchoring it to the substrate (Grelle & Sneed, 2013). The present study examined the effectiveness of an end-anchorage system for FRCM composites that is intended to limit the fiber slip, and thus increase the load carrying capacity of the composite. The composite utilized in this study consisted of steel fibers embedded in an inorganic cementitious matrix bonded to a concrete prism. Additionally, an end-anchorage system was implemented with the goal of limiting or preventing fiber slip by anchoring the free end of the steel fibers into a pre-drilled hole in the concrete prism. The results of anchored specimens were compared to unanchored specimens within the experimental campaign. Presently, there are very few (if any) studies that directly study the effect of an end-anchorage system utilized with FRCM composites. Accordingly, this is one of the first known studies on the subject.

1.2. OBJECTIVES

The overall goal of this research project was to determine the influence of an end-anchorage system on the applied load-global (i.e., loaded end) slip and strain profile of steel-FRCM composites. Specific objectives were to:

- Evaluate the load carrying capacity of steel-FRCM composites with an end-anchorage system compared to unanchored control specimens;
- Determine the influence of different parameters on the effectiveness of the end-anchorage system;
- Investigate a potential method for collecting strain data from steel-FRCM composites;

www.manaraa.com

- Determine the influence of an end-anchorage system on the strain distribution (profile) along the composite bonded length of steel-FRCM composites;
- Analyze the collected strain data to determine the shear stress-slip relationship for steel-FRCM composites; and
- Bridge the gap in the literature regarding direct testing of anchored FRCM composites.

1.3. SCOPE AND LIMITATIONS

This section provides the scope of the research program as well as the limitations that govern the experimental campaign.

1.3.1. Scope. The scope of this study included the following tasks to accomplish the objectives discussed above:

- Conduct a review of the current literature regarding FRP and FRCM anchorage systems;
- Design, fabricate, and test a matrix of test specimens where the parameters varied included anchor binder material (epoxy resin and inorganic cementitious matrix), anchor depth (75 mm and 150 mm), and composite bonded length (100 mm and 330 mm);
- Analyze the influence of the presence of an end-anchorage system on the load carrying capacity including the effects of each of the parameters mentioned above; and

www.manaraa.com

- Perform a nonlinear regression analysis on the strain distribution along the bonded length of the composite at debonding to determine the shear stress-slip relationship for steel-FRCM composites.

1.3.2. Limitations. This study is not intended to be an exhaustive campaign covering all possible variations. The following limitations should be considered:

- This study investigates steel-FRCM composites, and does not include other fiber types (PBO, carbon, glass, basalt, etc.);
- FRCM-concrete joints are the focus of this campaign, as opposed to other substrate materials (e.g., masonry);
- This study only investigates a single type of end-anchor; and
- The collected strain values represent strain in the steel fibers (embedded between the two matrix layers), not strain on the surface of the composite.

1.4. SUMMARY OF THESIS CONTENT

The problem statement, scope, objectives, and limitations of this study are presented in Section 1. Section 2 provides background information necessary to understand this study. This is accomplished with a literature review of previous and current research over a variety of topics, including: various FRCM strengthening systems as an introduction to the topic; an in-depth look at the bond behavior of FRCM composites (including PBO-FRCM and steel-FRCM composites); a summary of the current research on anchorage of FRP composites (both indirect and direct testing); and finally, a brief summary of the available research on FRCM anchorage (again, both indirect and direct testing). Section 3 of this thesis describes the experimental program.

www.manaraa.com

This includes specimen design, materials, specimen fabrication, and test setup. The results of the experimental campaign are presented in Section 4, as well as an analysis and discussion of the influence of the tested parameters. Section 5 contains a summary of key findings, conclusions from those findings, and recommendations for future research. Appendix A presents the applied load-global slip response for each individual specimen. The individual and average LVDT response for all specimens are presented in Appendix B. Finally, the curve fitting parameters for individual points for select specimens used in the determination of the shear stress-slip relationship (as discussed in Section 4.4) are presented in Appendix C.

www.manaraa.com

2. BACKGROUND

2.1. GENERAL

Fiber reinforced cementitious matrix (FRCM) composites have been studied over the past few decades as an alternative to fiber reinforced polymer (FRP) composites for retrofit and rehabilitation of concrete and masonry structures. Varying configurations of FRCM composites have shown positive results in flexural strengthening (Ambrisi & Focacci, 2011), shear strengthening (Loreto et al., 2015), confinement (Ombres, 2014) and torsional strengthening (Alabdulhady, Sneed, & Carloni, 2017) applications. Numerous other studies have been conducted in addition to those mentioned above, and the available data suggest that FRCM composites have the potential to provide increased capacity in a variety of applications.

To fully characterize the composite behavior, small scale tests have been conducted to describe the bond behavior. The general composite failure mode, applied load-global slip response, and stress transfer mechanisms for polyparaphenylene benzobisoxazole (PBO)-FRCM composite are discussed in Section 2.2. Previous FRP anchorage studies are discussed in Section 2.3 and provide a basis for studies regarding anchorage of an externally bonded composite system. For the sake of this background section, anchorage studies (both FRP and FRCM) have been divided into two categories: indirect anchorage testing and direct anchorage testing. Indirect anchorage studies are those that include a variety of strengthening schemes (flexural, shear, etc.) where some of the specimens include anchorage. These studies do not directly study the effect of the anchorage on the bond characteristics but provide a more general sense of the

www.manaraa.com

enhancement to the strengthening system provided by the anchorage in specific applications. Direct anchorage studies are those that directly test the bond characteristics of the composite system, including the effect of anchorage. These include small scale bond tests (typically single lap direct shear tests as discussed below) that directly examine the effect of an anchorage system on the bond behavior of the composite. Finally, a review of the current research on anchorage of FRCM composites is presented in Section 2.4.

2.2. FRCM BOND BEHAVIOR

This section discusses the general FRCM bond behavior, including mode of failure, testing methods, applied load-global slip response and stress transfer mechanism.

2.2.1. General. The bond behavior of FRCM composites has been the subject of several studies over the past decade (Carloni et al., 2015; D'Ambrisi et al., 2012; D'Antino et al., 2018; D'Antino et al., 2014; Sneed et al., 2015; Sneed et al., 2016). While these studies are only a portion of the available research on FRCM composites, they provide fundamental information regarding the bond behavior and shear stress transfer. Many of the techniques employed in these studies (and other studies investigating FRCM bond behavior) attempt to adapt the processes used by researchers studying FRP composites. Test setup, data collection, analysis methods from FRP research studies have been successfully adapted to FRCM studies. However, based on available research, FRCM composites do not behave in an identical manner to FRP composites. A basic understanding of the failure mode, applied load-global slip response, and strain distribution/stress transfer mechanisms are necessary to understand the

www.manaraa.com

behavior of FRCM composites. These topics are discussed in detail in the following subsections.

2.2.2. Experimental Testing Methods. Investigations of the bond characteristics of FRCM composites are primarily composed of small-scale tests. Flexural and shear beam tests provide valuable information regarding the performance of the composite in real world applications but lack the ability to simply study the bond behavior, stress transfer, and global slip response of the composite. Accordingly, several other testing methods have been adopted for FRCM bond study that have been previously used in FRP bond behavior research. Yao et al. (2005) presents a visual summary of the available test setups, as shown in Figure 2.1 (Yao et al. 2005). The configurations can generally be divided into three groups: single lap shear test, double lap shear test, and beam test. The variation within the single and double lap shear tests depends on the location of the support condition (near the loaded end or near the free end). The FRCM bond studies mentioned briefly in Section 2.2.1 employed the near end supported single lap shear test method (Figure 2.1d). Studies by D'Ambrisi et al. (2012) and Sneed et al. (2015) employed the near end supported double lap shear test method (Figure 2.1a). These testing methods have proven effective in both FRP and FRCM studies for studying the direct shear stress transfer from the composite to the substrate.

2.2.3. Failure Mode. One of the primary research objectives of FRCM bond behavior studies is to determine the debonding failure mode. Several bond studies report that failure of FRCM composites occurs at the matrix-fiber interface (Carloni et al., 2015; D'Antino et al., 2014; Sneed et al., 2016). For FRCM composites, failure is often initiated by considerable slippage of the fibers relative to the matrix layers.

www.manaraa.com

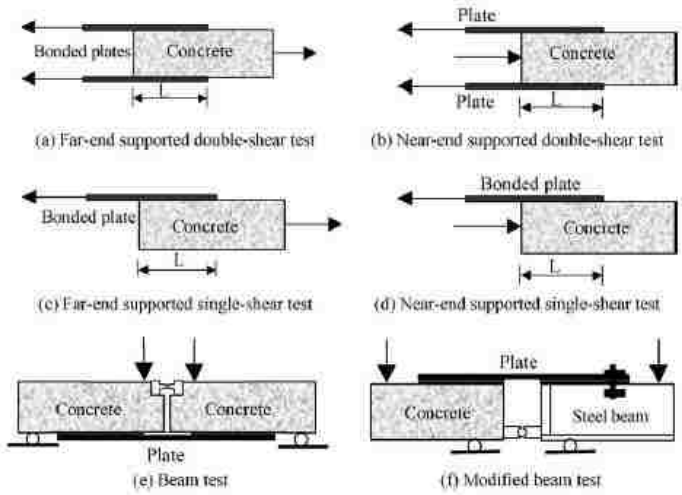

Figure 2.1. Summary of bond test types for FRP composites (Yao et al. 2005)

This is a key difference between FRP composites and FRCM composites. With FRP laminates bonded to a concrete substrate, failure is often observed at the FRP-concrete interface, suggesting that the strength of the substrate plays a key role in the bond performance. Zhang and Smith (2012) observed that in failed single lap shear specimens, a thin layer of concrete remained bonded to the laminates, identifying the FRP-concrete interface as the failure plane (Zhang & Smith, 2012). This failure mode has been reported frequently in the available literature and is generally accepted as typical for FRP composites.

Conversely, for many FRCM composites, failure does not occur at the matrix-concrete interface. An experimental study conducted by D'Antino et al. (2014) investigated the matrix-fiber bond behavior of PBO-FRCM composites (D'Antino et al., 2014). The FRCM composite consisted of PBO fibers embedded in a cementitious matrix bonded to a concrete substrate. The test program included 82 single lap direct shear

www.manaraa.com

specimens. D'Antino et al. (2014) reported that debonding occurred at the matrix-fiber interface (D'Antino et al., 2014). Other PBO-FRCM bond studies report similar results (Carloni et al., 2015; D'Ambrisi et al., 2012; D'Antino et al., 2014). A similar study on steel-FRCM composites, consisting of steel fibers embedded in a cementitious matrix, yielded similar results. The experimental program conducted by Sneed et al. in 2016 included seven single lap direct shear steel-FRCM specimens. The failure again was observed at the matrix-fiber interface. However, for steel-FRCM composites, failure was characterized as brittle detachment of the external matrix layer and steel fibers from the internal matrix layer. Failure was initiated by the propagation of a longitudinal (interfacial) crack between the internal and external matrix layer along the bonded length of the composite. Additionally, during testing, transverse surface cracks were observed on the surface of the external matrix layer. These failure markers are shown in Figure 2.2. Subsequent full-scale beams tests confirmed this failure mode in flexural strengthening applications as well (Sneed et al., 2016). Figure 2.3 shows the possible debonding surfaces for FRCM composites.

2.2.4. Load-Global Slip Response. In addition to the failure mode of FRCM composites, it is necessary to characterize the applied load-global slip response to further understand and predict the bond behavior. The applied load-global slip response of FRCM composites has been reported in almost every study of FRCM bond behavior. Based on an experimental campaign consisting of 82 PBO-FRCM single lap direct shear specimens, D'Antino et al. (2014) proposed a general bond-slip response (D'Antino et al., 2014). The relationship is shown in Figure 2.4 and provides the basis for the understanding of FRCM bond behavior as discussed below.

www.manaraa.com

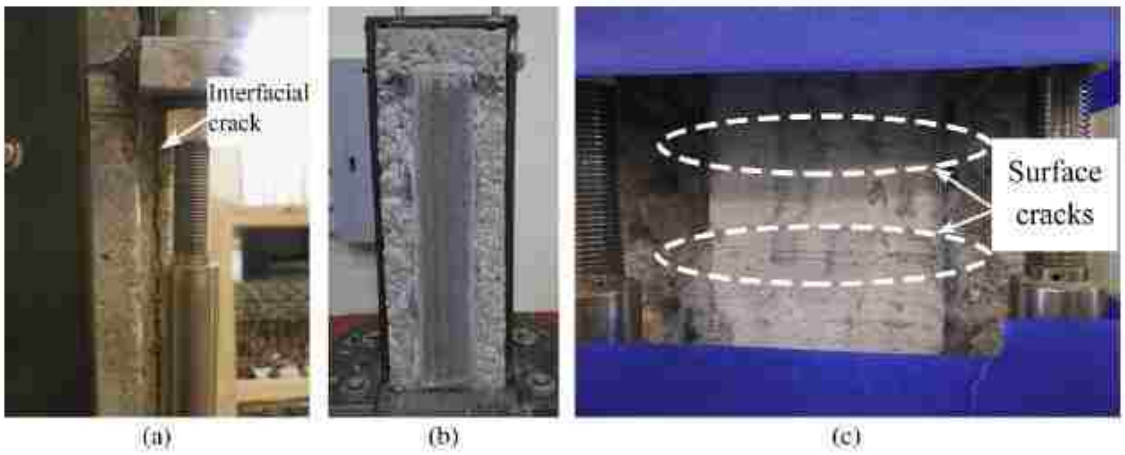

Figure 2.2. Failure of steel-FRCM specimens from Sneed et al. (2016)

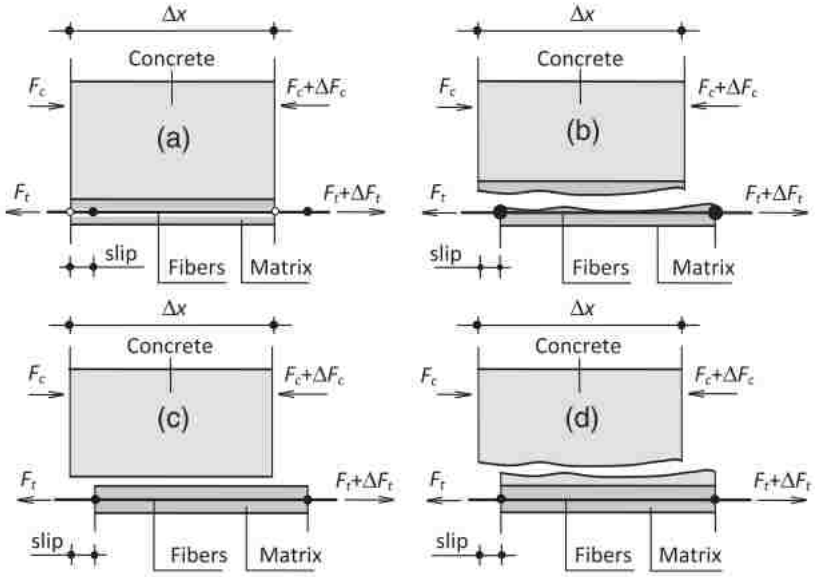

Figure 2.3. Different possible debonding surfaces for FRCM composites (Focacci, D'Antino, Carloni, Sneed, & Pellegrino, 2017)

The idealized curve is derived from the available PBO-FRCM single lap shear test specimen data. In Figure 2.3, the global slip refers to the slippage of the fiber at the

www.manaraa.com

loaded end relative to the internal matrix layer. Beginning at Point O, the linear portion of the curve up to Point A represents the elastic behavior of the composite.

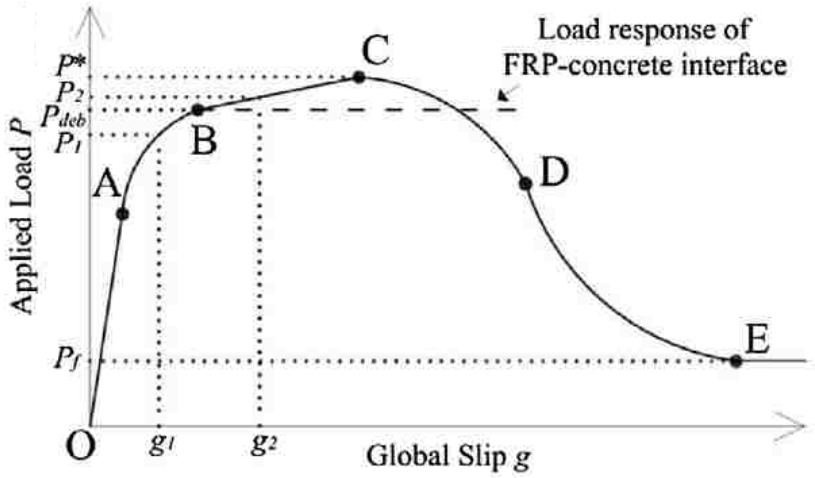

Figure 2.4. Idealized applied load vs. global slip response proposed by D'Antino et al. (2014)

This characterizes the bond between the matrix and the fibers. At Point A, as the load continues to increase, the response changes to a nonlinear trend. This is attributed to damage of the composite on a microscopic scale. Point B is labeled as the debonding load, or P_{deb}. This load marks the onset of debonding, which as discussed in Section 2.2.3, occurs at the matrix-fiber interface. Between Point B and Point C, after debonding has initiated between the matrix and fiber, the linearly increasing branch (and increase in load) are attributed to the friction (interlocking) between the fiber and matrix layers. For comparison, FRP composite bond behavior is marked in Figure 2.3 and is idealized as a constant load value for increasing values of slip. There is no friction mechanism that leads to an increase in load carrying capacity, which can be viewed as an advantage to

www.manaraa.com

FRCM systems. Point C, or P^*, represents the maximum load, and starts the beginning of a gradual decrease in load until the final branch at Point E. At Point E, the fibers are completely debonded from the matrix layers, and the load carrying capacity depends solely on the fiber fiction.

2.2.5. Stress Transfer Mechanism. The applied load-global slip response of FRCM composites can also be represented in terms of the load carrying portion of the bonded composite. Figure 2.5 is a visual representation presented by D'Antino et al. (2014) of the mechanisms that provide load carrying capacity. Figure 2.5 is intended to be interpreted with Figure 2.4, representing various points along the idealized applied load-global slip curve.

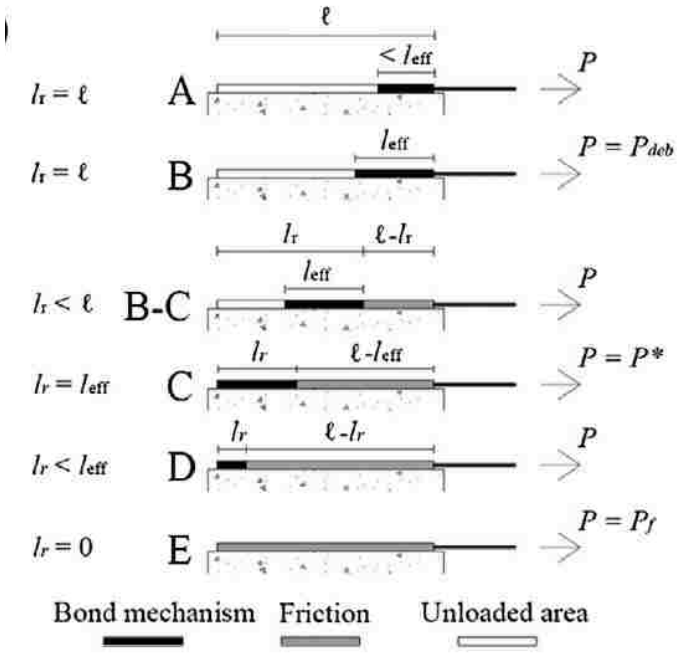

Figure 2.5. Visual representation of stress transfer mechanism proposed by D'Antino et al. (2014)

www.manaraa.com

Figure 2.4 introduces the concept of effective bond length (represented by l_{eff}). The effective bond length defined in D'Antino et al. (2014) is, "the minimum length needed to develop the load-carrying capacity of the interface." D'Ambrisi et al. (2012) define the concept similarly with an effective anchorage length, L_{eff}, such that "for bond lengths greater than L_{eff} the debonding force P_{deb} remains constant." These two ideas convey the same concept: for PBO-FRCM composites (and theoretically all FRCM composites), there exists a minimum length bonded length required to adequately develop the full stress transfer mechanism, and for lengths less than the minimum length, the composite will not reach a maximum peak load, or P^*.

Figure 2.5 shows that as the load increases, the bonded portion of the composite propagates along the bonded length of the composite after reaching the debonding load. Consequently, the load is carried by both the bonded portion (a segment of the bond equaling the effective bond length) and by friction between the fiber and matrix layers. This stress transfer continues until the length of the loaded portion of the composite becomes less than the effective bond length. At this point, the stress cannot be fully transferred through the composite, which is marked by a decrease in applied load (Point D in Figure 2.4). After this point, the load will continue to decrease as the portion of the bonded length carrying the load decreases, until finally, the stress is transferred only by friction between the fiber and matrix layers.

The proposed applied load-global slip response and stress transfer mechanism describe above have been validated for PBO-FRCM composites. There is very little research available on the bond behavior of steel-FRCM composites, which further necessitates this study. The experimental results (discussed in Section 4) will apply the

www.manaraa.com

principles discussed above to steel-FRCM in an attempt to characterize the bond behavior.

2.3. FRP ANCHORAGE TESTING

A comprehensive literature review was conducted by Grelle and Sneed in 2013 to compile and categorize the available literature regarding anchorage of FRP composites (Grelle & Sneed, 2013). Also, Grelle and Sneed categorized the test methods used to study the performance of anchorage devices used with FRP composites. The studies discussed below provide a basic review of the available FRP anchorage studies, both indirect and direct. Because the primary focus of this thesis is FRCM composites, only a select few studies are discussed below to provide general background on the subject of FRP anchorage.

2.3.1. Indirect FRP Anchorage Testing. This section discusses experimental programs that indirectly study the effect of anchorage of FRP composites.

2.3.1.1. Micelli, Annaiah, Nanni, 2002. The study by Micelli, Annaiah, and Nanni in 2002 investigated the use of carbon FRP and aramid FRP composites as a shear strengthening system. The experimental program consisted of 12 full-scale reinforced concrete joists in the Malcolm Bliss Hospital in St. Louis, Missouri. Ten of the 12 t-beams were retrofited with FRP sheets oriented at 90° to the beam axis following five different shear strengthening schemes. In addition to traditional shear strengthening schemes, six of the specimens included an end anchorage system, as shown in Figure 2.6. The anchor consisted of a glass FRP rod inserted into a groove at the flange-web intersection. The shear strengthening sheets were wrapped around the rod, and the groove

www.manaraa.com

was filled with an epoxy paste. The floor joists were loaded with a hydraulic jack reacting on the floor above. The resulting load vs. deflection curves were plotted for each specimen, and peak load and shear contribution were compared to calculated theoretical values.

A key finding of this study was that the specimens reinforced with anchored FRP composites reached higher peak loads than specimens retrofit with an unanchored composite. The maximum observed strength gain in the experimental program was a 39% increase in peak load over the control specimen, which was observed in a single U-wrapped member with end anchorage. The unanchored single U-wrapped member achieved only a 12% increase in peak load compared to the control specimen. Micelli et al. attribute this difference to the anchor's ability to prevent (or delay) premature peeling of the FRP sheets (Micelli, Annaiah, & Nanni, 2002).

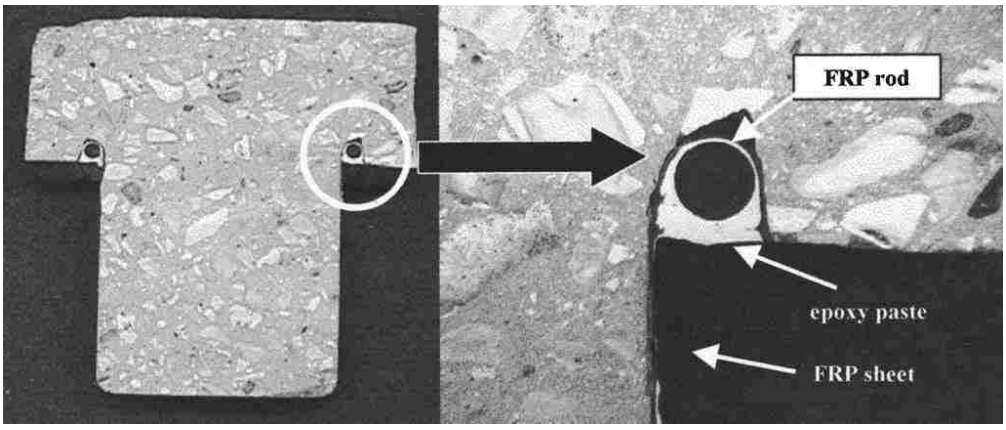

Figure 2.6. FRP anchorage used by Micelli et al. (2002)

www.manaraa.com

2.3.1.2. Mofidi, Chaallal, Benmokrane, Neale, 2012. The study by Mofidi, Chaallal, Benmokrane, and Neale in 2012 investigated end-anchorage for FRP composites in a shear strengthening application. A total of nine-full scale reinforced concrete T-beams were tested in three-point bending. The experimental program tested four end anchorage systems, shown in Figure 2.7: a) surface bonded, flat carbon FRP bar end anchorage (SBFA); b) double-aluminum-plate mechanical anchorage (DAMA); c) embedded, round CFRP bar end anchorage (ERBA); and d) embedded, flat carbon FRP laminate end anchorage (EFLA). Thus, the four anchorage systems can be divided into two groups: surface bonded anchors and embedded anchors. Each of the beams was tested under displacement control at a rate of 2 mm/min, and load, deflection, and strain data were recorded during testing.

Results of this study again suggest that an end-anchorage system can improve the performance of FRP composites used in shear strengthening applications. The beams strengthened with an externally bonded, anchored composite performed better than the corresponding unanchored beams, reaching higher peak loads and greater maximum deflections. The experimental data showed an increase in shear capacity as high as 41% for the anchored FRP composites, compared to an increase of only 25% for beams strengthened with an unanchored FRP composite. (Mofidi et al., 2012).

2.3.1.3. Skuturna and Valivonis, 2016. The study performed by Skuturna and Valivonis in 2016 investigated the use of anchorage to improve the flexural performance of concrete beams strengthened with FRP composites. Their experimental program consisted of 200 mm deep by 100 mm wide by 1500 mm long reinforced concrete beams strengthened with carbon FRP composite on the bottom (tension) surface. Three

www.manaraa.com

anchoring techniques were considered, including: 1) steel pin anchors; 2) U-wrap anchors; 3) steel clamps ranging from 50 cm^2 to 150 cm^2 with two and four bolts, pretensioned to pressures varying from 0.5 MPa to 2 MPa. Beams were simply supported and loaded in four-point bending. Strain gauges were mounted on the top, bottom and sides at midspan of each beam, and linear variable displacement transducers (LVDTs) measured deflection at midspan.

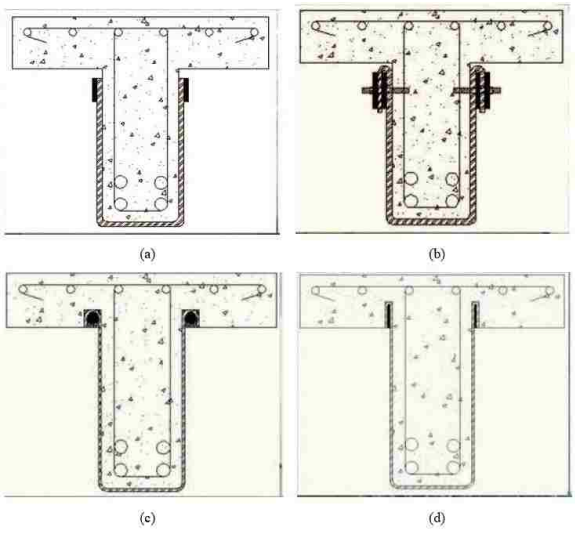

Figure 2.7. Anchorage schemes by Mofidi et al. (2012)

The experimental results suggested not only that a carbon FRP system could increase the flexural capacity of RC members, but also that the use of an anchorage system improved the bond capacity of the FRP composite, resulting in increased flexural capacity. Skuturna and Valivonis observed that in specimens with steel clamp anchorage, failure of the beams resulted from rupture of the carbon FRP composite at midspan. The

www.manaraa.com

additional anchorage prevented premature end debonding (the observed failure mode for the unanchored carbon FRP strengthened specimens) and allowed the FRP composite to reach its ultimate capacity at midspan. Additionally, the observed midspan deflections for the steel clamp anchored specimens was a minimum of 33% smaller than the control (unstrengthened) specimens, compared to the unanchored specimen's minimum value of 21%. Skuturna and Valivonis concluded that providing additional anchorage for carbon FRP composites (in a flexural application) can alter the failure mode of the composite and lead to greater strengthening improvement (Skuturna & Valivonis, 2016).

2.3.2. Direct FRP Anchorage Testing. This section discusses experimental programs that directly investigate the effect of anchorage of FRP composites.

2.3.2.1. Ceroni, Pecce, Matthys, Taerwe, 2008. In an experimental campaign conducted by Ceroni et al. in 2008, 14 T-shaped specimens were tested in double-lap shear to study the effect of various end-anchorage systems for FRP composites. Each specimen consisted of a "superior" prismatic block and an "inferior" T-shaped block as shown in Figure 2.8. To ensure failure of the composite at the "inferior" block, a mechanical external system comprised of steel plates and glue were used to adhere the FRP to the "superior" block. Of the 14 specimens, eight were fabricated so that the FRP composite was bonded to both the vertical and orthogonal surface of the T-section (Figure 2.8b), and six were fabricated with FRP composite only bonded to the web of the T-section (Figure 2.8a). Four anchorage systems were investigated: 1) steel plates glued to the FRP; 2) FRP plates glued to the FRP laminate; 3) steel plates bolted into the concrete; and 4) an FRP bar placed in a longitudinal groove (or Near Surface Mount

www.manaraa.com

anchor). Tests were conducted under displacement control at a rate of 0.1 mm/min (Ceroni et al., 2008).

From the experimental data, Ceroni et al. (2008) reported the failure mode of each specimen, the maximum load, and the variation in maximum load with respect to the unanchored specimens. Additionally, they presented strain profiles for a select few specimens, as well as the experimental shear stress-slip relationship for anchored and unanchored specimens. Their analysis brought forth the following key findings:

- In certain anchored specimens, the failure load was equal to or lower than the reference (unanchored) specimens. Ceroni et al. (2008) concluded that detailing and application of the anchorage system greatly influenced the performance of the system.
- Specimens with FRP reinforcement extending onto the orthogonal surface experienced peak loads as much as 30% lower than the equivalent specimen with fibers terminating on the web of the T-section. Interestingly, this suggests that a negative effect can be produced by extending fibers to an orthogonal surface.
- The experimental shear stress-slip relationship suggested that an anchorage system could be used to enhance the maximum strength with a more uniform shear stress distribution, while also reaching a lower peak value of shear stress (Figure 2.9).

www.manaraa.com

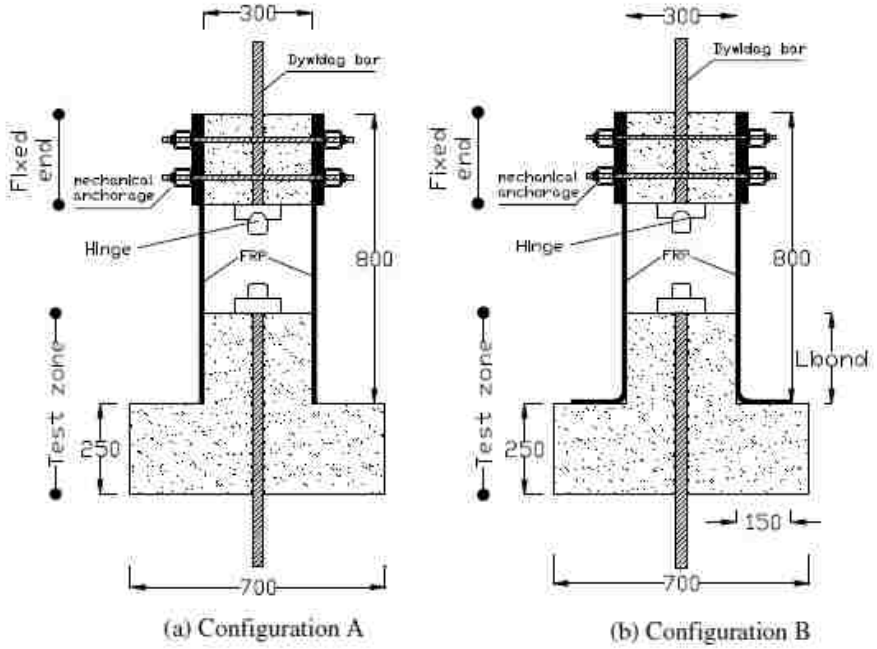

Figure 2.8. Specimen configurations used in Ceroni et al. (2008)

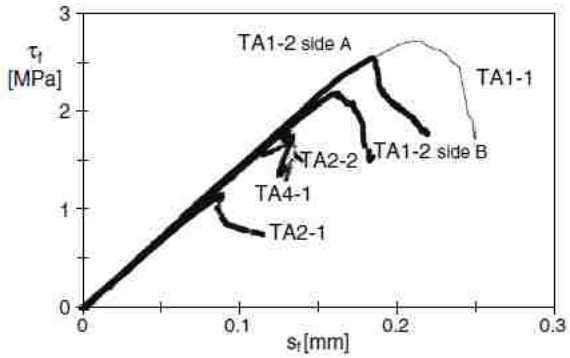

Figure 2.9. Shear stress-slip relationship from Ceroni et al. (2008)

2.3.2.2. Kalfat and Al-Mahaidi, 2010. The study completed by Kalfat and Al-Mahaidi in 2010 investigated the effect of a longitudinal chase anchorage on the bond behavior of carbon FRP composites. The experimental campaign included three test

www.manaraa.com

specimens, one unanchored control specimen and two anchored specimens. The sample size was intended to be part of the first stages of a study on shear/torsional strengthening of box girder bridge webs. The anchorage, as shown in Figure 2.10, consisted of a 40 mm deep by 40 mm wide by 500 mm long groove cut into the 300 mm side of the concrete block. A steel reinforcement bar was placed in the chase and filled with laminate adhesive. Kalfat and Al-Mahaidi note that the reinforcement bar likely played little-to-no part in the anchorage system, and that future testing omitting the bar would likely yield similar results. Specimens were tested in single-lap direct shear at a displacement control rate of 0.0167 mm/s. Strain in the composite was recorded with surface mounted strain gauges, as well as with 3D photogrammetry.

A key finding of the study was that the anchored specimens experienced a steeper slope in the load-strain response curves, which suggests a stiffer substrate in comparison to the control (unanchored) specimen. Also, Kalfat and Al-Mahaidi reported an increase in peak load between 95-100% for specimens including a longitudinal chase anchorage system, compared to the unanchored control specimens (Kalfat & Al-Mahaidi, 2010).

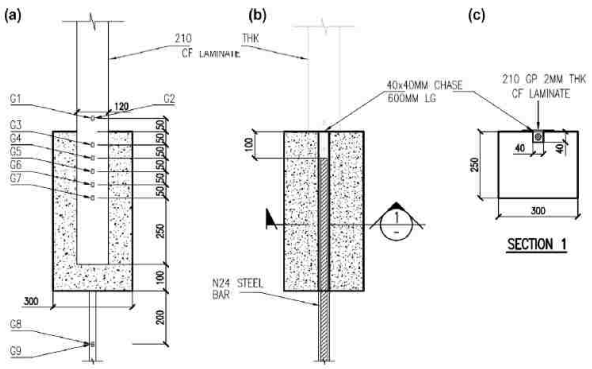

Figure 2.10. Specimen design used by Kalfat and Al-Mahaidi (2010)

www.manaraa.com

2.3.2.3. Niemitz, James, Brena, 2010. Niemitz, James, and Brena's study (2010) investigated the behavior of FRP sheets bonded to a concrete substrate anchored using CFRP anchors. The CFRP anchor consisted of a small piece of carbon fiber mesh that was inserted into a predrilled hole in the concrete substrate. The anchor was then secured with an epoxy resin within the predrilled hole, and the remaining fibers were splayed out in a circular configuration. Finally, the fiber sheet was placed and bonded to the existing anchor with an epoxy resin.

A total of eighteen specimens were fabricated following the scheme shown in Figure 2.11. Each specimen consisted of a concrete block measuring 860 mm in width and 1020 mm in length and an FRP laminate varying in length and width. Specimens were divided into three groups: Group A) an FRP laminate bonded to the concrete substrate without anchorage; Group B) an FRP laminate bonded to the concrete substrate and anchored at discrete points along the length with CFRP anchors (as shown in Figure 2.11); and Group C) an FRP laminate unbonded from the concrete substrate and anchored with FRP anchors at discrete points. The test variables included bonded length, anchor scheme, anchor diameter, and anchor splay diameter. Specimens were loaded with a manual hydraulic pump, and an array of strain gauges was placed on the composite surface.

A key finding of this study was that the specimens that relied on only bond or anchorage (Groups A and C, respectively) did not perform as well as specimens that relied on both bond and anchorage. Another key finding was that the anchored specimens achieved consistently higher peak loads, as well as greater ratios of peak load to failure load, compared to specimens that were unanchored or unbonded.

www.manaraa.com

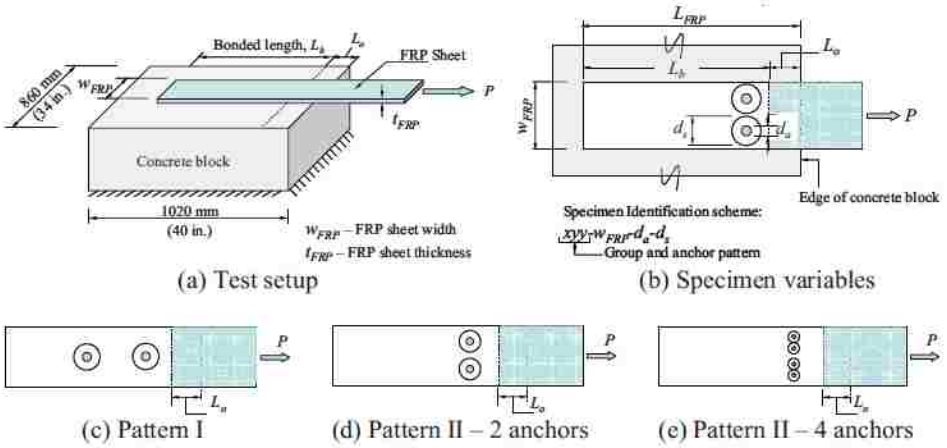

Figure 2.11. Specimen design used by Niemitz et al. (2010)

From the experimental results, Niemitz et al. suggested that the anchor splay diameter is proportional to the force that can be transferred into the FRP anchor (Niemitz, James, & Breña, 2010).

2.3.2.4. Zhang and Smith, 2012. The study conducted by Zhang and Smith in 2012 investigated the behavior of carbon FRP-concrete joints anchored with carbon FRP anchors (similar to the anchorage system discussed from Niemitz et al. (2010) in Section 2.3.2.3). Zhang and Smith tested a total of 43 single lap direct shear specimens, 41 of which included an anchorage system. The main variables investigated included number of anchors, position of anchors, and anchor installation procedure. Figure 2.12 depicts a typical test specimen. Rigid anchors were installed by impregnating the anchor fibers in the bend region with epoxy resin, making them "rigid" with respect to the FRP laminate. Flexible anchors were installed without epoxy resin in the bend region of the anchor and were thus "flexible" with respect to the FRP laminate and allowed deformation during plate slippage. The specimens were tested under displacement control at rate of 0.3

www.manaraa.com

mm/min. Throughout testing, load, slip at the loaded end of the composite, and strain data were recorded.

The experimental results from this study suggest that the presence of multiple anchors increased the load carrying capacity of the FRP composite. This was supported with an increased strain utilization of the FRP plates. The maximum observed strain in the FRP composite strip during testing was compared to the maximum strain observed in coupon tests of the bare FRP composite. The ratio of these values was referred to as the "strain efficiency." Specimens with one anchor were observed to have a strain efficiency increase of approximately 24% over the unanchored specimens. Also, the rigid anchor specimens were observed to have an increase of approximately 23% in strain efficiency over the flexible anchors. This suggests that the rigid anchor system was stronger than the flexible anchors, at the expense of deformability (Zhang & Smith, 2012).

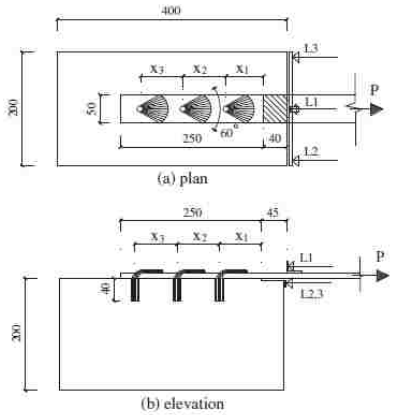

Figure 2.12. Specimen design used by Zhang and Smith (2012)

www.manaraa.com

2.3.2.5. Zhang, Smith, Kim, 2012. The study completed by Zhang, Smith, and Kim in 2012 investigated the bond behavior of carbon and glass FRP composites anchored to a concrete substrate. The study included 27 single lap direct shear specimens. Of the 27, 24 included a single FRP anchor, and three served as the unanchored control for comparison. The anchor design, installation, and test setup were similar to the procedure proposed in Zhang and Smith (2012) in Section 2.3.2.4. The test variables included fiber type, anchor size, and anchor installation procedure (dry or impregnated).

From the experimental load-slip response, Zhang et al. proposed a generalized applied load-slip response for both unanchored and anchored FRP composites. From Figure 2.13, the region of interest is between Point B and Point C. The line between Point B and Point B' represents the response of an unanchored composite, where Point B is the peak load. Accordingly, Point C represents the increase in peak load for anchored composites, which was measured to be, on average, 53% over the unanchored control specimens. Additionally, Zhang et al. concluded that the level of strain in the FRP composite in the region between the anchor and the free (unloaded) end was generally lower in the anchored specimens compared to unanchored specimens. They attribute this difference to the contribution of the anchorage (Zhang, Smith, & Kim, 2012).

2.4. FRCM ANCHORAGE TESTING

This section describes previous studies that investigate anchorage systems for FRCM composites. Section 2.4.1 discusses indirect anchorage studies and Section 2.4.2 discusses direct anchorage studies.

www.manaraa.com

2.4.1. Indirect FRCM Anchorage Testing. This section describes previous experimental studies that investigate the effect of anchorage systems on FRCM composites

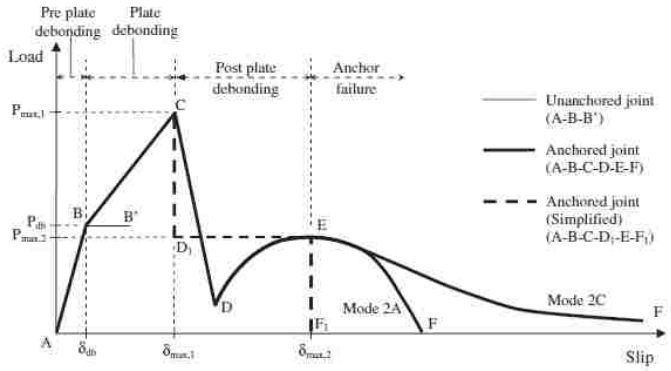

Figure 2.13. Generalized load-slip response proposed by Zhang et al. (2012)

2.4.1.1. Al-Kubaisy and Jumaat, 2000. The study completed in 2000 by Al-Kubaisy and Jumaat investigated the use of anchorage devices to improve performance of ferrocement reinforced concrete beams. Ferrocement is typically applied in much thicker layers compared to FRCM composites (e.g. 25 mm thick in this study compared to between 8-10 mm thick recommended by most FRCM system manufacturers). However, ferrocement is a similar system to FRCM composites in that a reinforcing fiber is embedded into a cementitious material, unlike FRP where a reinforcing fiber is embedded into an epoxy resin. Al-Kubaisy and Jumaat's study investigated the flexural capacity of 11 reinforced concrete beams, eight of which included some type of anchorage device. The study investigated the use of Hilti bolts, predrilled and epoxied mild steel bars, and steel dowels attached to the main

www.manaraa.com

reinforcement cage. Each beam measured 150 mm wide by 250 mm deep by 2200 mm long and was loaded in three point bending over a span of 2000 mm. The ferrocement laminate consisted of 2R6 skeletal steel bars and four layers of square welded wire mesh (Jumaat & Al-Kubaisy, 2000).

A 50-ton manual hydraulic jack was used to apply load in 2 kN increments up to the cracking load, where the interval was then decreased to 1 kN. A single LVDT recorded midspan deflection during testing. Al-Kubaisy and Jumaat report that "in general, the structural behavior of the strengthened or repaired beams was similar to the control beams." Their conclusion is likely based on the observed crack widths and cracking pattern being similar in the ferrocement beams to the control beams. Al-Kubaisy and Jumaat do report, however, an increase in ultimate moment capacity between 32-55% for the ferrocement strengthened beams over the control beam. Based on this metric, a final key finding of this study was that shear anchorage (whether Hilti bolts, epoxied steel bars, or steel dowels) can improve composite action between the concrete substrate and the external ferrocement laminate.

2.4.1.2. Prota, Tan, Nanni, Pecce, Manfredi, 2006. The study conducted by Prota et al. in 2006 investigated the use of steel-reinforced polymers (both epoxy-based, SRP, and cementitious based, SRG) for external strengthening of reinforced concrete beams. Additionally, the study included specimens utilizing nail anchors along the centerline of the beam intended to improve the bond between the external composite and the concrete substrate. A total of 11 shallow reinforced concrete beams measuring 400 mm wide by 200 mm deep by 3700 mm long were reinforced with either: 1) high density steel chord embedded in an epoxy matrix; 2) medium density steel chord embedded in an

www.manaraa.com

epoxy matrix; 3) medium density steel chord embedded in a cementitious matrix; or 4) unidirectional carbon fibers embedded in an epoxy resin. Apart from the control beam, 10 of the reinforced concrete specimens were designed with deficient flexural reinforcement. Additionally, nine of the remaining 10 were strengthened with one of the systems described above. Within the steel-reinforced cementitious systems, two specimens utilized nail anchors (Figure 2.14) along the centerline of the beam for additional anchorage. Beams were loaded in a four-point bending configuration and loaded with a 500 kN hydraulic actuator under displacement control (Prota et al., 2006).

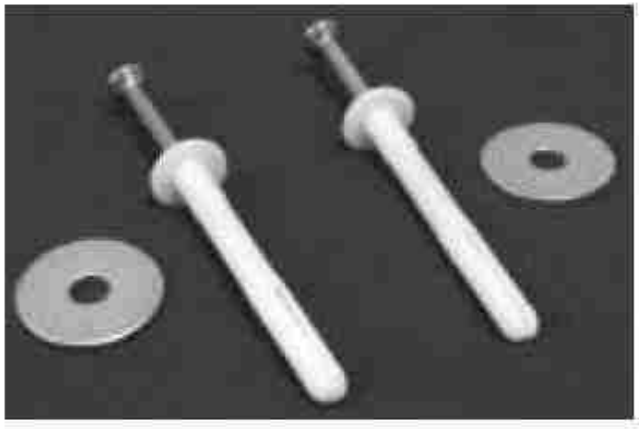

Figure 2.14. Nail anchors utilized by Prota et al. (2006)

From the experimental results, Prota et al. (2006) concluded that the nail anchors were not able to improve the bond behavior of the steel fibers impregnated in cementitious grout. This was primarily due to the failure of the anchors to effectively transfer the local stresses from the steel tape into the anchor. Because of this lack of

www.manaraa.com

stress transfer, the nails were not able to delay premature debonding of the composite. The study did suggest, however, that steel tape impregnated in a cementitious matrix could be used as a potential external strengthening system.

2.4.1.3. Baggio, Soudki, Noel, 2014. The study completed by Baggio, Soudki, and Noel in 2014 studied the performance of shear deficient reinforced concrete beams strengthened with FRP and FRCM composite systems. Nine slender RC beams were constructed and eight were retrofitted with one of the following systems: 1) carbon fiber reinforced polymer full depth U-wrap; 2) glass fiber reinforced polymer partial depth U-wrap; or 3) glass fiber reinforced cementitious matrix full depth U-wrap. Additionally, one specimen from each group included the use of carbon FRP anchors installed in pre-drilled holes near the top surface of the beam. A schematic of the anchor locations is shown in Figure 2.15. The beams measured 150 mm wide by 350 mm deep by 2440 mm long and were supported over a clear span of 2200 mm. Load was applied with a hydraulic testing machine under displacement control at a rate of 0.3 mm/min. During testing, load, midspan deflection, and strain data at discrete points along the beam were recorded.

The experimental results found that the FRCM composite strengthening system resulted in only a 32% increase in peak load carrying capacity. Additionally, the use of carbon FRP anchors with the FRCM system increased the peak load by only 3% over the unanchored FRCM beam (load vs. displacement response shown in Figure 2.16). These increases in peak load were considerably smaller than the load increase observed in the unanchored FRP strengthened beams (67% for carbon FRP and 50% for glass FRP). The use of an FRCM strengthening system ultimately did not change the mode of failure for

www.manaraa.com

the beams compared to the control beam. The experimental data suggests that the use of an FRP anchor with an FRCM system in shear strengthening applications will not increase the load carrying capacity of the composite by a substantial amount.

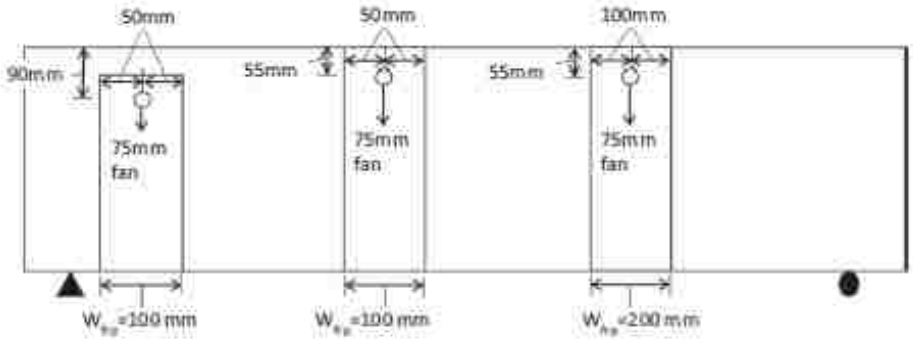

Figure 2.15. Anchor details for specimens used by Baggio et al. (2014)

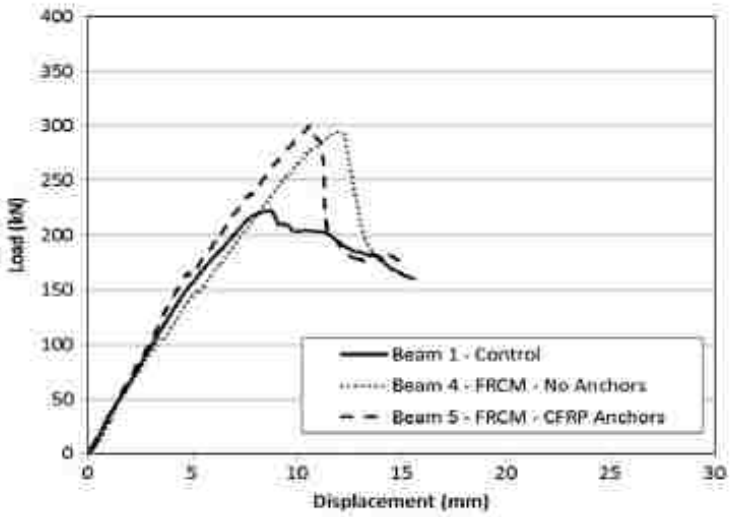

Figure 2.16. Load vs. displacement response for FRCM specimens in Baggio et al. (2014)

www.manaraa.com

2.4.1.4. Trapko, Urbanska, Kaminski, 2015. Trapko, Urbanska, and Kaminski studied shear deficient beams strengthened with PBO-FRCM composites to investigate the role of an anchorage system on bond performance. Trapko et al. tested three reinforced concrete beams (B1, B2, and B3) strengthened with three configurations of PBO-FRCM composites, as shown in Figure 2.17. Each of the beams was preloaded to a level that produced 0.1 mm wide cracks (approximately 55 kN). This approach was taken to simulate loading conditions of real structures in need of retrofit/strengthening. For beams B2 and B3, the ends of the PBO fibers were anchored in a longitudinal groove cut in the top and bottom face of the beams. For beam B2, both grooves were filled with an epoxy resin. For beam B3, the top groove was filled with a mineral mortar, and the bottom groove was filled with an epoxy resin. Beams were loaded manually at increments of 10 kN, and load, deflection, and strain measurements were taken during testing (Trapko, Urbanska, & Kaminski, 2015).

At beam failure, Trapko et al. observed that none of the PBO fibers had ruptured, indicating that the anchorage was not able to restrain the fiber enough to reach its tensile capacity. Additionally, beam B2 failed because the anchor at the top surface of the beam (filled with epoxy resin) was crushed, causing the fibers to pull out of the anchorage. Beam B3 is reported to have failed in a similar manner. It was reported, however, that the anchorage on the bottom (tension) surface of the beam did fulfill its purpose in preventing pullout of the PBO fibers. Trapko et al. were not, however, able to compare their experimental results to a control specimen because all specimens tested in their program were strengthened with FRCM.

www.manaraa.com

2.4.1.5. Donatelli, 2016. The research conducted by Donatelli in 2016 investigated the effect of an end-anchorage system on the flexural performance of reinforced concrete beams strengthened with a steel-FRCM system. The anchorage was formed by inserting the end of the steel fibers into a pre-drilled hole at each end of the beam.

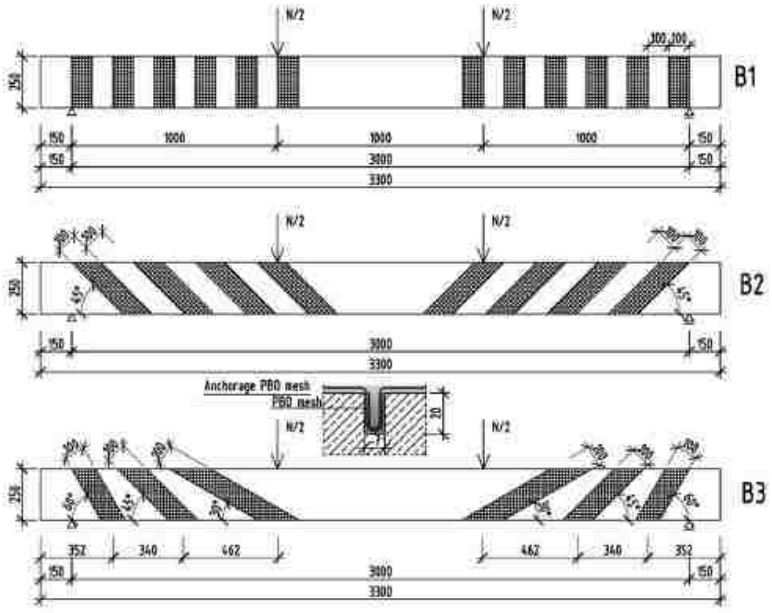

Figure 2.17. Strengthening configurations used by Trapko et al. (2015)

The holes were then filled with either an epoxy resin or a cementitious material. A schematic of the anchorage system is shown in Figure 2.18. A total of nine beams were included in the study, including four previously tested steel-FRCM strengthened beams (all unanchored) and five newly constructed steel-FRCM beams (four with end-anchorage). Beams were tested in a four-point bending configuration, and the load was

www.manaraa.com

applied under displacement control at a rate of 0.03 mm/s. The test setup is shown in Figure 2.19.

From the experimental results, Donatelli reported that the beams anchored with KeraKoll Eco Binder (mortar) reached the highest peak load (138.17 kN) – an increase of 25% over the unstrengthened control beam and 13% over the unanchored specimen. Also, Donatelli noted that the steel-FRCM fibers near the end of the anchored beams did not prematurely peel off of the substrate. The presence of an end anchorage system positively effected the load carrying capacity of the composite. Another key finding was that beams with a longer anchor depth experienced a larger midspan deflection. This suggests that the presence of an end anchorage system can improve ductility. Moreover, the GeoLite Gel anchor material was found to be the best anchor material in terms of ductility, regardless of anchor depth (Donatelli, 2016).

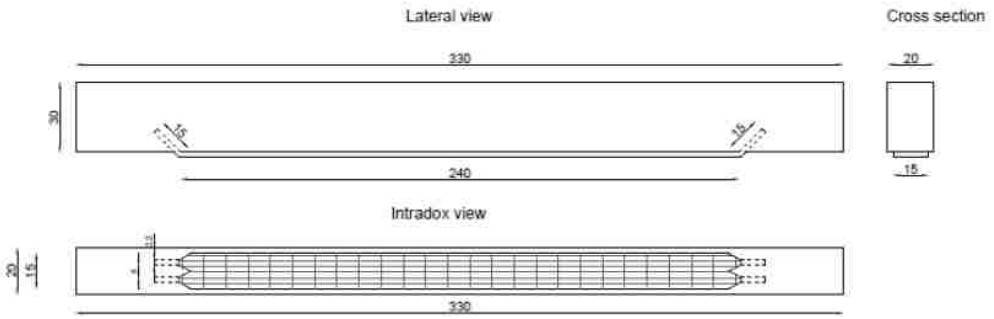

Figure 2.18. Strengthening and anchorage configuration used by Donatelli (2016)

www.manaraa.com

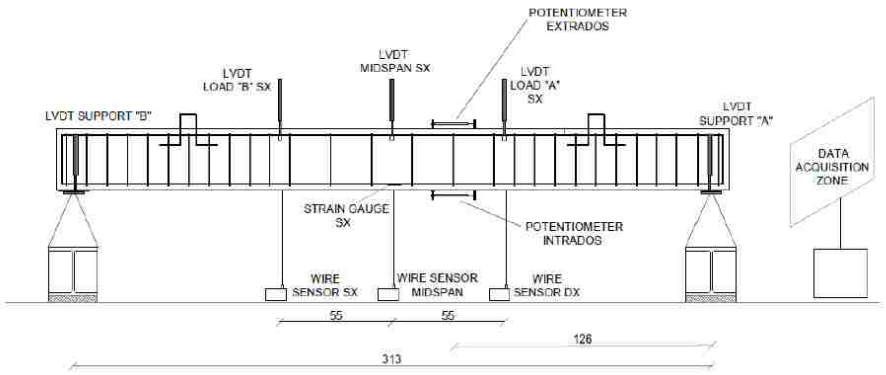

Figure 2.19. Test setup used by Donatelli (2016)

2.4.1.6. Sneed, Verre, Carloni, Ombres, 2016. This study, as previously discussed in Section 2.2.3, also included reinforced concrete beams strengthened with steel-FRCM composite. The study included five reinforced concrete beams, three of which were retrofitted with steel-FRCM composite bonded to the tension face and reported in their paper. The first strengthened beam was tested at the standard load rate of 0.013 mm/s, the second was tested at two times the standard load rate (0.025 mm/s), the third was tested at the standard load rate with the external matrix layer omitted, and the fourth was tested at the standard load rate and included U-wraps at each end of the composite strip. Additionally, the fourth strengthened beam was loaded to approximately 90% of the yield load, then unloaded prior to applying the composite strengthening system. The beams measured 203 mm wide by 305 mm deep by 3048 mm long and were tested in a four-point loading configuration.

Sneed et al. reported that the failure of beams without U-wrap anchorage was similar to the beams with U-wrap anchorage. Flexural cracks were observed in the constant moment region, which extended through the matrix layers and were observed on

www.manaraa.com

the external matrix layer. The failure was characterized by the propagation of an interfacial crack between the internal matrix layer and the steel fibers, which was similar to the failure of the single lap shear specimens (as reported in Section 2.2). Additionally, beams with and without an external matrix layer had similar yield load, debonding load, and corresponding midspan deflection. Based on this observation, Sneed et al. concluded that the external matrix layer does not play a significant role in improving the strengthening system. This conclusion was also supported with the single lap direct shear tests. While the U-wrap anchorages did restrain the composite peeling effect, it did not restrain the interfacial slip at the ends of the composite. Thus, the U-warp anchorage did not improve the performance of the strengthening system (Lesley H. Sneed et al., 2016).

2.4.1.7. Younis, Ebead, Shrestha, 2017. In the study completed by Younis, Ebead, and Shrestha in 2017 tested 16 shear-critical (no shear reinforcement in the shear critical region) reinforced concrete beams strengthened with PBO, glass, and carbon FRCM systems. Additionally, six of the strengthened beams included a mechanical anchorage consisting of two FRP plates at the top and bottom of the composite strip. Details of the anchorage are shown in Figure 2.20. The beams measured 150 mm wide, 330 mm deep, and 2100 mm long and were tested in a three-point loading configuration. Load was applied under displacement control at a rate of 1 mm/min. Midspan deflection was measured beneath the load with an LVDT, and strain values were recorded at each applied load step.

The experimental results suggested that the FRCM composite strengthening system was successful in improving the load carrying capacity of the tested beams. Of the three systems, the carbon FRCM system performed the best, with peak load increases of

www.manaraa.com

approximately 68% over the control (unstrengthened) beam. Additionally, the use of continuous FRCM application led to a greater increase in peak load compared to intermittent FRCM strips. This conclusion is logical, suggesting that an increase in the amount of strengthening material leads to an increase in load carrying capacity. Regarding the anchored specimens, the additional capacity for anchored specimens was observed to be no more than 5% over the unanchored counterpart. This small difference suggests that the contribution of the FRP end anchorage in shear strengthening applications did not significantly increase the performance of the FRCM system.

Figure 2.20. FRP anchorage system used by Younis et al. (2017)

www.manaraa.com

2.4.2. Direct FRCM Anchorage Testing. As discussed in Section 2.1, there are currently no studies that directly investigate the effect of anchorage on the bond behavior of FRCM composites. There have been several studies that investigate the bond behavior of FRCM composites (as discussed in Section 2.2), but none that involve any type of anchorage system. While there are many studies that indirectly investigate the use of anchorage systems in FRCM strengthening applications, the direct effect of the anchorage on bond behavior cannot be determined from these types of tests. That gap in the available literature necessitates the content in this thesis.

www.manaraa.com

3. EXPERIMENTAL PROGRAM

3.1. OVERVIEW

This section provides a summary of the experimental campaign including specimen design, materials, specimen fabrication procedure, and test setup. The experimental results are presented and analyzed in Section 4.

3.2. SPECIMEN DESIGN

The experimental program included 33 single lap direct shear specimens used to study the bond behavior of steel-FRCM composites, as well as the influence of an end anchorage system on load carrying capacity. The general specimen layout used in this study was similar to the specimen design used in previous FRCM bond studies (C. Carloni et al., 2015; T. D'Antino et al., 2014; Tommaso D'Antino et al., 2018; Lesley H. Sneed et al., 2016). The test variables included anchor material, anchor depth, and composite bonded length. Each specimen was designated with the convention shown in Figure 3.1. Two bonded lengths were used in conjunction with two anchor materials and two anchor depths, as shown in Table 3.1. Specimens with a bonded length of 330 mm were cast onto a concrete prism with a cross section of 150 mm by 150 mm and a length of 500 mm. Specimens with a bonded length of 100 mm were cast onto a concrete prism with a cross section of 150 mm by 150 mm and a length of 380 mm. The bonded width of the composite was set at 50 mm for all specimens to remain consistent with the available steel-FRCM literature. A bonded width of 50 mm corresponding to 16 fiber cords was used in this study.

www.manaraa.com

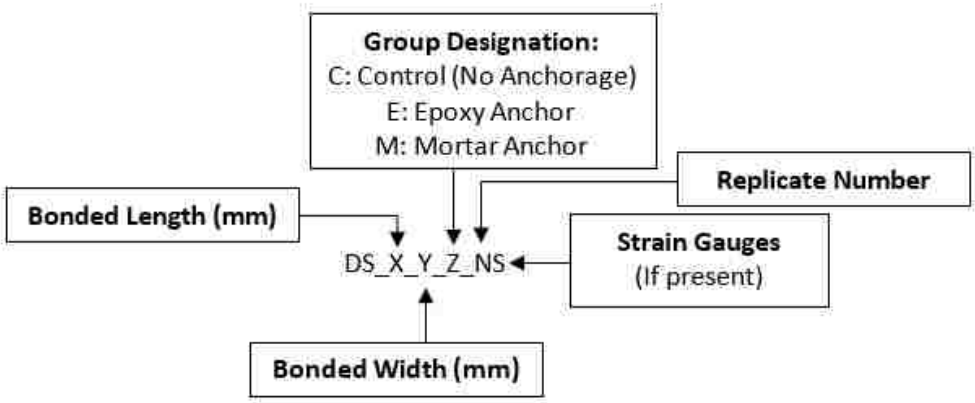

Figure 3.1. Specimen designation notation

Table 3.1. Test matrix

Bonded Length (mm)	Anchor Material	Anchor Depth (mm)	Specimen ID
330	Control	-	DS_330_50_C_1
			DS_330_50_C_2
			DS_330_50_C_3
			DS_330_50_C_4
			DS_330_50_C_5
			DS_330_50_C_6S
			DS_330_50_C_7S
	Epoxy Resin	75	DS_330_50_E_1
			DS_330_50_E_2
			DS_330_50_E_3
			DS_330_50_E_4
		150	DS_330_50_E_5
			DS_330_50_E_6S
			DS_330_50_E_7S
	Cementitious Mortar	75	DS_330_50_M_1
			DS_330_50_M_2
			DS_330_50_M_3
			DS_330_50_M_4
		150	DS_330_50_M_5
			DS_330_50_M_6S
			DS_330_50_M_7S

www.manaraa.com

Table 3.1. Test matrix (cont.)

100	Control	-	DS_100_50_C_1
			DS_100_50_C_2
			DS_100_50_C_3S
			DS_100_50_C_4S
	Epoxy Resin	75	DS_100_50_E_1
			DS_100_50_E_2
			DS_100_50_E_3S
			DS_100_50_E_4S
	Cementitious Mortar		DS_100_50_M_1
			DS_100_50_M_2
			DS_100_50_M_3S
			DS_100_50_M_4S

3.3. MATERIALS

The materials used in this study included a steel fiber reinforced cementitious matrix composite system bonded to unreinforced concrete prisms. Additionally, an epoxy resin was used in certain specimens to bond the anchor to the concrete substrate. The concrete prisms are described in Section 3.3.1, and the steel-FRCM components, steel fiber and cementitious matrix, are discussed in Sections 3.3.2 and 3.3.3, respectively. Finally, the epoxy resin properties are discussed in Section 3.3.4.

3.3.1. Concrete. The concrete prisms utilized in this experimental program fall into one of two categories: concrete blocks repurposed from a previous FRCM study or newly cast concrete blocks. All concrete prisms were composed of unreinforced normalweight concrete. The repurposed concrete prisms used in this study were from a previous PBO-FRCM bond study conducted by D'Antino et al. (2014). The results presented in their paper were from experimental work conducted in Butler-Carlton Hall at Missouri S&T by Tommaso D'Antino, a Visiting Scholar from the University of

www.manaraa.com

Padova. After completion of his experimental program, the blocks were stored at an off-site storage warehouse. Upon retrieval of the prisms in Fall 2017, the surface intended to form the FRCM-concrete joint was sandblasted to remove any previous FRCM material and prepare the substrate per the manufacturer's recommended target roughness profile. The prism dimensions and properties (as reported in D'Antino et al. 2014b) are shown in Table 3.2.

To accommodate a 150 mm anchor depth, new concrete blocks were fabricated with a deeper cross section. The concrete mixture design was adapted from a previous steel-FRCM bond study conducted by Sneed et al. (2016). All concrete mixing and casting took place in the Concrete Materials Laboratory in Butler-Carlton Hall at Missouri S&T (Figure 3.2). Compressive strength tests were conducted on 100 mm x 200 mm concrete cylinders according to ASTM C39/C39M-18. The newly cast concrete prism dimensions and properties are also listed in Tables 3.2.

Table 3.2. Concrete prism dimensions and compressive strength

Prism Description	**Dimensions**	**Compressive Strength (MPa)**	**CoV**
D'Antino et al. (2014) - Short	125 mm x 125 mm x 375 mm	42.5	0.013
D'Antino et al. (2014) - Long	125 mm x 125 mm x 510 mm	33.5	0.085
Newly Cast Prisms	125 mm x 200 mm x 510 mm	34.4	0.084

www.manaraa.com

Figure 3.2. Load frame used for concrete and mortar testing

3.3.2. Steel Fiber Sheets. KeraKoll GeoSteel G1200 fibers were used in this experimental program as the fiber component of the FRCM composite. The technical data for the fiber is listed in Table 3.3 for an individual wire, an individual cord, and for a section of the fiber sheet. Additionally, experimental work by Donatelli (2016) confirmed the accuracy of the manufacturer specifications. GeoSteel G1200 is a unidirectional sheet made of micro-cord fiber bundles adhered to a fiberglass micromesh, as shown in Figure 3.3. Each micro-cord consists of five extra-high strength galvanized steel fibers; three internal fibers wrapped in two external fibers, resulting in a braided strand. The galvanization process promotes high durability of the steel fibers, even in corrosive, humid, and temperature variable (freeze-thaw) environments. GeoSteel G1200 fibers also have higher mechanical properties compared to traditional fibers (carbon, glass, aramid), making them an effective strengthening alternative.

www.manaraa.com

Table 3.3. GeoSteel G1200 Manufacturer Properties (KeraKoll 2017)

Wire	
Tensile Strength	>2900 MPa
Elastic Modulus	>205 GPa
Area	0.1076 mm^2
Cord	
Area	0.538 mm^2
Cords/cm	3.19
Tensile Breakign Load	>1500 N
Sheet (Non-Impregnated)	
Tensile Strength	>3000 MPa
Elastic Modulus	>190 GPa
Density	7.955 g/cm^3
Equivalent Thickness	0.169 mm
Mass	1200 g/m^2

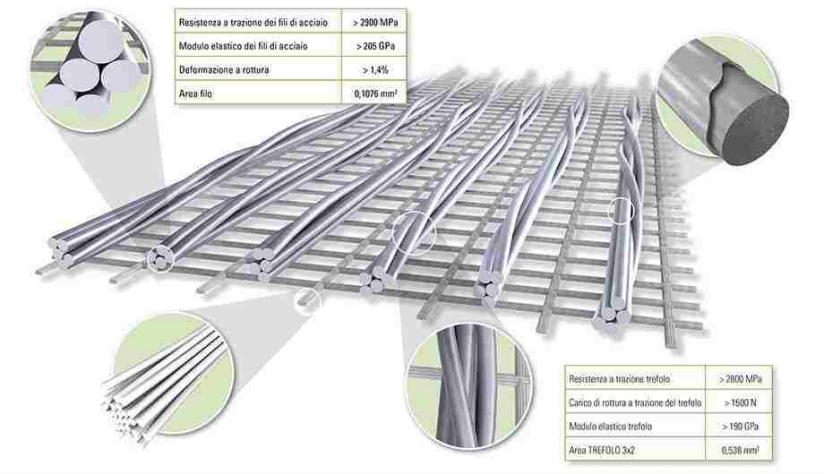

Figure 3.3. Detailed graphic of GeoSteel G1200 fabric (KeraKoll 2017)

www.manaraa.com

3.3.3. Cementitious Matrix. KeraKoll GeoLite geo-mortar was utilized as the cementitious matrix for all FRCM composites tested in this study. GeoLite is a thixotropic inorganic mineral mortar manufactured as a suitable matrix for composite reinforcement systems that utilize KeraKoll GeoSteel products. GeoLite mortar is marketed for concrete and masonry repair and reinforcement and has very low petrochemical polymer content (KeraKoll 2017). Mixture proportions recommended by the manufacturer were utilized for all specimens, resulting in a ratio of approximately 5 liters of water to 25 kilograms of dry mortar material. Smaller quantities of mortar were typically utilized by reducing the above ratio by a factor of four.

Compressive strength and flexural tensile strength values are provided by the manufacturer and are summarized in Table 3.4. Additionally, six 50 mm by 100 mm mortar cylinders were cast from each batch of mortar produced during specimen fabrication. Cylinders were formed in two equal lifts with adequate compaction of the mortar to reduce air voids in the specimens. After fabrication, the cylinders were placed near the single-lap shear specimens and cured following the same procedure (as discussed in Section 3.4.3. All material testing was conducted after 28 days of curing. Compression tests were conducted on three of the six cylinders following the procedure outlined in ASTM C39/C39M-18. Compression tests were conducted in the Load Frame Laboratory in Butler-Carlton Hall at Missouri S&T. Specimens were tested in an 800 kN capacity servo-controlled Tinius Olsen Universal Compression/Tension Machine with a data acquisition PC workstation (Figure 3.4). All cylinders were tested at a rate of approximately 0.25 MPa/sec. The average experimental compressive strength is listed in Table 3.4.

www.manaraa.com

Splitting tensile tests were conducted on the remaining three mortar cylinders. Splitting tensile tests were conducted following the procedure outlined in ASTM C496/C496M-17. The test setup is shown in Figure 3.5. Load was applied to the cylinders at a rate of approximately 90 N/sec. Splitting tensile tests were also conducted in the Load Frame Laboratory in Butler-Carlton Hall at Missouri S&T, using the same testing machine as the compressive strength tests. The manufacturer reported flexural tensile strength is reported in Table 3.3, as well as the average experimental splitting tensile strength for all cylinders cast throughout the experimental program.

Table 3.4. Cementitious matrix measured material properties

Batch Number	Specimens	Average Compressive Strength (MPa)	Coefficient of Variation	Average Splitting Tensile Strength (MPa)	Coefficient of Variation
1	DS_330_50_C_1	32.8	0.132	7.5	0.119
	DS_330_50_C_2				
	DS_330_50_C_3				
	DS_330_50_C_4				
2	DS_330_50_E_1	26.1	0.214	5.1	0.084
	DS_330_50_E_2				
	DS_330_50_E_3				
	DS_330_50_E_4				
3	DS_330_50_M_1	35.0	0.024	5.9	0.119
	DS_330_50_M_2				
	DS_330_50_M_3				
	DS_330_50_M_4				
4	DS_330_50_C_5	33.8	0.192	6.2	0.077
	DS_330_50_C_6S				
	DS_330_50_C_7S				
5	DS_330_50_E_5	35.1	0.052	6.2	0.064
	DS_330_50_E_6S				
	DS_330_50_E_7S				

www.manaraa.com

Table 3.4. Cementitious matrix measured material properties (cont.)

6	DS_330_50_M_5	30.4	0.158	6.0	0.066
	DS_330_50_M_6S				
	DS_330_50_M_7S				
7	DS_100_50_C_1	31.6	0.117	6.7	0.070
	DS_100_50_C_2				
	DS_100_50_C_3S				
	DS_100_50_C_4S				
8	DS_100_50_E_1	30.0	0.095	6.1	0.129
	DS_100_50_E_2				
	DS_100_50_E_3S				
	DS_100_50_E_4S				
9	DS_100_50_M_1	26.5	0.179	6.1	0.039
	DS_100_50_M_2				
	DS_100_50_M_3S				
	DS_100_50_M_4S				
	Average (MPa) =	31.3	0.129	6.2	0.085
	Manufacturer reported values (MPa) =	>50	-	>8	-

Figure 3.4. Compressive strength test setup

www.manaraa.com

Figure 3.5. Splitting tensile strength test setup

A brief discussion of the above material properties is warranted due to the difference between the manufacturer's reported values and the experimental test values. First, Table 3.4 shows that the compressive strength values obtained during the experimental program were considerably lower than the value reported by the matrix manufacturer. This is likely attributed to two things: first, the age of the matrix was nearing the end of its shelf life; and second, the curing procedures followed in this program and followed by the manufacturer were likely different. To the first point, the bags of cementitious material were previously donated by the material manufacturer for another experimental program and were properly stored after initial use. Even though a new bag of matrix material for each batch of prepared mortar, the age of the material

www.manaraa.com

could have affected the material properties (including compressive strength). Additionally, the cylinders cast in this program were cured in the same manner as the single lap shear specimens to give a more accurate representation of the final material properties. Compressive strength cubes were likely cast by the manufacturer and cured in a moist cure room for the duration of the required 28 days. This would also result in tested experimental values to be lower than the manufacturer's reported values.

The tensile strength properties reported by the manufacturer are flexural strength tests conducted on small beams of the matrix material. This method of testing produces a slightly different tension failure, and generally produces higher values. The tensile strength test used in this experimental program was a splitting tensile test conducted on small mortar cylinders, which was expected to produce slightly smaller values. The curing procedure comments also apply to the splitting tensile specimens. Ultimately, the single lap direct shear specimens experienced failure due to delamination between the fiber and inner matrix layer, which is a tensile failure mode. The difference between the expected tensile strength and the experimental tensile strength of the mortar is small enough to be considered acceptable in validating material properties, considering the test setup.

3.3.4. Epoxy Resin. In addition to a cementitious anchor material, an epoxy resin was also investigated as a potential anchor binder and bonding material. The epoxy resin selected was KeraKoll GeoLite Gel (Figure 3.6), a two-part epoxy system. GeoLite Gel is an epoxy mineral adhesive designed by KeraKoll to be used in composite strengthening systems, such as steel-FRP. The compatibility with the steel fibers made it the best choice for use in this study. Part A is a grey paste, and Part B, the hardener, is a beige paste. The

www.manaraa.com

two parts are combined at a mass mixing ratio of 3 kg Part A to 1 kg Part B. Key performance characteristics presented by the manufacturer are listed in Table 3.5. Because the epoxy resin was only utilized in the anchorage, the above mix proportions were reduced by a factor of approximately sixteen.

To mix the epoxy, 180 grams of Part A were placed in a small paper cup on a balance. Then, Part B was slowly added to the cup until the total mass reached 240 grams (fulfilling the ratio requirement with 180 grams to 60 grams). A disposable, plastic stirring stick (due to the small quantity) was used to mix the epoxy until uniform consistency and color were reached.

Figure 3.6. KeraKoll GeoLite Gel epoxy system (KeraKoll, 2017)

Table 3.5. GeoLite Gel manufacturer material properties (KeraKoll 2017)

Performance Characteristic	
Tensile Strength	> 14 N/mm^2
Shear Strength	> 20 N/mm^2
Glass Transition Temperature	+60 °C
Flexural Modulus	> 2500 N/mm^2

www.manaraa.com

3.4. SPECIMEN FABRICATION

Fabrication of specimens took place during the fall of 2017, spring of 2018, and fall of 2018. A total of 33 specimens were cast and tested as a part of the experimental program. The specimen fabrication process, as discussed in Section 3.4.1, was adapted from previous FRCM bond studies conducted at Missouri S&T. The additional anchorage installation procedure is discussed in Section 3.4.2 for both mortar and epoxy anchorages. The curing procedure is discussed in Section 3.4.3, and finally, the strain gauge installation process is outlined in Section 3.4.4.

3.4.1. Control Specimens. All specimens used in this study were cast following the procedure proposed by D'Antino et al. (2014) and Sneed et al. (2016), with slight modification for the specimens with an end anchorage system. Before applying the composite, the concrete prism face of interest (the face where the composite would be applied) was sandblasted to achieve a target roughness profile recommended by the mortar manufacturer. Using coal slag and sandblasting equipment, the surface of the concrete prism was roughened to a profile of approximately 5 mm to ensure proper impregnation of the mortar into the concrete substrate. Figure 3.7 shows the pallet of newly cast concrete prisms prior to sandblasting, and subsequent figures show the exposed aggregate of the sandblasted surface during specimen fabrication.

All specimen casting took place in the Materials Laboratory in Butler-Carlton Hall at Missouri S&T. The external composite was applied to the concrete substrate in a "layer-by-layer" procedure. The mortar layer dimensions and location were controlled with formwork made from foam posterboard. The posterboard forms were cut to 125 mm

www.manaraa.com

by 510 mm rectangles, with a 50 mm by 330 mm rectangle removed from the center (for the 100 mm bonded length specimens, the rectangle measured 50 mm by 100 mm).

Figure 3.7. Newly cast concrete prisms prior to sandblasting

A typical form is shown in Figure 3.8. This process ensured a number of important items: first, using this type of form ensured a uniform thickness of the matrix layer of 5 mm, the thickness of the posterboard (per the manufacturers recommendation); second, it ensured that the composite was centered on the concrete block; finally, it ensured that the composite bond length began 38 mm from the edge of the concrete block. This distance has been specified in other FRCM bond studies and was adopted in this program.

Two forms were required for each specimen, corresponding to the two (internal and external) matrix layers. First, one of the two forms were secured to the concrete

www.manaraa.com

prism with painters' tape to restrain it from moving during composite installation (Figure 3.8). A small amount of water was then applied to the concrete substrate. Proper hydration of the concrete was necessary for matrix-concrete compatibility (per the manufacturer's recommendation). Then, the first layer of cementitious matrix was applied within the rectangular opening in the form, as shown in Figure 3.9. The matrix was impregnated into the concrete substrate with a small hand trowel and compacted to ensure the matrix filled the entire form void. Excess matrix was removed from the first layer by running the hand trowel over the form, smoothing out the top surface of the composite (Figure 3.9). Then, a precut strip of the steel fiber sheet was placed into the matrix layer (Figure 3.10). Fiber sheets were cut to include the total bonded length plus an additional 370 mm of unbonded fibers (as discussed in Section 3.5.1). The steel cords were pressed into the internal matrix layer to promote proper bond between the matrix and the steel fibers. The steel fiber sheet was placed so that the fiberglass backing was bonded to the external matrix layer and the bare steel cords were against the internal matrix layer. The second form was then placed on top of the first, and again secured with tape after being aligned with the internal matrix layer (Figure 3.11). The matrix application process was repeated for the external matrix layer (Figure 3.12).

The procedure outlined above and illustrated in Figures 3.8 through 3.12 was utilized for all specimens in the experimental program. Specimens with a bonded length of 330 mm are shown in the above figures, with the procedure for 100 mm bonded length utilizing shorter forms.

www.manaraa.com

Figure 3.8. First form layer secured to concrete prism

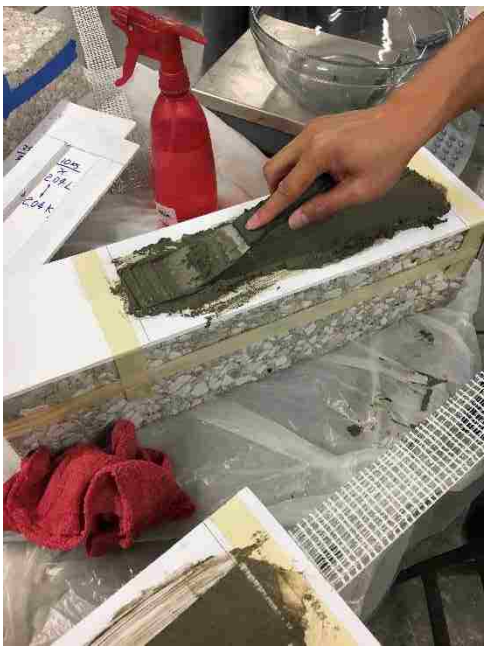

Figure 3.9. Application of first mortar layer to concrete prism

www.manaraa.com

Figure 3.10. Fibers impregnated into internal matrix layer (anchored specimen shown, control specimen similar)

Figure 3.11. Second (external) form secured to concrete prism (anchored specimen shown, control specimen similar)

www.manaraa.com

Figure 3.12. Final (external) matrix layer applied over steel fibers

The specimens were left undisturbed for 24 hours, at which time they were moved into the High Bay Laboratory. The forms were removed, and the specimens were cured following the procedure outlined in Section 3.4.3.

3.4.2. Anchored Specimens. The specimens with an end-anchorage system were fabricated following the same procedure as the control specimens (described in Section 3.4.1), with slight modification to accommodate the anchorage. The first variation in procedure occurred after sandblasting the concrete prisms. For specimens with an anchorage system, a 20 mm diameter hole was drilled into the concrete prism using a Hilti concrete hammer drill (Figure 3.13) at an angle of approximately 45 degrees with respect to the composite bonded length. The location of the hole was marked prior to drilling by reference location of the poasterboard form to ensure proper alignment of the

www.manaraa.com

steel fiber strip. The hole depth varied, either 75 mm or 150 mm, depending on the specimen series. A 20 mm diameter hole was selected to accommodate the 50 mm bonded width of steel fibers that would be placed into the anchor hole. After drilling to the proper depth with a premarked drill bit, excess dust and debris were removed from the hole with compressed air and a shop vacuum. Additionally, the fiber strips were cut to include the bonded length, the additional unbonded portion from the edge of the concrete block to the start of the composite, and the anchorage length. The anchor was assumed to be located directly at the end of the bonded length, and an additional 4 mm were included to account for the height of the internal matrix layer. The fibers were bent prior to installation with the crimping tool shown in Figure 3.14 to match the inclination of the anchor hole. Additionally, the fiberglass backing was removed from the portion of steel fabric being inserted into the anchor hole.

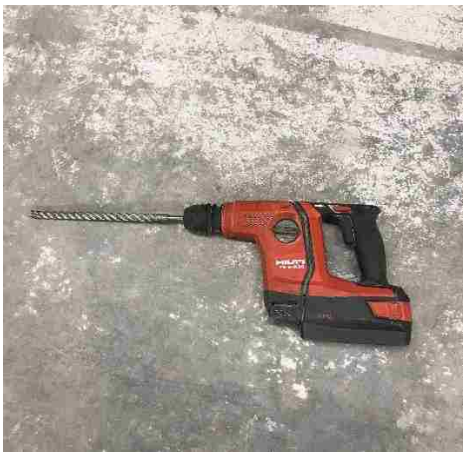

Figure 3.13. Concrete drill used to drill anchor hole into prisms

www.manaraa.com

Figure 3.14. Fiberglass backing removed from anchor portion of steel fibers (75 mm anchor shown, 150 mm anchor similar)

Similar forms were used in fabricating the anchored specimens, with the exception that the bottom portion of the form was removed, as shown in Figure 3.15. The initial internal matrix layer application procedure was identical to the control specimens, as described above (Figure 3.16). Before applying the steel fiber layer, a small amount of anchor material (either epoxy or cementitious matrix) was placed in the bottom of the anchor hole. This was to help ensure that the anchor hole was filled with the anchor-matrix material. Then, the steel fiber strip was placed onto the internal matrix layer, with the anchor portion of the sheet inserted into the anchor hole (Figure 3.17). Additional anchor-matrix material was placed into the anchor hole and compacted with a small, plastic placement device. Material placement was concluded when no additional anchor-matrix material could be placed into the hole, as shown in Figure 3.18. The fabrication

www.manaraa.com

process continued following the procedure outlined for the control specimens, as shown in Figures 3.19 and 3.20.

Figure 3.15. Anchorage hole drilled into concrete prism and internal matrix layer form (100 mm bond length shown, 330 mm bond length similar)

As previously discussed, the anchorage installation procedure was identical, regardless of anchor-matrix material (cementitious mortar or epoxy resin). A close-up of a typical epoxy anchor is shown below in Figure 3.21.

3.4.3. Specimen Curing. After applying the composite, the specimens were left undisturbed for 24 hours to allow for an initial set of the cementitious matrix. After the first 24 hours, the specimens were moved into the High Bay Laboratory in Butler-Carlton Hall at Missouri S&T, where they remained until testing.

www.manaraa.com

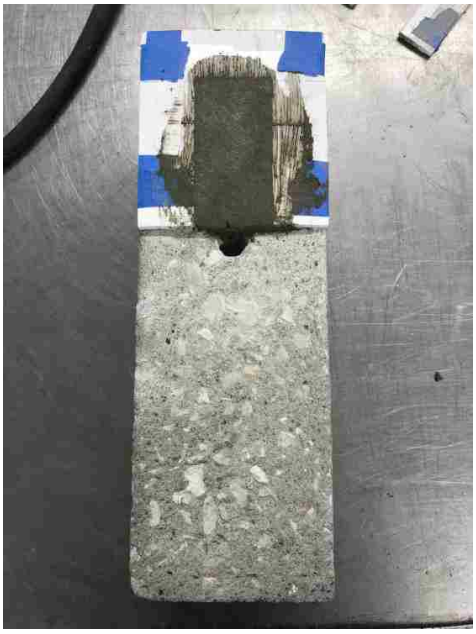

Figure 3.16. Internal matrix layer application for anchorage specimens (100 mm bond length shown, 330 bond length similar)

Figure 3.17. Steel fiber anchor inserted into anchorage hole (100 mm bond length shown, 330 mm bond length similar)

www.manaraa.com

Figure 3.18. Additional anchor-matrix material placement (mortar anchor shown, epoxy anchor similar)

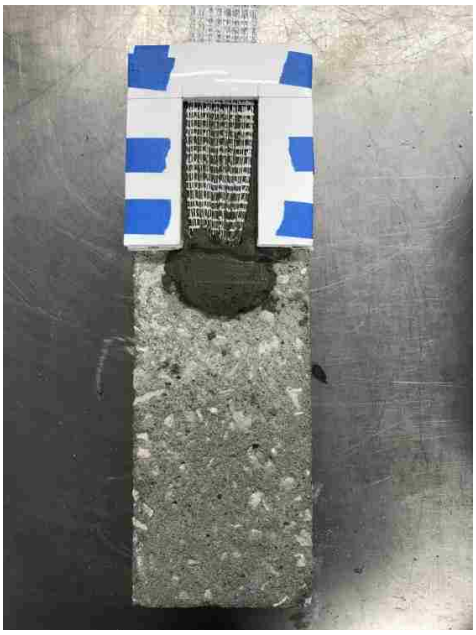

Figure 3.19. External matrix layer form secured onto internal matrix layer form (100 mm bond length shown, 330 mm bond length similar)

www.manaraa.com

Figure 3.20. External matrix layer application (100 mm bond length shown, 330 mm bond length similar)

The specimens were hydrated once per day by placing wet rags over the surface of the composite strip. This process was completed once per day, each day, leading up to the 28-day material testing of the composite. The mortar cylinders (as discussed above in Section 3.3.3) were cured in a similar manner to replicate the curing process of the single lap direct shear specimens.

3.4.4. Installation of Strain Gauges. For specimens denoted with an "S" after the specimen number, strain gauges were applied at discrete points along the centerline of the bonded length of the composite.

www.manaraa.com

Figure 3.21. Detail of epoxy anchor

Further details about the strain gauges are discussed in Section 3.5.3.2. Figure 3.22 shows the strain gauges (depicted as black boxes) along the bonded length. Locations of the strain gauges for 330 mm and 100 mm bond lengths are listed in Table 3.6. Four strain gauges were placed within the composite bonded region, and one strain gauge was placed on the bare steel fibers at the loaded end. While Figure 3.22 seems to suggest that the strain gauges were placed on the exterior matrix layer of the composite, it should be noted that this image is only a visual representation of the location relative to the free end of the composite. The strain gauges were placed directly onto the steel fiber strips, which will be discussed below.

Due to the size and configuration of the steel fiber strands, applying the strain gauges directly to the steel cords was not possible. The braided nature of the wire would not produce direct axial strains, and the small diameter (0.169 mm) would make it nearly impossible to directly attach a strain gauge to a single steel cord.

www.manaraa.com

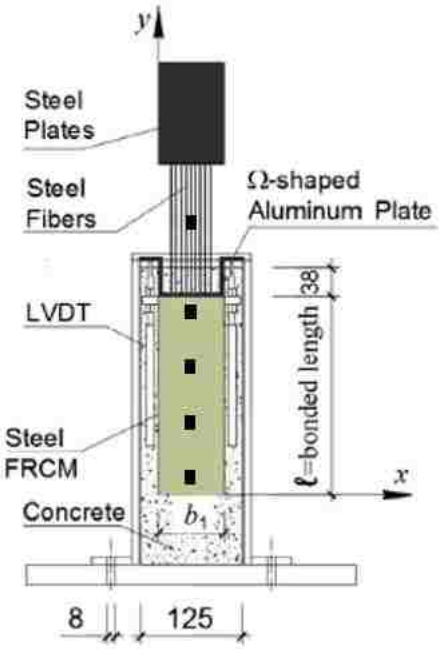

Figure 3.22. Strain gauge layout (adapted from Sneed et al. 2016)

Table 3.6. Strain gauge locations

Bond Length (mm)	Gauge Number	Distance from Free End (mm)
330	0	-
	1	315
	2	215
	3	115
	4	15
100	0	-
	1	87.5
	2	75
	3	50
	4	12.5

Alternatively, the strain gauges were adhered to a small epoxy patch. The strain gauge installation procedure was identical for both the 330 mm and 100 mm bond length specimens. First, the strain gauge locations were marked at discrete points along the fiber

www.manaraa.com

length. Then, the fiberglass backing was removed from behind the future location of each strain gauge as shown in Figure 3.23.

After removing the fiberglass backing, a small amount of GeoLite Gel epoxy was applied to create a surface for the strain gauge to be mounted. The GeoLite Gel was selected due to its compatibility with the GeoSteel G1200 fabric. A typical epoxy patch is shown in Figure 3.24. After hardening, the surface of the epoxy patch was non-uniform and rough (Figure 3.24). The patches were smoothed over with a series of sandpapers, applied in the following successive order: 60 grit, 180 grit, 220 grit, and 400 grit. Additionally, care was taken to try to remove any excess epoxy that had seeped onto the underside of the steel fiber sheet. A final, sanded, epoxy patch is shown in Figure 3.25.

After preparing the epoxy patches, strain gauges were adhered to the center of each patch, directly over two discrete fiber bundles with the centerline of the gauge aligned with the location described in Table 3.5. The strain gauges were applied following the manufacturer's recommendations. Prior to installation of each gauge, the installation instruments, preparation surface, and gauge location were all neutralized with a two-part system to prevent debris from building up under or on the strain gauges. First, each gauge was placed on a clean, dry surface. A small piece of clear tape was placed over the gauge, as shown in Figure 3.26.

The tape was used as an installation aid to help align each gauge in the proper location. Each gauge was transferred from the prepping surface to its final location on the steel fibers (epoxy patch). With the tape peeled back, a small amount of accelerator was applied to the bond surface of each gauge (Figure 3.27).

www.manaraa.com

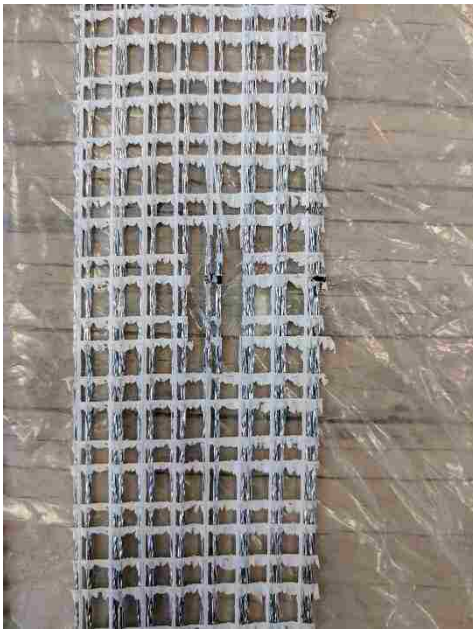

Figure 3.23. Location of strain gauge without fiberglass backing

Figure 3.24. Hardened epoxy patch prior to sanding

www.manaraa.com

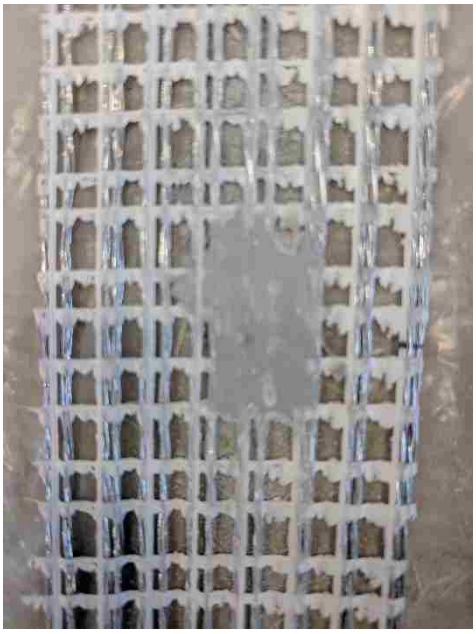

Figure 3.25. Sanded epoxy patch prior to strain gauge installation

After one minute, a drop of adhesive was placed on the epoxy patch and the strain gauge was taped back down to the location within five seconds. One additional minute of firm pressure was applied to the gauge to ensure proper bond. The clear tape remained on the strain gauges until wire leads were attached prior to specimen casting (Figure 3.27). Additionally, a layer of polyurethane was applied over each strain gauge to protect it within the cementitious matrix (Figure 3.28). During specimen fabrication, great care was taken to ensure that the strain gauge leads remained in-tact during the installation of the external matrix layer.

www.manaraa.com

Figure 3.26. Strain gauge prepared for installation

Figure 3.27. Application of accelerant to strain gauge

www.manaraa.com

Figure 3.28. Strain gauge with external leads

3.5. TEST SETUP

Several studies have been conducted to investigate the bond behavior of both FRP and FRCM composites as discussed in Sections 2.2, 2.3, and 2.4. The single lap-direct shear test setup has been utilized successfully in many of these studies and was adopted for this experimental program. Specifically, the single lap direct shear test setup used by D'Antino et al. (2014) and Sneed et al. (2016) was utilized for all tests in this study. This section describes the overall test setup, including the geometry and support conditions, the loading protocol, and the instruments used for data acquisition.

3.5.1. Support Conditions. As previously discussed, the near end supported (NES) single lap shear test setup was implemented in this study. This testing configuration has been used successfully in both FRP and FRCM bond studies and was used during this investigation. Figure 3.29 shows a graphical representation of the test

www.manaraa.com

setup presented in Sneed et al. (2016), and Figure 3.30 shows the actual test setup modeled after Figure 3.29.

As shown in Figures 3.29 and 3.30, each specimen was supported by a steel restraint frame near the loaded end of the composite. The frame was fabricated from strap steel and was secured to the load frame plate with four steel bolts. To accommodate slight tolerances in prism dimensions, thin steel plates were placed between the top of the concrete prism and the top section of the restraint frame to uniformly apply pressure to the top surface of the concrete prism. Two steel plates were attached to the unbonded end of the steel fibers. The steel plates were adhered with a two-part epoxy, QuakeBond by QuakeWrap Inc, to help mitigate slippage of the fiber relative to the crosshead. The plates were also bolted together at each of the four corners to provide a uniform pressure on the gripped fiber. Previous research confirmed that the strength of the epoxy system was adequate to restrain slippage of the fibers relative to the steel plates.

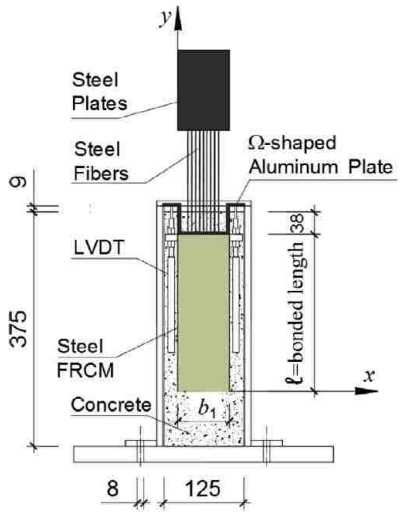

Figure 3.29. Schematic of test setup utilized by Sneed et al. (2016)

www.manaraa.com

Figure 3.30. Test setup

3.5.2. Loading Protocol. The testing frame used in the study was the 250-kip MTS 880 uniaxial servo-hydraulic universal testing machine located in the High Bay Laboratory in Butler-Carlton Hall at Missouri S&T. All specimens were tested under displacement control at a rate of 0.00084 mm/s, controlled by the average of two LVDT readings (further discussion below). This load rate has been used in previous FRCM bond investigations, including steel-FRCM bond studies as discussed in Chapter 2.

Specimens were tested until one of the following criteria was reached: the composite failed due to debonding of the composite at the matrix-fiber interface, the applied load dropped significantly below the peak load (loss of load-carrying capacity), or a global slip value of approximately 1.5 mm was reached. A preload of approximately 350 N was applied to each specimen prior to testing. This preload assisted in the specimen alignment check, verifying that the unbonded fibers were parallel to the load

www.manaraa.com

frame and that there was very little-to-no eccentricity in the specimen at the start of the test. The preload amount was approximately 5% of the peak load and can be considered negligible.

3.5.3. Data Acquisition and Instrumentation. Five channels of the data acquisition system were used during the testing of every specimen. An additional five channels were introduced for specimens with strain gauges. Direct-current linear variable differential transducers (DC-LVDTs) were used on two channels and, when applicable, strain gauges measured uniaxial strain on five channels. The load was recorded by the on-board load cell in the MTS 880 testing machine. The final channel, which determined the displacement control rate, was an average of the two DC-LVDTs. Data were acquired at a rate of 2 samples per second.

3.5.3.1. Direct current-LVDTs. Direct current-linear variable differential transducers (DC-LVDTs) were used to monitor the slip of the steel fiber relative to the cementitious matrix. Each DC-LVDT had a measurable range of ±30 mm. This measurement was taken by utilizing a thin "omega-shaped" steel plate adhered directly to the steel fibers. Figure 3.31 shows a close-up view of the instrumentation. As shown in Figure 3.31, one DC-LVDTs measured the relative displacement of one side of the steel omega. The steel omega was bonded to the first transverse fiberglass bundle outside the bonded region. This location was selected to reduce the influence of elastic elongation of the steel fiber on the measured global slip values. A 2500 psi two-part epoxy was used to adhere the steel omega to limit slippage of the omega along the steel fiber. Additionally, a rectangular piece of foam board was placed behind the omega between the steel fiber and the concrete blocks to limit out-of-plane rotation of the omega

www.manaraa.com

Figure 3.31. Close-up view of instrumentation

Each DC-LVDT was secured by two threaded nuts screwed on either side of an aluminum mounting bracket. The mounting brackets were adhered to the concrete blocks with a quick setting two-part epoxy. Care was taken during installation to make sure that the mounting brackets were placed square to the composite to prevent misalignment of the DC-LVDTs.

The load rate of the MTS machine was controlled based on the readings of the two DC-LVDTs. Load was applied to the composite strip at a rate that would increase the average of the two readings by 0.00084 mm/s. This test method has been used in other FRCM bond investigations to directly measure fiber slippage with limited influence of elastic fiber elongation, matrix-concrete slippage and uneven stress distribution along the width of fiber.

www.manaraa.com

3.5.3.2. Uniaxial strain gauges. Five 120 Ω electrical resistance uniaxial strain gauges were used on 12 of the 33 specimens. Gauges were applied in the longitudinal direction of the composite length. Special care was taken to ensure that the gauges were functioning properly prior to testing. Only one strain gauge malfunctioned during testing and experienced partial blackout that resulted in a loss of some collected values. During installation, care was taken to make sure that the strain gauge interfered with as little of the bond between steel fibers and cementitious matrix as possible. The strain gauges were hooked up to a standard two-wire configuration testing machine and were manually zeroed prior to the start of testing.

www.manaraa.com

4. EXPERIMENTAL RESULTS AND DISCUSSION

4.1. OVERVIEW

This section discusses the results of the experimental test program. A summary of the key test results is presented below in Section 4.1.1. The general specimen behavior and failure mode are discussed in Section 4.1.2 and 4.1.3, respectively. The applied load vs. global slip response is presented in Section 4.2, and the strain distribution results are presented and discussed in Section 4.3. In Section 4.4, the influence of the test parameters is presented, with a summary of key findings in Section 4.5.

4.1.1. Summary of Results. This section summarizes the collected data from the experimental program. Table 4.1 provides a summary of key values obtained during testing, including peak load P^*, global (i.e. loaded end) slip at peak load g^*, ultimate (failure) load P_{ult}, global slip at ultimate load g_{ult}, and absorbed energy E_{ult}. P^* corresponds to the maximum applied load P reached during testing. The ultimate load corresponds to the applied load at failure of the composite, as discussed further in Section 4.1.3. The absorbed energy corresponds to the area under the applied load-global slip curve up to the ultimate load P_{ult} and corresponding ultimate global slip g_{ult}. This value is an indication of the energy absorbed during testing but does not represent a specific energy value. It can be used as a basis of comparison only. Averages values are shown in Table 4.2. Specimens denoted with a "+" were not included in the calculation of average values. Inspection of the peak load values from Table 4.1 for the 100 mm bonded length specimens with strain gauges shows a considerable difference in peak load. A complete discussion on this issue can be found in Section 4.2.

www.manaraa.com

Table 4.1. Summary of test results

Specimen ID	Peak Load, P^* (kN)	Global Slip at Peak Load, g^* (mm)	Ultimate Load, P_{ult} (kN)	Global Slip at Ultimate Load, g_{ult} (mm)	g^*/g_{ult}	Absorbed Energy, E_{ult} (J)
DS_330_50_C_1	6.36	1.67	6.28	1.68	1.00	9.13
DS_330_50_C_2	7.34	0.56	5.66	1.17	0.48	7.08
DS_330_50_C_3	8.06	1.61	7.73	1.79	0.90	12.86
DS_330_50_C_4	8.49	1.36	7.11	1.52	0.89	11.38
DS_330_50_C_5	6.98	1.44	6.70	1.53	0.94	8.84
DS_330_50_C_6s	7.44	1.24	7.30	1.27	0.97	7.93
DS_330_50_C_7s	9.68	1.52	8.97	1.71	0.89	13.78
DS_330_50_E_1	9.59	0.53	7.32	1.34	0.39	11.81
DS_330_50_E_2	8.09	0.10	6.05	1.26	0.08	7.48
DS_330_50_E_3	7.89	1.00	6.61	1.28	0.78	9.19
DS_330_50_E_4	8.88	1.63	6.89	1.78	0.91	14.62
DS_330_50_E_5	10.77	0.29	8.14	1.46	0.20	11.08
DS_330_50_E_6s	9.00	0.59	3.33	1.22	0.48	7.59
DS_330_50_E_7s	5.97	0.83	4.39	1.23	0.68	5.75
DS_330_50_M_1	8.78	1.34	8.54	1.46	0.92	11.02
DS_330_50_M_2	9.07	1.84	8.92	1.96	0.94	15.84
DS_330_50_M_3	7.53	0.37	7.46	1.30	0.29	7.84
DS_330_50_M_4	8.24	1.17	7.46	1.20	0.97	8.45
DS_330_50_M_5	8.00	1.57	7.53	1.64	0.96	10.45
DS_330_50_M_6s	7.01	1.24	5.89	1.28	0.97	7.45
DS_330_50_M_7s	5.79	0.94	4.92	0.98	0.96	4.59
DS_100_50_C_1	6.33	0.15	1.91	0.32	0.46	1.47
DS_100_50_C_2	6.30	0.18	2.37	0.30	0.59	1.47
DS_100_50_C_3s$^+$	3.66	0.12	0.90	0.41	0.30	1.06
DS_100_50_C_4s$^+$	3.22	0.16	0.55	0.46	0.33	0.76
DS_100_50_E_1	8.22	0.27	1.38	0.60	0.45	2.38
DS_100_50_E_2	7.48	0.25	0.80	1.08	0.23	4.40
DS_100_50_E_3s$^+$	4.15	0.19	0.79	0.67	0.28	1.62
DS_100_50_E_4s$^+$	4.65	0.22	0.61	0.64	0.35	1.59
DS_100_50_M_1	7.72	0.19	0.86	0.60	0.32	2.55
DS_100_50_M_2	7.74	0.27	2.19	0.60	0.44	2.83
DS_100_50_M_3s$^+$	5.96	0.31	5.75	0.61	0.51	3.16
DS_100_50_M_4s$^+$	4.50	0.16	1.02	0.64	0.25	1.55

المنارة للاستشارات
www.manaraa.com

Table 4.2. Average of test results for each series

Specimen ID	Average Peak Load, $\overline{P^*}$ (kN)	Average Global Slip at Peak Load, $\overline{g^*}$ (mm)	Average Ultimate Load, $\overline{P_{ult}}$ (kN)	Average Global Slip at Ultimate Load, $\overline{g_{ult}}$ (mm)	Average $\overline{g^*/g_{ult}}$, $\overline{g^*}/\overline{g_{ult}}$	Average Absorbed Energy, $\overline{E_{ult}}$ (J)
DS_330_50_C_1	7.76 (CoV = 0.141)	1.34 (CoV = 0.279)	7.11 (CoV = 0.15)	1.52 (CoV = 0.151)	0.87 (CoV = 0.202)	10.14 (CoV = 0.252)
DS_330_50_C_2						
DS_330_50_C_3						
DS_330_50_C_4						
DS_330_50_C_5						
DS_330_50_C_6s						
DS_330_50_C_7s						
DS_330_50_E_1	8.61 (CoV = 0.091)	0.82 (CoV = 0.802)	6.72 (CoV = 0.079)	1.42 (CoV = 0.175)	0.54 (CoV = 0.696)	10.77 (CoV = 0.29)
DS_330_50_E_2						
DS_330_50_E_3						
DS_330_50_E_4						
DS_330_50_E_5	8.58 (CoV = 0.283)	0.57 (CoV = 0.48)	5.29 (CoV = 0.478)	1.3 (CoV = 0.103)	0.45 (CoV = 0.533)	8.14 (CoV = 0.332)
DS_330_50_E_6s						
DS_330_50_E_7s						
DS_330_50_M_1	8.4 (CoV = 0.08)	1.18 (CoV = 0.518)	8.1 (CoV = 0.093)	1.48 (CoV = 0.228)	0.78 (CoV = 0.423)	10.79 (CoV = 0.337)
DS_330_50_M_2						
DS_330_50_M_3						
DS_330_50_M_4						
DS_330_50_M_5	6.93 (CoV = 0.159)	1.25 (CoV = 0.251)	6.11 (CoV = 0.216)	1.3 (CoV = 0.254)	0.96 (CoV = 0.009)	7.5 (CoV = 0.391)
DS_330_50_M_6s						
DS_330_50_M_7s						
DS_100_50_C_1	6.31 (CoV = 0.003)	0.16 (CoV = 0.135)	2.14 (CoV = 0.152)	0.31 (CoV = 0.038)	0.53 (CoV = 0.173)	1.47 (CoV = 0.001)
DS_100_50_C_2						
DS_100_50_C_3s$^+$						
DS_100_50_C_4s$^+$						
DS_100_50_E_1	7.85 (CoV = 0.066)	0.26 (CoV = 0.044)	1.09 (CoV = 0.377)	0.84 (CoV = 0.403)	0.34 (CoV = 0.443)	3.39 (CoV = 0.422)
DS_100_50_E_2						
DS_100_50_E_3s$^+$						
DS_100_50_E_4s$^+$						
DS_100_50_M_1	7.73 (CoV = 0.001)	0.23 (CoV = 0.234)	1.52 (CoV = 0.617)	0.6 (CoV = 0.002)	0.38 (CoV = 0.233)	2.69 (CoV = 0.073)
DS_100_50_M_2						
DS_100_50_M_3s$^+$						
DS_100_50_M_4s$^+$						

www.manaraa.com

4.1.2. Specimen Behavior. All specimens were tested in the single-lap direct shear test set-up as discussed in Section 3.5. One primary assumption of the test set-up is that the applied load is evenly distributed across the width of the steel fibers. The load distribution can be indirectly observed based on the individual LVDT readings (see Figure 3.29). While the test was controlled by the average of the two LVDT readings, the individual readings can be used to determine the symmetry of the system. Figure 4.1 and 4.2 show individual LVDT readings and the average of the two LVDT readings versus virtual time for two specimens. This comparison shows how the individual readings vary compared to the average reading used to control the test. Figure 4.1 shows a "well-behaved" specimen, meaning the individual LVDT readings do not significantly vary compared to the average (or rather, the difference between the two LVDT readings is small, as discussed below). Figure 4.2 shows a "poorly-behaved" specimen. This specimen was classified as "poorly-behaved" due to the large difference in the individual LVDT readings between t=250 and t=3250. This difference in readings shows that the applied load was not applied evenly across the width of the composite, causing rotation of the steel "omega" shape used to monitor global slip. This phenomenon is shown in Figure 4.3.

The study conducted by Carloni et al. (2015) based their classification criterion on the results of a fracture mechanics analysis. Specimens were classified as "well-behaved" if the absolute value of the difference between the two LVDT readings was less than the average slip value corresponding to the peak shear stress (C. Carloni et al., 2015). Their criterion was based on available experimental test data, but due to the limited availability of steel-FRCM test data, a similar criterion was not adopted in this study. Rather, all

www.manaraa.com

specimens were included for analysis. The global slip vs. virtual time plots for all specimens are presented in Appendix B, which were evaluated on a qualitative basis for comparison. All specimens in the experimental program show a reasonable relationship between LVDT readings compared to the average. Moreover, if a considerable difference was observed in the LVDT readings, it was typically after the peak load (shown by the dashed line in Figure 4.1 and Figure 4.2), or in the case of anchored specimens, after the ultimate load. This suggests an even applied load distribution up to points of interest, demonstrating the reasonable reliability of the collected data.

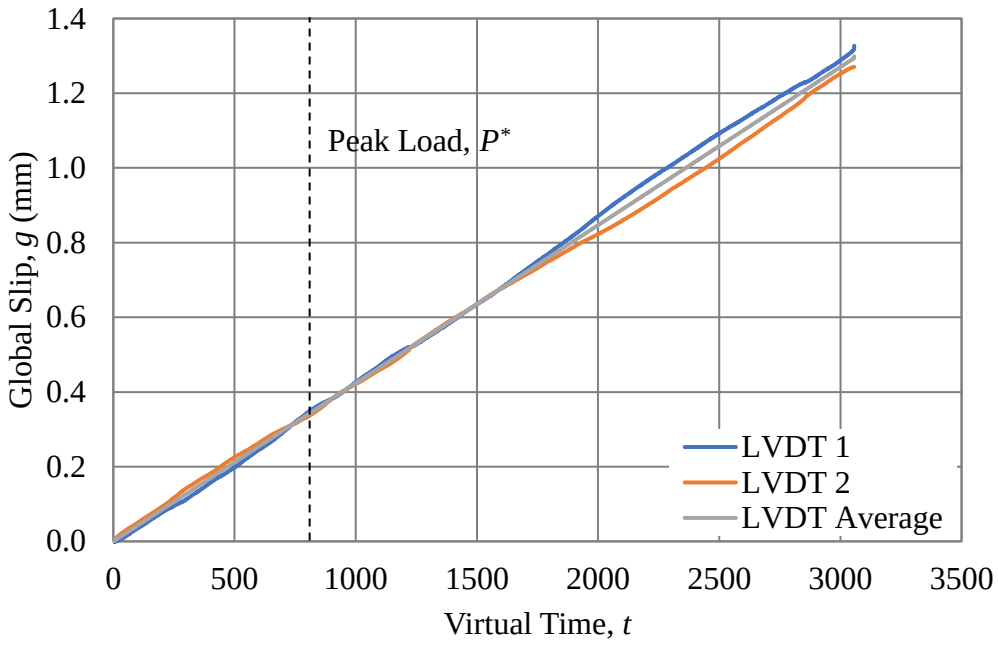

Figure 4.1. Individual LVDT and average LVDT comparison for well-behaved specimen (DS_330_50_M_3)

www.manaraa.com

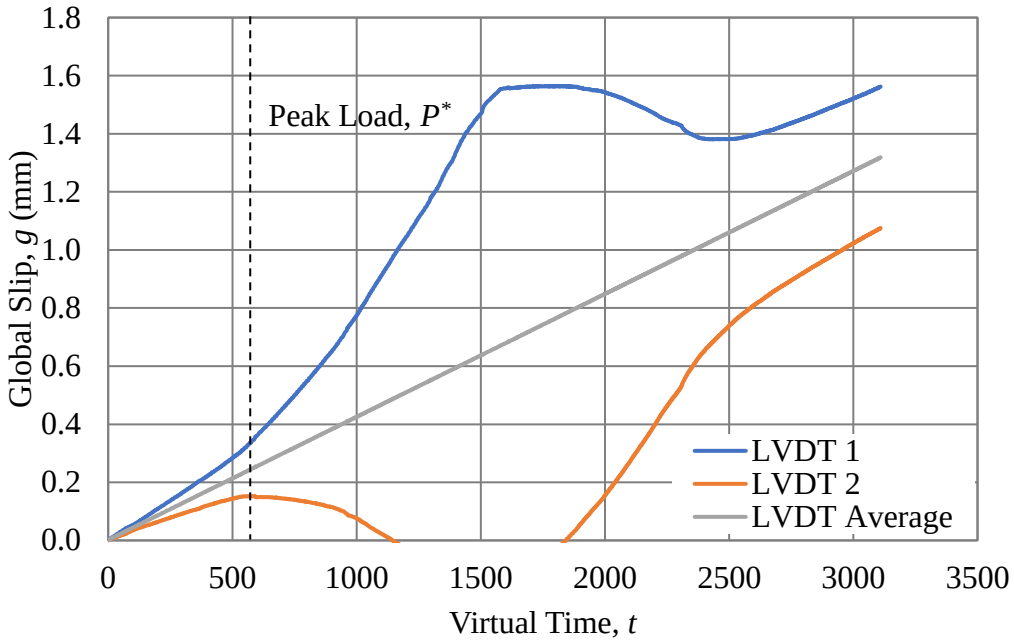

Figure 4.2. Individual LVDT and average LVDT comparison for poorly-behaved specimen (DS_100_50_E_2)

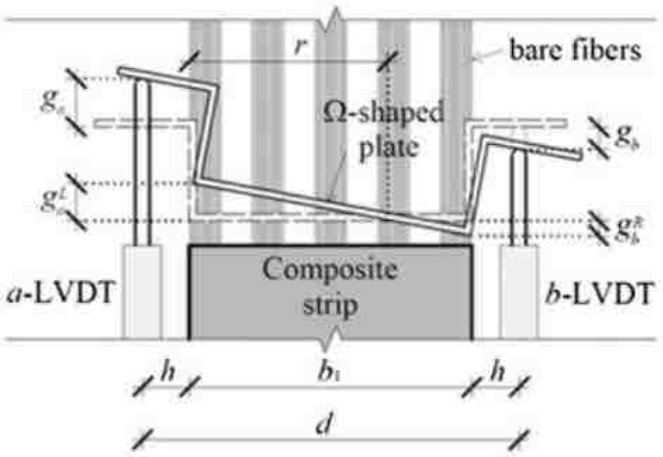

Figure 4.3. Rotation of Ω-shaped plate (Carloni et al. 2015)

www.manaraa.com

4.1.3. Failure Mode. Each specimen was tested until it reached a predetermined failure criterion, which was primarily based on a significant drop in applied load. For the control specimens, failure was observed by complete debonding of the fiber strip and external matrix layer, as discussed in Section 4.1.3.1. For the anchored specimens, the specimen was considered to have reached failure after the applied load dropped significantly compared to the peak load, and the only mechanism keeping the fiber strip attached to the concrete prism was the end-anchor. This failure mode is thoroughly discussed in Section 4.1.3.2.

4.1.3.1. Control specimens. The failure mode of all control specimens without an end anchorage system was characterized by composite debonding at the fiber-internal matrix interface. This failure plane is shown in Figure 2.3b in Section 2. This failure plane is different from the PBO-FRCM failure plane, which occurs between both the internal and external matrix layers (as shown in Figure 2.3a). For PBO-FRCM, the matrix layer initially does not fracture at failure as the fibers continue to slip relative to both the internal and external matrix layers (Carloni et al., 2015; D'Antino et al., 2014). Steel-FRCM composites, however, do not experience this failure phenomenon. At the start of testing, as the load was applied, the composite showed no visible signs of damage on the external matrix layer surface. After a certain load point, however, small hairline cracks began to form on the external matrix layer in the transverse direction. Figure 4.4 shows the formation of the first hairline crack formed on specimen DS_330_50_C_1. This cracking phenomenon was observed in all of the control specimens.

www.manaraa.com

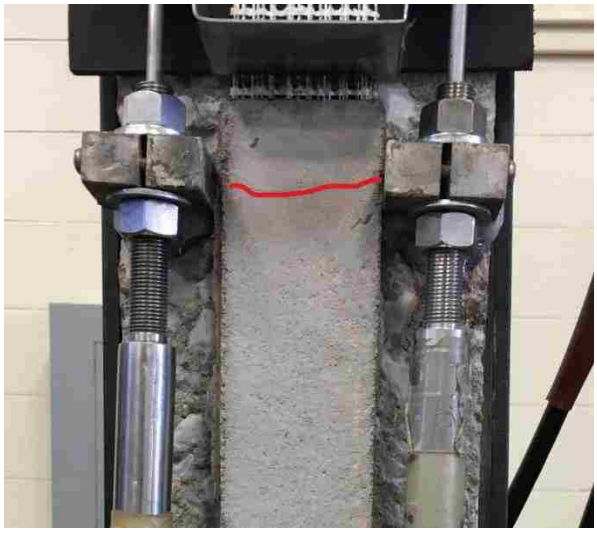

Figure 4.4. Formation of first hairline crack during load application (crack shown in red)

As loading continued, additional hairline cracks began to form at other locations along the exterior face of the composite. Figure 4.5 shows the exterior matrix layer of specimen DS_330_50_C_1 prior to failure. Six visible transverse cracks formed on the external matrix layer, which developed throughout the testing process. The cracks formed first at the loaded end of the composite, with each successive crack forming closer to the free (unloaded) end of the composite during testing. The spacing of the transverse cracks varied for each specimen, and transverse cracking was not observed in the internal matrix layer after testing was complete and the load was removed.

In addition to the transverse cracks along the external matrix layer, longitudinal (interfacial) cracking was also observed during testing. Beginning from the loaded end of the composite, a longitudinal crack propagated down towards the free end of the composite throughout testing on both sides of the composite strip. Figure 4.6 shows the

www.manaraa.com

formation and location of the longitudinal (interfacial) crack for specimen DS_330_50_C_1.

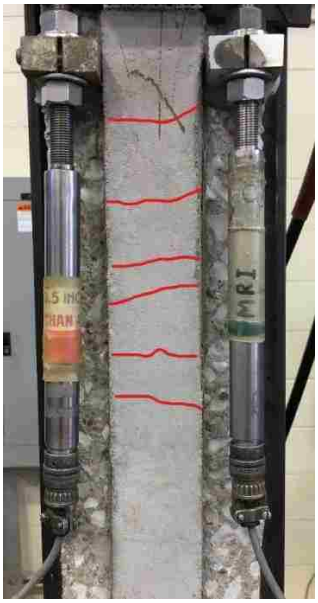

Figure 4.5. Transverse cracking for specimen DS_330_50_C_1 (cracks shown in red)

In addition to the transverse cracks along the external matrix layer, longitudinal (interfacial) cracking was also observed during testing. Beginning from the loaded end of the composite, a longitudinal crack propagated down towards the free end of the composite throughout testing on both sides of the composite strip. Figure 4.6 shows the formation and location of the longitudinal (interfacial) crack for specimen DS_330_50_C_1.

www.manaraa.com

Figure 4.6. Longitudinal crack between internal and external matrix layer for specimen DS_330_50_C_1 (longitudinal crack shown in blue)

As previously mentioned, the longitudinal crack formed progressively throughout testing as it propagated along the bonded length of the composite. While not visible in this photo due to the aluminum LVDT mounts, the longitudinal crack did originate at the loaded end of the composite. Figure 4.6 shows that the longitudinal crack only slightly propagates past the formation of the last transverse crack. This relationship suggests that the transverse cracks are a consequence of the longitudinal crack propagation.

Failure of the control specimens was ultimately observed after sudden and brittle debonding of the steel fibers and external matrix layer from the internal matrix layer. The longitudinal crack propagation signified debonding between the internal matrix layer and steel fibers. At a certain length of longitudinal crack propagation, the external matrix layer and steel fibers suddenly debonded from the internal matrix layer. Figure 4.7 shows specimen DS_330_50_C_1 after failure.

www.manaraa.com

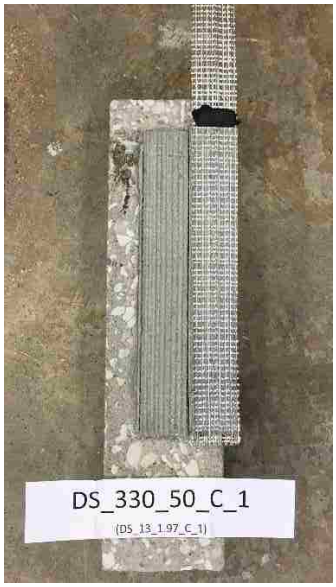

Figure 4.7. Failure of control specimen DS_330_50_C_1

In Figure 4.7, the internal matrix layer is still bonded to the concrete substrate. Longitudinal grooves in the internal matrix layer indicate the bond between the steel fibers and the internal matrix layer. Additionally, the external matrix layer is shown attached to the steel fibers. A study conducted by Sneed et al. (2016) investigated the role of the external matrix layer in steel-FRCM composites tested in single lap direct shear. Their results suggested minimal contribution from the external matrix layer due to little variation in performance from specimens with and without an external matrix layer (Sneed et al., 2016). This conclusion is supported based on the failure of the control specimens in this experimental program.

4.1.3.2. Anchored specimens. The failure of the anchored specimens was also characterized by composite debonding at the fiber-internal matrix layer interface. The failure mode was very similar to the control specimens in that a longitudinal crack

www.manaraa.com

propagated along the bonded length of the composite, causing transverse cracks to form on the external matrix layer. Figure 4.8 shows the transverse crack pattern for specimen DS_330_50_E_3. Figure 4.9 shows the longitudinal crack propagation along the length of the composite.

Failure of the anchored specimens was ultimately observed after a significant reduction in the applied load (as shown in the applied load vs. global slip response in Section 4.2). This drop was often accompanied by a loud popping sound, which was attributed to the remaining bonded portion fracturing in a similar manner to the control specimens. However, unlike the control specimens, the significant reduction in applied load did not end the test. At failure, the longitudinal crack had propagated along the bonded length of the composite and reached the end anchor, as shown in Figure 4.10. After failure, the only load carrying mechanism was the end anchorage – the steel fiber strip had completely debonded from the internal matrix layer, as shown in Figure 4.11. After failure, data collection continued for a short period to capture the post-failure response. This portion of the applied load-global sip curve was recorded for a select few specimens, as shown in Section 4.2. This portion of the data, however, is not reliable for quantitative data analysis as a result of the significant disruption from composite debonding. Specimens were not tested to anchor failure, as the shock from the composite debonding failure caused significant rotation of the Ω-shape, which distorted the collected data.

www.manaraa.com

Figure 4.8. Transverse crack pattern for typical anchored specimen (specimen DS_330_50_E_3 shown, transverse cracks shown in red)

Figure 4.9. Side view of specimen DS_330_50_E_3 showing longitudinal crack between internal and external matrix layer (shown in blue)

www.manaraa.com

Figure 4.10. Longitudinal crack propagation into end anchorage at failure (specimen DS_330_50_E_4)

Figure 4.11. Complete debonding of steel fiber at failure (specimen DS_330_50_E_4)

www.manaraa.com

4.2. APPLIED LOAD-GLOBAL SLIP RESPONSE

This section presents the applied load vs. global slip (*P-g)* response for all specimens in this experimental program. The applied load *P* is defined as the load applied to the bare steel fibers from the testing machine. The global slip *g* is defined as the average value obtained from the two LVDT readings and represents the slip of the steel fibers relative to the concrete block at the loaded end of the composite. The applied load-global slip response of the control specimens is presented in Section 4.2.1. Section 4.2.2 includes the *P-g* curves for the epoxy anchor series specimens, and Section 4.2.3 presents the *P-g* curves for the mortar anchor series specimens. For each curve, the ultimate load, P_{ult} is denoted with a black "x". The individual applied load-global slip response curves of specimens not shown individually in Section 4.3 can be found in Appendix A.

4.2.1. Control Specimens. This section presents the *P-g* curves for the control specimens without an end anchorage system tested in this program.

4.2.1.1. 330 mm bonded length specimens. The applied load vs global slip response for each of the 330 mm bonded length control series specimens is shown in Figure 4.12. The overall shape of the response is similar to the general *P-g* curve discussed in Section 2.2. All tested control specimens show a consistent initial stiffness in the elastic portion of the response. After the initial elastic portion of the curve, the slope decreases, and the response becomes non-linear, signifying the start of damage up to the debonding load, P_{deb}. The increase in applied load after this point is attributed partially to the friction between the internal matrix layer and the steel fiber at points within the longitudinal crack region, as well as the bond mechanism between the steel fiber and the matrix layer beyond the longitudinal crack formation. The load increases almost linearly

www.manaraa.com

up to the peak load, P^*, and ultimately the failure load, P_{ult} where the remaining length of bonded composite is unable to support the applied load, leading to failure of the composite. Specimen DS_330_50_C_3 is a good representation of this response, with the other specimens mirroring the behavior with slight experimental variability.

Specimen DS_330_50_C_1 shows a sudden decrease in applied load after the initial linear branch, but before reaching the debonding load (note it is not possible to identify the location of the debonding load without strain readings, so this is only an estimation of its location based on the applied load-global slip response). This is attributed to some internal damage at the matrix-fiber interface (not debonding), a phenomenon that was observed in a select few other specimens.

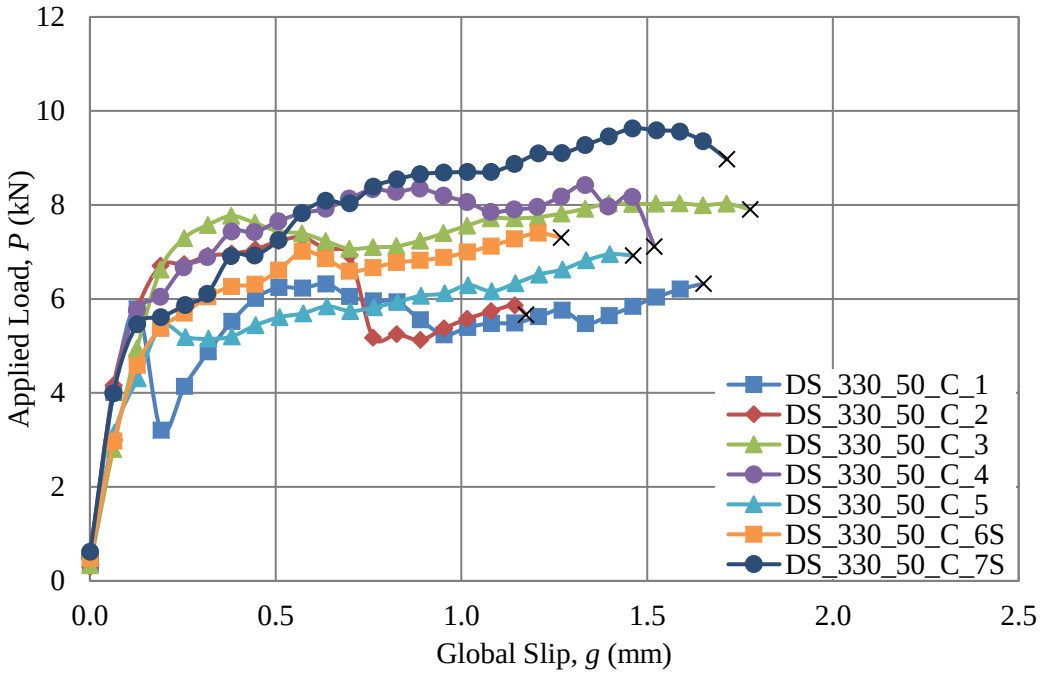

Figure 4.12. Applied load vs. global slip response for 330 mm bonded length control series specimens

www.manaraa.com

4.2.1.2. 100 mm bonded length specimens. The applied load vs. global slip response for each of the 100 mm bonded length control series specimens is shown in Figure 4.13. The response of the 100 mm bonded length specimens is initially similar to the response of the 330 mm bonded length specimens, marked by a consistent initial slope in the elastic stage. However, for the 100 mm bonded length specimens, the peak load is reached immediately in the following the softening stage. The 100 mm bonded length specimens lack a linearly increasing portion of the *P-g* response, which is attributed to the inability of the composite to fully develop the stress transfer zone. This concept is fully discussed in terms of the strain analysis in Section 4.3.

The peak load of specimens DS_100_50_C_3S and DS_100_50_C_4S is considerably lower compared to the peak load of specimens DS_100_50_C_1 and DS_100_50_C_2. The only difference between the specimens was the presence of strain gauges, which is likely the cause of the decreased performance. During strain gauge installation, a small epoxy patch was placed at discrete locations along the centerline of the steel fibers. A small portion of that epoxy patch disrupted the bond between the steel fiber and the internal matrix layer. For the 330 mm bonded length specimens, this disruption was relatively small compared to the overall bonded area. For the 100 mm bonded length specimens, however, this reduction in contact area between the steel fibers and the internal matrix layer was significant. The *P-g* curves for the 100 mm bonded length control specimens with strain gauges performed poorly compared to the counterpart without strain gauges, suggesting that the strain gauge installation technique used in this study did have an adverse effect on the bond performance for the 100 mm

www.manaraa.com

bonded length specimens. The reduction in peak load for strain gauge specimens was also observed in the anchor series specimens (discussed in Section 4.2.2 and Section 4.2.3).

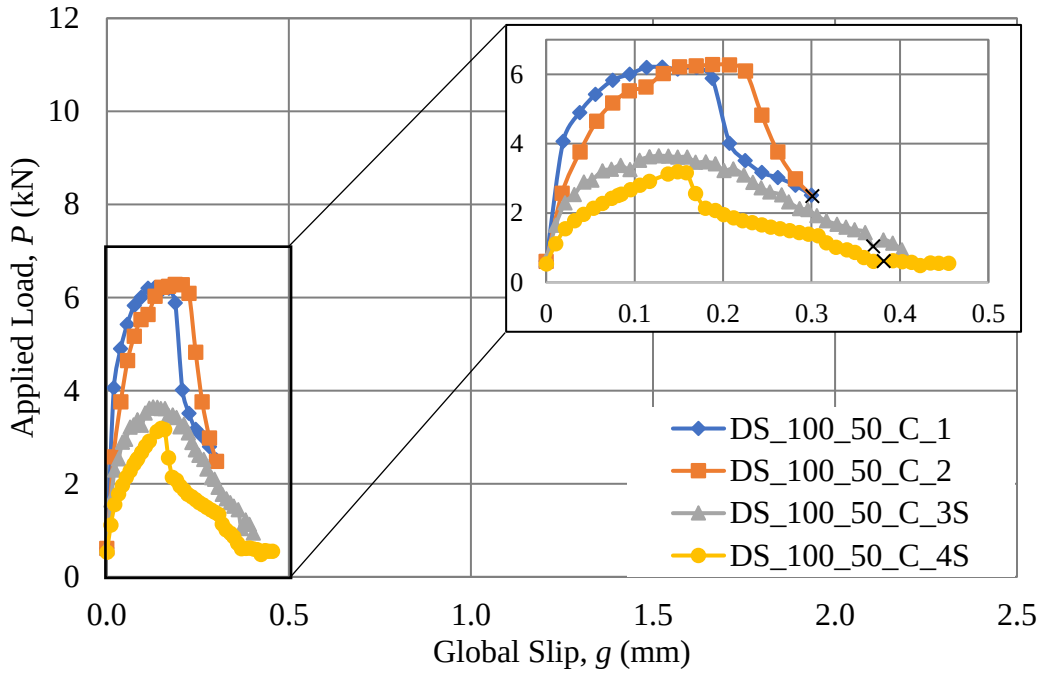

Figure 4.13. Applied load vs. global slip response for 100 mm bonded length control series specimens

4.2.2. Epoxy Anchored Specimens. This section presents the applied load-global slip response for the specimens anchored with an epoxy anchor binder material.

4.2.2.1. 330 mm bonded length specimens. The P-g response for each of the 330 mm bonded length specimens anchored with an epoxy anchor binder material is shown in Figure 4.14. The same applied load-global slip curves are shown in Figure 4.15 with three control specimens plotted in gray for comparison. The behavior of the epoxy

www.manaraa.com

anchored specimens is similar to the control specimens before reaching the failure load. A similar initial slope is observed in the epoxy anchor specimens compared to the control specimens, which was expected. Figure 4.14 shows some experimental variability in the response of the tested specimens. Specimens DS_330_50_E_2, DS_330_50_E_5, and DS_330_50_E_6S all experienced a sharp decrease in applied load after reaching an early peak load. Specimen DS_330_50_E_7S also experience a similar decrease much earlier in the applied load-global slip response, which caused the peak load to be lower than other replicate specimens.

After failure, the *P*-g response for specimens DS_330_50_E_3, DS_330_50_E_4, and DS_330_50_E_5 shows that the applied load did not drop to zero , but rather decreased to a constant value. This is a key difference from the response of the control specimens. At failure, the control specimens' load carrying capacity dropped to zero due to the complete debonding of the composite at the internal matrix layer-steel fiber interface. While the same debonding occurred at failure for the epoxy anchored specimens, the steel fibers remained anchored at the end of the concrete block, which allowed for some sustained load carrying capacity. It should be noted that the end of the response plotted in Figure 4.14 was not due to pullout failure of the anchor. As previously mentioned, the debonding failure of the composite caused excessive rotation of the instrumentation used to control the loading during testing, making the collected data after failure unreliable. The data points plotted after failure are shown only to illustrate the capacity of the anchor to maintain some load carrying capacity.

The area under the *P-g* curve is an indication of the amount of energy absorbed by the composite during testing. The individual and average values reported in Table 4.1 and

www.manaraa.com

Table 4.2, respectively, show an insignificant increase in the absorbed energy for the epoxy anchor specimens compared to the control specimens. The coefficient of variation (CoV) reported in Table 4.2 suggests a scattering of the collected data, so further test results may show a measurable increase due to the anchorage system. Additionally, the energy calculations only include data points up to the failure load, P_{ult} (marked with a black "x" on the *P-g* curves), which does not include a significant portion of the *P-g* curve after failure (when load is sustained by the anchor after composite debonding). If that portion of the curve was included, the absorbed energy would likely be higher for the epoxy anchor specimens compared to the control specimens.

4.2.2.2. 100 mm bonded length specimens. Figure 4.16 shows the applied load vs. global slip response for the 100 mm bonded length specimens anchored with an epoxy anchor binder material. Just as in the 100 mm bonded length control series specimens, a considerable decrease in peak load was observed in the 100 mm bonded length epoxy anchor series specimens with strain gauges compared to their non-strain gauge counterparts. The general response of the 100 mm bonded length specimens was similar to that of the control specimens prior to failure. However, an increase in peak load was observed for the specimens without strain gauges relative to the control specimens of a similar bonded length. Figure 4.17 shows the *P-g* response of the epoxy anchor specimens plotted with the control specimen response. Not only was the observed peak load P^* larger compared to the control specimens, but the slip at failure g_{ult} was also larger. As with the 330 mm bonded length specimens, the end of the plotted data points in Figure 4.16 and 4.17 do not represent failure of the anchor, but rather represent the sustained load reached after debonding of the composite strip.

www.manaraa.com

The absorbed energy for the 100 mm bonded length epoxy anchor specimens was higher than for the 100 mm bonded length control specimens. This is a significant advantage of the anchor system. Even without considering any portion of the *P-g* curve after failure (where a sustained load would increase the absorbed energy), the total absorbed energy, or area under the *P-g* curve, was still larger than the control specimens.

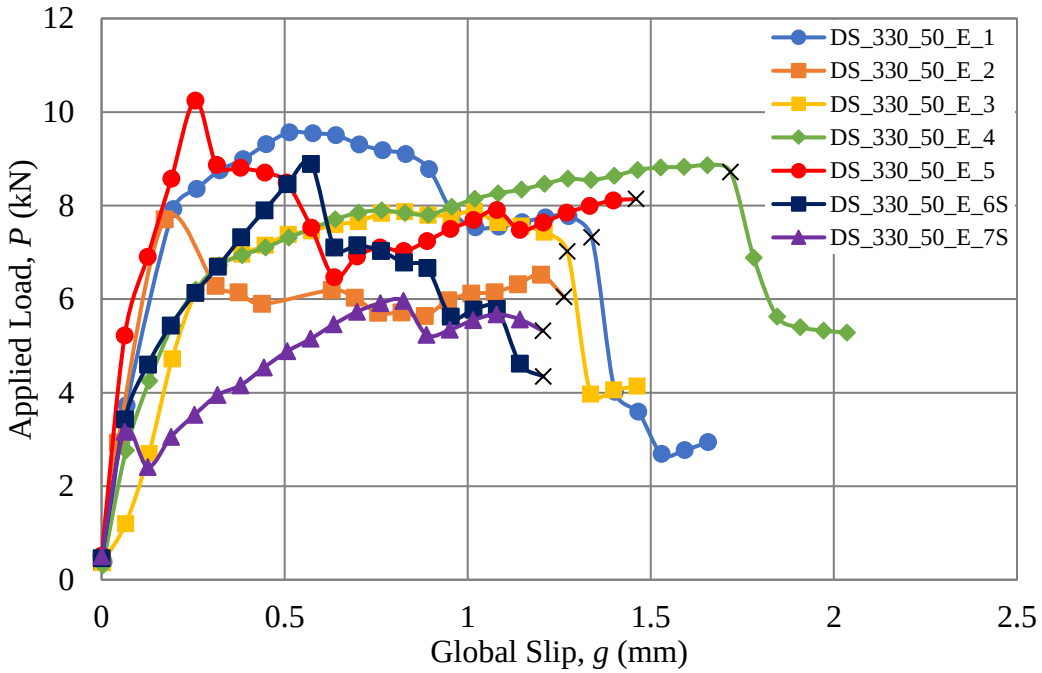

Figure 4.14. Applied load vs. global slip response for 330 mm bonded length epoxy anchor series specimens

www.manaraa.com

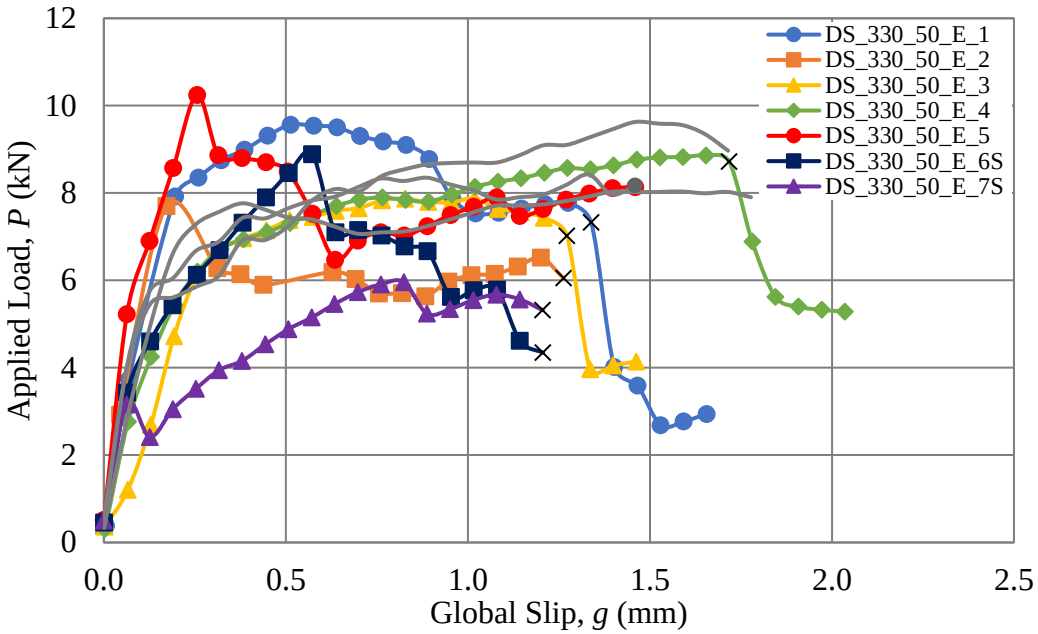

Figure 4.15. Applied load vs. global slip response for 330 mm bonded length epoxy anchor series specimens compared to 330 mm bonded length control specimens

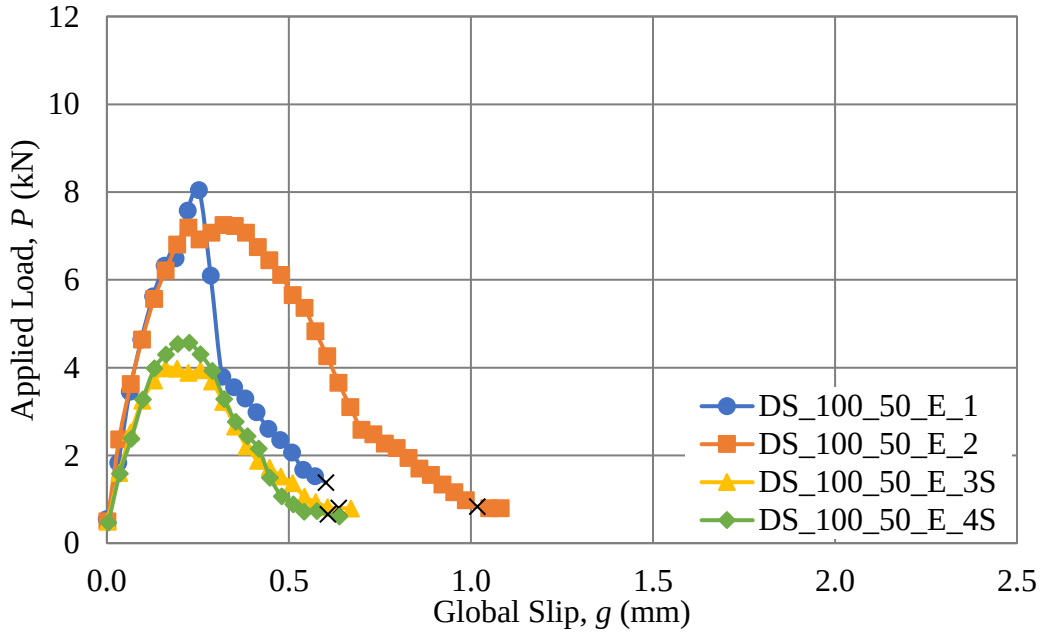

Figure 4.16. Applied load vs. global slip response for 100 mm bonded length epoxy anchor series specimens

www.manaraa.com

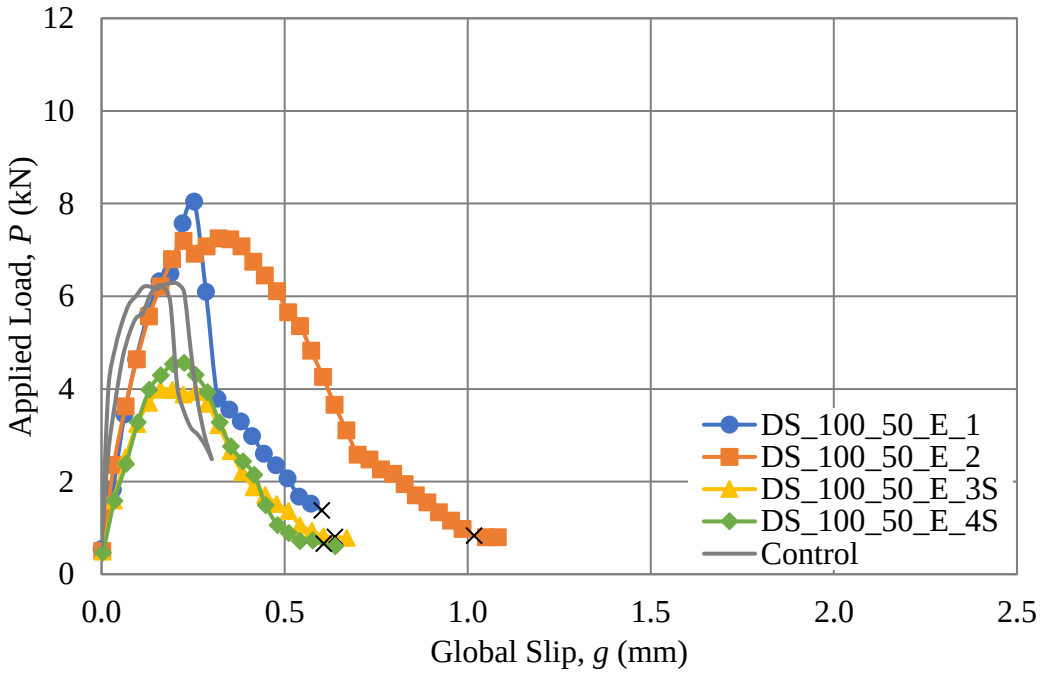

Figure 4.17. Applied load vs. global slip response for 100 mm bonded length epoxy anchor series specimens compared to 100 mm bonded length control specimens

4.2.3. Mortar Anchor Specimens. This section presents the applied load-global slip response of the specimens anchored with a mortar anchor binder material.

4.2.3.1. 330 mm bonded length specimens. The P-g response for each of the 330 mm bonded length mortar anchor series specimens is shown in Figure 4.18. The response prior to reaching the failure load was again similar to the response of the control specimens (as shown in Figure 4.19) and the epoxy anchor binder material specimens. The post failure response is shown for specimens DS_330_50_M_1, DS_330_50_M_2, DS_330_50_M_3, and DS_330_50_M_4. The load reached after failure was somewhat inconsistent between specimens. For example, after failure, the applied load for specimen DS_330_50_M_3 dropped steeply to 0 kN, while the applied load for specimen DS_330_50_M_1 maintained a constant value of approximately 1 kN and approximately

www.manaraa.com

2 kN for DS_330_50_M_2. This difference is attributed to the bond between the steel fibers and the anchor binder material, but could also be partially attributed to the influence of the testing equipment as mentioned in Section 4.2.2.1. For specimens with a higher sustained load post-failure, a superior bond was formed within the anchor compared to the specimens with a lower sustained post-failure load. This was a consequence of the anchor binder material. During fabrication, care was taken to completely fill the anchor hole with the anchor binder material. With an epoxy resin, this was much easier due to the high viscosity of the epoxy. With the cementitious mortar, however, this was much more difficult, and it is possible that small voids were present in the anchor, thus degrading the bond between the steel fiber and anchor binder material. Destructive testing was not conducted on the specimens to determine the presence or lack of voids in the anchor material.

4.2.3.2. 100 mm bonded length specimens. Figure 4.20 shows the applied load-global slip response for the 100 mm bonded length specimens anchored with a cementitious mortar anchor binder material. As mentioned above with other 100 mm bonded length specimens, the response of specimens DS_100_50_M_3S and DS_100_50_M_4S with strain gauges varies significantly from the response of specimens DS_100_50_M_1 and DS_100_50_M_2. Again, this variation is attributed to the reduction in bond contact area between the steel fibers and the internal matrix layer. Specimen DS_100_50_M_3S exhibited a behavior unlike the response observed in any of the other 100 mm bonded length specimens, as shown in Figure 4.20. After reaching a peak value of applied load, the response did not begin to decline (as expected) but continued to maintain the peak load value as global slip increased.

www.manaraa.com

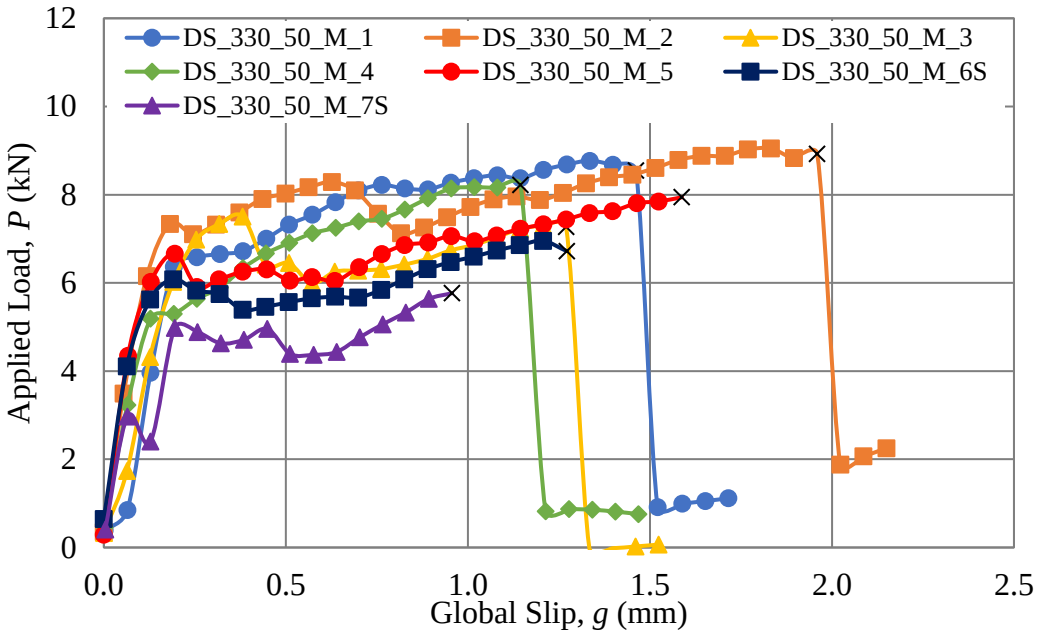

Figure 4.18. Applied load vs. global slip response for 330 mm bonded length mortar anchor series specimens

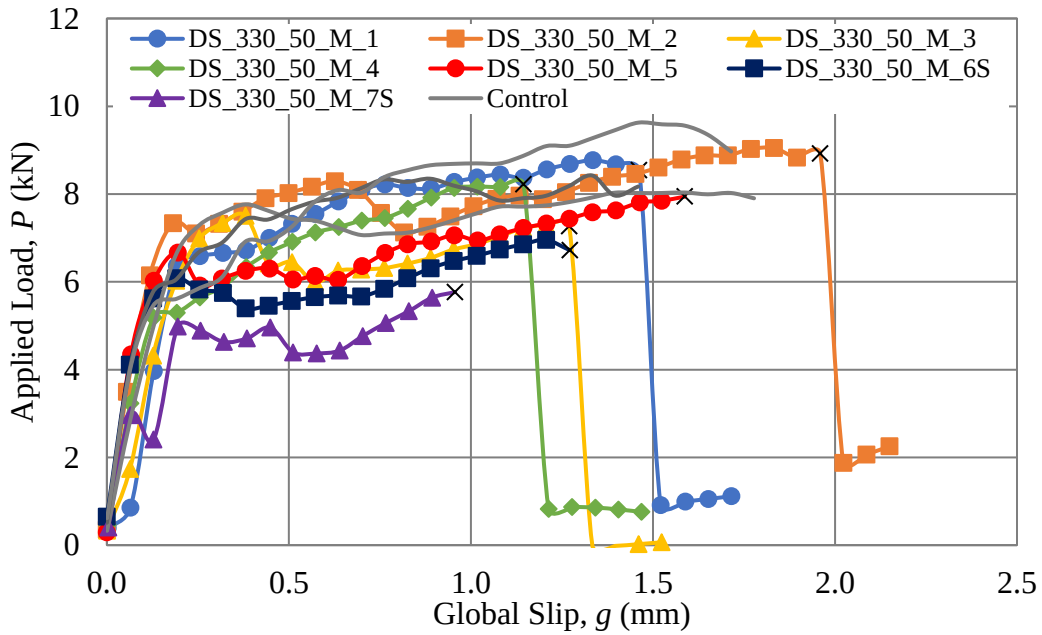

Figure 4.19. Applied load vs. global slip response for 330 mm bonded length mortar anchor series specimens compared to 330 mm bonded length control specimens

www.manaraa.com

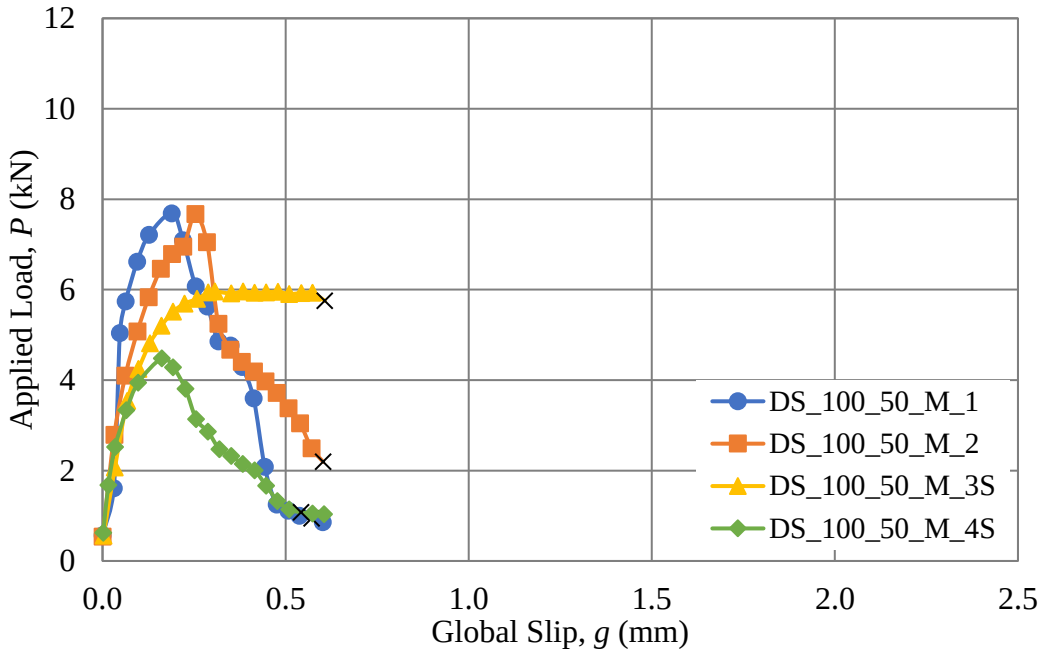

Figure 4.20. Applied load vs. global slip response of 100 mm bonded length mortar anchor series specimens

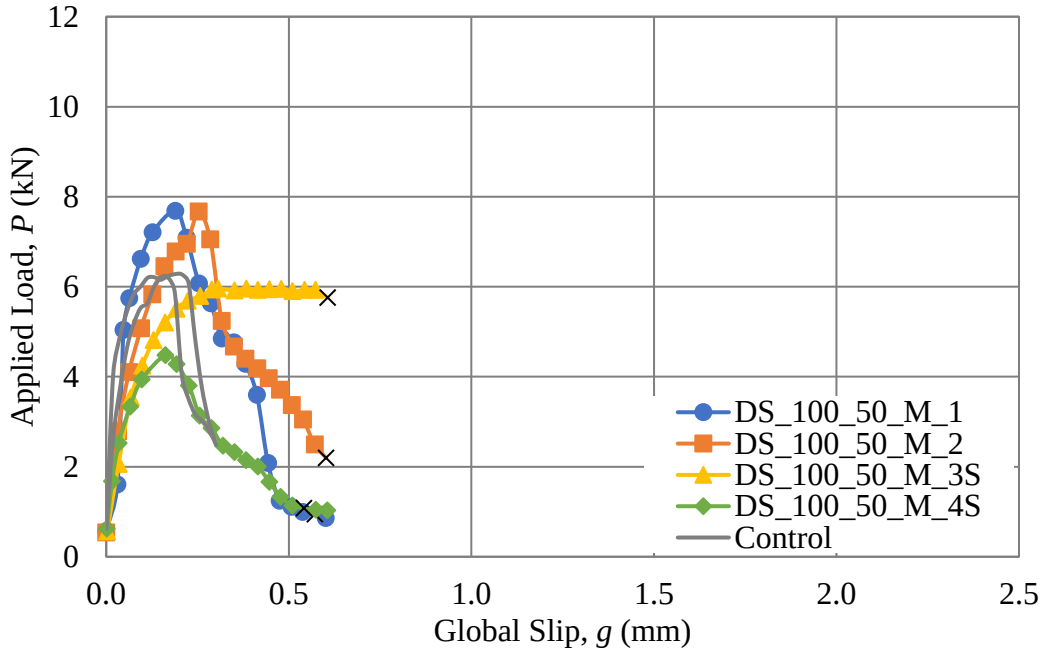

Figure 4.21. Applied load vs. global slip response for 100 mm bonded length mortar anchor series specimens compared to 100 mm bonded length control specimens

www.manaraa.com

The specimens without strain gauges, however, do show a significant increase in peak load P^* and global slip at failure g_{ult} compared to the unanchored control specimens (show in Figure 4.21). These increases also result in an increase in absorbed energy relative to the control specimens.

4.3. STRAIN DISTRIBUTION

As discussed in Section 3.3.4, an array of strain gauges was installed along the centerline of the steel fiber strip of 12 specimens. Specimens denoted with an "S" at the end of the specimen ID include four strain gauges at discrete locations along the bonded length of the composite and one on the bare steel fibers. The readings from these strain gauges illustrate the distribution of longitudinal strain along the composite length during testing. For each specimen, the distribution of strain is plotted at various values of global slip. For reference, a plot of the complete applied load-global slip response is presented with the location of the plotted strain values marked with a red box. The two figures work in conjunction to show how the distribution of strain changes along the composite length as loading progresses to failure. The gauge location is reported by its distance from the free (unloaded) end of the composite and is plotted on the x-axis of the strain distribution plots. The reading of each strain gauge, in units of microstrain, is plotted on the y-axis.

4.3.1. Control Specimens. This section presents the strain distribution for the control specimens.

4.3.1.1. 330 mm bonded length specimens. The P-g curves for specimens DS_330_50_C_6S and DS_330_50_C_7S are shown in Figure 4.22 and Figure 4.24, respectively. Additionally, the strain distributions are shown in Figure 4.23 and Figure

www.manaraa.com

4.25, respectively. The applied load-global slip response for both specimens was similar, including an initial elastic linear branch, followed by a softened non-linear portion with decreased slope that leads to a final increasing branch to the peak load, and ultimately failure of the composite. For both specimens, at points in the initial linear elastic region, the maximum value of strain was measured by the gauge bonded to the bare steel fibers (and not within the bonded region of the composite). This response was typical of all specimens in the experimental program. Once the response moved into the non-linear portion of the response (Point B in Figure 4.22 and Point D in Figure 4.24), the maximum strain value was recorded by the first gauge within the bonded region of the composite (315 mm from the free end).

In Figure 4.22 and Figure 4.23, up to Point E on the *P-g* curve, the strain gauge located 115 mm from the free end (and thus 215 mm from the loaded end) of the composite measured zero strain. Sometime between Point E and Point F in Figure 4.22, however, the strain gauge began reading a strain value. Figure 4.22 also shows a slight decrease in applied load at Point E, which corresponded to the formation of the first transverse crack (and propagation of the longitudinal crack). A similar phenomenon was observed in specimen DS_330_50_C_7S based on Point D and Point E in Figure 4.23 and the associated strain profile in Figure 4.24. Further discussion of these observations is provided in Section 4.3.4.

After Point F in Figure 4.22 and Figure 4.24, the measured strain values in the gauges located 15 mm and 115 mm from the free end continued to increase as the applied load and global slip values increased.

www.manaraa.com

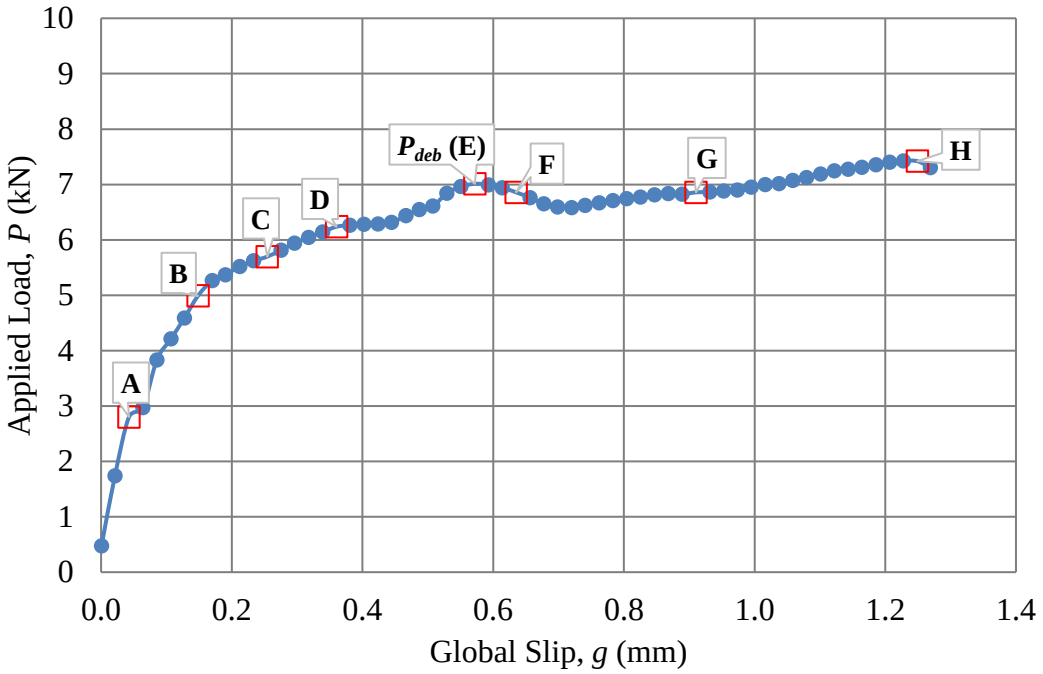

Figure 4.22. Applied load vs. global slip response for specimen DS_330_50_C_6S

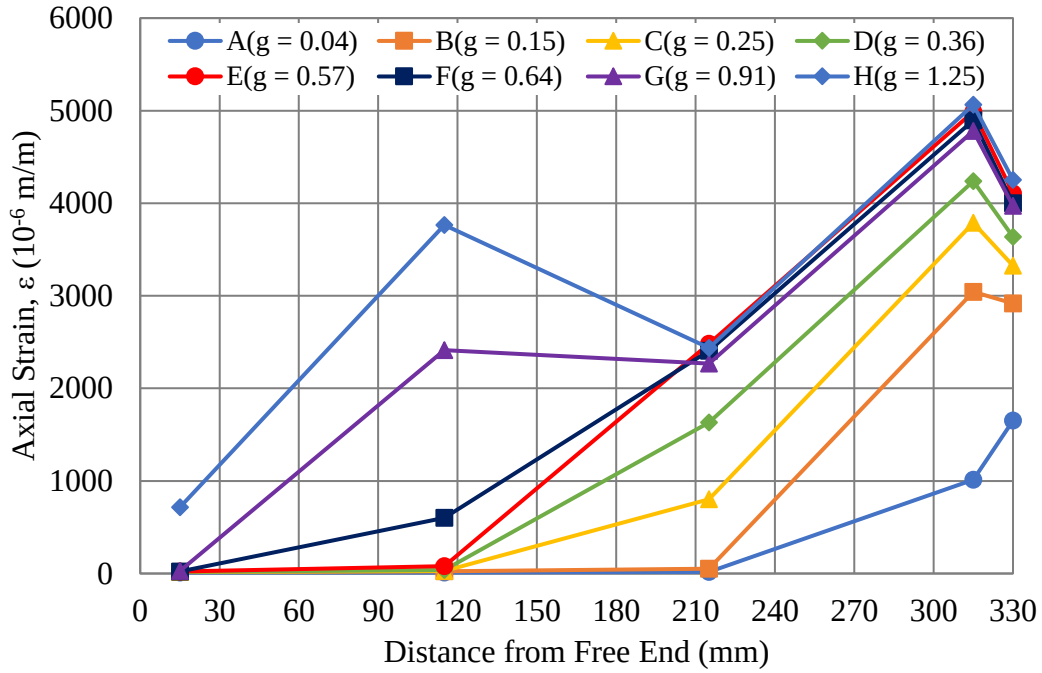

Figure 4.23. Strain distribution at various global slip values for specimen DS_330_50_C_6S

www.manaraa.com

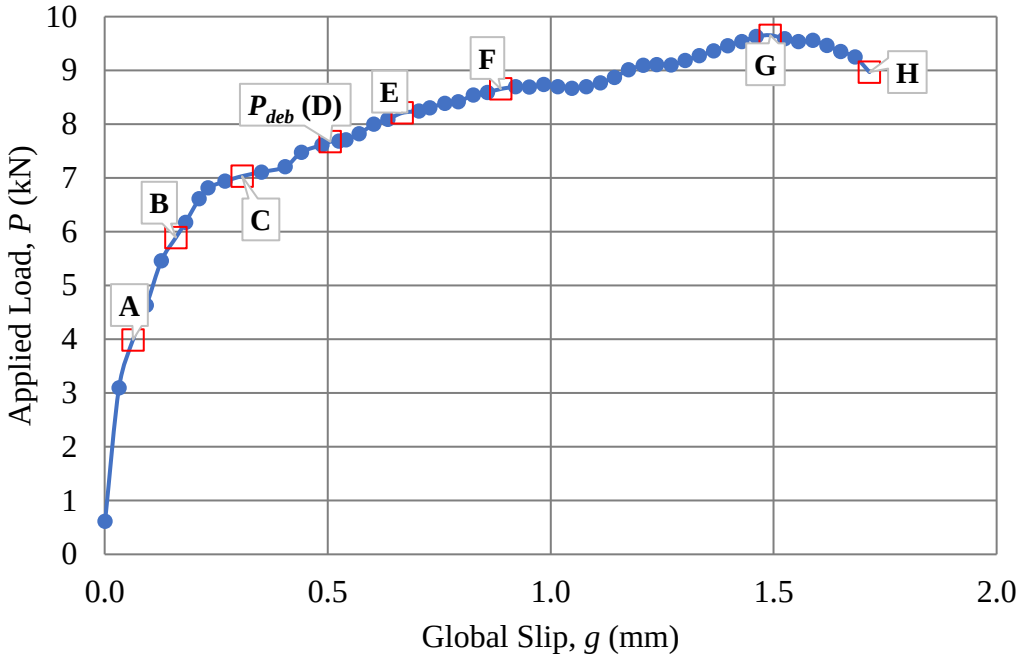

Figure 4.24. Applied load vs. global slip response for specimen DS_330_50_C_7S

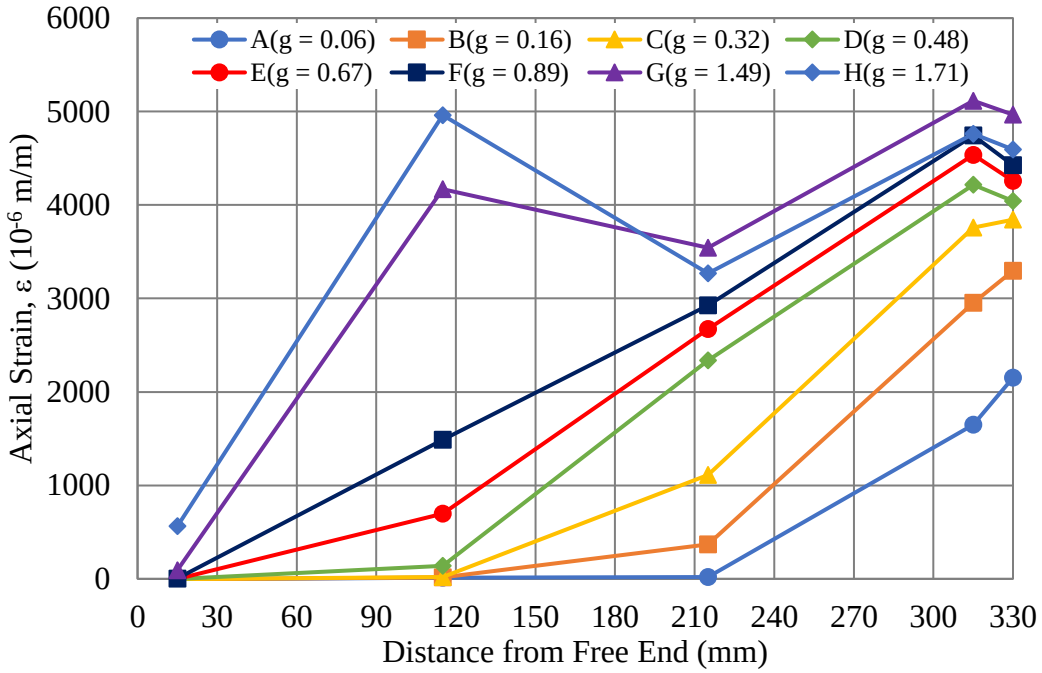

Figure 4.25. Strain distribution at various global slip values for specimen DS_330_50_C_7S

www.manaraa.com

This general trend illustrates at what point portions of the bonded length begin to carry the applied load. This trend continued until failure of the composite after Point H in Figure 4.22 and 4.24.

4.3.1.2. 100 mm bonded length specimens. The P-g curves for specimens DS_100_50_C_3S and DS_100_50_C_4S are shown in Figure 4.26 and Figure 4.28, with the corresponding strain distributions shown in Figure 4.27 and Figure 4.29, respectively. As discussed in Section 4.2.1.2, the general shape of the applied load-global slip response of the 100 mm bonded length specimens was different from the 330 mm bonded length specimens. Accordingly, the observed strain distributions were also different. The strain distributions in Figure 4.27 and Figure 4.29 show positive strain readings from gauges at all locations along the bonded length early in the applied load-global slip response. This is a key difference from the 330 mm bonded length specimens, for which no measured strain at certain points along the bonded length of the composite was recorded for the first part of the applied load-global slip response.

Progressing from Point A to Point D in Figure 4.26 along the *P-g* curve, increasing the applied load resulted in an increase in the measured strain values at all locations along the bonded length. After Point D until failure at Point K, the measured strain values decreased, corresponding to the decrease in applied load. Based on Figure 4.27 and 4.29, the measured strain values decreased at locations closer to the free (unloaded) end of the composite.

In Figure 4.29, strain values for series C, D, F, and H are not reported at the gauge located 12.5 mm from the free end. This was the only instance of a strain gauge malfunctioning during testing (Figure 4.29).

www.manaraa.com

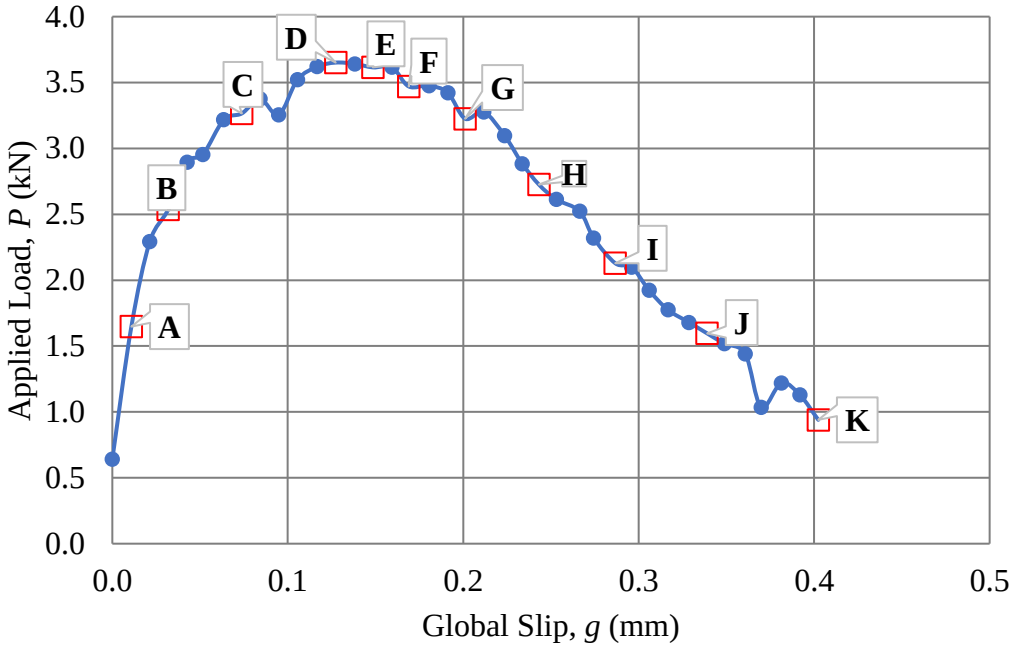

Figure 4.26. Applied load vs. global slip response for specimen DS_100_50_C_3S

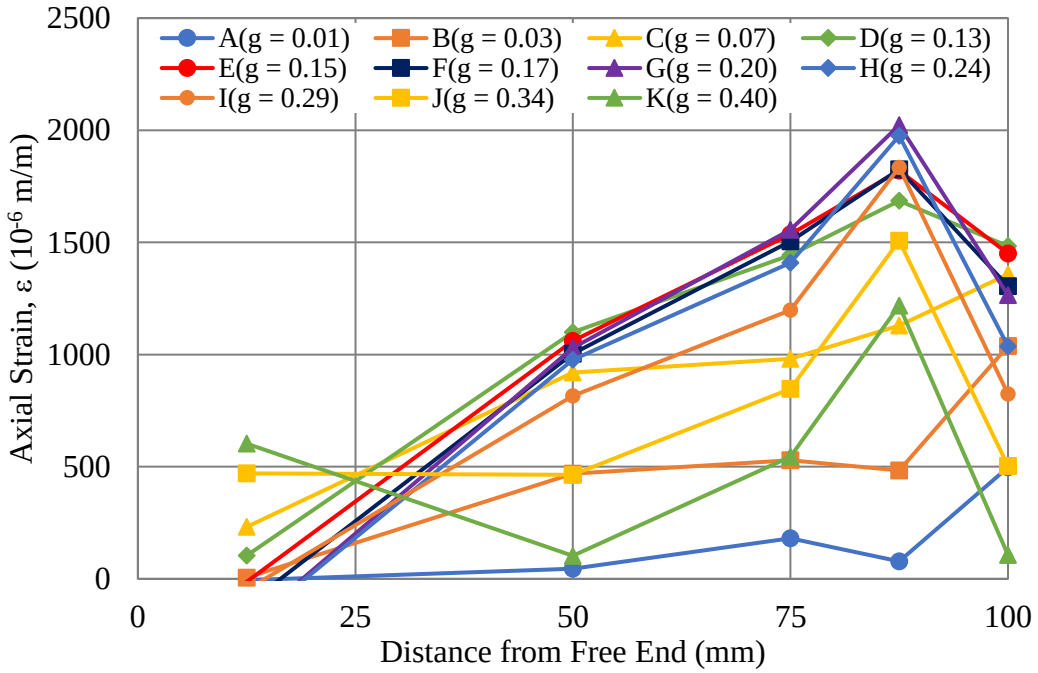

Figure 4.27. Strain distribution at various global slip values for specimen DS_100_50_C_3S

www.manaraa.com

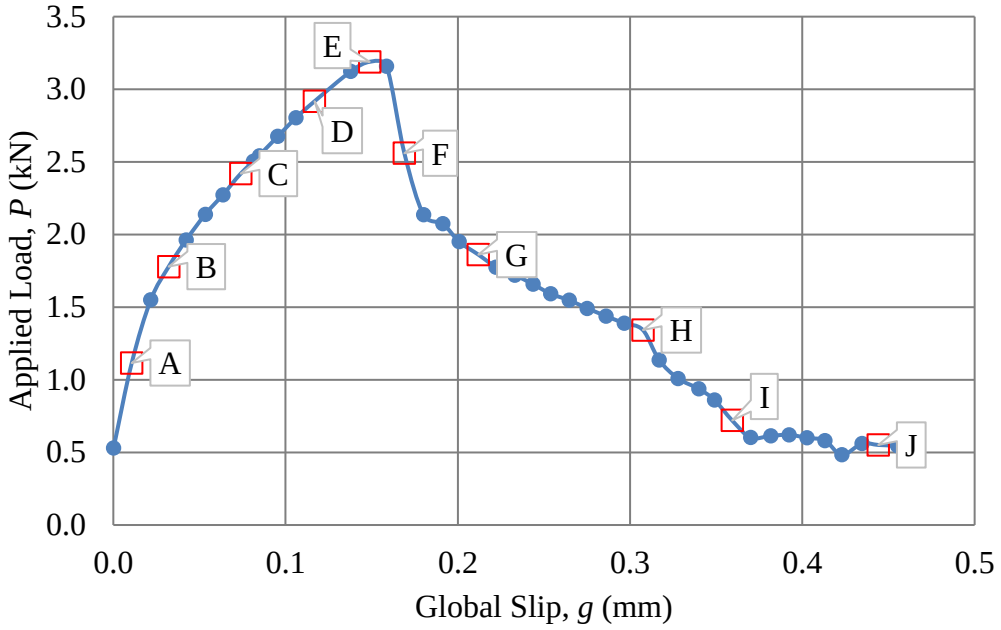

Figure 4.28. Applied load vs. global slip response for specimen DS_100_50_C_4S

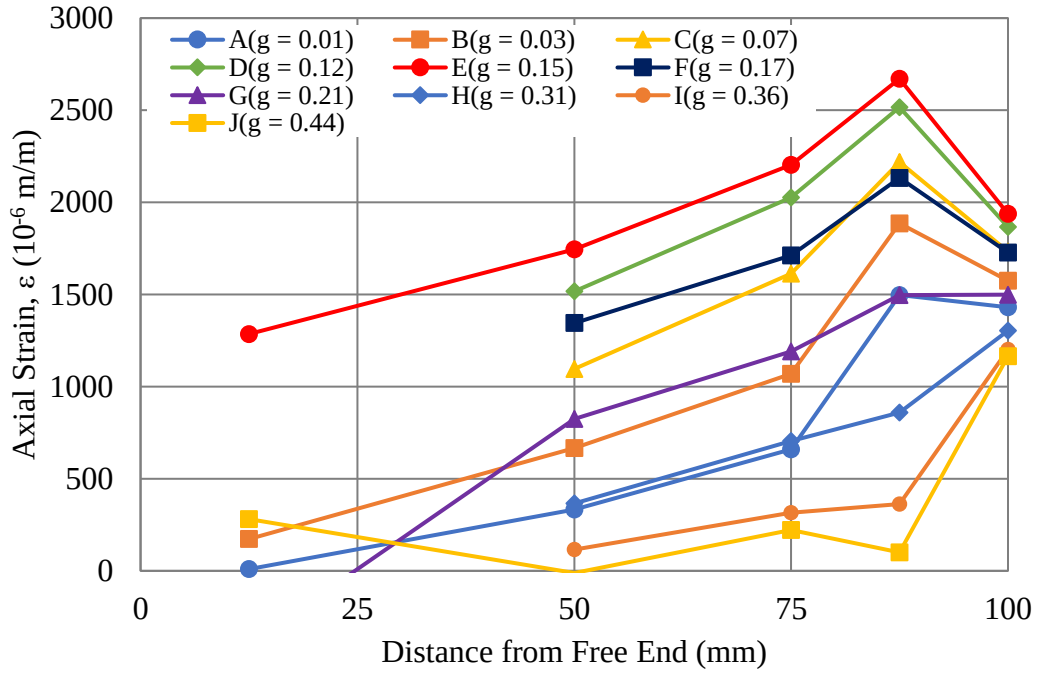

Figure 4.29. Strain distribution at various global slip values for specimen DS_100_50_C_4S

www.manaraa.com

The gauge did not completely malfunction, as readings were taken for other values of global slip (as shown in Figure 4.29).

4.3.2. Epoxy Anchor Specimens. This section presents the strain distributions for the epoxy anchor specimens.

4.3.2.1. 330 mm bonded length specimens. Figure 4.30 shows the applied load-global slip response for specimen DS_330_50_E_6S, and Figure 4.31 shows the corresponding strain distribution. The *P-g* curve in Figure 4.30 is not similar to the typical response of the control specimens. First, the peak load (Point E) does not occur near the end of the response curve. Instead, the peak load occurs near the middle of the response curve. Second, the overall response shape is characterized by an increasing branch followed by a decreasing branch. The response of the control specimens was characterized by a steeply increasing branch followed by a shallow, softened increasing branch. Third, a significant decrease in applied load occurred right after Point E. This phenomenon was not typical in the response of the control specimens.

The strain distribution shown in Figure 4.31 shows similar strain profiles compared to the control specimens, up to Point E in Figure 4.30. At Points A, B, and C in Figure 4.30, the corresponding strain profiles show that the maximum strain value was recorded on the bare steel fibers. After Point C, the peak strain value was recorded at the first gauge within the bonded region of the composite (315 mm from the free end). After Point E, the strain readings at locations 215 mm, 315 mm and 330 mm from the free end of the composite remain almost constant. The strain readings 115 mm and 15 mm from the free end continue to gradually increase up to failure of the composite at Point J. The maximum strain in the bonded region of the composite shown in Figure 4.31 occurred at

www.manaraa.com

Point E in Figure 4.30, corresponding to the peak load. Interestingly, at the ultimate load, the strain reading at the strain gauge 15 mm from the free end of the composite (closest to the end-anchor) was not significantly higher than for the control (unanchored) specimens. The presence of the end anchor was not able to significantly increase the strain utilization at the free end of the composite prior to failure.

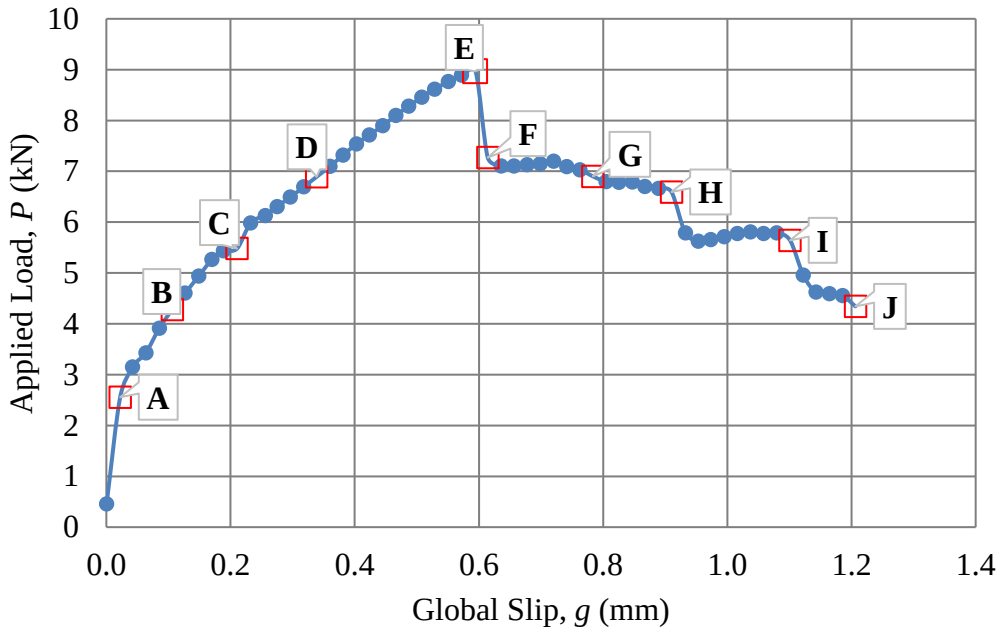

Figure 4.30. Applied load vs. global slip response for specimen DS_330_50_E_6S

Figure 4.32 shows the *P-g* curve for specimen DS_330_50_E_7S, with the corresponding strain distribution shown in Figure 4.33. The overall shape of the applied load-global slip response was similar to the response of specimen DS_330_50_E_6S.

www.manaraa.com

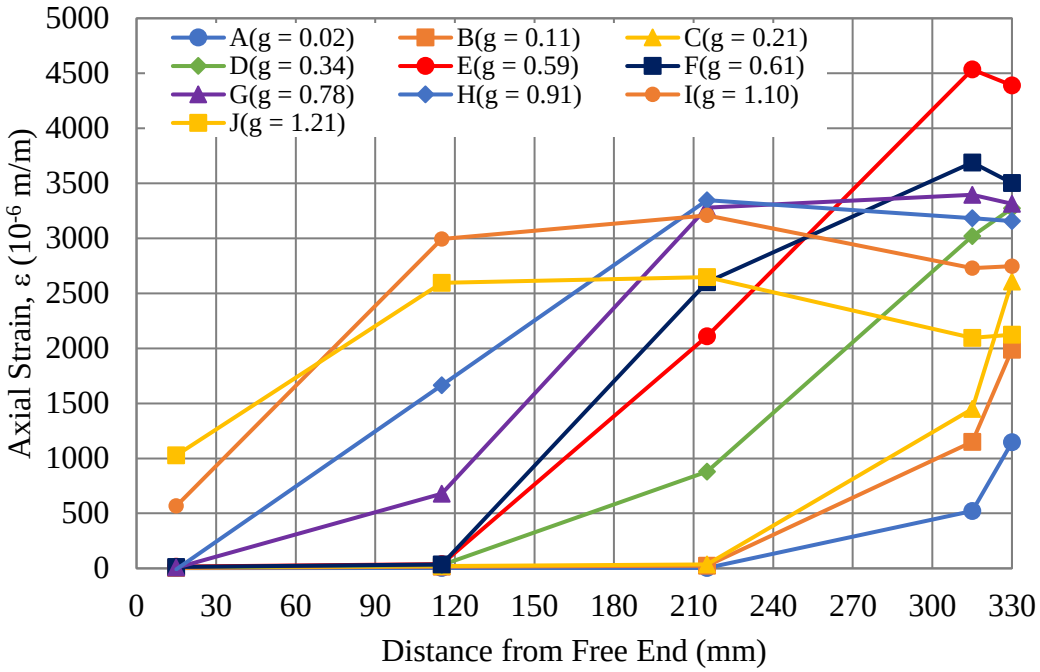

Figure 4.31. Strain distribution at various global slip values for specimen DS_330_50_E_6S

A significant drop in applied load occurred first between Point B and Point C, and again between Point G and Point H. The first significant drop was observed at an applied load significantly lower than the expected peak load, suggesting that some damage was present at the matrix-fiber interface which led to premature initial debonding. This was also shown in the strain distributions, as the strain gauge 215 mm from the free end showed increased reading somewhere between Point B and Point C. After the initial drop in applied load, the slope of the curve (stiffness) was significantly reduced up to Point G. However, the strain measured 215 mm from the free end dramatically increased between Point C and Point D, with the maximum strain reading measured within the bonded region of the composite (and not on the bare steel fibers).

www.manaraa.com

Between Point H and Point I, Figure 4.32 shows an increase in applied load corresponding to an increase in the strain measured 115 mm from the free end, with minimal increase at other locations. This local concentration was observed in other specimens, including the control specimens (Figure 4.23 and Figure 4.25). Again, at failure of the composite (Point J), the strain reading 15 mm from the free end (i.e. near the anchor location) was not significantly higher than that of the control specimens.

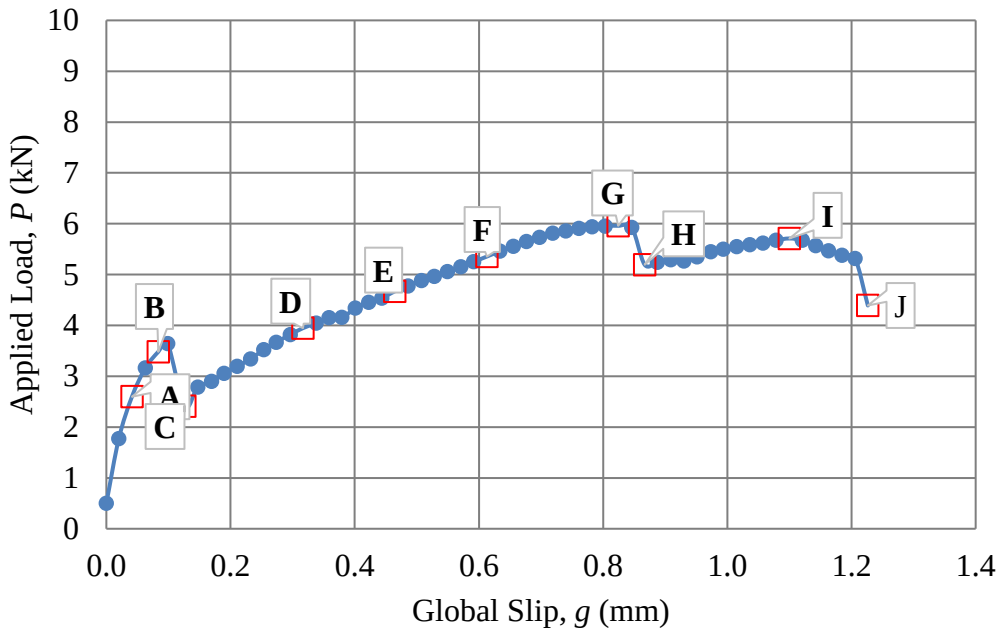

Figure 4.32. Applied load vs. global slip response for specimen DS_330_50_E_7S

4.3.2.2. 100 mm bonded length specimens. The applied load vs. global slip response for specimen DS_100_50_E_3S and corresponding strain distribution are shown in Figure 4.34 and Figure 4.35, respectively.

www.manaraa.com

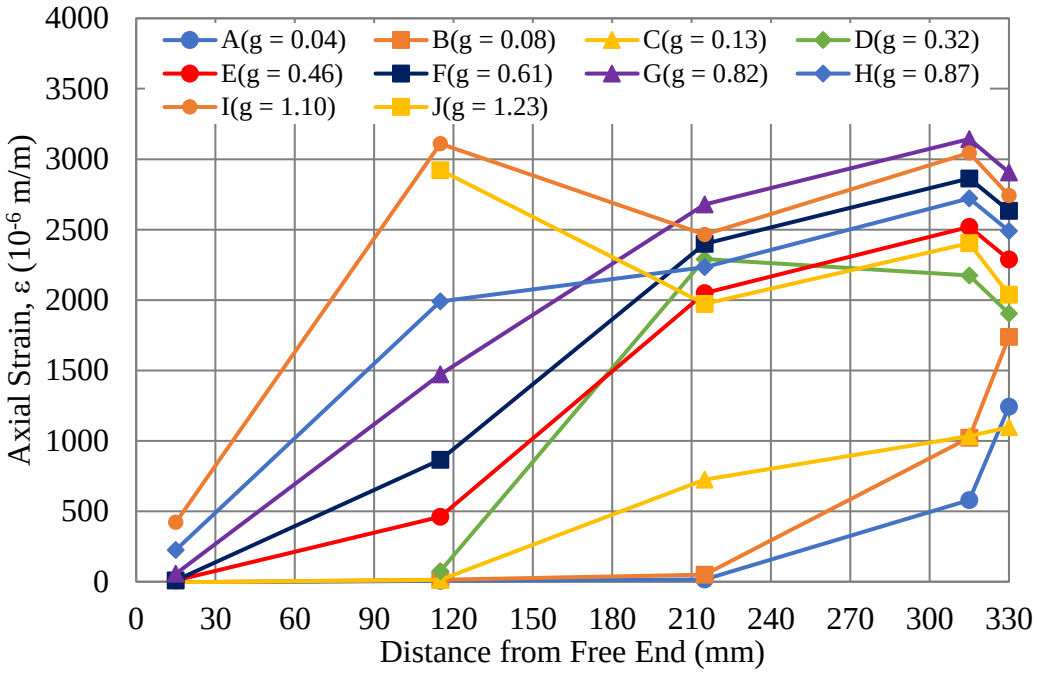

Figure 4.33. Strain distribution at various global slip values for specimen DS_330_50_E_7S

The general shape of the *P-g* curve is similar to the response of the control specimens, but with a higher peak load value and a larger global slip value at failure (resulting in a higher absorbed energy). Figure 4.35 shows that the strain profiles have a consistent shape for most points along the applied load-global slip response. The general shape resembles the response of the 100 mm bonded length control specimens shown in Figure 4.27 and Figure 4.28. The strain profile in Figure 4.35 corresponding to Point B in Figure 4.34 shows each gauge reading a positive value of strain, suggesting that the entire bonded length was already activated in transferring the applied load. Point C in Figure 4.34 marks the peak load, which also corresponds to the highest strain value recorded 100 mm from the free end of the composite (on the bare steel fibers). The highest measured strain value within the bonded region of the composite occurred at Point E and was

www.manaraa.com

measured by the strain gauge 87.5 mm from the free end (or the first gauge within the bonded region of the composite). Points G, H, and I in Figure 4.34 correspond to increased strain values at the gauge located 12.5 mm from the free end of the composite in Figure 4.35.

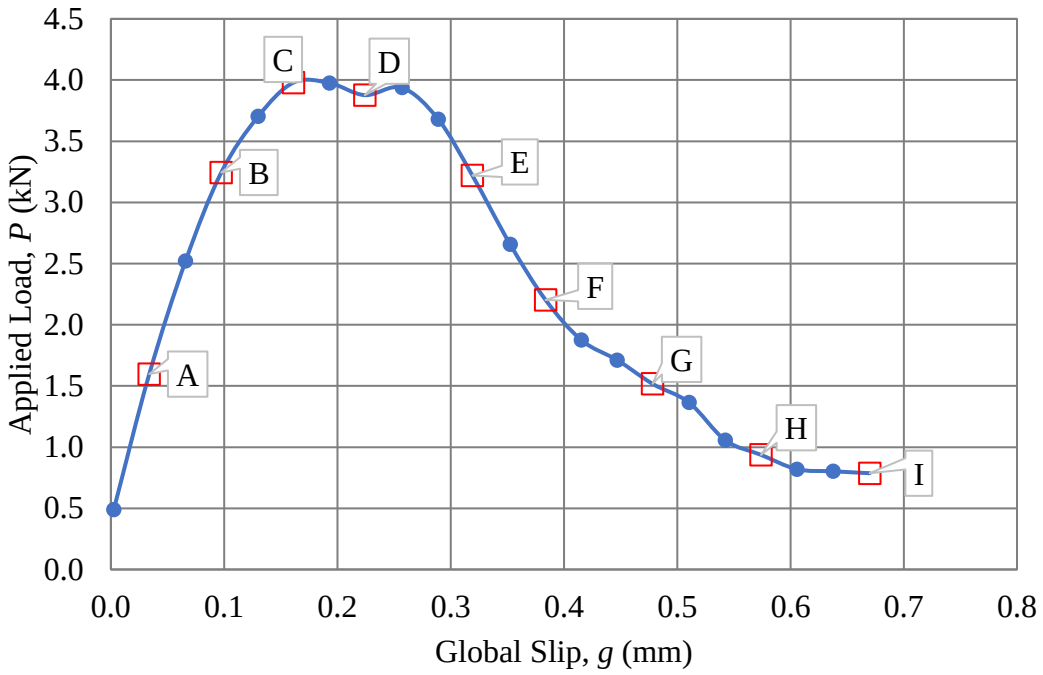

Figure 4.34. Applied load vs. global slip response for specimen DS_100_50_E_3S

Figure 4.36 shows the applied load-global slip response for specimen DS_100_50_E_4S, and Figure 4.37 shows the corresponding strain distribution. The overall response shown in both Figure 4.36 and 4.37 is very similar to the response of specimen DS_100_50_E_3S (Figure 4.34 and Figure 4.35). Again, peak strain values were recorded at the corresponding peak load in Figure 4.36 at Point D. The measured

www.manaraa.com

strain values near the free end of the composite at Points H and I are slightly lower than the measured values shown in Figure 4.35 at Points H and I, but the failure load for specimen DS_100_50_E_4S was also slightly lower than for DS_100_50_E_3S, which would account for this difference.

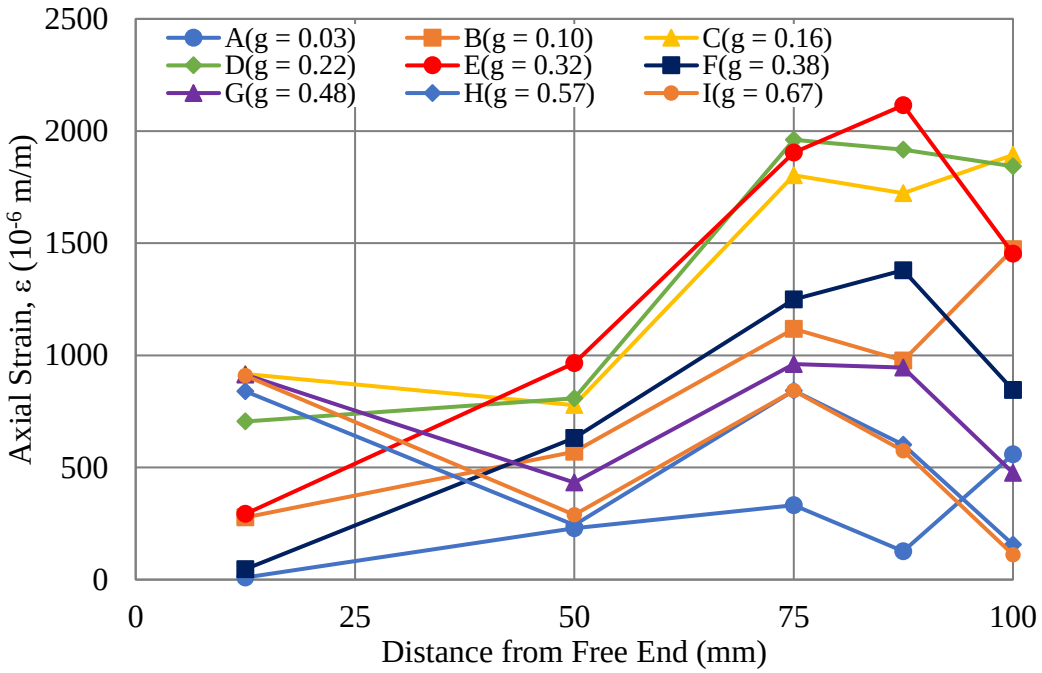

Figure 4.35. Strain distribution at various global slip values for specimen DS_100_50_E_3S

4.3.3. Mortar Anchor Specimens. This section presents the strain distributions for the mortar anchor specimens.

www.manaraa.com

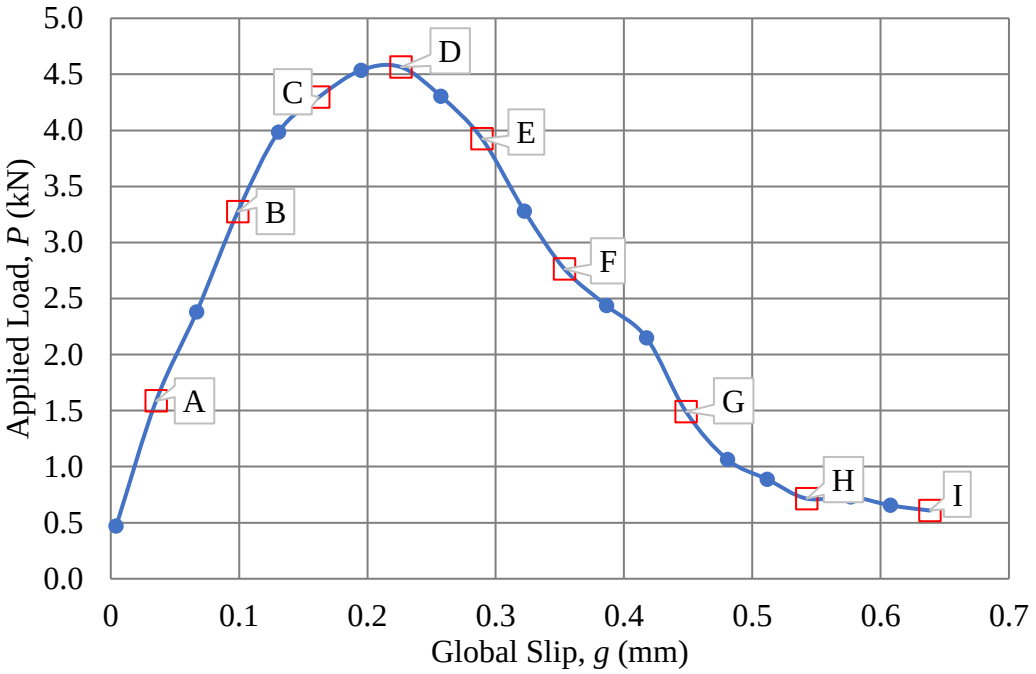

Figure 4.36. Applied load vs. global slip response for specimen DS_100_50_E_4S

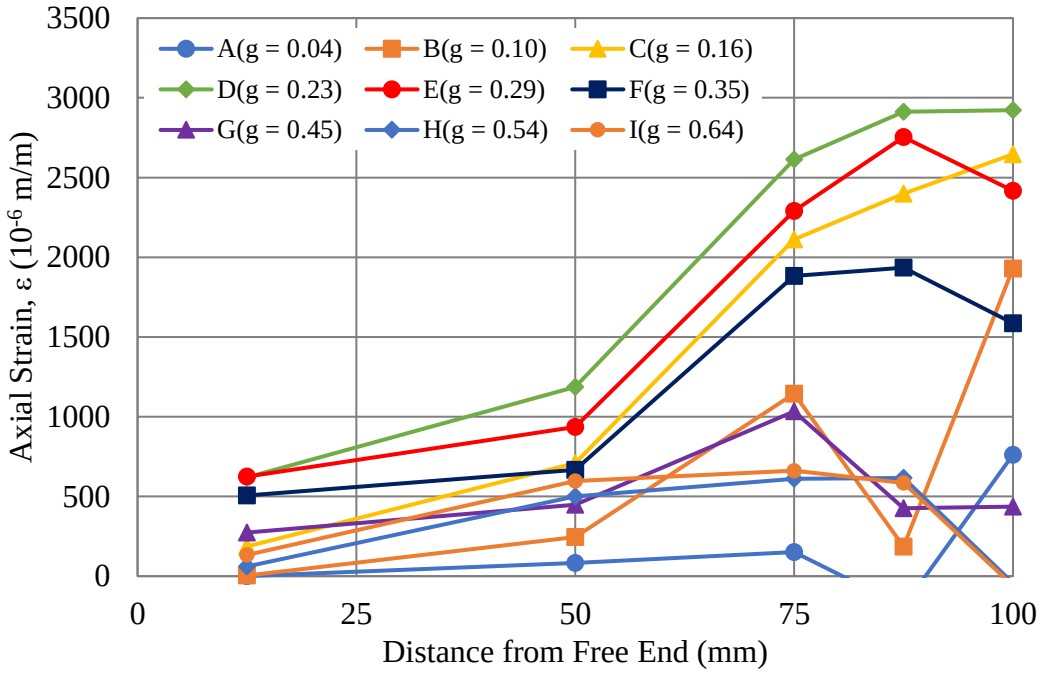

Figure 4.37. Strain distribution at various global slip values for specimen DS_100_50_E_4S

www.manaraa.com

4.3.3.1. 330 mm bonded length specimens. Figure 4.38 shows the applied load-global slip response for specimen DS_330_50_M_6S, and the corresponding strain distribution is shown in Figure 4.39. Both the *P-g* curve and the strain distributions are similar to the response of the control specimens. The drop in applied load between Point C and Point D corresponds to an increase in the measured strain at the gauge located 115 mm from the free end of the composite. A similar behavior was observed in the control specimens. After Point A, the maximum strain value was measured at the gauge 315 mm from the free end, meaning that the strain within the bonded composite region was larger than the strain in the bare steel fibers. Between Point F and Point G, a significant increase in the strain measured 115 mm from the free end of the composite was observed but was interestingly not associated with a noticeable drop in applied load. Point J in Figure 4.38 (the failure point) corresponded to an increase in the measured strain closest to the free end of the composite. Again, this measured strain value was not significantly higher than that of the control or epoxy anchor specimens with the same bonded length.

The applied load-global slip response for specimen DS_330_50_M_7S is shown in Figure 4.40, with the corresponding strain distribution shown in Figure 4.41. The strain distributions shown in Figure 4.41 are very similar to the distributions observed in specimen DS_330_50_M_6S, as well as in the control specimens (DS_330_50_C_6S and DS_330_50_C_7S). At points on the *P-g* curve after Point H, a local maximum strain value was observed at the gauge 115 mm from the free end of the composite. This phenomenon was observed in other specimens (DS_330_50_C_6S, DS_330_50_C_7S, and DS_330_50_E_7S).

www.manaraa.com

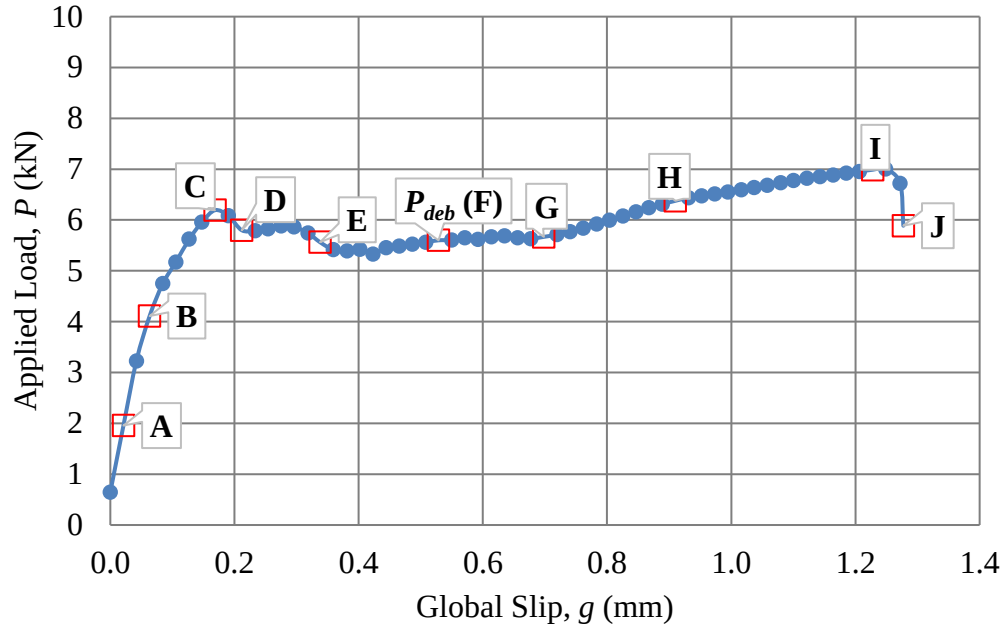

Figure 4.38. Applied load vs. global slip response for specimen DS_330_50_M_6S

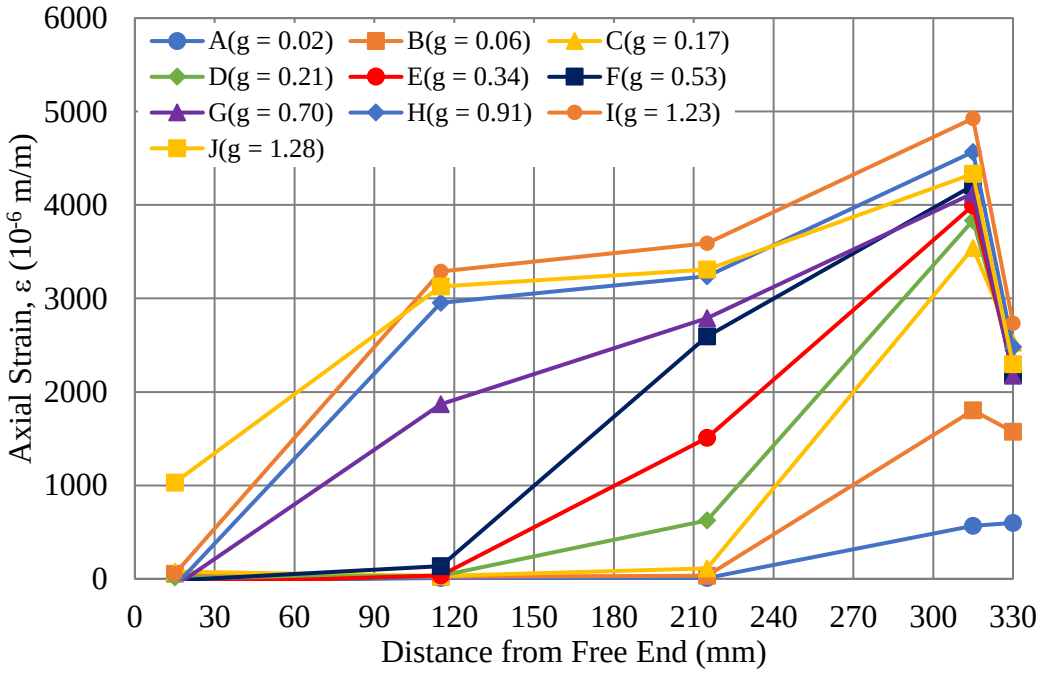

Figure 4.39. Strain distribution at various global slip values for specimen DS_330_50_M_6S

www.manaraa.com

At failure, the value of strain at the gauge located 15 mm from the free end of the composite was slightly higher than the measured values for other specimens (both control and epoxy anchor), but this may or may not be attributed to the end anchorage system (and could be a result of experimental variability).

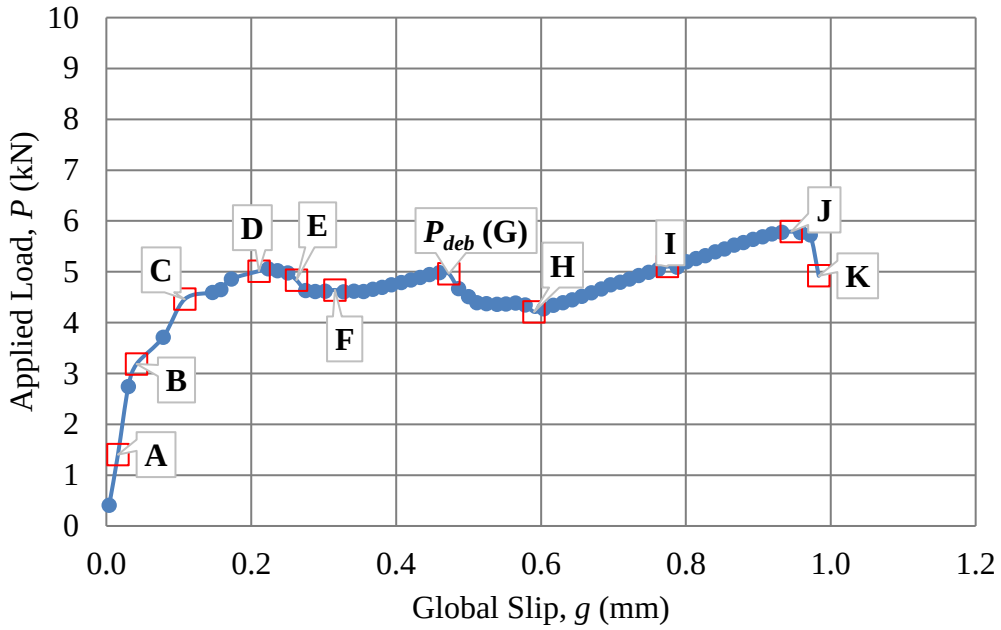

Figure 4.40. Applied load vs. global slip response for specimen DS_330_50_M_7S

4.3.3.2. 100 mm bonded length specimens. The applied load-global slip response for specimen DS_100_50_M_3S is shown in Figure 4.42, and the corresponding strain distribution is shown in Figure 4.43. As previously discussed, the *P-g* response of specimen DS_100_50_M_3S was not similar to the other replicates in the experimental program. After reaching a peak load near Point E, the applied load did not decrease (as expected) but remained relatively constant for increasing values of global slip.

www.manaraa.com

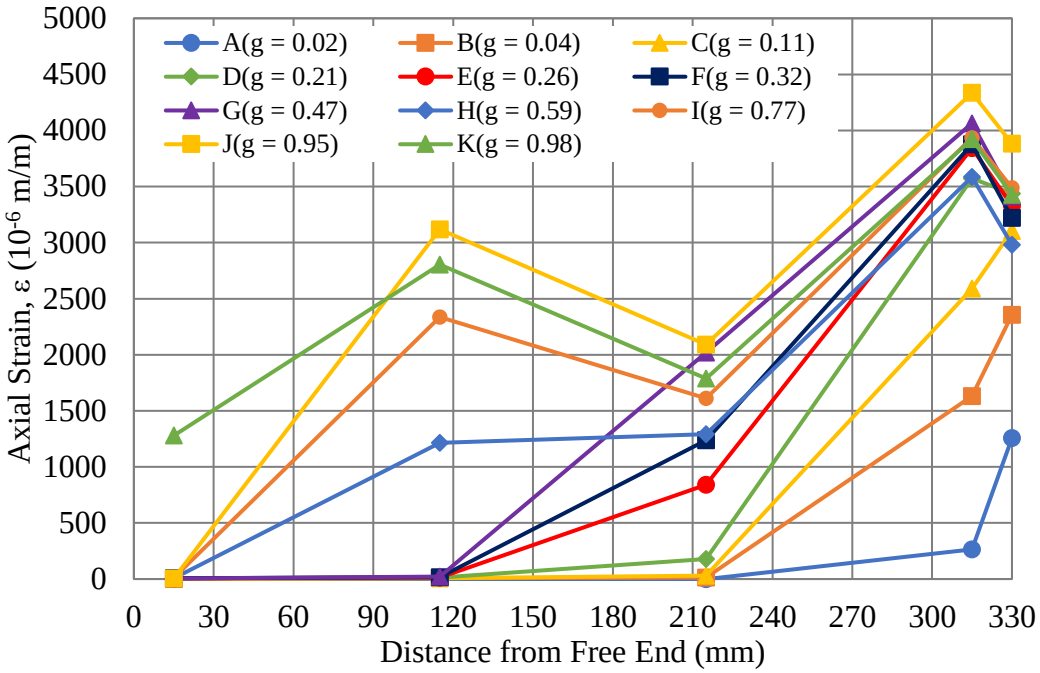

Figure 4.41. Strain distribution at various global slip values for specimen DS_330_50_M_7S

Testing was concluded at Point I, which corresponded to a similar value of ultimate slip at failure observed in other replicates. The strain distributions shown in Figure 4.43 depict a similar distribution of strain along the bonded length of the composite, regardless of the unusual *P-g* response. Interestingly, the strain measured at the gauge located 12.5 mm from the free end of the composite was approximately equal to the strain measured at the gauge 50 mm from the free end of the composite at all locations. This phenomenon was not observed in any other specimens and should be considered an anomaly.

www.manaraa.com

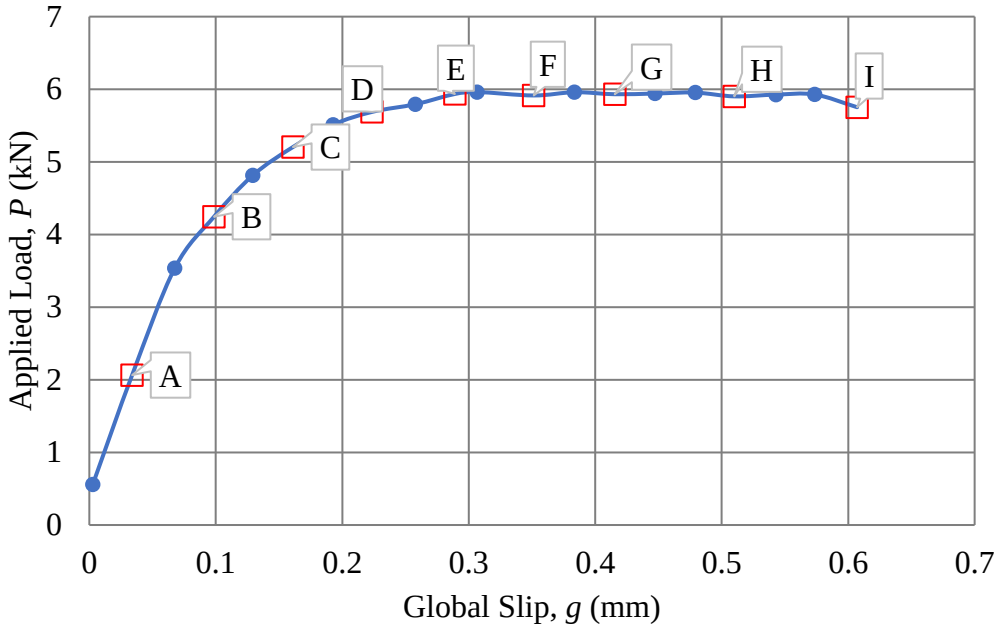

Figure 4.42. Applied load vs. global slip response for specimen DS_100_50_M_3S

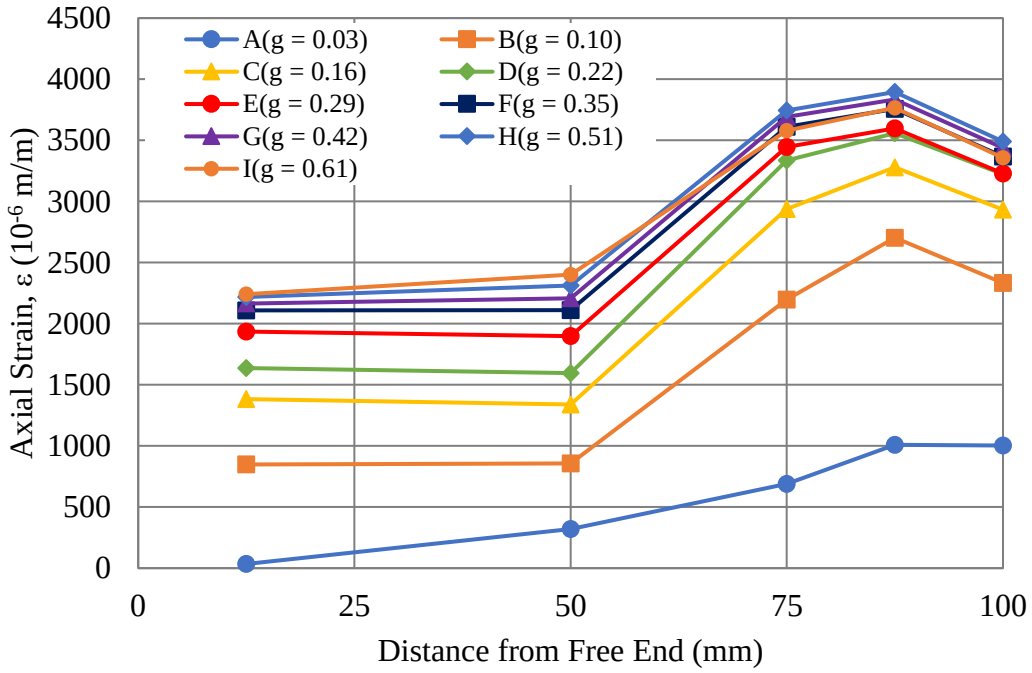

Figure 4.43. Strain distribution at various global slip values for specimen DS_100_50_M_3S

www.manaraa.com

Figure 4.44 shows the *P-g* response for specimen DS_100_50_M_4S, and Figure 4.45 shows the corresponding strain distribution. As expected, peak strain values were measured at the corresponding peak load (Point E), with decreasing values for locations after Point E in Figure 4.44. Overall, however, the strain data collected from DS_100_50_M_4S may be unreliable. The measured strain values 100 mm from the free end of the composite (on the bare steel fibers at the loaded end) are very low at failure, while the applied load is approximately 1 kN. Additionally, there are a few instances where the measured strain values 75 mm from the free end of the composite are lower than the values measured 50 mm from the free end. Based on the strain profiles of the other 100 mm bonded length specimens, the contour shape shown in Figure 4.45 for Points H, I, and J do not seem to accurately depict the strain distribution in the composite. This is likely attributed to a malfunction of the strain gauge during testing.

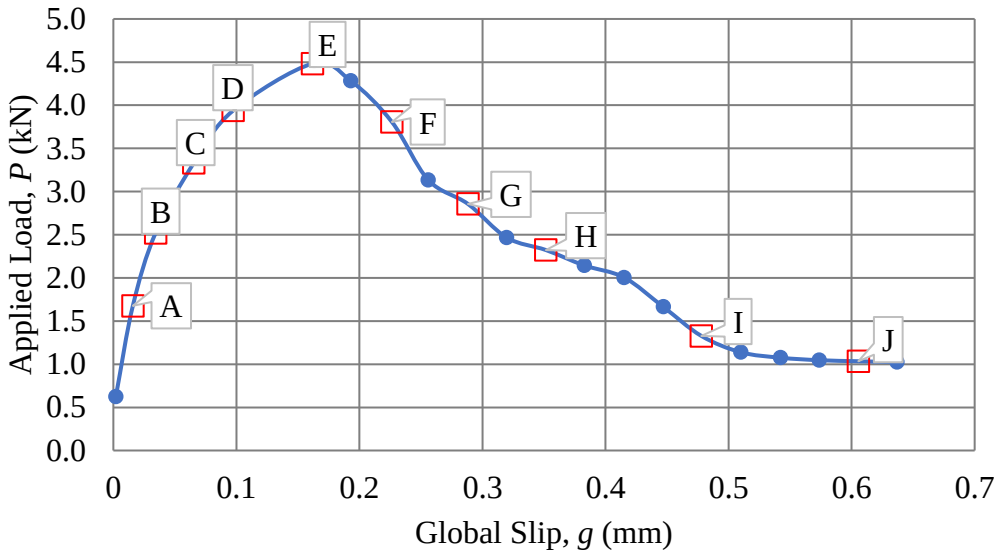

Figure 4.44. Applied load vs. global slip response for specimen DS_100_50_M_4S

www.manaraa.com

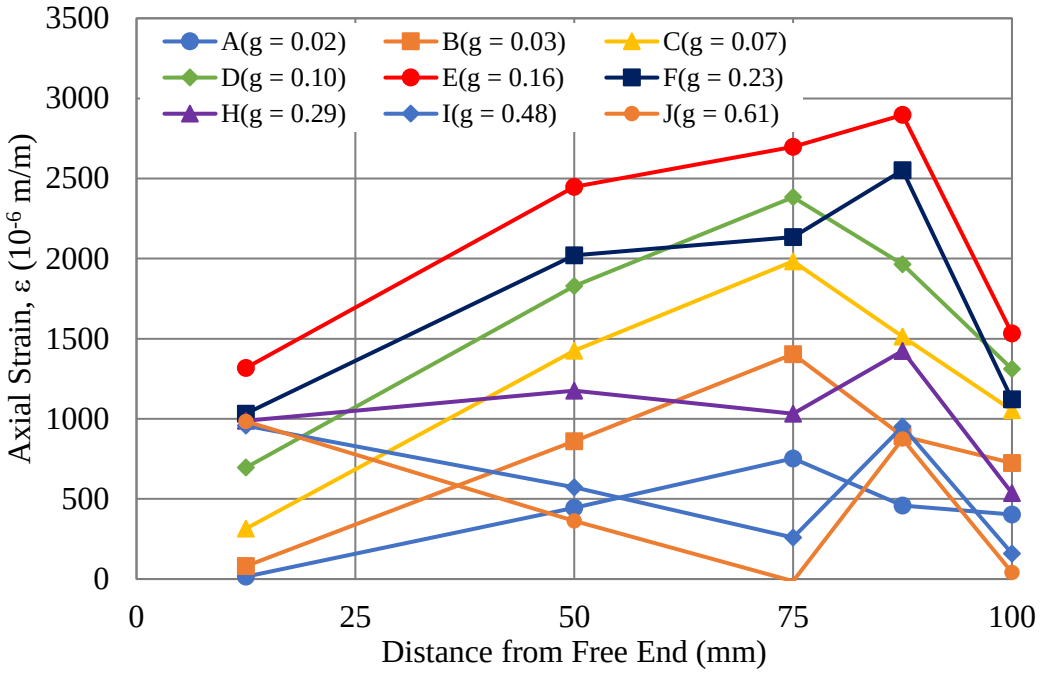

Figure 4.45. Strain distribution at various global slip values for specimen DS_100_50_M_4S

4.4. STRAIN ANALYSIS

This thesis aimed to obtain the cohesive material law (CML) for steel-FRCM composites-concrete joints from certain specimens with strain measurements. First, a mathematical expression for the strain along the bonded length of the composite at the debonding load, P_{deb}, was used to fit the discrete strain measurements. Then, the slip and shear stress were obtained by the integration and derivation of the strain profile expression, respectively. Finally, the CML was obtained by combining the slip and shear stress. Similar approximations have been conducted on experimental FRP specimen data (Yao et al., 2005) and on PBO-FRCM test data (D'Antino et al., 2014; D'Antino et al., 2018). Currently, there are few (if any) published studies that use a similar procedure to analytically model the strain distribution along the bonded length of steel-FRCM

www.manaraa.com

composites. While this study has few specimens that can be used for this purpose, the results herein provide introductory results of such analysis.

4.4.1. Specimen Selection. Because the analysis was based on measured strain data, only specimens fitted with strain gauges were considered in this portion of the analysis. Additionally, only specimens with a bonded length of 330 mm were considered in the analysis because they have a debonding load at which the stress transfer zone (STZ) was fully developed. Based on the experimental results, the strain data for the 100 mm bonded length specimens may not be truly representative of the actual response due to the interference of the strain gauge installation procedure. Also, the specimens with a 100 mm composite bonded length have not fully developed the STZ, which makes accurately identifying the debonding load nearly impossible. Finally, the previous PBO-FRCM studies that performed a strain analysis (mentioned above) used specimens with a bonded length greater than the effective bond length, ℓ_{eff}. Based on a preliminary strain analysis of the steel-FRCM specimens, the effective bond length was estimated to be between 200 mm and 260 mm, so all 100 mm bonded length specimens were excluded from this portion of the analysis. Additionally, the epoxy anchor specimens were excluded from consideration due to the variability in applied load-global slip response and strain distribution.

Based on the aforementioned criteria, control specimens DS_330_50_C_6S and DS_330_50_C_7S were included in the strain analysis. Additionally, specimen DS_330_50_M_6S and DS_330_50_M_7S, which had mortar anchors, were also included in the analysis. The strain analysis was conducted with respect to the debonding load, or P_{deb}. As previously discussed in Section 2.2, the debonding load is the point at

www.manaraa.com

which the full STZ is established, and where bond between the fiber and matrix is the only load-carrying mechanism. Because this stress transfer zone relates to the effective bond length (which was estimated to be between 200 mm and 260 mm), all of the 330 mm bonded length specimens would be able to fully develop the stress transfer zone activating a portion of the bonded length without interference from the end-anchorage. Moreover, at the debonding load, the strain at the free end of the composite is assumed to be zero, suggesting that the presence or lack of an end anchorage system would have no effect on the response of the composite up to the point of debonding. Thus, the results of both anchored and unanchored composites were included together in the strain analysis.

4.4.2. Determining Debonding Load. The first step in the analysis was to determine the debonding load, P_{deb}. Determining the point of debonding is somewhat of a challenge based on a number of factors. First, the strain profiles presented in Section 4.3 only truly represent strain values at discrete points. The accuracy of the overall profile is somewhat based on the number of strain gauges along the bonded length. With a limited number of gauges at a limited number of points, the full resolution of the strain profile was not captured. By the same measure, it is very difficult to precisely identify the point in which strain increases in portions of the bonded length due to the limited number of gauge readings. In order to mitigate some of the uncertainty, five points on the applied load-global slip response (and thus five strain profiles) were analyzed in a small region around the assumed point of debonding.

The applied load-global slip response for the four specimens utilized in the strain analysis are shown again below in Figure 4.46, Figure 4.47, Figure 4.48, and Figure 4.49. For brevity, the strain profiles are not repeated, but can be found above in Section 4.3.

www.manaraa.com

The assumed debonding load is marked on each plot with the marker, $P_{deb.}$ The debonding load was identified based on an observed drop in applied load and an increase in strain measured by the strain gauge located 115 mm from the free end of the composite. This assumes that the effective bond length of the composite is 215 mm. This assumption does have some level of uncertainty due to the limited availability of strain readings. However, this is a reasonable value based on the applied load-global slip response of the control specimens, considering also the strain distributions. It is worth restating that the location of the debonding load was determined by both the applied load-global slip response and the strain distribution at various global slip values. Both components were utilized in determining the location of the debonding load.

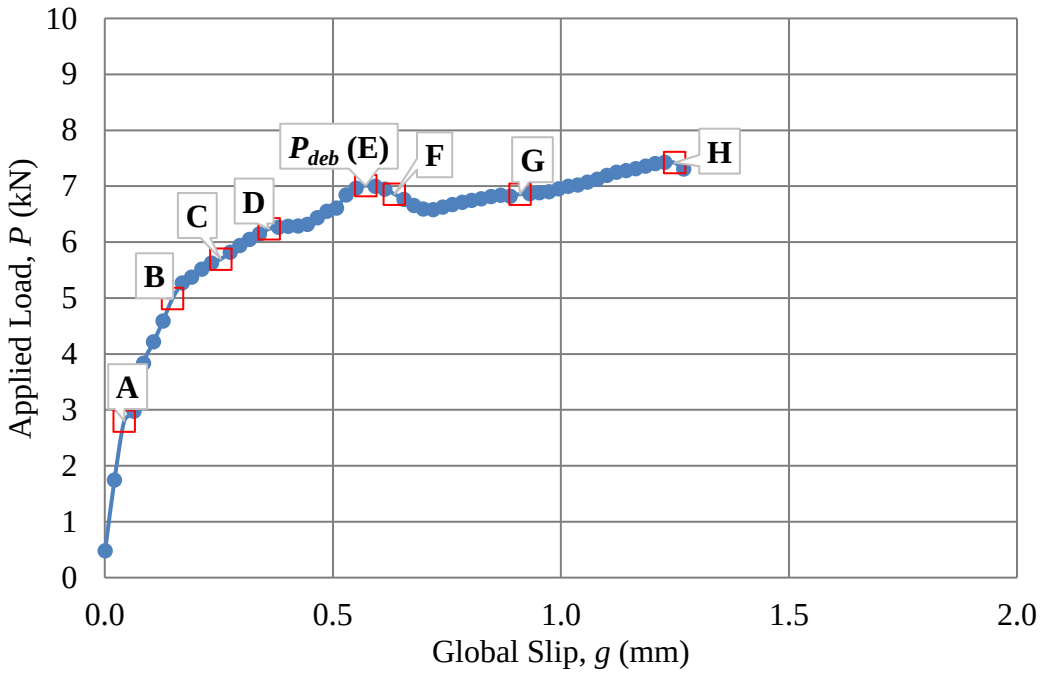

Figure 4.46. Location of debonding load for specimen DS_330_50_C_6S

www.manaraa.com

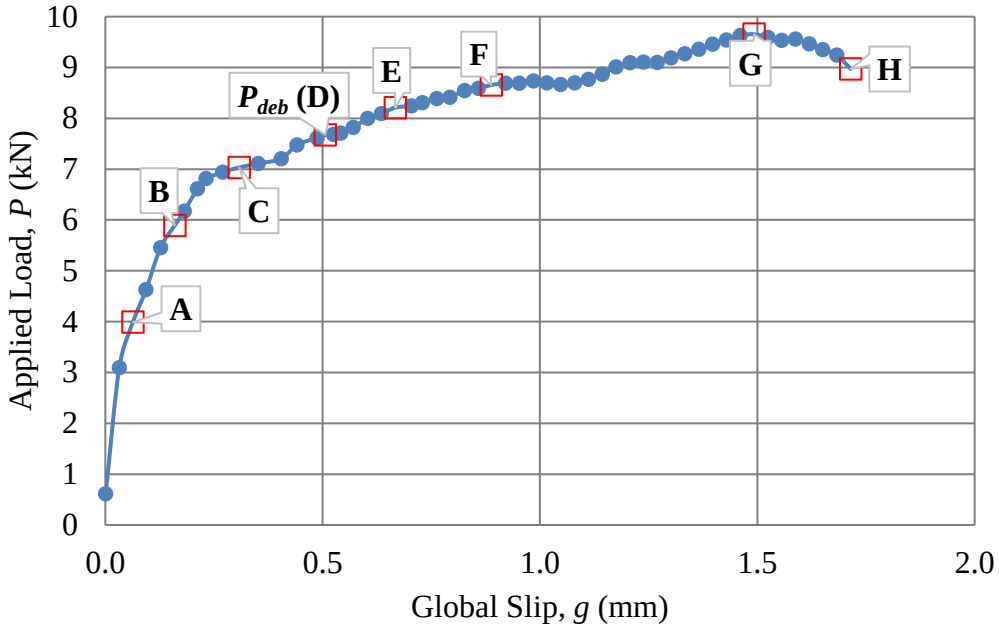

Figure 4.47. Location of debonding load for specimen DS_330_50_C_7S

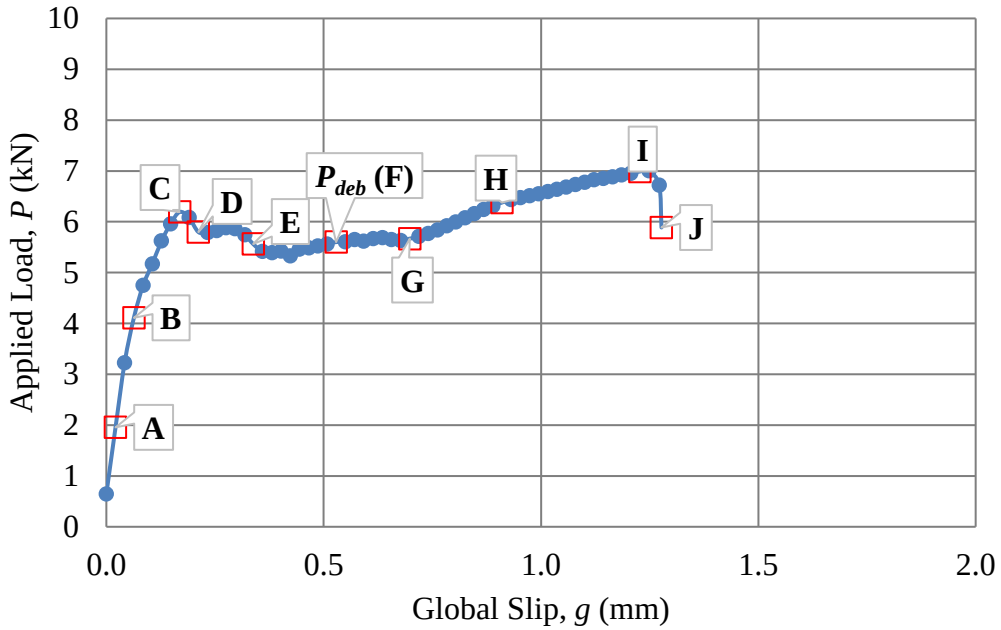

Figure 4.48. Location of debonding load for specimen DS_330_50_M_6S

www.manaraa.com

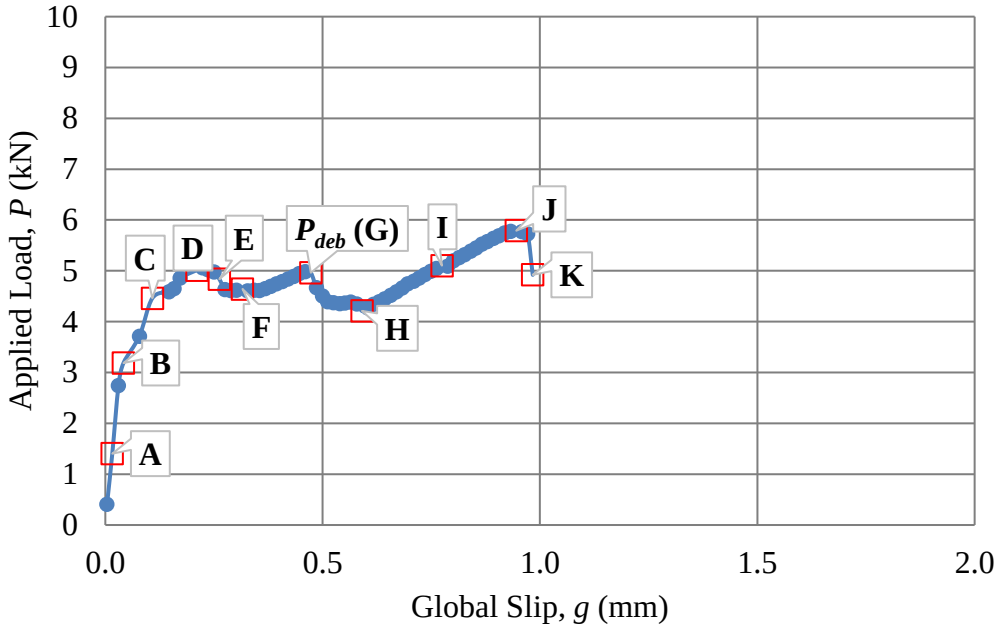

Figure 4.49. Location of debonding load for specimen DS_330_50_M_7S

After identifying the debonding load, five points were selected in a small region around the assumed point of interest. The selection of five points near the assumed debonding load increased the likelihood of capturing the true debonding load within the values. Table 4.3, Table 4.4, Table 4.5, and Table 4.6 list the corresponding applied load, global slip, and strain values at the points of interest for the analyzed specimens.

Table 4.3. Strain, load and global slip data for specimen DS_330_50_C_6S

	Point 1	Point 2	Point 3	Point 4	Point 5
Strain @ y = 315 mm (με)	4847	4934	4989	4979	4949
Strain @ y = 215 mm (με)	2282	2395	2481	2504	2489
Strain @ y = 115 mm (με)	50	55	78	168	370
Strain @ y = 15 mm (με)	23	25	22	25	21
Applied Load, P (kN)	6.84	6.96	7.01	6.99	6.94
Global Slip, g (mm)	0.53	0.55	0.57	0.59	0.61

www.manaraa.com

Table 4.4. Strain, load and global slip data for specimen DS_330_50_C_7S

	Point 1	Point 2	Point 3	Point 4	Point 5
Strain @ y = 315 mm (με)	4061	4185	4216	4268	4276
Strain @ y = 215 mm (με)	2067	2259	2338	2422	2459
Strain @ y = 115 mm (με)	37	83	139	195	250
Strain @ y = 15 mm (με)	-1	-1	-1	0	-2
Applied Load, P (kN)	7.48	7.61	7.67	7.68	7.71
Global Slip, g (mm)	0.44	0.49	0.51	0.53	0.54

Table 4.5. Strain, load and global slip data for specimen DS_330_50_M_6S

	Point 1	Point 2	Point 3	Point 4	Point 5
Strain @ y = 315 mm (με)	4169	4194	4209	4175	4175
Strain @ y = 215 mm (με)	2455	2539	2593	2620	2662
Strain @ y = 115 mm (με)	56	78	135	527	703
Strain @ y = 15 mm (με)	68	16	-17	-74	21
Applied Load, P (kN)	5.53	5.56	5.60	5.61	5.65
Global Slip, g (mm)	0.49	0.51	0.53	0.55	0.57

Table 4.6. Strain, load and global slip data for specimen DS_330_50_M_7S

	Point 1	Point 2	Point 3	Point 4	Point 5
Strain @ y = 315 mm (με)	4044	4071	4064	3887	3786
Strain @ y = 215 mm (με)	2218	2148	2021	1734	1563
Strain @ y = 115 mm (με)	15	20	22	28	57
Strain @ y = 15 mm (με)	9	7	5	7	7
Applied Load, P (kN)	4.94	4.98	4.96	4.67	4.51
Global Slip, g (mm)	0.45	0.46	0.47	0.49	0.50

As shown in the above tables, the strain values at the free end of the composite (15 mm from the free end) approximately are zero, relative to the strain values measured at other gauge locations. The measured experimental values shown in Table 4.3, Table 4.4, Table 4.5, and Table 4.6 are not listed as zero, but this difference is attributed to the precision of the strain gauges and the ability of the data acquisition system to tare the

www.manaraa.com

readings prior to testing. This minor difference, as shown in the analysis to follow, will only slightly influence the final result to a negligible level.

4.4.3. Nonlinear Regression Analysis of Measured Strains. After obtaining the measured strain values at points near the assumed debonding load, the strain profiles were approximated using Equation 4.1.

$$\varepsilon(y) = \varepsilon_0 + \frac{\alpha + ky}{1 + e^{-\frac{y-y_0}{\beta}}} \tag{4.1}$$

Equation 4.1 was presented by D'Antino et al. (2014) in their study investigating the bond behavior of PBO-FRCM composites. The equation is a modification a function used in the analysis of FRP-concrete joints (Carloni & Subramaniam, 2012) that accounts for the friction interface between the fiber and matrix layer in the unbonded region. The approximation was conducted using MATLAB's curve fitting application. The parameters ε_0, α, β, and y_0 were determined by nonlinear regression analysis, and k was determined using Equation 4.2.

$$k = \frac{\tau_f}{E_f t_f} \tag{4.2}$$

In Equation 4.2, E_f is the elastic modulus of the steel fiber, and t_f is the nominal thickness of the steel fiber (as reported in Section 3.3). τ_f corresponds to the shear stress associated with only friction. For PBO-FRCM composites, this value is typically determined by the sustained load level at the end of the applied load-global slip response.

www.manaraa.com

The difference between the peak load, P^*, and the debonding load, P_{deb}, is also related to friction, as reported by D'Antino et al. (2014) in Equation 4.3:

$$P^* - P_{deb} = 2\tau_f nb^*(\ell - \ell_{eff}) \quad (4.3)$$

In Equation 4.3, b^* represents the nominal width of a single longitudinal fiber bundle, n represents the number of longitudinal fiber bundles, and ℓ represents the bonded length of the composite. The quantity $nb^*(\ell-\ell_{eff})$ represents the portion of the original bonded area in which the fiber bundles are subject to friction (T. D'Antino et al., 2014). Equation 4.3 is based on the results of PBO-FRCM bond studies, in which the failure interface was observed between both the internal and external matrix layer. Based on this failure surface, the shear stress is attributed to both sides of the fiber net, represented by the factor "2" in Equation 4.3. Because the failure interface for steel-FRCM composites is only between the internal matrix layer and the steel fiber, a modified version of Equation 4.3 was used in determining the associated shear stress due to friction as shown in Equation 4.4:

$$P^* - P_{deb} = \tau_f nb(\ell - \ell_{eff}) \quad (4.4)$$

For specimen DS_330_50_C_6S, the calculated value of k was determined to be 2.187 (10^{-6})/mm. The debonding load was most easily located for this specimen based on the strain distributions and the applied load-global slip response. This value should be a material property and was thus used for all specimens in the curve fitting process. As

www.manaraa.com

previously mentioned, there are no published steel-FRCM bond studies to compare this experimental value of *k* against but based on the available PBO-FRCM bond studies, the value is reasonable. Based on the available PBO-FRCM studies, this calculated value of *k* is on the same order of magnitude as other determined *k* values. This metric, however, does not determine the precision of the calculation. Accordingly, future steel-FRCM bond studies should work to confirm this value.

Table 4.7, Table 4.8, Table 4.9 and Table 4.10 list the results of the nonlinear regression analysis for specimens DS_330_50_C_6S, DS_330_50_C_7S, DS_330_50_M_6S and DS_330_50_M_7S, respectively. Also, Figure 4.50 shows the curve fitting of the measured strain values for specimen DS_330_50_C_6S at the assumed debonding load. Similar curves were generated for each of the points analyzed for each specimen and are included in Appendix C. Table 4.11 presents the average value of each parameter for each specimen, as well as an overall average of all analyzed specimens in the experimental program. In Table 4.11, and average value for k is not reported, as the same k value was used for each specimen. Also, the coefficient of variation is not reported for ε_0 due to the interference of positive and negative values.

Table 4.7. Summary of curve fitting parameters for DS_330_50_C_6S

Parameter	Point 1	Point 2	Point 3	Point 4	Point 5	Average	CoV
α (10^{-6})	4169	4253	4336	4422	4767	4389	0.047
β (mm)	19.9	20.0	22.6	28.9	41.7	26.6	0.308
y_o (mm)	216.0	214.9	213.9	214.1	218.7	215.5	0.008
ε_o (10^{-6})	23	25	21	21	-15	15	-

www.manaraa.com

Table 4.8. Summary of curve fitting parameters for DS_330_50_C_7S

Parameter	Point 1	Point 2	Point 3	Point 4	Point 5	Average	CoV
α (10^{-6})	3771	4618	4702	4079	5154	4465	0.122
β (mm)	21.4	20.0	22.6	30.9	41.6	27.3	0.332
y_o (mm)	213.5	215.8	215	206.9	220.7	214.4	0.023
ε_o (10^{-6})	-2	25	21	-8	-16	4	-

Table 4.9. Summary of curve fitting parameters for DS_330_50_M_6S

Parameter	Point 1	Point 2	Point 3	Point 4	Point 5	Average	CoV
α (10^{-6})	3418	3513	3595	3939	3968	3687	0.061
β (mm)	2.9	21.6	26.6	46.3	51.5	29.8	0.589
y_o (mm)	213.6	203.2	199.4	190.2	188.7	199.0	0.046
ε_o (10^{-6})	62	16	-20	-162	-112	-43	-

Table 4.10. Summary of curve fitting parameters for DS_330_50_M_7S

Parameter	Point 1	Point 2	Point 3	Point 4	Point 5	Average	CoV
α (10^{-6})	3350	3385	3386	3222	3065	3282	0.038
β (mm)	15.1	17.0	18.4	20.2	3.4	14.8	0.402
y_o (mm)	210.2	211.2	213.3	217.6	215.9	213.6	0.013
ε_o (10^{-6})	9	7	5	7	32	12	-

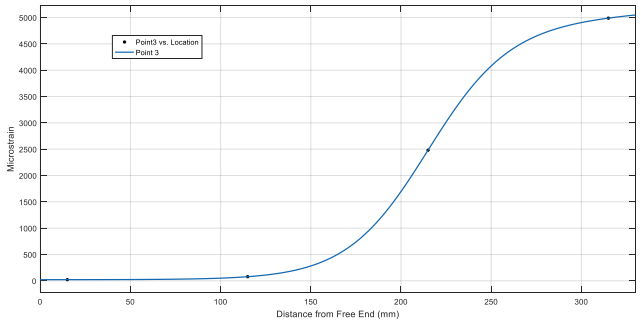

Figure 4.50. Curve fitting of measured strain values at assumed debonding load for specimen DS_330_50_C_6S

www.manaraa.com

Table 4.11. Average curve fitting parameters from all analyzed specimens

	k ((10^{-6})/mm)	α (10^{-6})	β (mm)	y_o (mm)	ε_o (10^{-6})
DS_330_50_C_6S	2.19	4389	26.6	215.5	15
DS_330_50_C_7S	1.03	4465	27.3	214.4	4
DS_330_50_M_6S	2.19	3687	29.8	199.0	-43
DS_330_50_M_7S	2.19	3282	14.8	213.6	12
Average	-	3956	24.6	210.6	-3
CoV	-	0.144	0.272	0.037	-8.833

4.4.4. Shear Stress-Slip Relationship. The average parameters in Table 4.11 in conjunction with Equation 4.1 give an equation for the strain distribution along the bonded length of the composite with *y* as the distance from the free end of the composite (in millimeters) and ε(y) as the strain in the composite (in microstrain). With a discrete function for the strain at various locations along the length, the shear stress at corresponding locations can be determined using Equation 4.5. Additionally, the slip can also be determined using Equation 4.6.

$$\tau(y) = E_f t_f \frac{d\varepsilon(y)}{dy} \tag{4.5}$$

$$s(y) = \int_0^y \varepsilon(y)dy \tag{4.6}$$

Based on the values calculated using Equation 4.5 and Equation 4.6, and the average values from Table 4.11 into Equation 4.1, the shear stress-slip relationship is shown in Figure 4.51.

www.manaraa.com

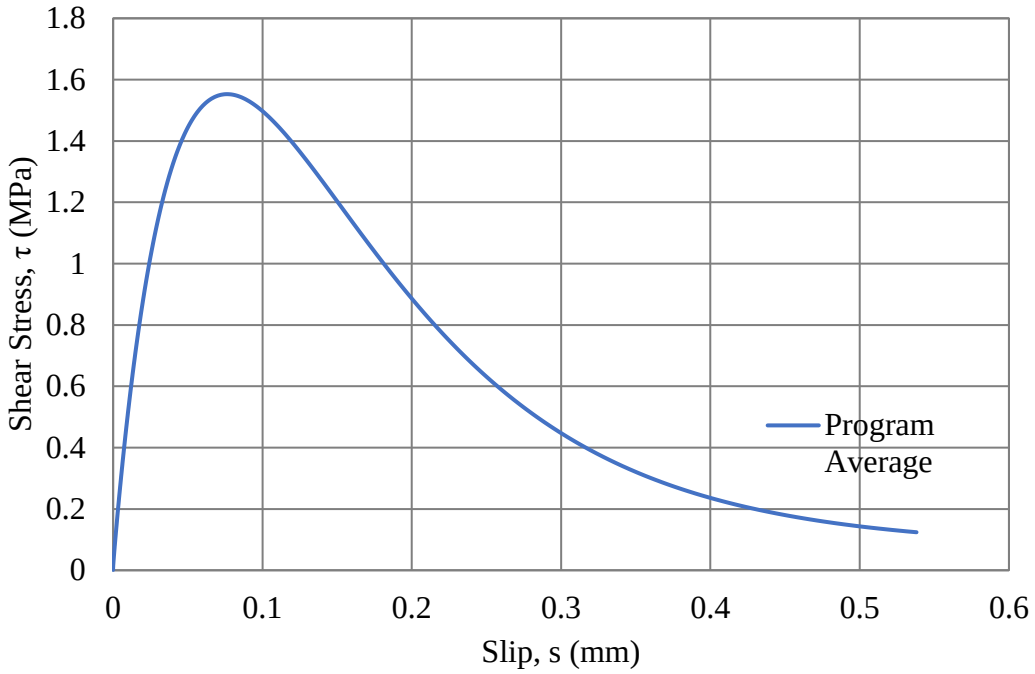

Figure 4.51. Proposed shear stress-slip relationship for steel-FRCM composites

In Figure 4.51, the maximum shear stress, τ_m, was calculated as 1.55 MPa, and the corresponding slip at peak shear stress, s_o, was found to be 0.076 mm. Additionally, the maximum value of slip at failure, s_f, was calculated as 0.543 mm. As previously mentioned, there are no published values for comparison, but these values do seem reasonable compared to the available PBO-FRCM bond studies that report values of the same magnitude. Additionally, the fracture energy of the matrix-fiber interface, G_F, can be calculated using Equation 4.7:

$$G_F = \int_0^{s_f} \tau(s)ds \tag{4.7}$$

www.manaraa.com

Based on Equations 4.5, 4.6, and 4.7, the fracture energy was calculated as G_F = 0.364 N/mm. This value is slightly lower than the value presented by D'Antino et al. (2018), which was reported as 0.481 N/mm based on analysis of 330 mm composite bonded length PBO-FRCM composites. Currently, researchers are studying the bond behavior of PBO-FRCM composites based on a similar procedure in order to approximate the shear stress-slip relationship with a numerical function. A function τ(s) is a necessary first step to accurately model the interfacial behavior of FRCM composites and could then be used to predict debonding and other failure parameters in externally bonded strengthening applications.

4.5. INFLUENCE OF TEST VARIABLES

This section presents a comparison of the experimental results in order to show the influence of certain test variables. The varied parameters in this study were the presence of an end-anchorage system, composite bonded length, anchor depth, and anchor material. Average values of measured parameters are used below, as summarized in Table 4.2. Specimens were compared on the basis of average peak load, $\overline{P^*}$, average absorbed energy, $\overline{E_{ult}}$, and applied load-global slip response.

4.5.1. General Effect of End-Anchorage System. Specimens tested in this program included specimens with and without an end-anchorage system as discussed in Section 3.2. This section compares the results of the experimental program regarding the effect of the end-anchorage system. Due to the difference in the general behavior of the 100 mm bonded length specimens and the 330 mm bonded length specimens, the two groups are compared separately.

www.manaraa.com

The applied load-global slip response of the 330 mm and 100 mm bonded length anchored specimens (both epoxy and mortar anchor binder material) are shown against the response of the corresponding control specimens in Section 4.2. Average values of peak load, $\overline{P^*}$ are shown in the form of a bar graph in Figure 4.52 for 330 mm bonded length specimens with a 75 mm anchor depth and Figure 4.53 for 100 mm bonded length specimens. Additionally, the average values of absorbed energy $\overline{E_{ult}}$ for 330 mm bonded length specimens and 100 mm bonded length specimens are shown in Figure 4.54 and Figure 4.55, respectively. Table 4.12 summarizes the comparison of the anchored specimens to the control specimens.

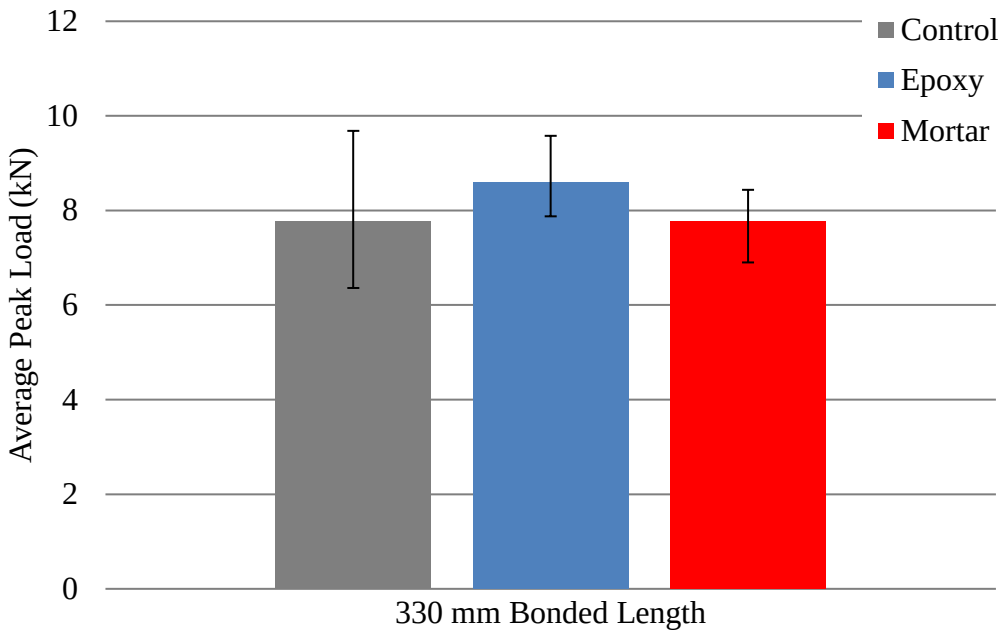

Figure 4.52. Effect of end-anchorage system on average peak load for 330 mm bonded length specimens

www.manaraa.com

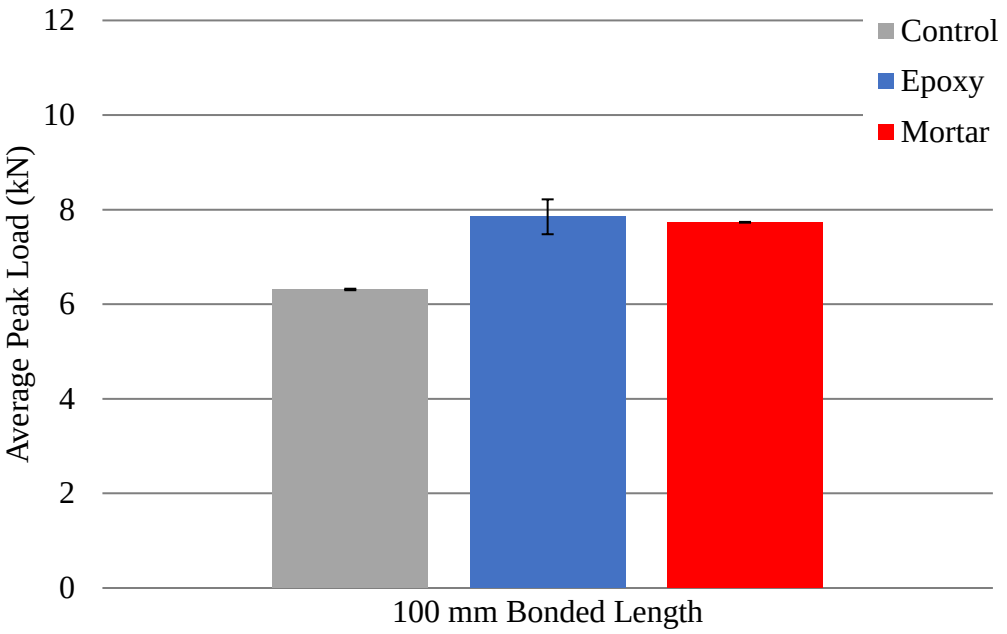

Figure 4.53. Effect of end-anchorage system on average peak load for 100 mm bonded length specimens

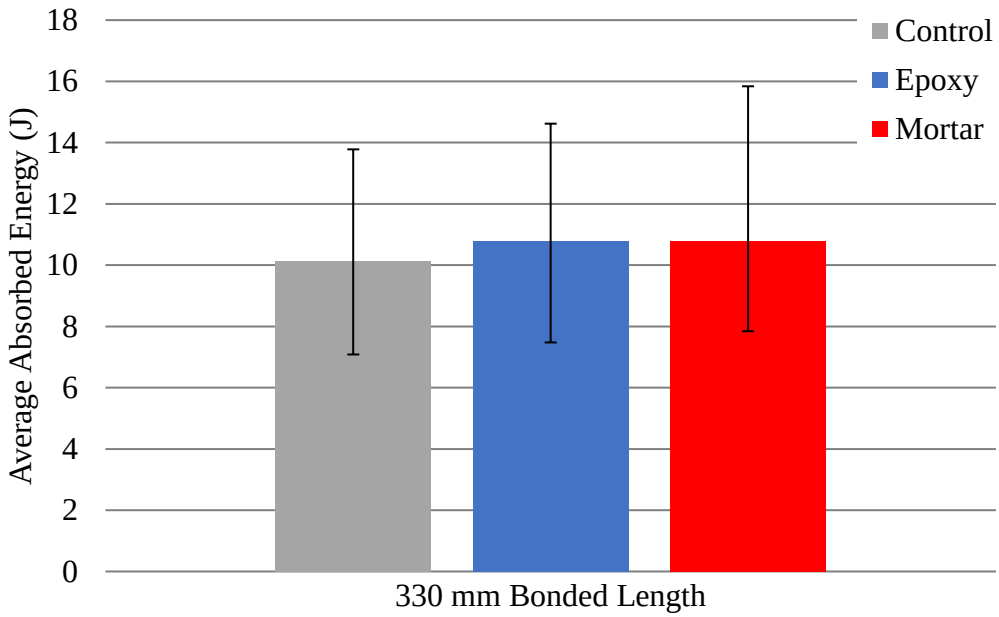

Figure 4.54. Effect of end-anchorage on average absorbed energy for 330 mm bonded length specimens

www.manaraa.com

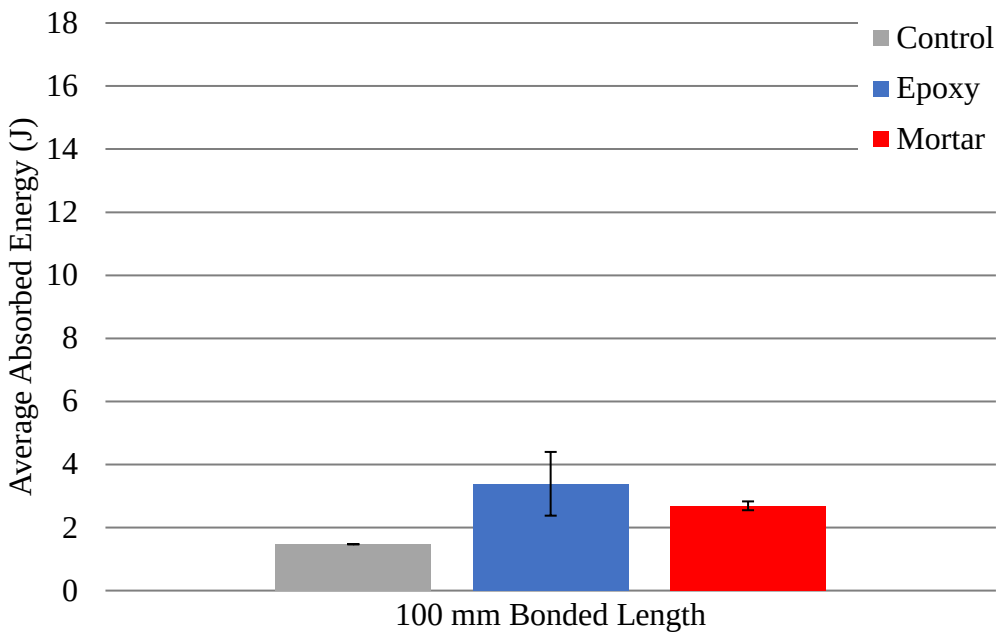

Figure 4.55. Effect of end-anchorage on average absorbed energy for 100 mm bonded length specimens

Table 4.12. Summary of effect of end-anchorage system

Bonded Length	Group	$\overline{P^*}$ (kN)	Increase (%)	$\overline{E_{ult}}$ (J)	Increase (%)
100 mm	Control	6.31	-	1.47	-
	Epoxy	7.85	24	3.39	92
	Mortar	7.73	23	2.69	83
330 mm	Control	7.76	-	10.14	-
	Epoxy	8.61	11	10.77	6
	Mortar	8.40	8	10.79	6

Based on Figure 4.52, Figure 4.54, and the values in Table 4.12, the presence of an end-anchorage system had little effect on the peak load carrying capacity of the 330 mm bonded length specimens. Additionally, the end-anchorage system did not increase

www.manaraa.com

the energy absorption of the composite prior to failure (debonding of the steel fiber). As previously discussed in Section 4.2, testing was completed once the steel fiber had completely debonded from the internal matrix layer. For anchored specimens, this meant that the end anchor was still intact, while the bonded length of the composite was debonded. At this point, in some cases (as discussed in Section 4.2) the anchor was able to sustain some applied load, which would result in an increase in the absorbed energy. This phenomenon should be considered in light of the average increase values shown in Table 4.12.

The effect of the end anchorage was much more significant for the 100 mm bonded length specimens. Figure 4.53 and Figure 4.55 show significant increases in both peak load and absorbed energy over the control specimen. The increase in absorbed energy was attributed to both the increase in peak load and also the increase in global slip at failure. The influence of the end anchor for the 100 mm bonded length specimens compared to the 300 mm bonded length specimens likely is attributed to the bond behavior. For specimens with a length less than the effective bond length, the entire portion of the composite is involved in the stress transfer mechanism at all points along the *P-g* response. This means that from the initial load application, the end-anchor was involved in carrying some of the applied load. For specimens with bonded lengths longer than the effective bond length, initially, only a portion of the bonded region is involved in the stress transfer mechanism. This means that the end-anchor does not "activate" and become involved until the stress transfer zone propagates down along the bonded length.

www.manaraa.com

4.5.2. Effect of Anchor Binder Material. Two anchor binder materials were used in this study. An epoxy resin and a cementitious material were used on select specimens, as discussed in Section 3.2. Figure 4.56 and Figure 4.57 show the average peak load values for epoxy and mortar anchor binder material specimens in the form of a bar graph for 330 mm bonded length (75 mm anchor depth) and 100 mm bonded length specimens, respectively. Also, Figure 4.58 and Figure 4.59 show the average values of absorbed energy for the two anchor materials for the 330 mm and 100 mm bonded length specimens (75 mm anchor depth). Table 4.13 summarizes the average values shown in the previously mentioned figures.

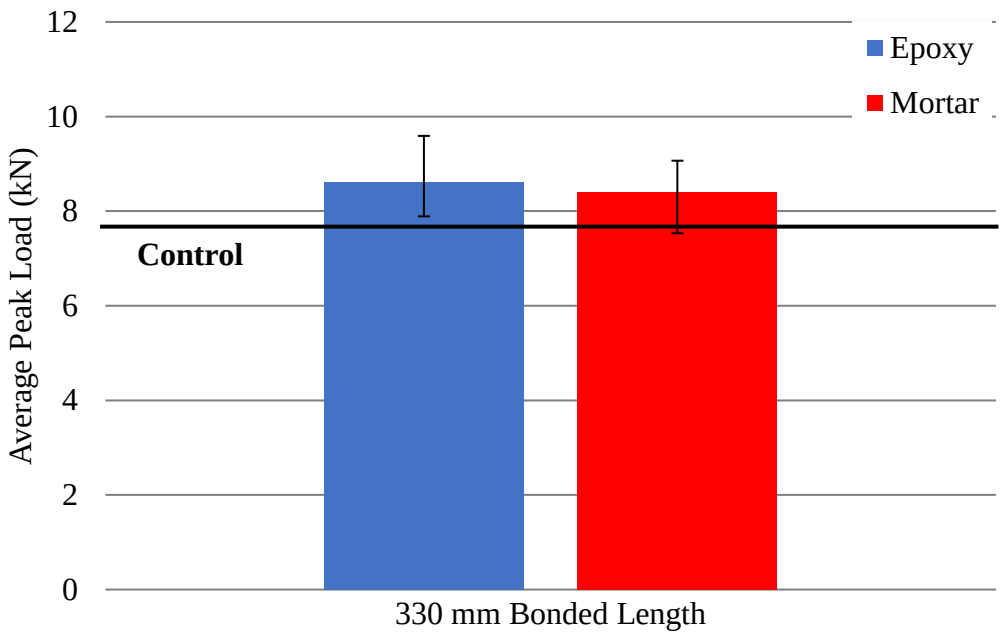

Figure 4.56. Effect of anchor binder material on average peak load for 330 mm bonded length specimens

www.manaraa.com

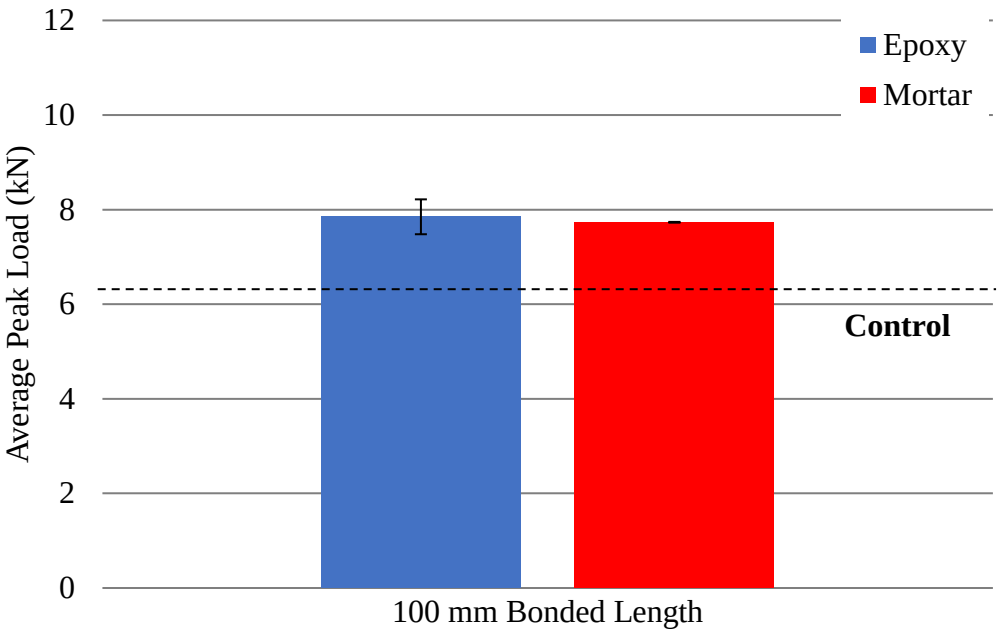

Figure 4.57. Effect of anchor binder material on average peak load for 100 mm bonded length specimens

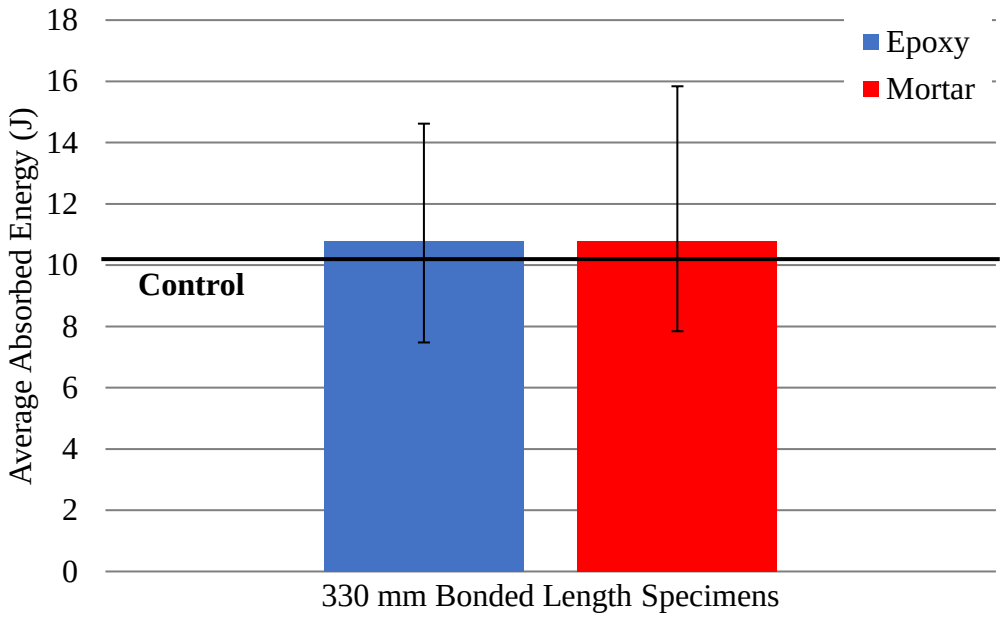

Figure 4.58. Effect of anchor binder material on average absorbed energy for 330 mm bonded length specimens

www.manaraa.com

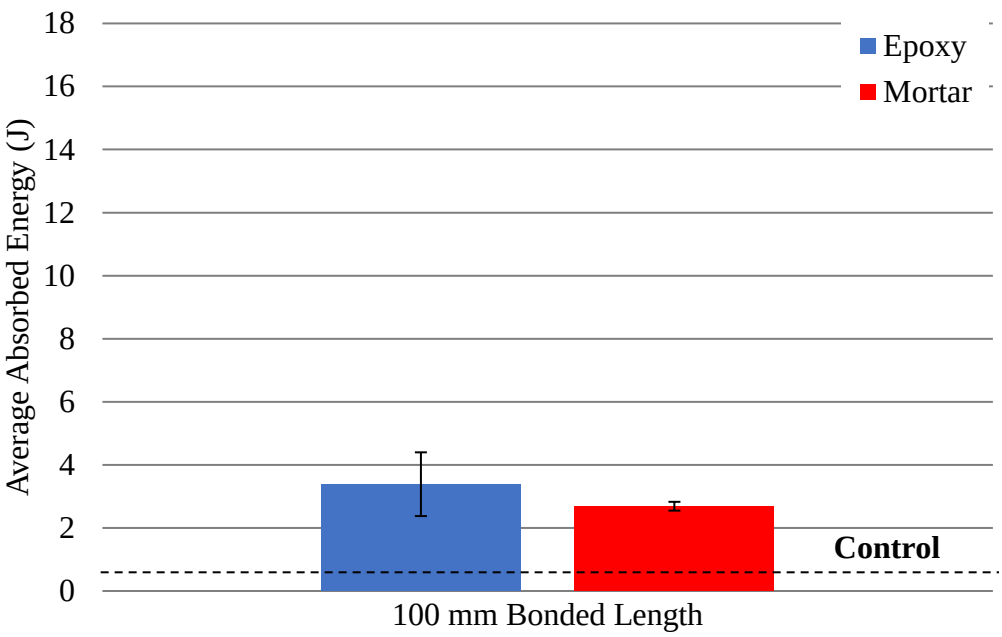

Figure 4.59. Effect of anchor binder material on average absorbed energy for 100 mm bonded length specimens

Table 4.13. Summary of effect of anchor binder material

Bonded Length	Anchor Material	$\overline{P^*}$ (kN)	Difference (%)	$\overline{E_{ult}}$ (J)	Difference (%)
100 mm	Epoxy	7.85	1.49	3.39	22.98
	Mortar	7.73		2.69	
330 mm	Epoxy	8.61	2.46	9.65	0.14
	Mortar	8.40		9.38	

As previously discussed, the effect of the end-anchorage system was minimal for the 330 mm bonded length specimens. Accordingly, the effect of the anchor binder material was also minimal. The percent difference in peak load and absorbed energy between the epoxy anchor binder specimens and the cementitious mortar anchor binder specimens are both relatively small at 2.46% and 0.14%, respectively. A 2% difference in

www.manaraa.com

peak load cannot be considered an advantage of the epoxy resin, considering how small the difference is and the possibility of experimental variability. Also, a 0.14% difference in absorbed energy is certainly within the margin for experimental variation.

The comparison of anchor binder materials for the 100 mm bonded length specimens shows a considerable increase in the absorbed energy for the epoxy anchored specimens compared to the cementitious mortar anchor specimens. A difference of 23% between absorbed energy values does suggest that specimens anchored with the epoxy anchor binder material were able to absorb a substantial amount more energy. Interestingly, the difference in average peak load between the epoxy and mortar anchor specimens was less than 2%. This demonstrates that the increase in absorbed energy came not from an increase in peak load, but from an increase in global slip due to the epoxy anchor. Thus, the 100 mm epoxy anchor specimens behaved in a more ductile manner compared to the mortar anchor specimens.

4.5.3. Effect of Anchor Depth. In addition to two anchor binder materials, two anchor depths were investigated for select specimens as discussed in Section 3.2. Variable anchor depth was limited to 330 mm bonded length specimens. Figure 4.60 and Figure 4.61 shows the average peak load values for the 75 mm and 150 mm anchor depths for the epoxy anchor specimens and mortar anchor specimens, respectively. Figure 4.62 and Figure 4.63 shows the average absorbed energy values for the 75 mm and 150 mm anchor depths for the epoxy anchor specimens and the mortar anchor specimens, respectively. Table 4.14 summarizes the average values from Figures 4.60 through 4.63.

www.manaraa.com

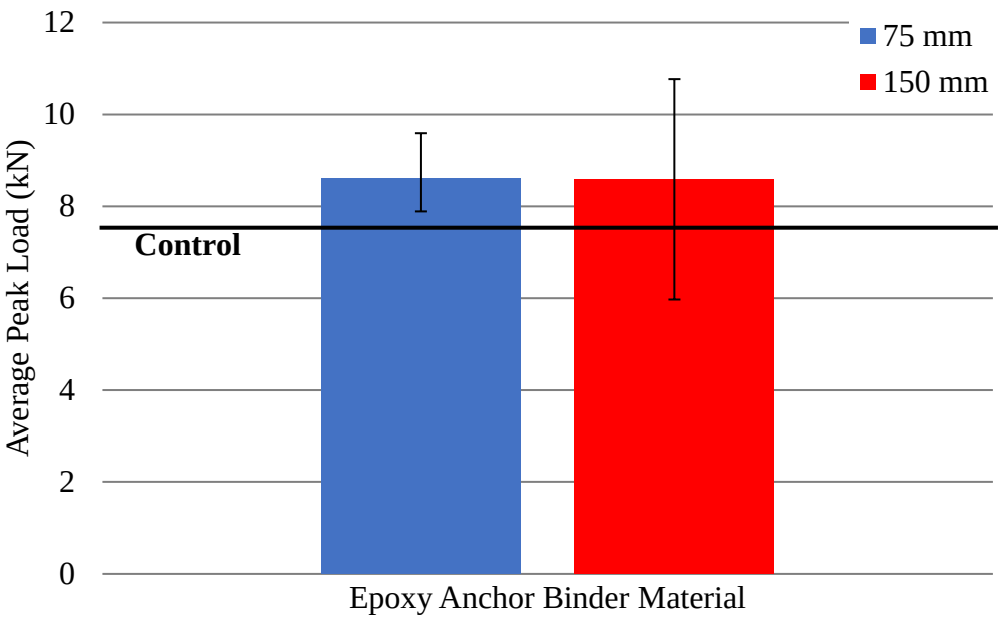

Figure 4.60. Effect of anchor depth on average peak load for 330 mm bonded length epoxy anchor specimens

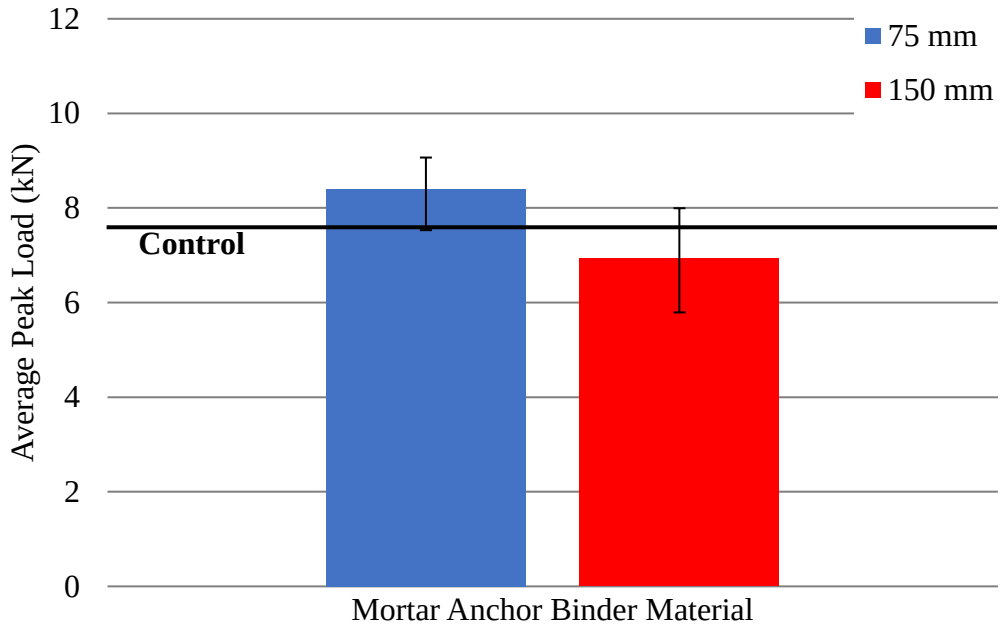

Figure 4.61. Effect of anchor depth on average peak load for 330 mm bonded length mortar anchor specimens

www.manaraa.com

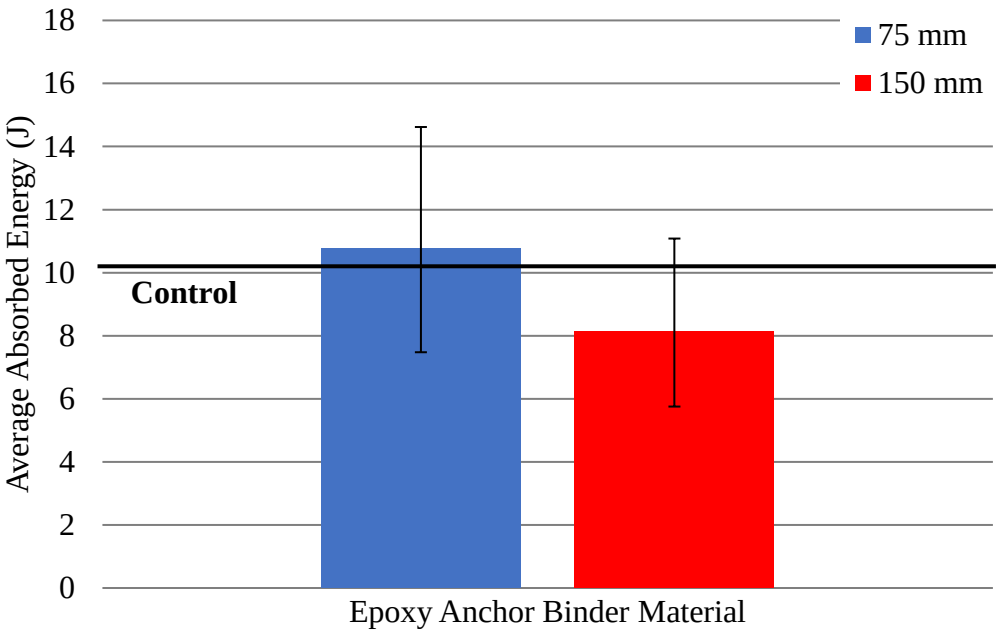

Figure 4.62. Effect of anchor depth on average absorbed energy for 330 mm bonded length epoxy anchor specimens

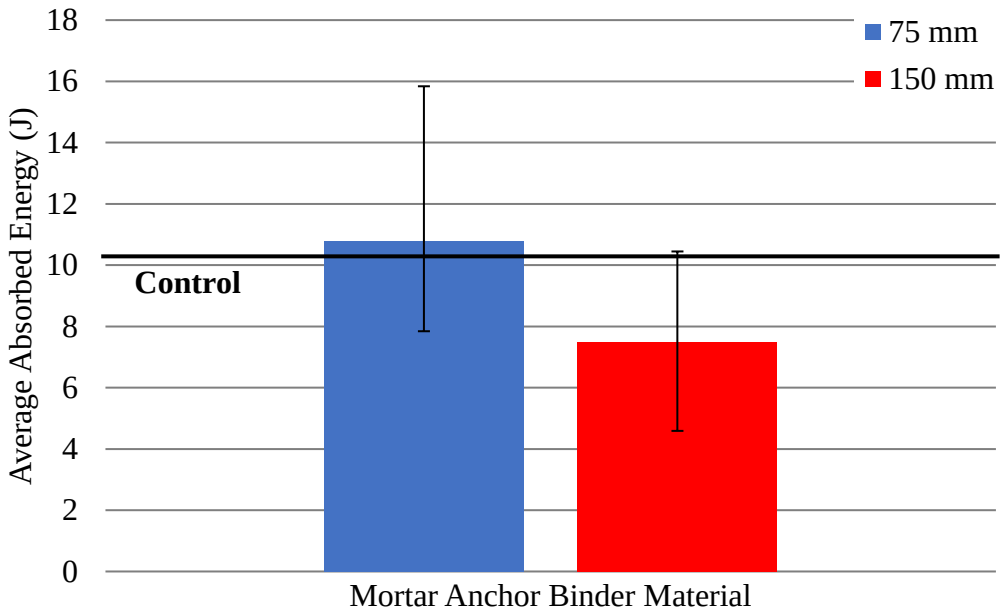

Figure 4.63. Effect of anchor depth on average absorbed energy for 330 mm bonded length mortar anchor specimens

www.manaraa.com

Table 4.14. Summary of effect of anchor depth

Anchor Material	Anchor Depth	$\overline{P^*}$ (kN)	Difference (%)	$\overline{E_{ult}}$ (J)	Difference (%)
Epoxy	75 mm	8.61	0.36	10.77	27.82
	150 mm	8.58		8.14	
Cementitious Mortar	75 mm	8.40	19.17	10.79	36.01
	150 mm	6.93		7.50	

The effect of the anchor depth shows very little effect on the average peak load for the epoxy anchor specimens. This is not surprising, considering the 75 mm anchor depth was determined to be enough to adequately anchor the steel fibers. After failure of one of the 100 mm bonded length epoxy anchor specimens, the load was manually increased up to failure. After reaching a peak applied load value of almost 20 kN, the steel fiber ruptured in tension. Figure 4.64 shows the steel fiber failure. Because the steel fiber failed in tension before pullout failure of the anchor, it can be assumed that the steel fiber was adequately anchored at a depth of 75 mm. Any additional anchor depth would thus not be expected to alter the response (as supported by the average peak load values in Table 4.14).

Interestingly, the mortar anchor specimens show a decrease in both average applied load and average absorbed energy for the 150 mm anchor depth compared to the 75 mm anchor depth. This difference could be accounted for with variation in fabrication of the anchor. It is possible that some voids existed in the anchor due to the increased depth, which increased the difficulty in forming the anchor. Specimen DS_330_50_M_7S could be considered an outlier, which would bring the 150 mm anchor depth average values closer in agreement with the 75 mm anchor depth average values. It is unclear at

www.manaraa.com

this time what caused the decreased response in the 150 mm anchor depth specimens compared to the 75 mm anchor depth specimens.

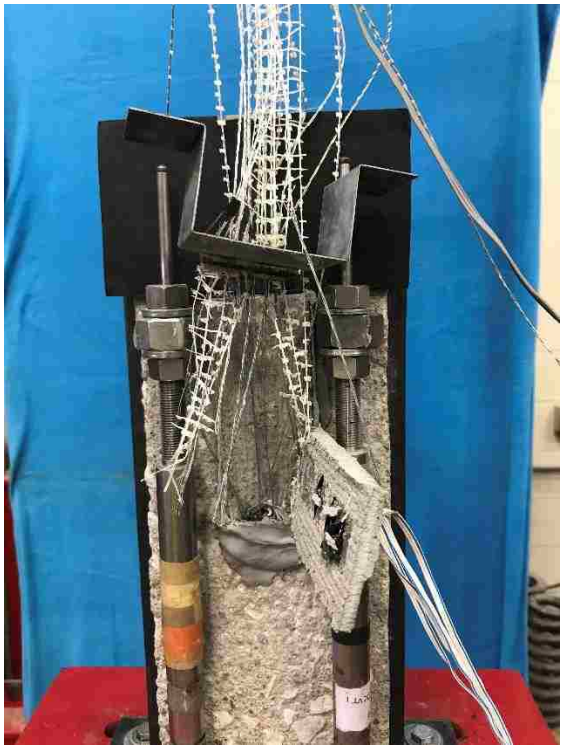

Figure 4.64. Tension failure of steel fibers after manual load application for specimen DS_100_50_E_4S

4.5.4. Effect of Bonded Length. Two different composite bonded lengths were investigated in this study for select specimens as outlined in Section 3.2. A bonded length of 330 mm was selected based on the assumed effective bond length and replication of the available steel-FRCM bond studies. A bonded length of 100 mm was chosen to be intentionally less than the assumed effective bond length to observe the effect of the end anchor with specimens exhibiting different applied load-global slip behavior. Figure 4.65

www.manaraa.com

shows the average peak load values in a bar chart for the 330 mm bonded length and 100 mm bonded length epoxy specimens. Figure 4.66 shows the average absorbed energy values in a bar chart for the 330 mm bonded length and 100 mm bonded length epoxy specimens. Additionally, Figure 4.67 and Figure 4.68 shows the same relationships as Figure 4.65 and Figure 4.66, but for the mortar anchor specimens, respectively. Finally, Table 4.15 summarizes the average values.

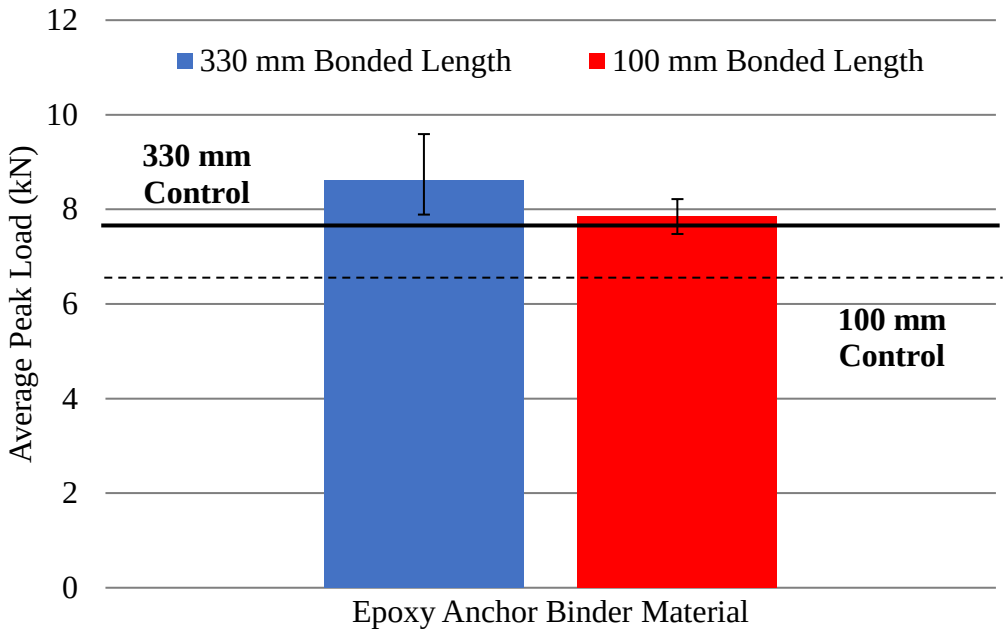

Figure 4.65. Effect of bonded length on average peak load for epoxy anchor specimens

www.manaraa.com

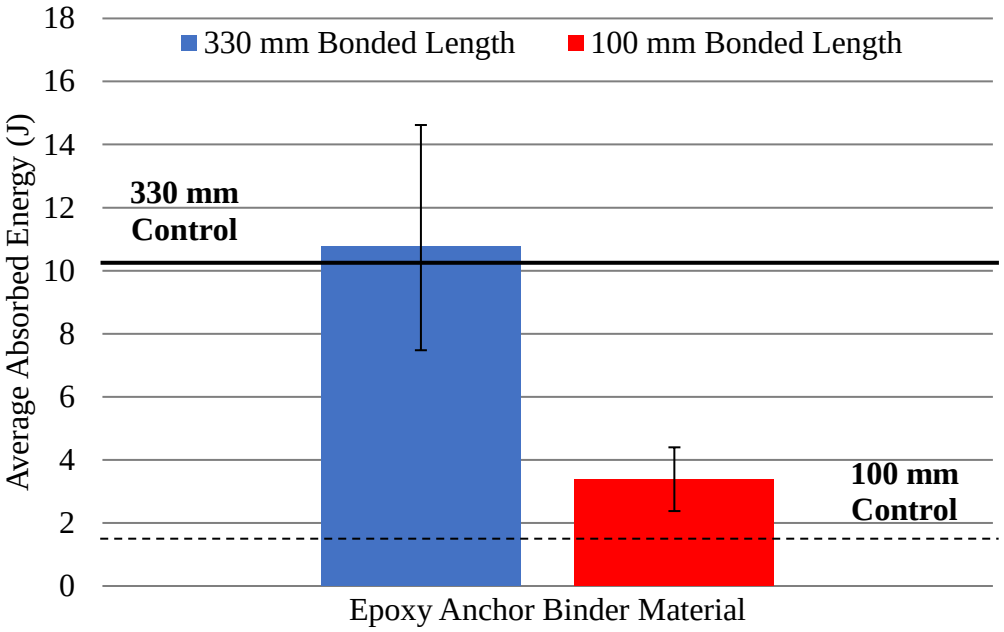

Figure 4.66. Effect of bonded length on average absorbed energy for epoxy anchor specimens

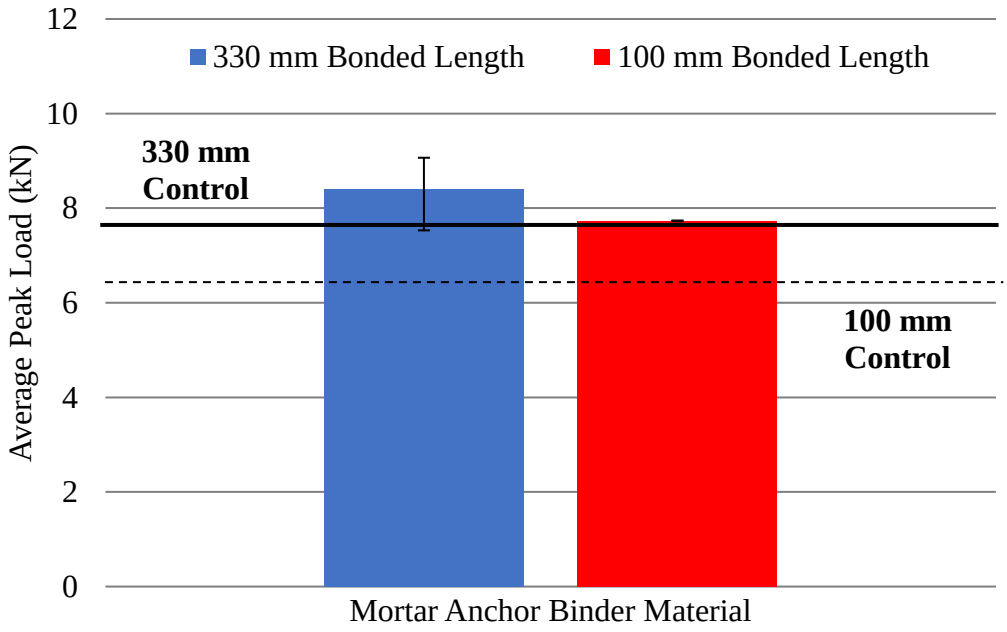

Figure 4.67. Effect of bonded length on average peak load for mortar anchor specimens

www.manaraa.com

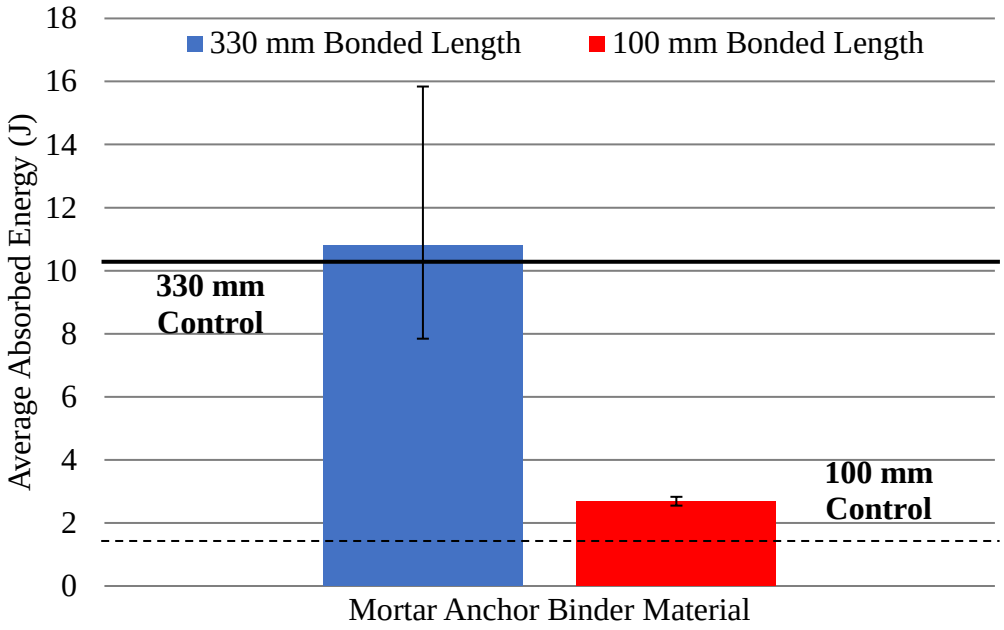

Figure 4.68. Effect of bonded length on average absorbed energy for mortar anchor specimens

Table 4.15. Summary of effect of bonded length

Anchor Material	Bonded Length	$\overline{P^*}$ (kN)	Difference (%)	$\overline{E_{ult}}$ (J)	Difference (%)
Epoxy	100 mm	7.85	9.29	3.39	104.32
	330 mm	8.61		10.77	
Mortar	100 mm	7.73	8.32	2.69	120.20
	330 mm	8.40		10.79	

Interestingly, based on Figure 4.65 and Figure 4.67, the average peak load for the 100 mm anchored specimens was almost equal to the average peak load for the 330 mm bonded length anchored specimens for both anchor types. Also, the average peak load for the 100 mm bonded length epoxy and mortar anchor specimens was larger than the response of the 330 mm bonded length control specimens. This phenomenon should not

www.manaraa.com

be attributed to the additional length alone, because even including the 75 mm anchor depth, the total length of the anchored 100 mm bonded length specimens would be 175 mm, which is still considerably less than the 330 mm bonded length specimens (neglecting that the anchor is oriented in a different plane with respect to the composite bonded length). Average absorbed energy values for the 330 mm bonded length specimens, however, remain consistently higher than the 100 mm bonded length specimens. Again, this was due to the larger observed values of global slip at failure, which resulted in a larger area under the applied load-global slip curve (and thus a larger absorbed energy).

4.6. SUMMARY OF KEY FINDINGS

Based on the experimental results and analysis presented in Section 4.2 through Section 4.5, the following summarizes the key finding of the experimental program:

1. The applied load-global slip response of the 330 mm bonded length control specimens exhibited similar behavior to the response of PBO-FRCM composites. The failure, however, was due to debonding of the steel fiber at the internal matrix-fiber interface as opposed to both the internal and external interfaces. This is a key difference compared to PBO-FRCM composites.
2. Generally, the presence of an end anchorage system had little effect on the peak load carrying capacity for specimens with a bonded length greater than the assumed effective bond length. The average increase in peak load due to an end-anchorage system was approximately 11% for 330 mm

www.manaraa.com

bonded length specimens. The end-anchorage system was also not able to influence the failure mechanism as observed in the unanchored specimens.

3. The anchor binder material also had little effect on the performance of the composite regarding peak load, for both 330 mm and 100 mm bonded length specimens. Only a 1.5% and 2.5% difference were observed in peak load values for the 100 mm and 330 mm bonded length specimens, respectively.
4. The 100 mm bonded length specimens were much more sensitive to the presence of an end-anchorage system. This was observed in both the increase in average peak load and average absorbed energy. A 24% increase in average peak load was observed for the epoxy anchored specimens, and a 23% increase in average peak load was observed for the mortar anchor specimens. Additionally, a 92% increase in average absorbed energy was observed in the epoxy anchor specimens (83% increase for the mortar anchor specimens).
5. Interestingly, the measured average peak load for the 100 mm bonded length anchored specimens was within 10% of the measured average peak load for the 330 mm bonded length anchored specimens. Also, the average peak load for the 100 mm bonded length anchored specimens was within 1% of the average peak load of the 330 mm bonded length control specimen.

www.manaraa.com

6. The post-failure response of the anchor was not characterized in the experimental or analytical portion of this thesis. The preliminary results, however, do suggest that after composite debonding, the end-anchor was still intact, had not failed due to pullout, and did provide some remaining load-carrying capacity.
7. The results of the strain distribution analysis in Section 4.5 suggest an effective bond length of approximately 215 mm. This estimate is based on the available strain profiles collected from the control and mortar anchored specimens at the predicted debonding load. Additionally, from the shear stress-slip relationship, a maximum value of shear stress was determined as τ_m = 1.55 MPa, and the corresponding value of slip was determined as s_m = 0.076 mm. While there are no available published values for comparison, the results of the strain analysis are reasonable when compared to similar analysis of PBO-FRCM composites.
8. The strain gauge installation procedure used in this study did cause some interference in the behavior of the 100 mm bonded length specimens. The reduction in contact area due to the interference of the epoxy patch, while generally insignificant in the 330 mm bonded length specimens, was not negligible in the 100 mm bonded length specimens.

www.manaraa.com

5. SUMMARY, CONCLUSIONS, AND RECOMMENDATIONS

5.1. SUMMARY

This study examined the effect of an end-anchorage system on the bond behavior of steel-FRCM composites. This type of composite has become a popular topic of study in the past decade due to the increase in need for retrofit and repair systems for reinforced concrete and masonry elements. Failure of many types of FRCM composites has been characterized by debonding of the fiber from the matrix layers due to excessive slip at the interface. Accordingly, an end-anchorage system was theorized based on the available literature to potentially restrain the slip of the fibers. Previous studies have investigated the use of anchorage systems in FRP composites, which provided the basis for this experimental program. Currently, there are few published studies investigating the effect of anchorage systems in FRCM applications, and this is the first study that directly investigates the effect of an end-anchorage system on the bond behavior of FRCM composites.

The composite utilized in this study consisted of steel fibers embedded in an inorganic cementitious matrix bonded to a concrete prism. Additionally, an end-anchorage system was implemented with the goal of limiting or preventing fiber slip by anchoring the free end of the steel fibers into a pre-drilled hole in the concrete prism. A total of 33 single-lap direct shear specimens were tested as a part of this experimental program. Eleven specimens were fabricated without an end-anchorage system, and 22 were fabricated with and end-anchorage system oriented at 45° with respect to the composite strip. Test variables included anchor binder material (epoxy resin or

www.manaraa.com

cementitious mortar), composite bonded length (100 mm or 330 mm), and anchor depth (75 mm or 150 mm). The composite was cast onto an unreinforced concrete prism measuring 125 mm by 125 mm and 125 mm by 200 mm, with lengths varying from 375 mm to 510 mm. The FRCM composite consisted of a steel fiber sheet embedded into an inorganic cementitious matrix. Data presented for each specimen included the applied load-global slip relationship. For select specimens, an array of uniaxial strain gauges was attached along the centerline of the steel fiber. Accordingly, the strain distributions at various values of global slip were presented for specimens with a strain gauge array. Results were compared on the basis of peak load and absorbed energy, as well as general specimen behavior.

5.2. CONCLUSIONS

Based on the results of this study, the following conclusions can be made:

1. The presence of an end-anchorage system had minimal effect on the average peak load carrying capacity of specimens with a bonded length greater than the assumed effective bond length (approximately 10% increase). Conversely, the presence of an end anchorage system did have considerable effect on the performance of specimens with a bonded length less than the assumed effective bond length (approximately 24% increase in average peak load and 90% increase in average absorbed energy).
2. The anchor binder material had minimal effect on the peak load carrying capacity for all specimens on the basis of average peak load. For the 330 mm specimens, only a 2.5% difference in average peak load was measured

www.manaraa.com

between the epoxy and mortar anchor binder material, as well as a 0.14% difference in average absorbed energy. Additionally, for the 100 mm specimens, only a 1.5% difference in average peak load was measured between epoxy and mortar anchor binder material. However, a 23% difference in average absorbed energy was observed in the 100 mm composite bonded length specimens.

3. The anchor depth had minimal effect on the average peak load capacity of the epoxy anchor binder material specimens (0.36% difference between 75 mm and 150 mm anchor depth). This suggests that 75 mm is adequate depth to fully anchor the steel fibers in epoxy. A difference of 19% in average peak load was observed for the mortar anchor specimens, with a decrease in the 150 mm anchor specimens. This trend may not accurately suggest a relationship between anchor depths in the mortar anchor binder material specimens.
4. The presence of an end-anchorage system improved the performance of the 100 mm bonded length specimens to similar peak load values as those of the 330 mm bonded length specimens, both with and without an end anchorage. The average peak load values for the 100 mm composite bonded length specimens were within 10% of the average peak load values for the anchored 330 mm bonded length specimens (both epoxy and mortar anchor binder material). The average absorbed energy values, however, were considerably larger for the 330 mm composite bonded length specimens.

www.manaraa.com

5. Interestingly, the 100 mm composite bonded length anchored specimens average peak load values were within 1% of the unanchored 330 mm composite bonded length specimens.
6. The results of the strain distribution analysis suggest a shear stress-slip relationship similar to the reported relationship for PBO-FRCM composites. The results from D'Antino et al. (2018) give a maximum value of shear stress and corresponding slip as τ_m = 0.77 MPa and s_o = 0.18 mm, respectively for PBO-FRCM composites. Similar values are reported in Section 4.4 of this thesis for steel-FRCM composites. Additionally, D'Antino et al. (2018) reported a fracture energy, G_F, of 0.481 N/mm, which is again similar to the value reported in Section 4.4.

5.3. RECOMMENDATIONS FOR FUTURE WORK

The topic of anchorage of FRCM composites has not been extensively reported in the available literature. This thesis work provided an introductory study of the effect of an end-anchorage system on the bond behavior of steel-FRCM composites, but there are still many aspects of the topic that need to be investigated before drawing conclusions. Accordingly, the following are recommendations for future work:

1. For specimens tested in this study, only two bonded lengths were investigated. Further investigation is necessary to determine at what point the presence of an end-anchor effects the performance of the composite.
2. The angle at which the anchor was drilled into the concrete prism was not considered as a variable of this study. Future studies should investigate the

www.manaraa.com

effect of the angle of inclination of the anchor, including an anchor that is oriented parallel to (i.e. in line with) the longitudinal axis of the composite.

3. Investigation should be conducted to determine the effect of fiber type for anchorage of FRCM composites. This study investigated steel-FRCM composites, so future work should include steel fibers of varying density, as well as PBO, carbon, glass, or basalt FRCM composites.
4. Future studies should investigate an alternate method of measuring the strain profiles along the bonded length of the composite for steel-FRCM specimens. Gauges could not be directly attached to the steel cords (like for PBO-FRCM specimens), but the application of a small epoxy bonding patch proved to interfere with the bond between the steel fiber and internal matrix layer for relatively small bonded lengths.
5. This study investigated an end-anchorage system, but future studies should also attempt to anchor the composite at points along the bonded length. The results of this study demonstrate that for long bonded lengths, the anchor does not activate at the initial load application. Anchorage at points closer to the loaded end may change this phenomenon.
6. Finally, future studies should also focus on the bond behavior of unanchored steel-FRCM composites. A more complete understanding of the bond-slip relationship will help in refining design equations for future use. The strain analysis presented in Section 4.5 provided the bond-slip

www.manaraa.com

model for only a limited number of specimens. In order to more accurately refine this model and determine the effective bond length of steel-FRCM composites, additional tests should be conducted in a similar manner to the procedure outlined in this thesis.

www.manaraa.com

APPENDIX A.

INDIVIDUAL APPLIED LOAD-GLOBAL SLIP RESPONSE CURVES

www.manaraa.com

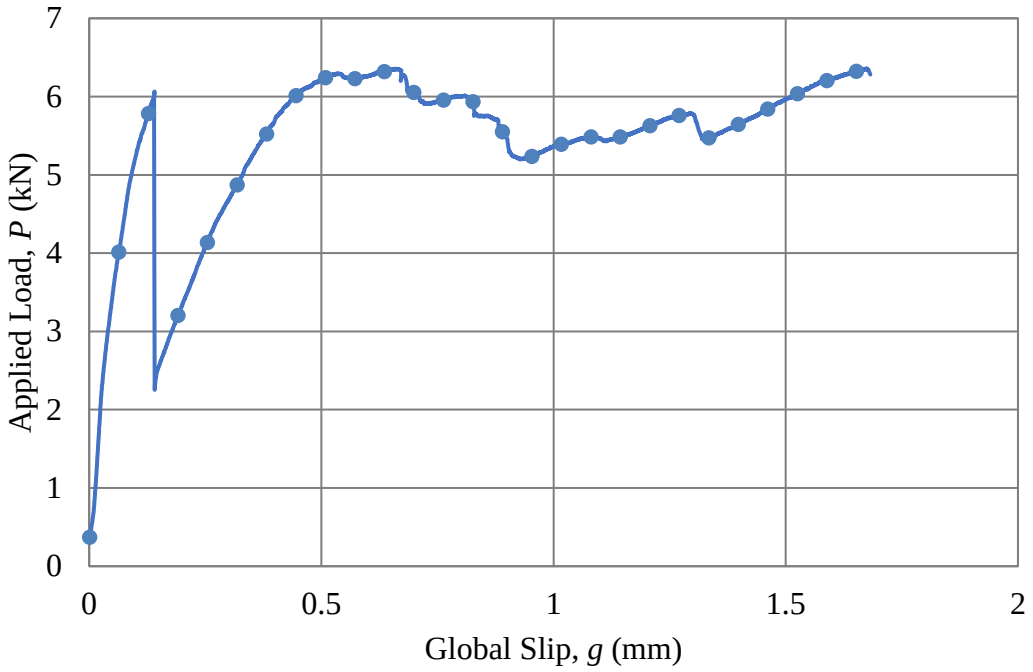

Figure A.1. Applied load-global slip response for specimen DS_330_50_C_1

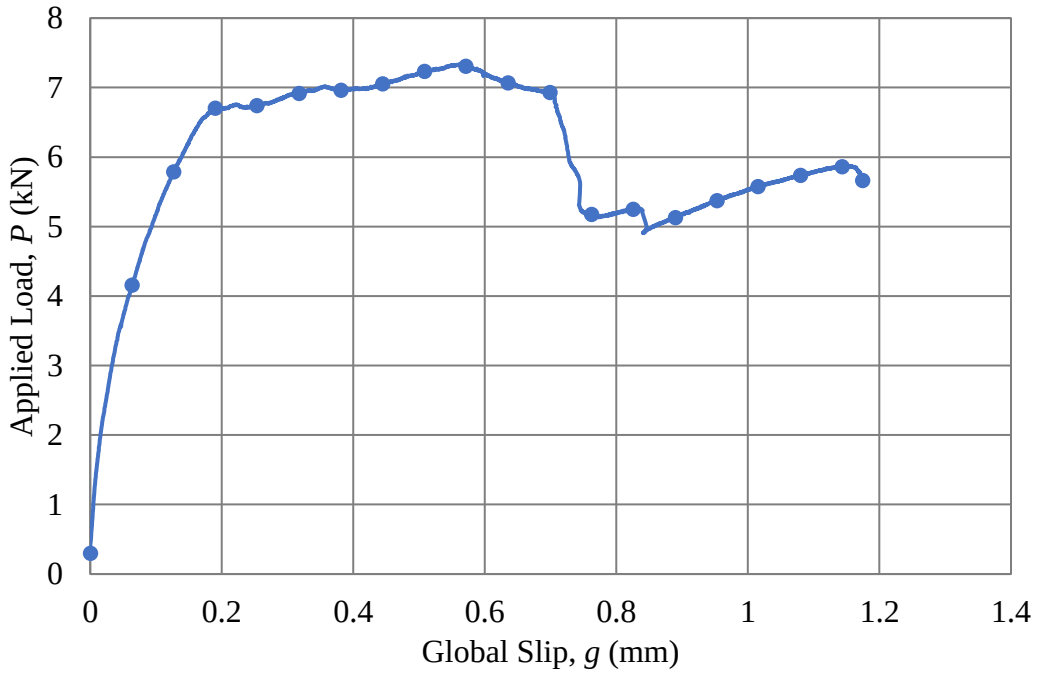

Figure A.2. Applied load-global slip response for specimen DS_330_50_C_2

www.manaraa.com

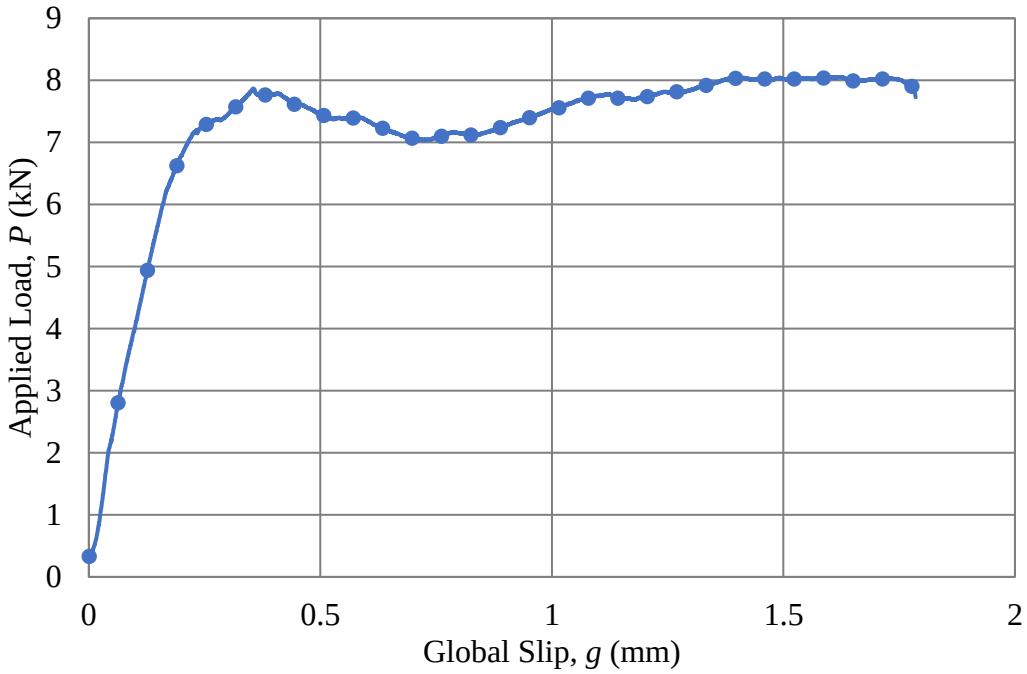

Figure A. 3. Applied load-global slip response for specimen DS_330_50_C_3

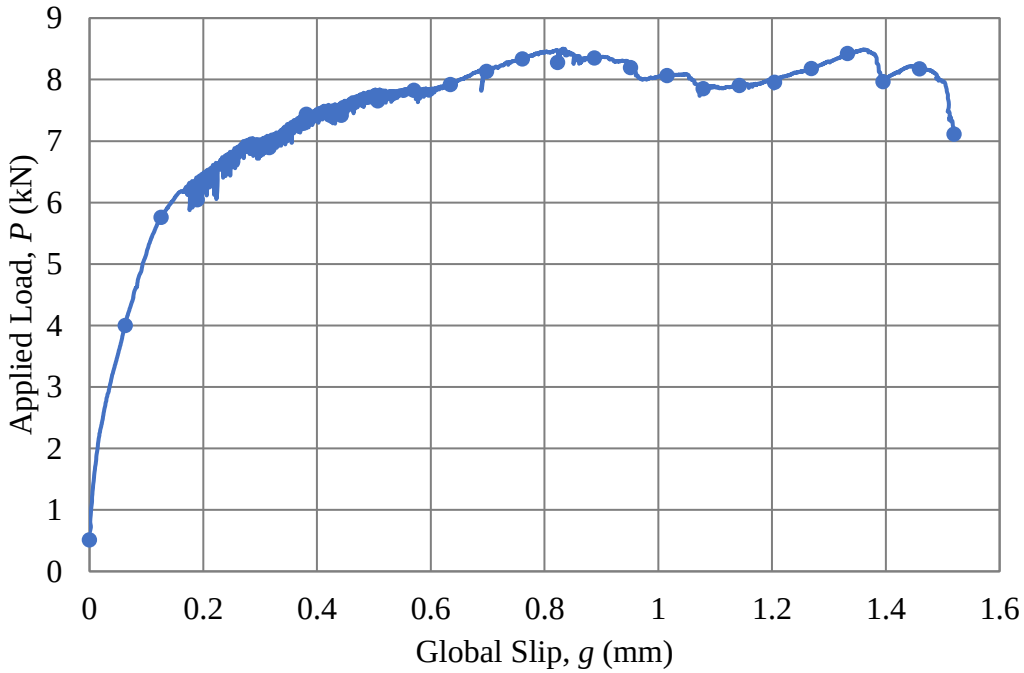

Figure A.4. Applied load-global slip response for specimen DS_330_50_C_4

www.manaraa.com

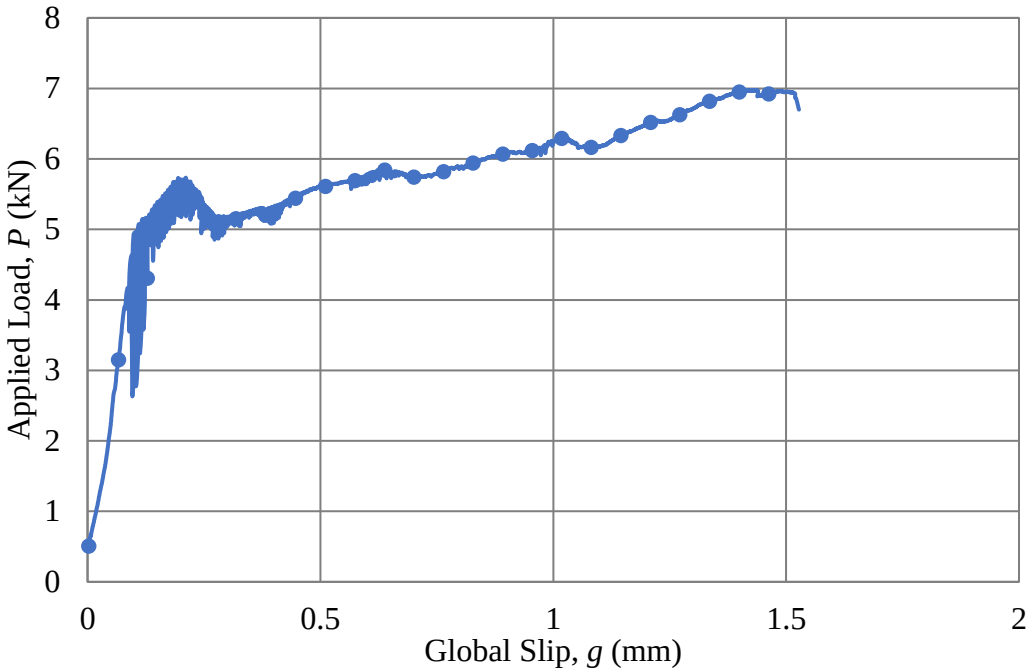

Figure A.5. Applied load-global slip response for specimen DS_330_50_C_5

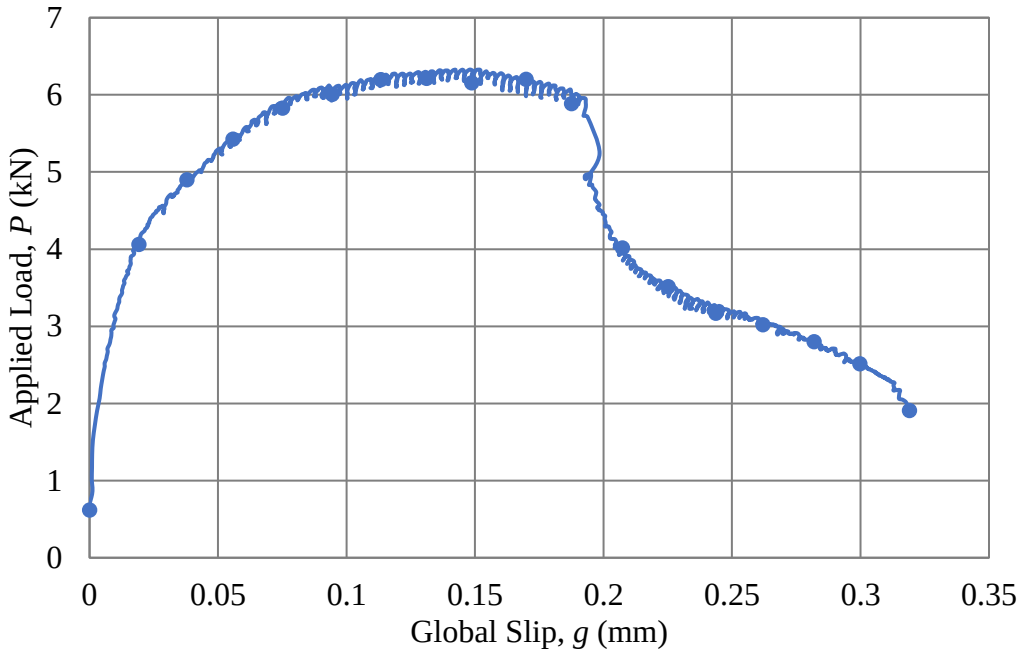

Figure A.6. Applied load-global slip response for specimen DS_100_50_C_1

www.manaraa.com

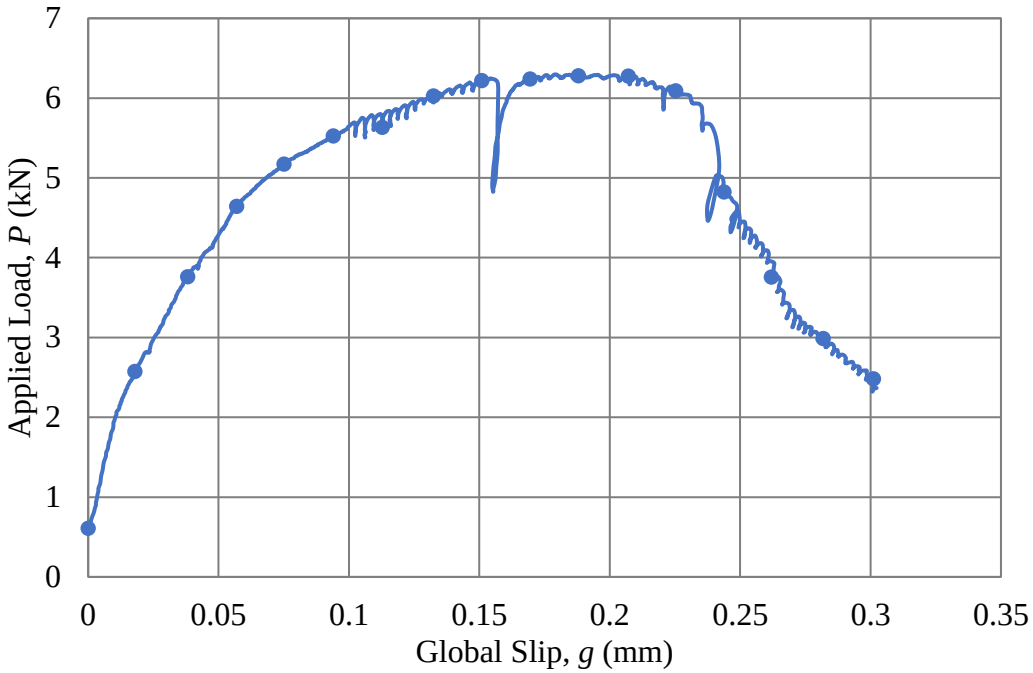

Figure A.7. Applied load-global slip response for specimen DS_100_50_C_2

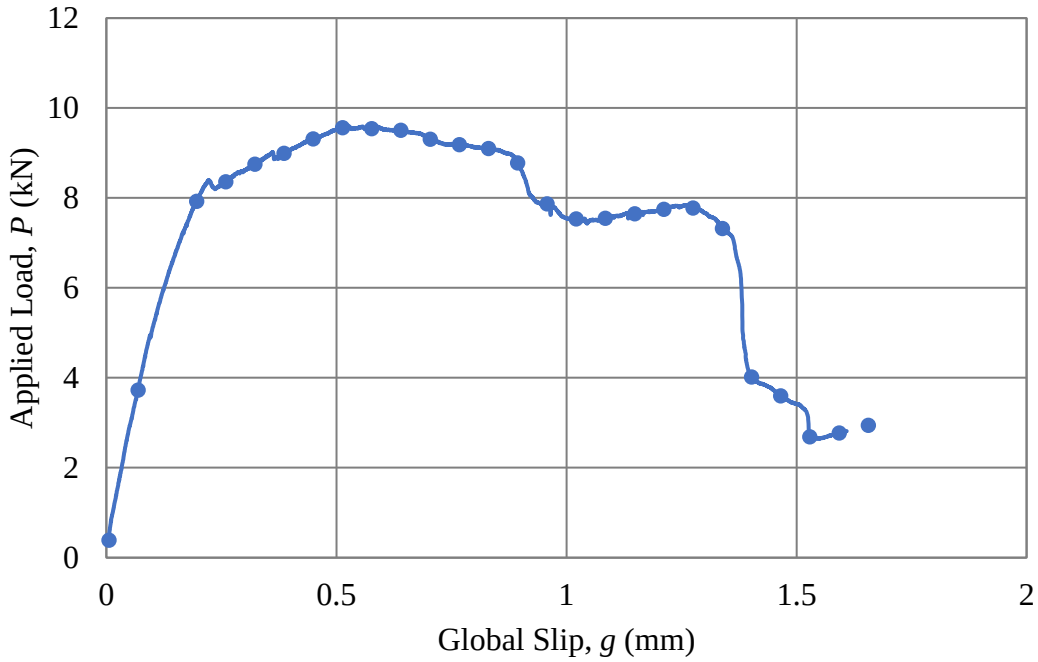

Figure A.8. Applied load-global slip response for specimen DS_330_50_E_1

www.manaraa.com

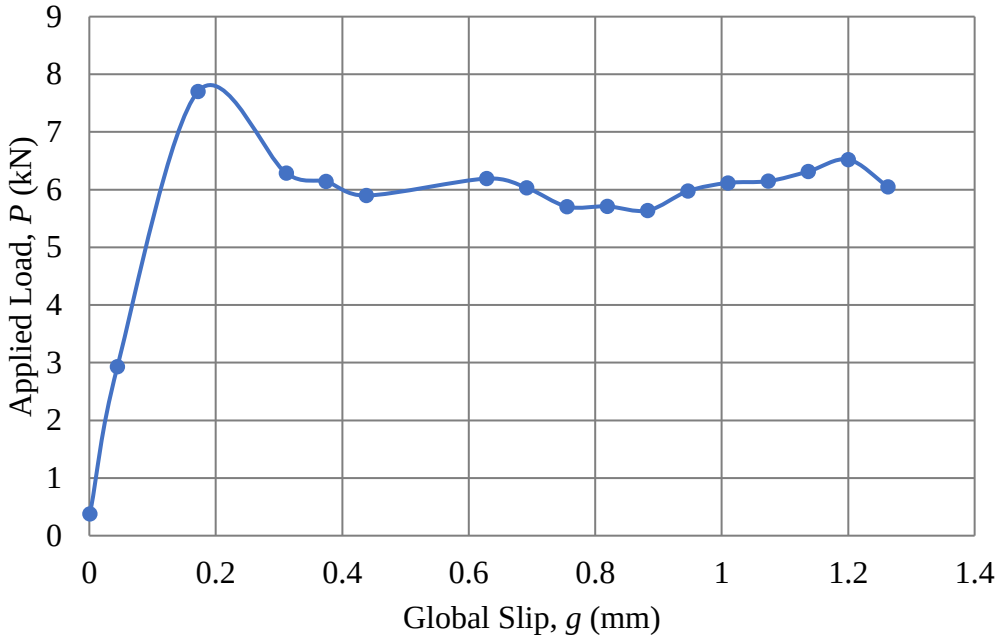

Figure A.9. Applied load-global slip response for specimen DS_330_50_E_2

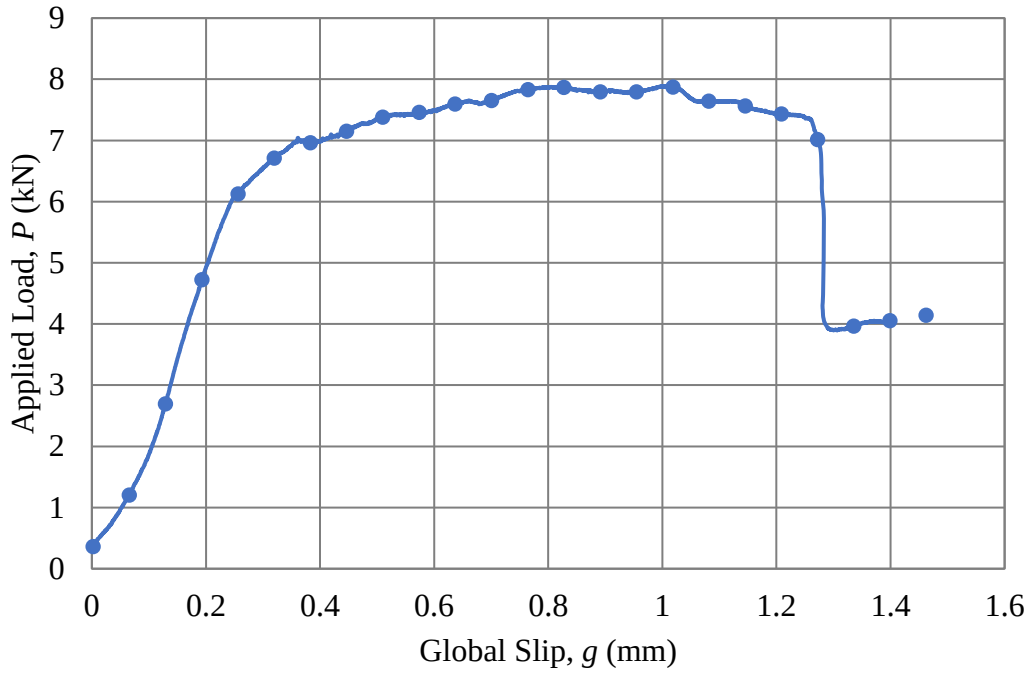

Figure A.10. Applied load-global slip response for specimen DS_330_50_E_3

www.manaraa.com

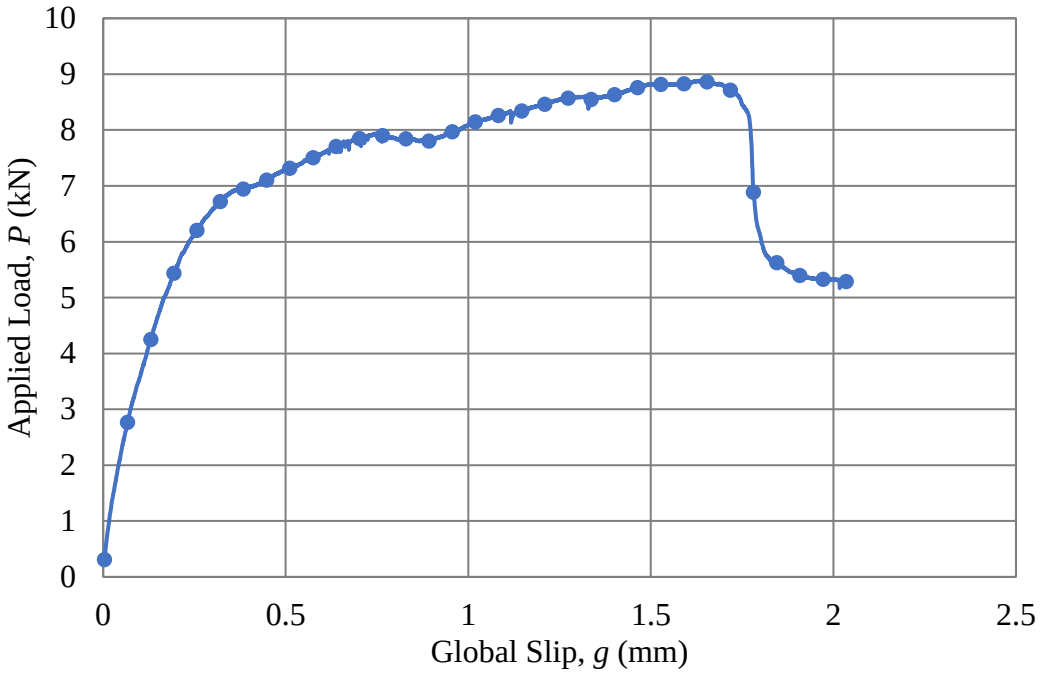

Figure A.11. Applied load-global slip response for specimen DS_330_50_E_4

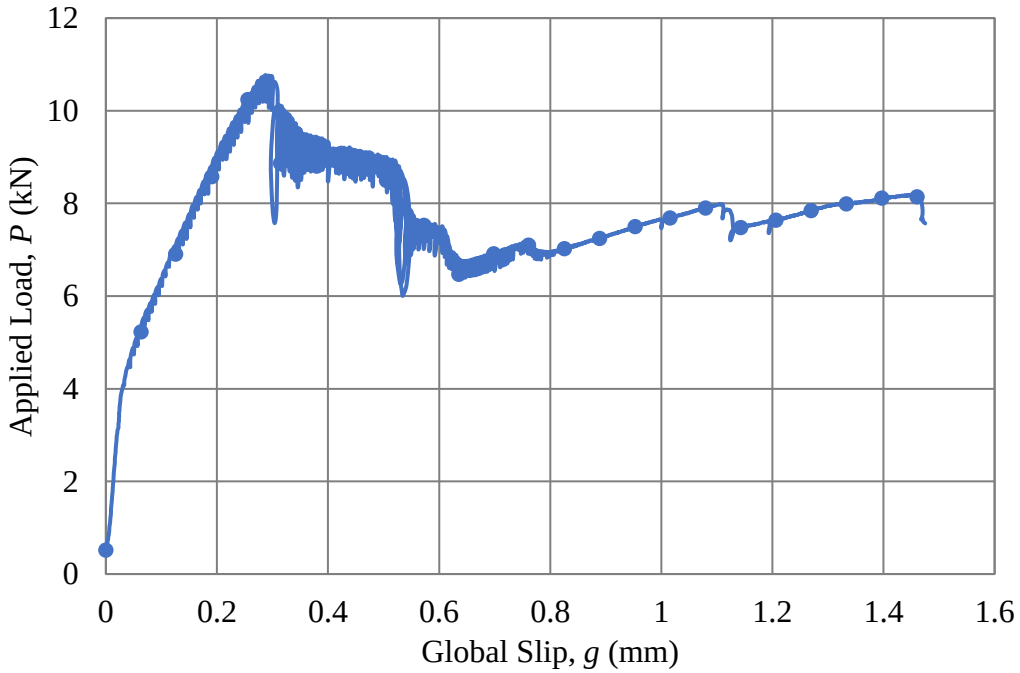

Figure A.12. Applied load-global slip response for specimen DS_330_50_E_5

www.manaraa.com

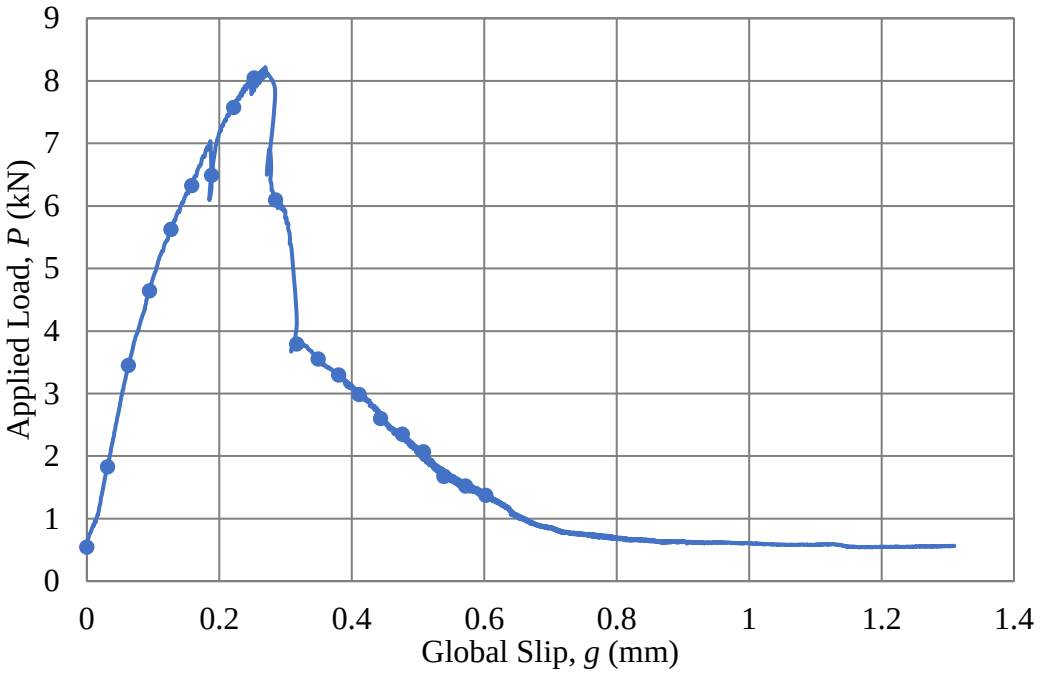

Figure A.13. Applied load-global slip response for specimen DS_100_50_E_1

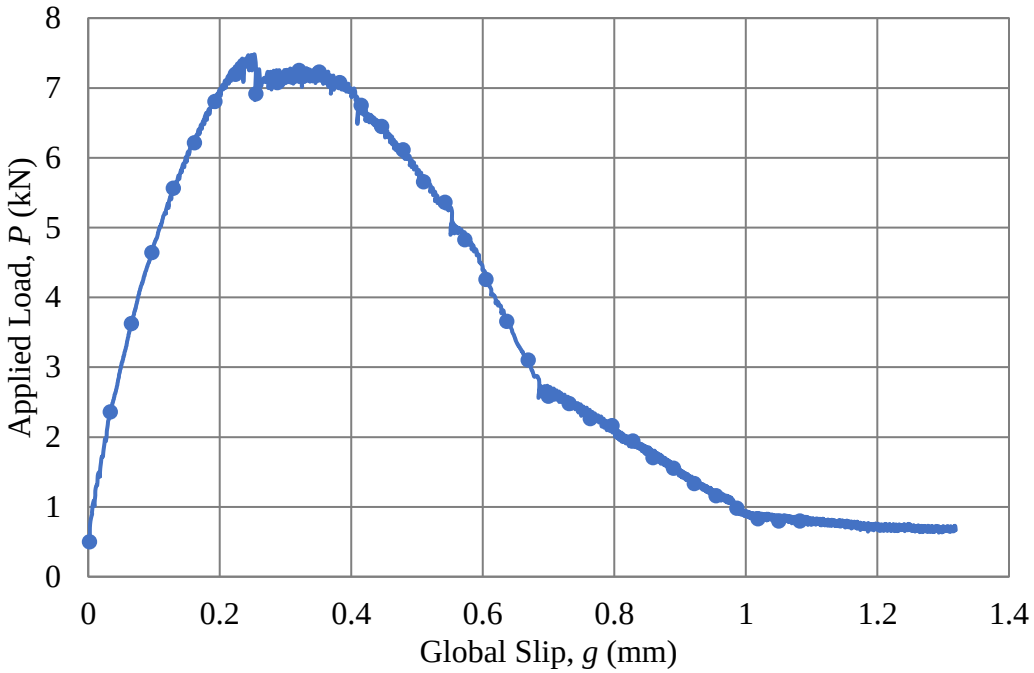

Figure A.14. Applied load-global slip response for specimen DS_100_50_E_2

www.manaraa.com

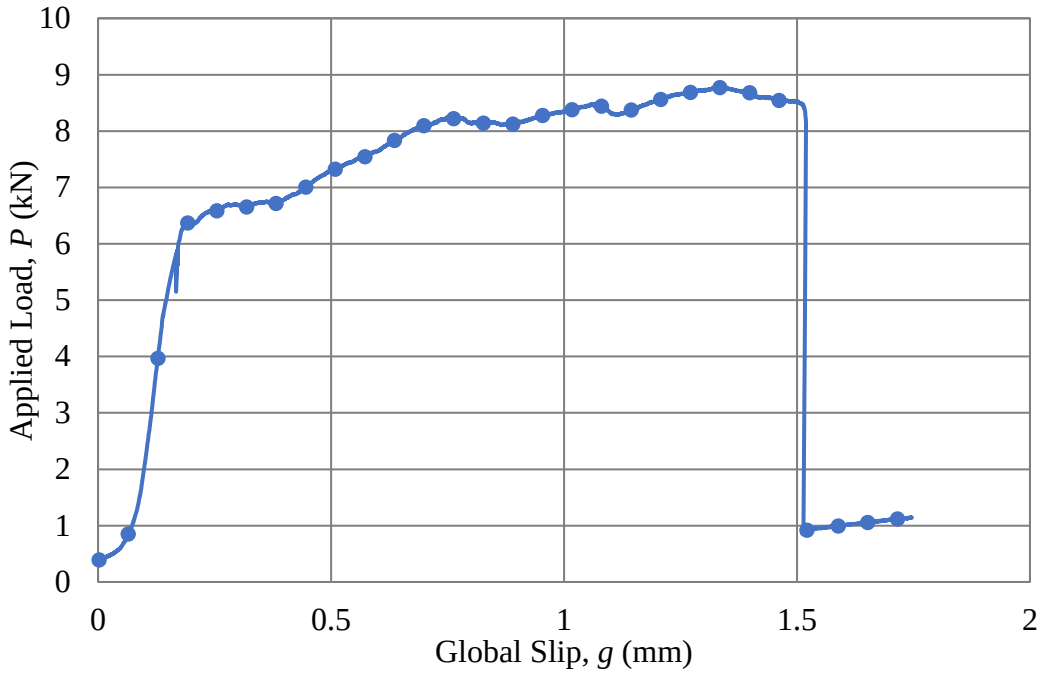

Figure A.15. Applied load-global slip response for specimen DS_330_50_M_1

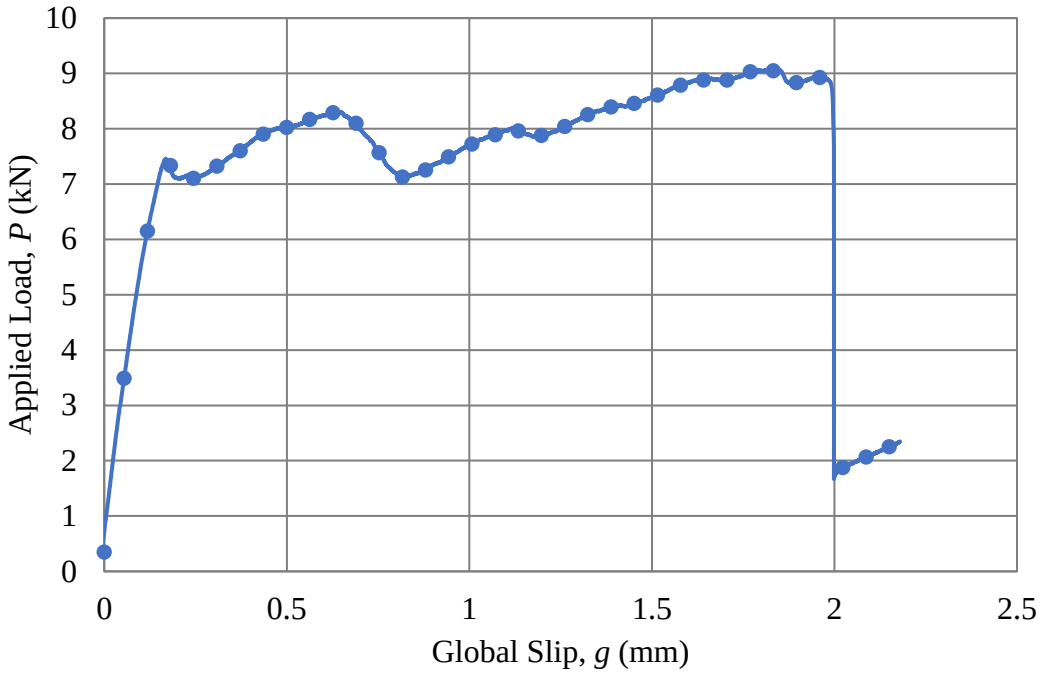

Figure A.16. Applied load-global slip response for specimen DS_330_50_M_2

www.manaraa.com

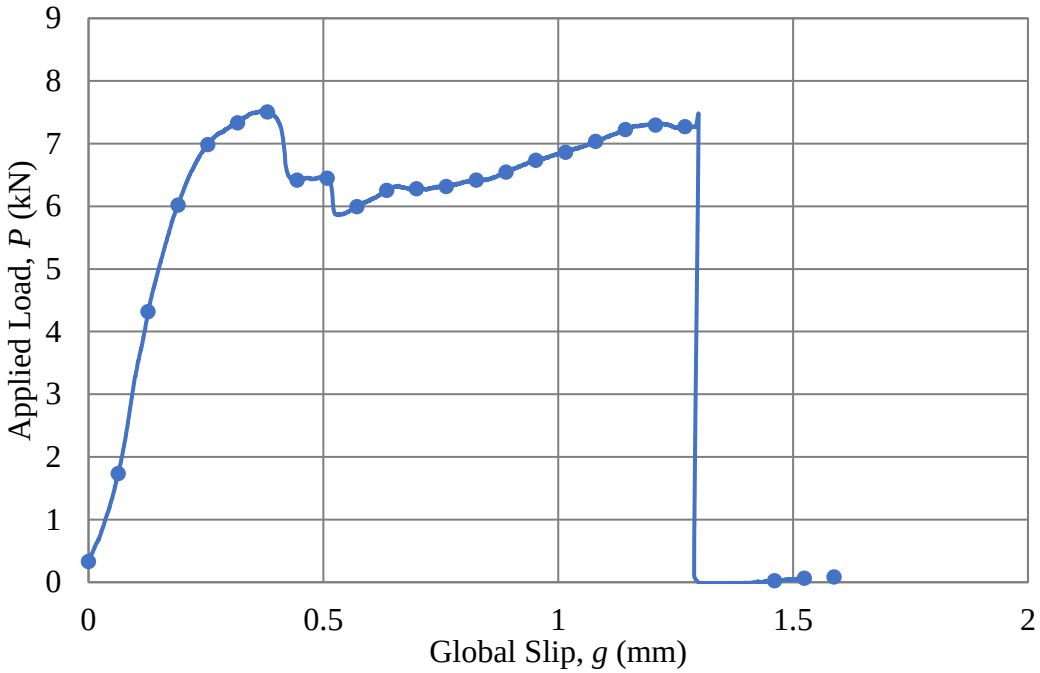

Figure A.17. Applied load-global slip response for specimen DS_330_50_M_3

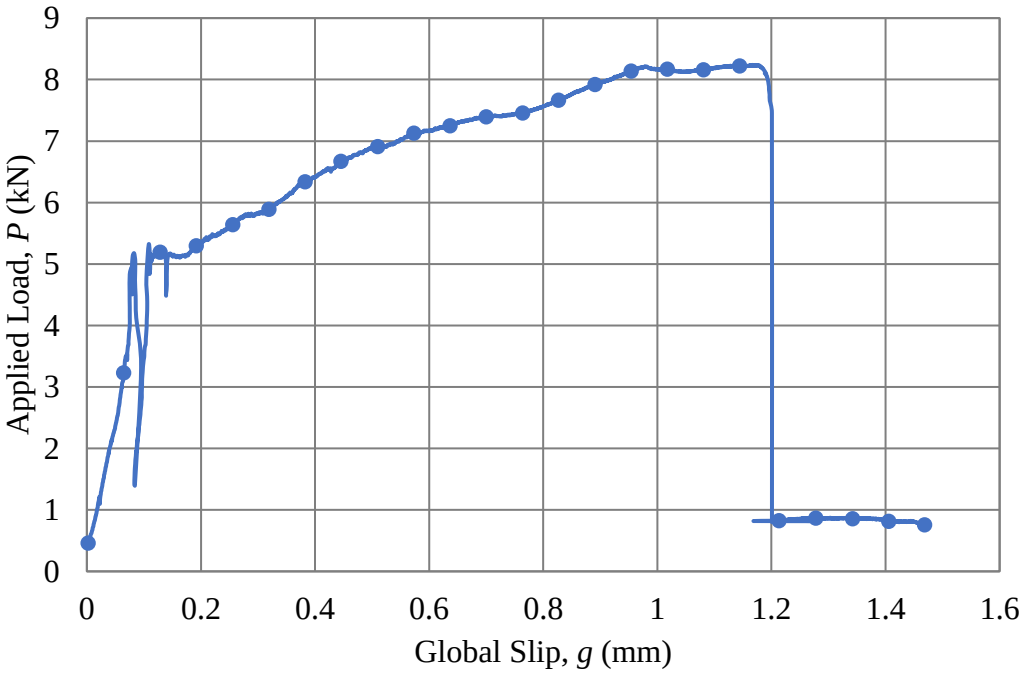

Figure A.18. Applied load-global slip response for specimen DS_330_50_M_4

www.manaraa.com

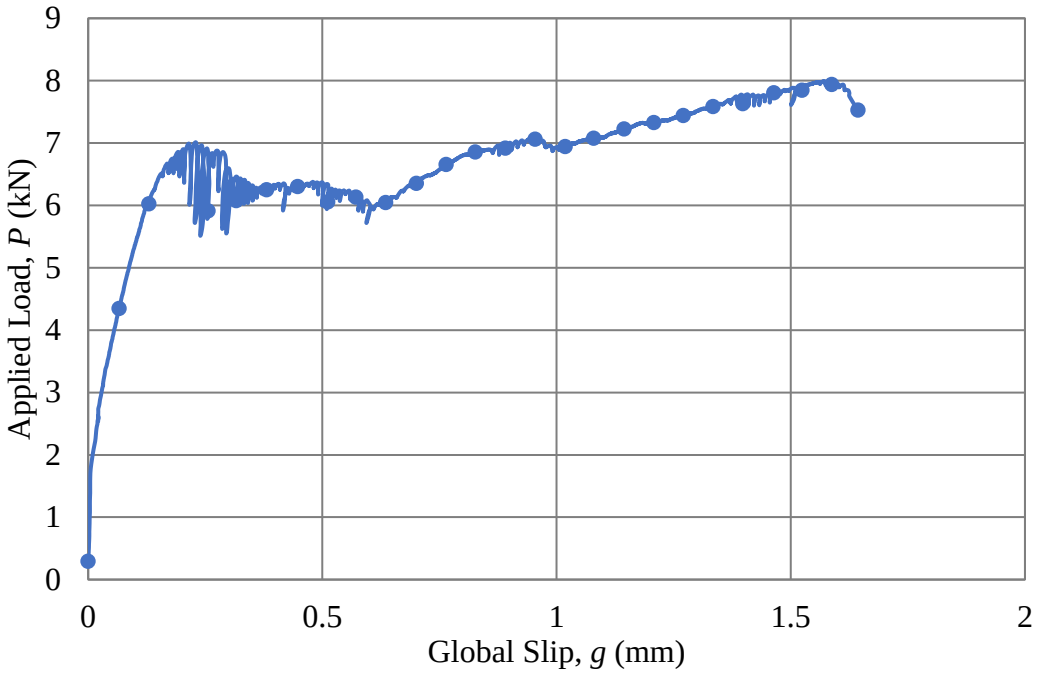

Figure A.19. Applied load-global slip response for specimen DS_330_50_M_5

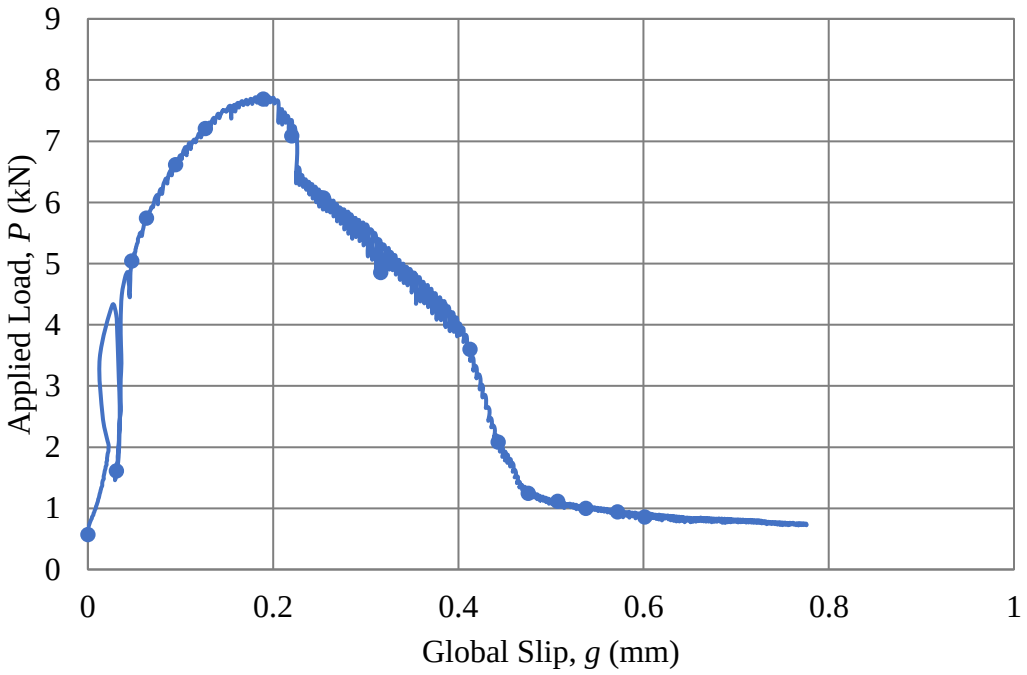

Figure A.20. Applied load-global slip response for specimen DS_100_50_M_1

www.manaraa.com

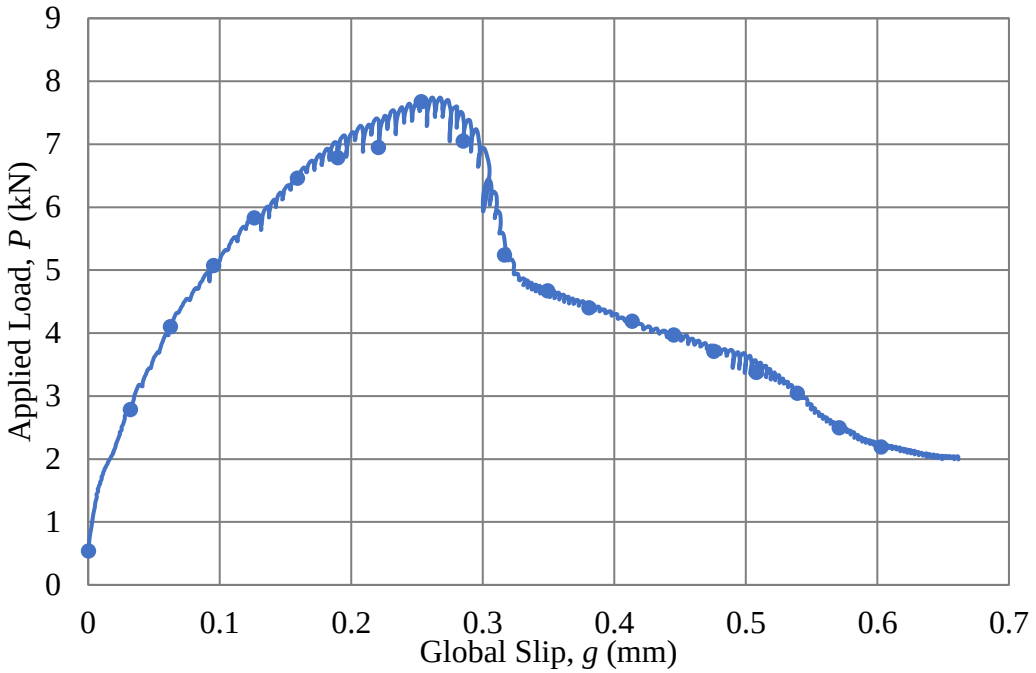

Figure A.21. Applied load-global slip response for specimen DS_100_50_M_2

www.manaraa.com

APPENDIX B.

LVDT READINGS

www.manaraa.com

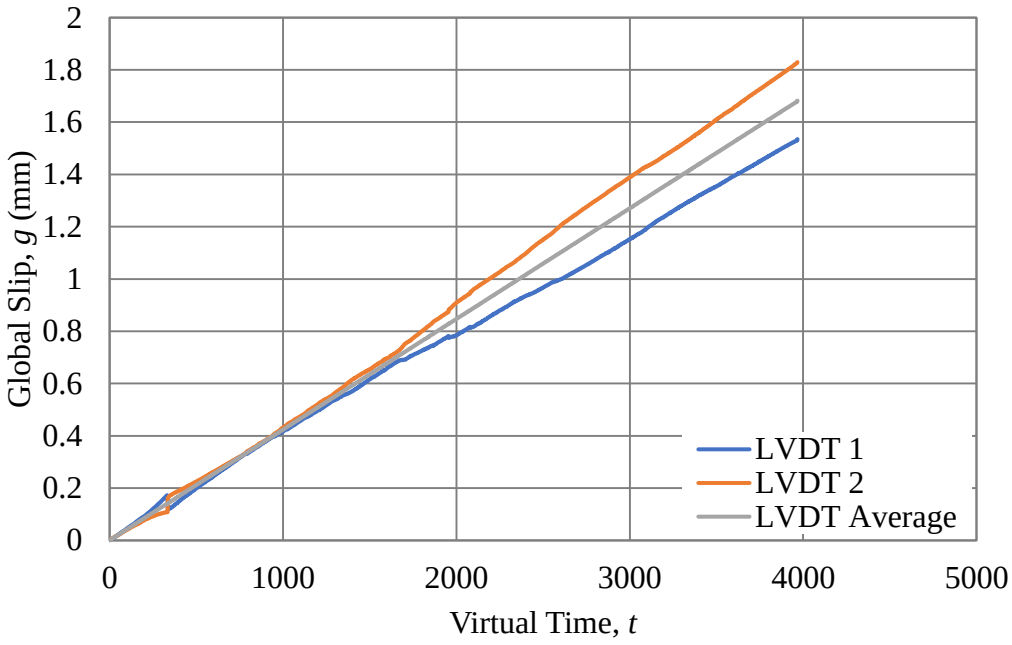

Figure B.1. LVDT response for specimen DS_330_50_C_1

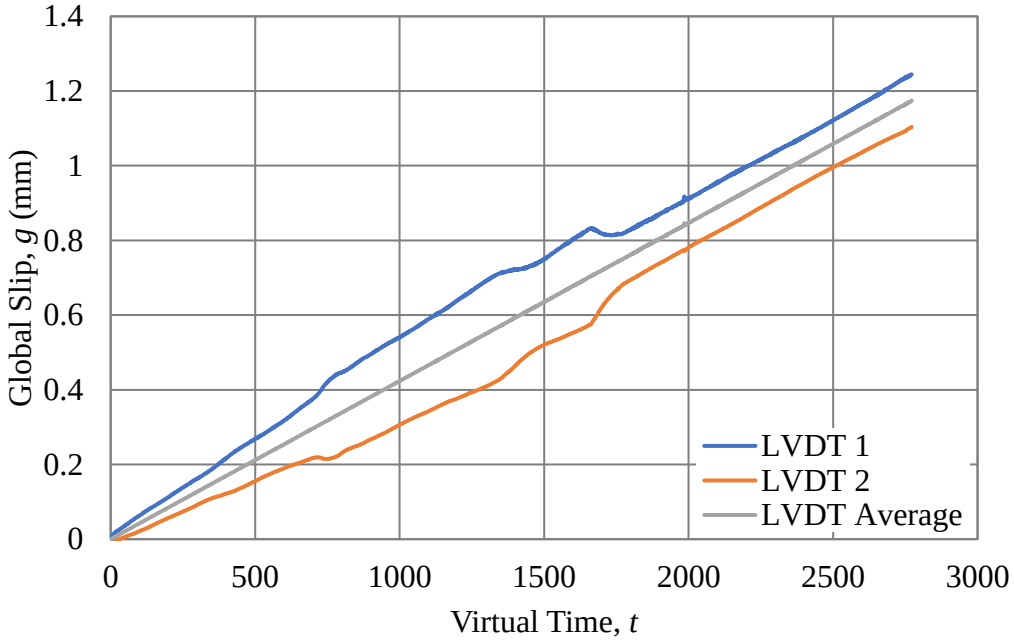

Figure B.1. LVDT response for specimen DS_330_50_C_2

www.manaraa.com

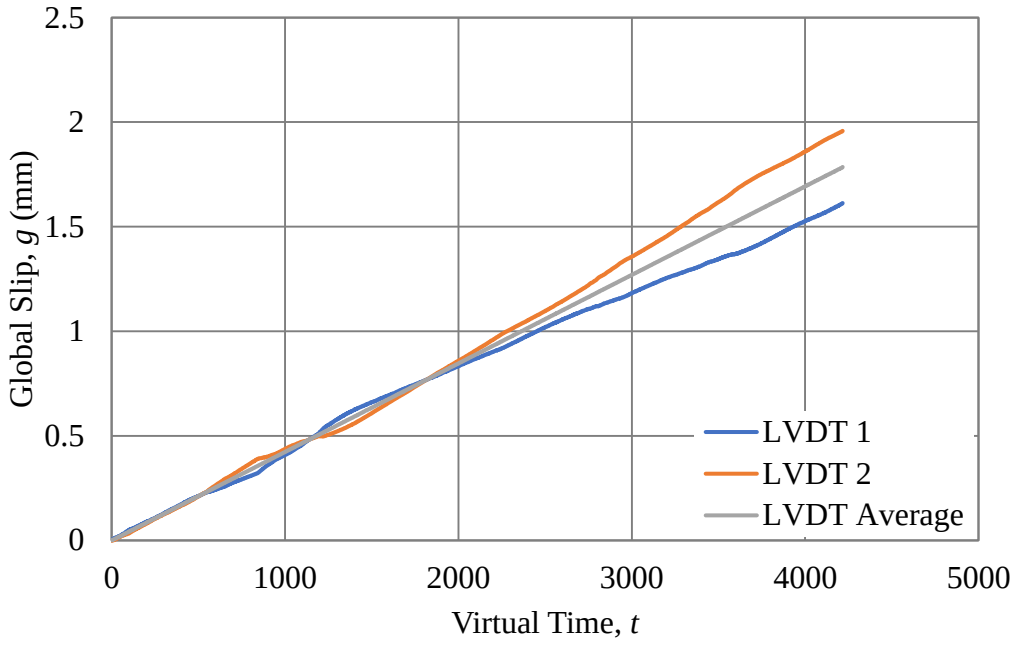

Figure B.3. LVDT response for specimen DS_330_50_C_3

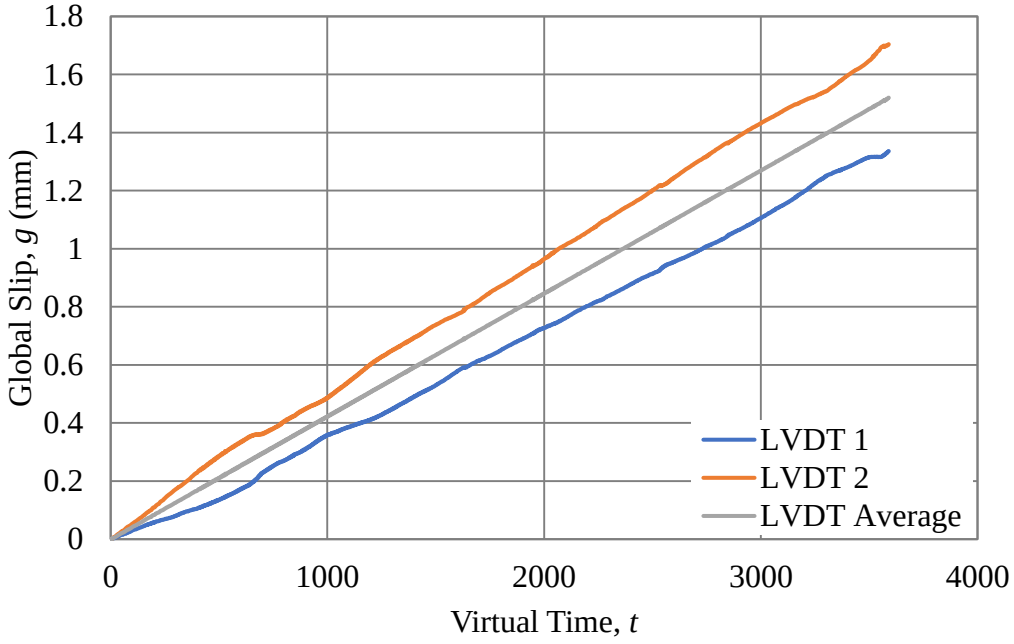

Figure B.4. LVDT response for specimen DS_330_50_C_4

www.manaraa.com

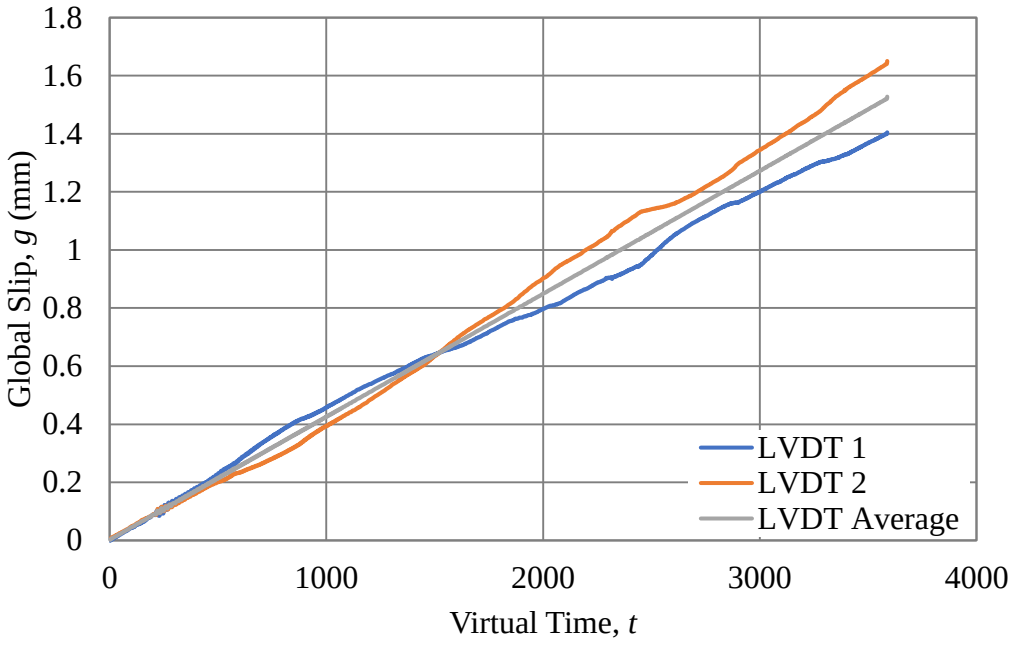

Figure B.5. LVDT response for specimen DS_330_50_C_5

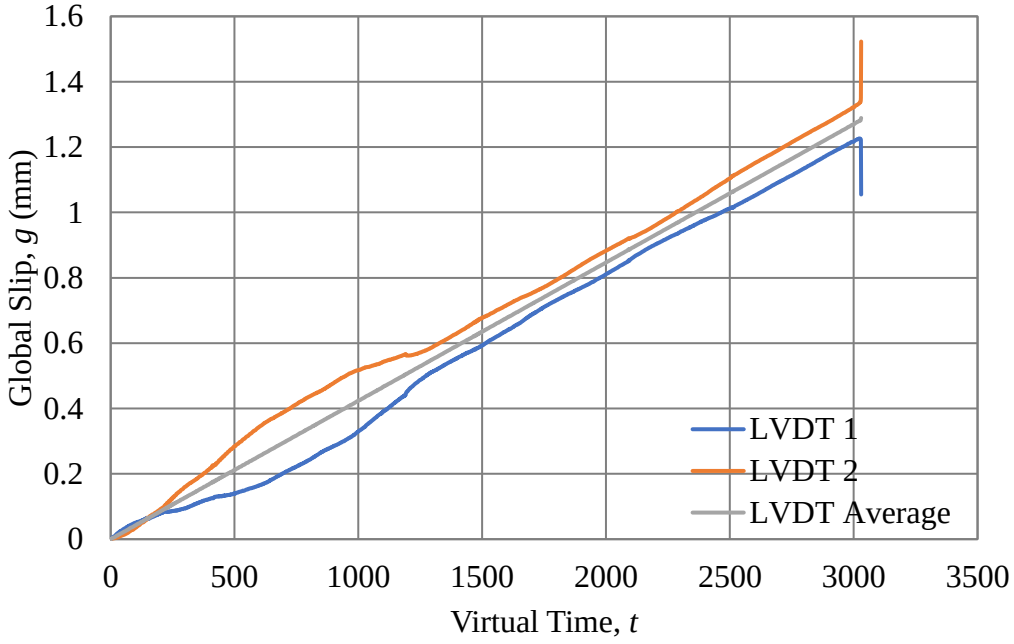

Figure B.6. LVDT Response for specimen DS_330_50_C_6S

www.manaraa.com

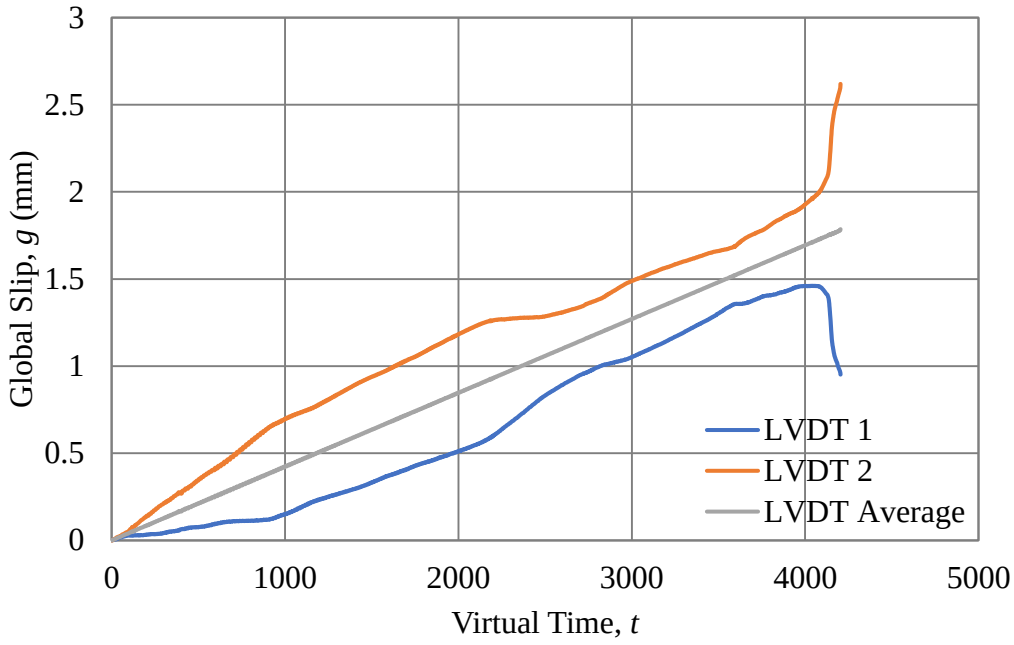

Figure B.7. LVDT response for specimen DS_330_50_C_7S

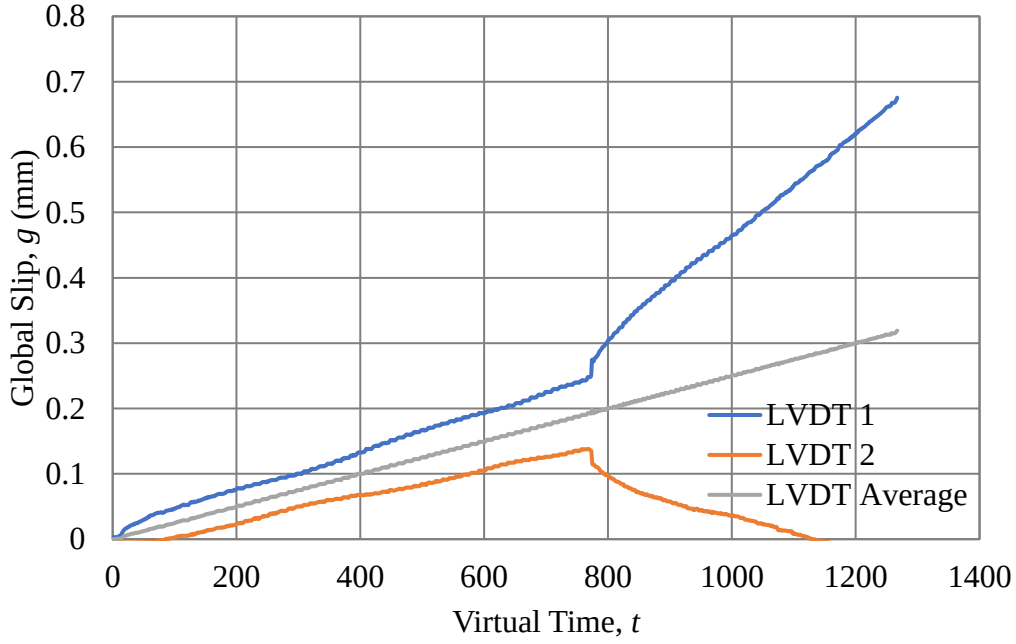

Figure B.8. LVDT response for specimen DS_100_50_C_1

www.manaraa.com

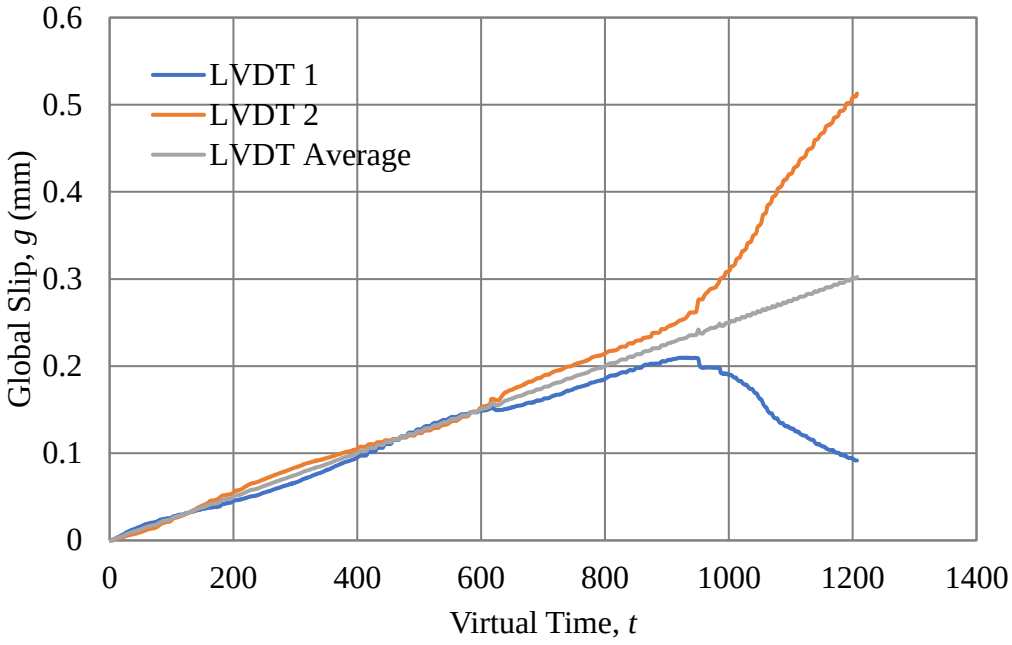

Figure B.9. LVDT response for specimen DS_100_50_C_2

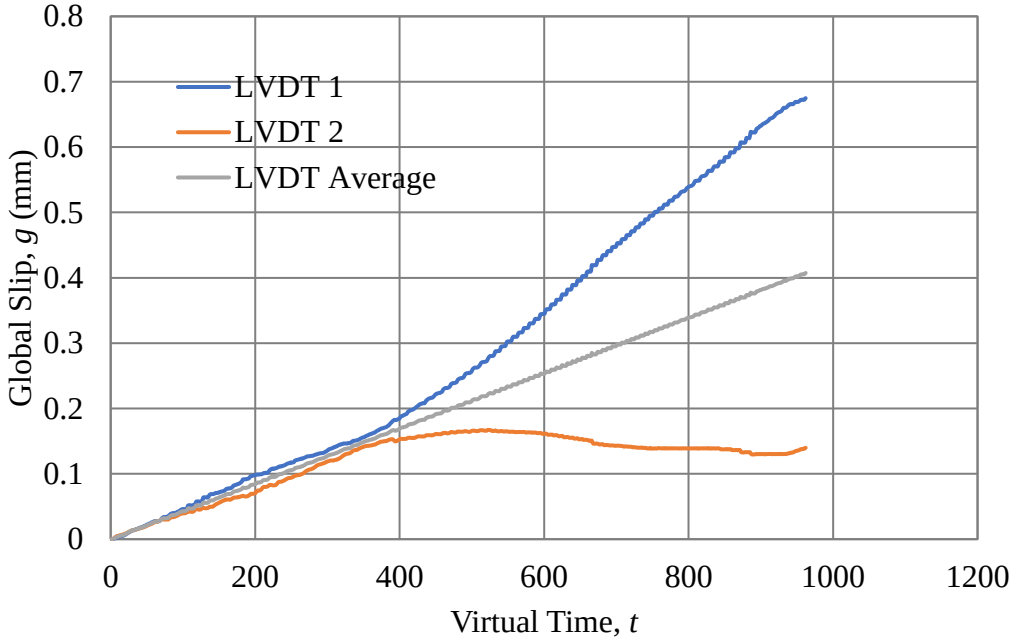

Figure B.10. LVDT response for specimen DS_100_50_C_3S

www.manaraa.com

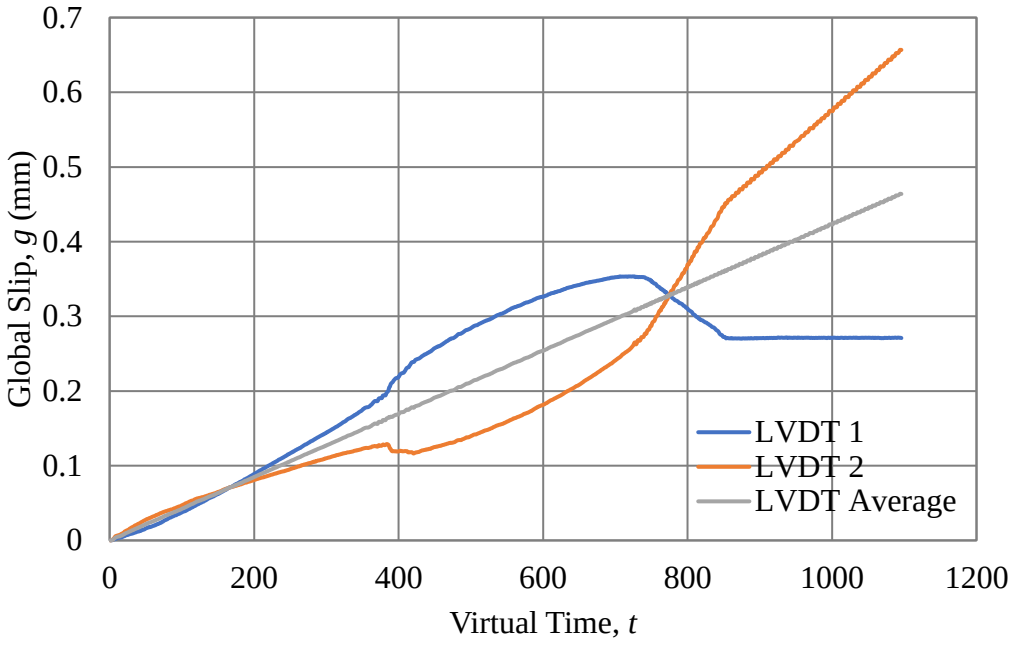

Figure B.11. LVDT response for specimen DS_100_50_C_4S

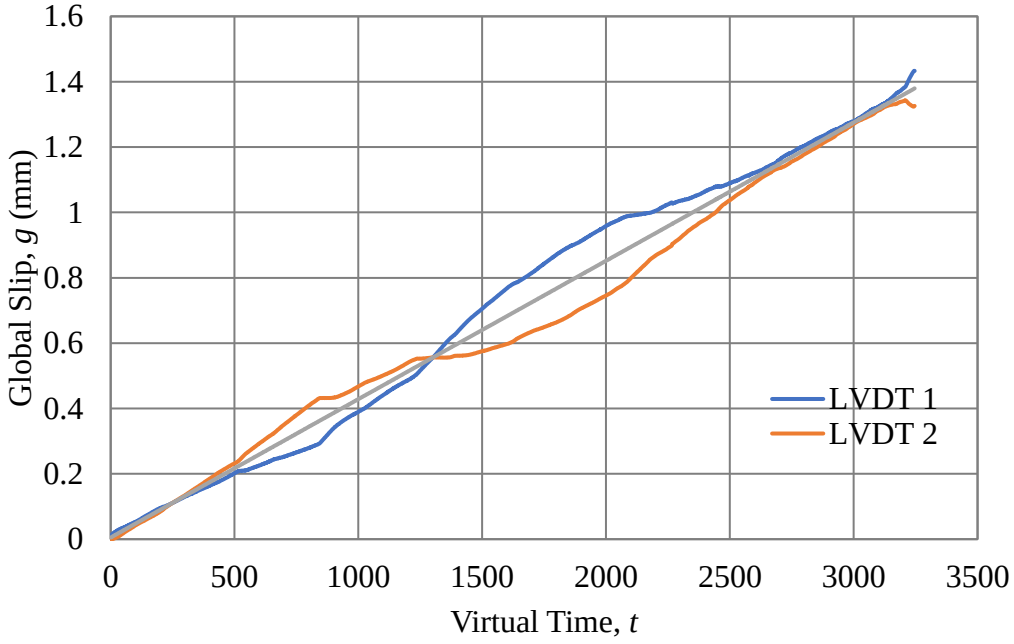

Figure B.12. LVDT response for specimen DS_330_50_E_1

www.manaraa.com

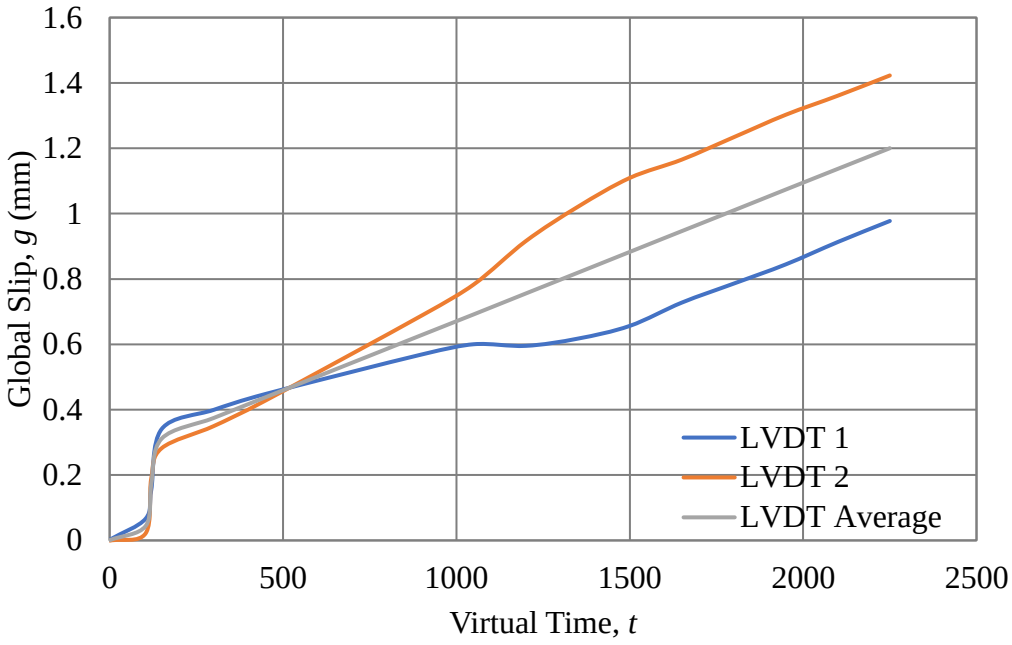

Figure B.13. LVDT Response for specimen DS_330_50_E_2

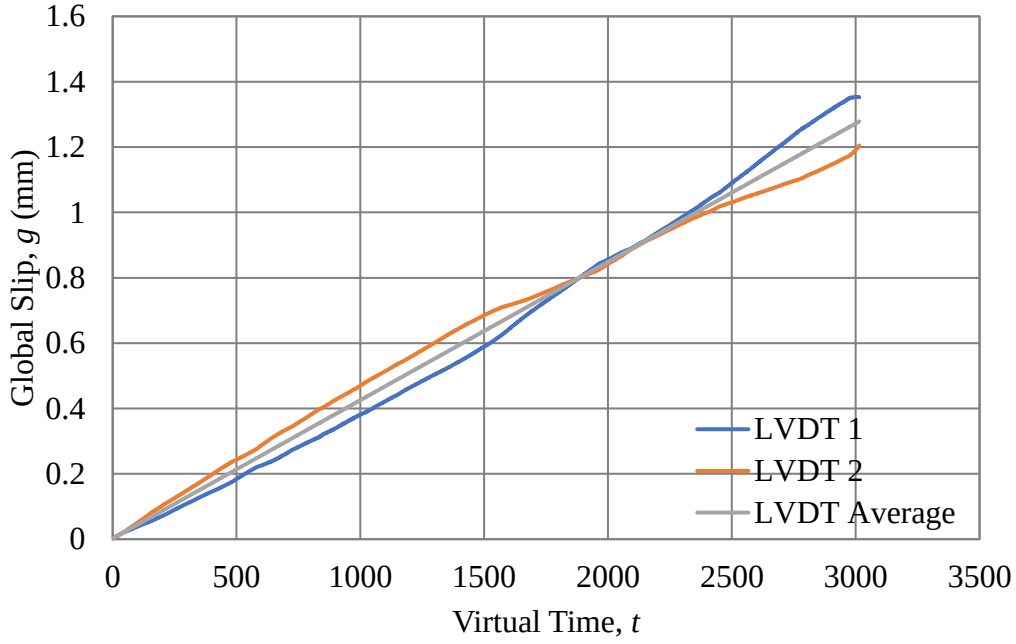

Figure B.14. LVDT Response for specimen DS_330_50_E_3

www.manaraa.com

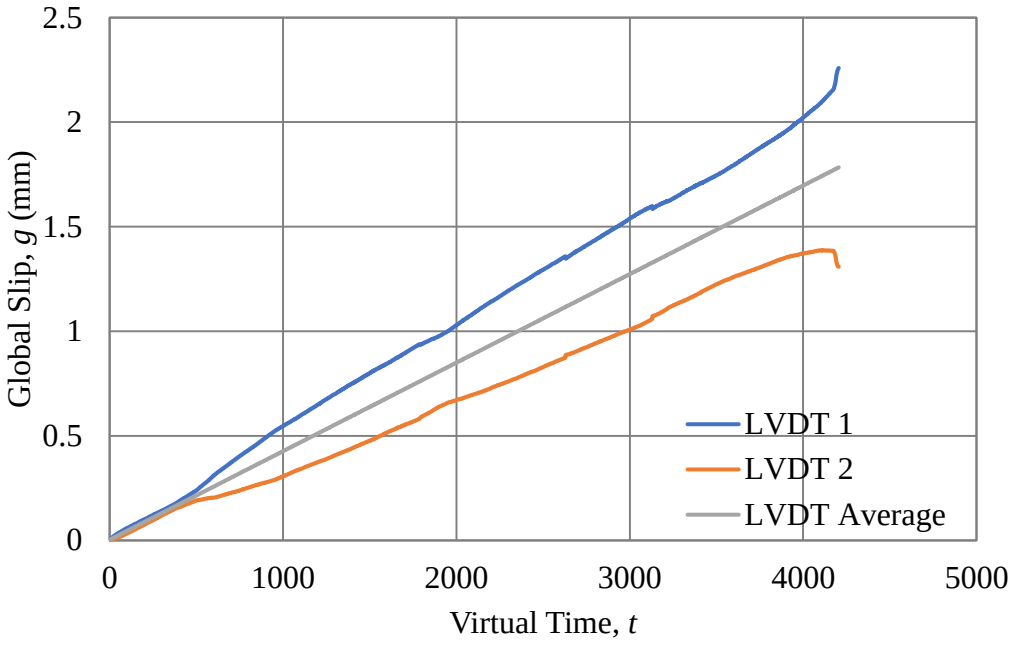

Figure B.15. LVDT response for specimen DS_330_50_E_4

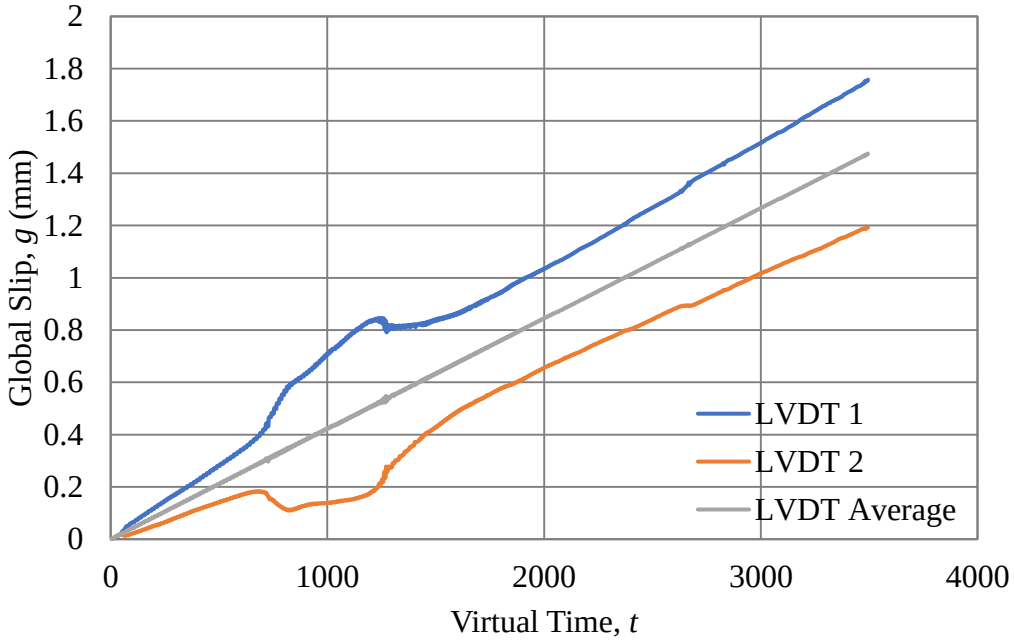

Figure B.16. LVDT response for specimen DS_330_50_E_5

www.manaraa.com

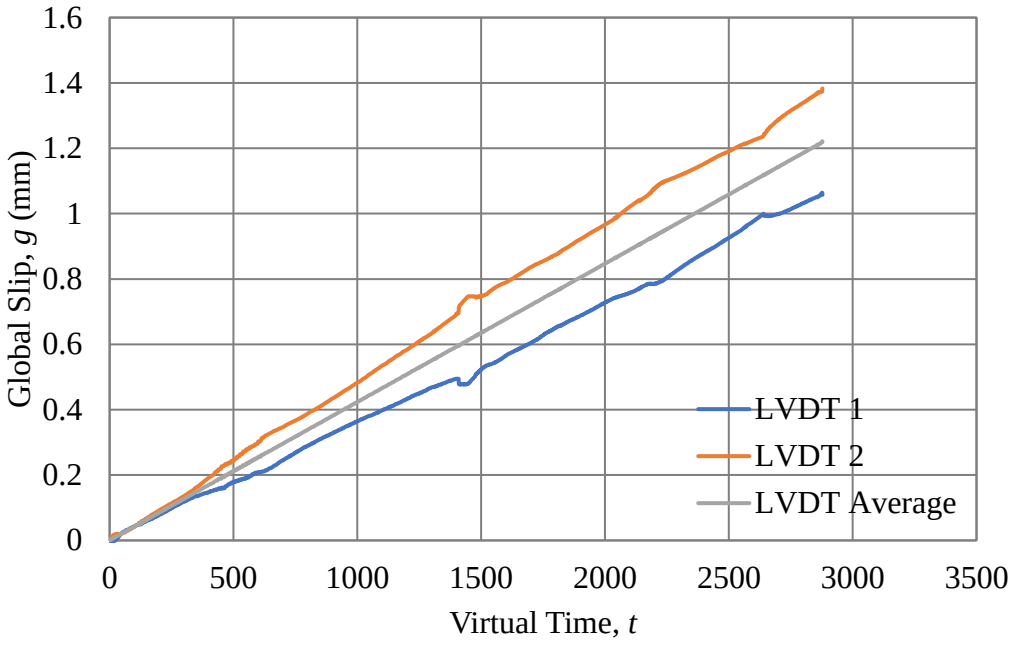

Figure B.17. LVDT response for specimen DS_330_50_E_6S

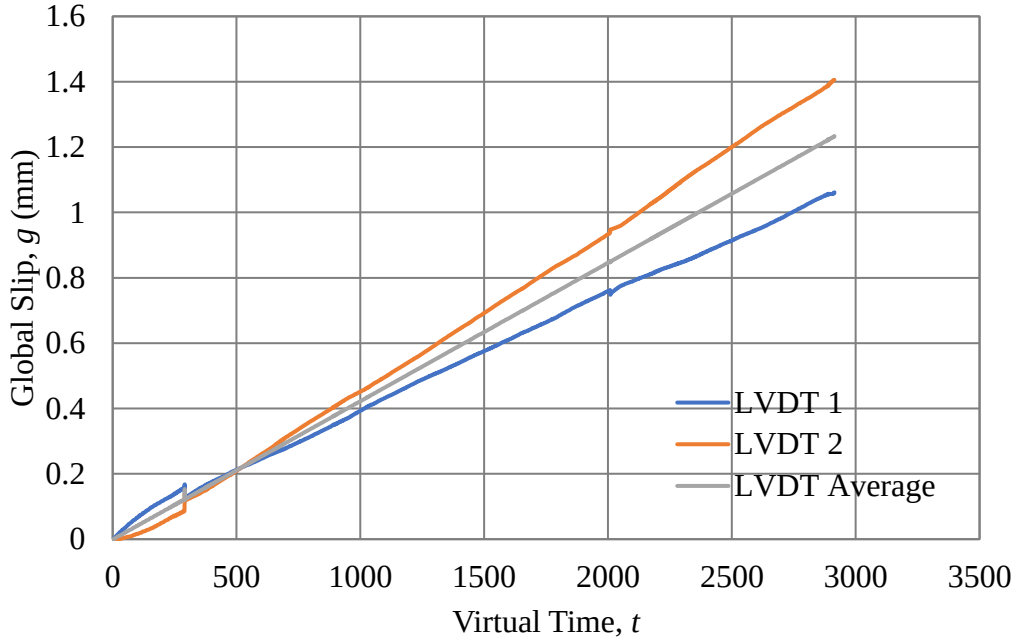

Figure B.18. LVDT response for specimen DS_330_50_E_7S

www.manaraa.com

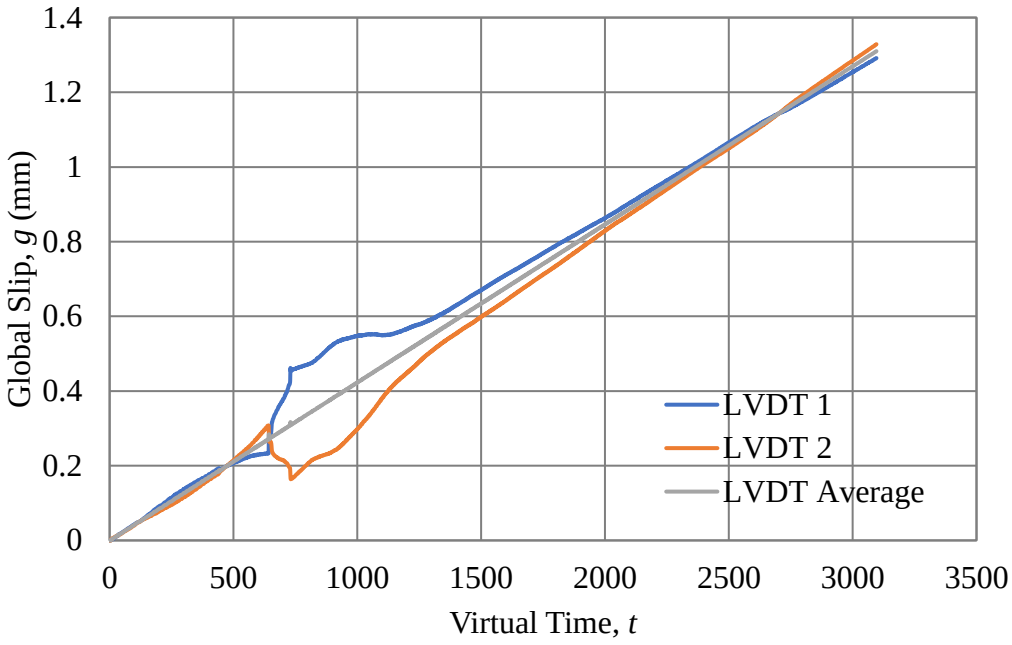

Figure B.19. LVDT response for specimen DS_100_50_E_1

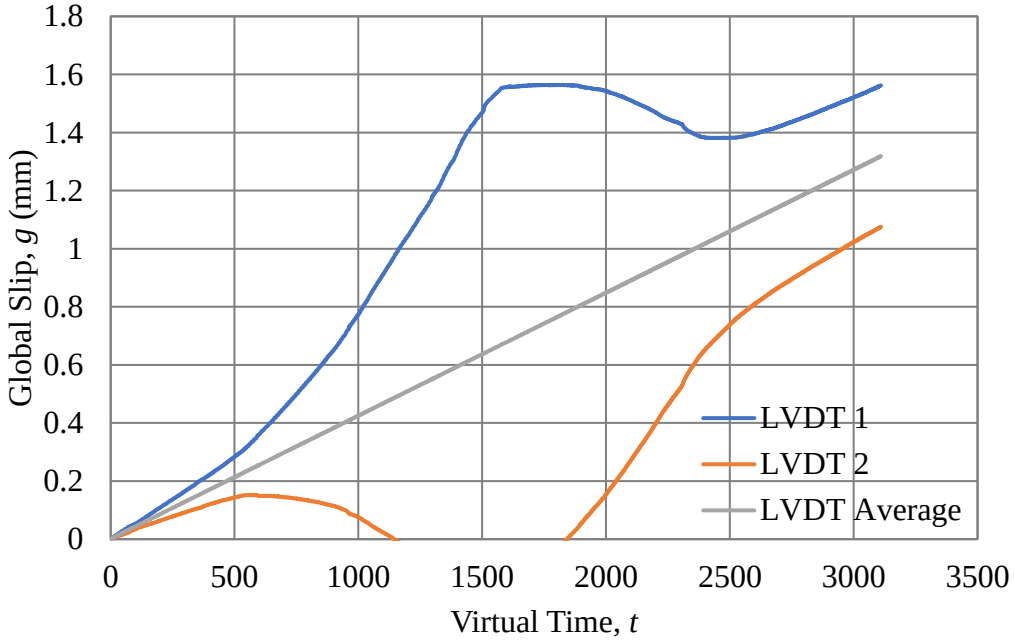

Figure B.20. LVDT response for specimen DS_100_50_E_2

www.manaraa.com

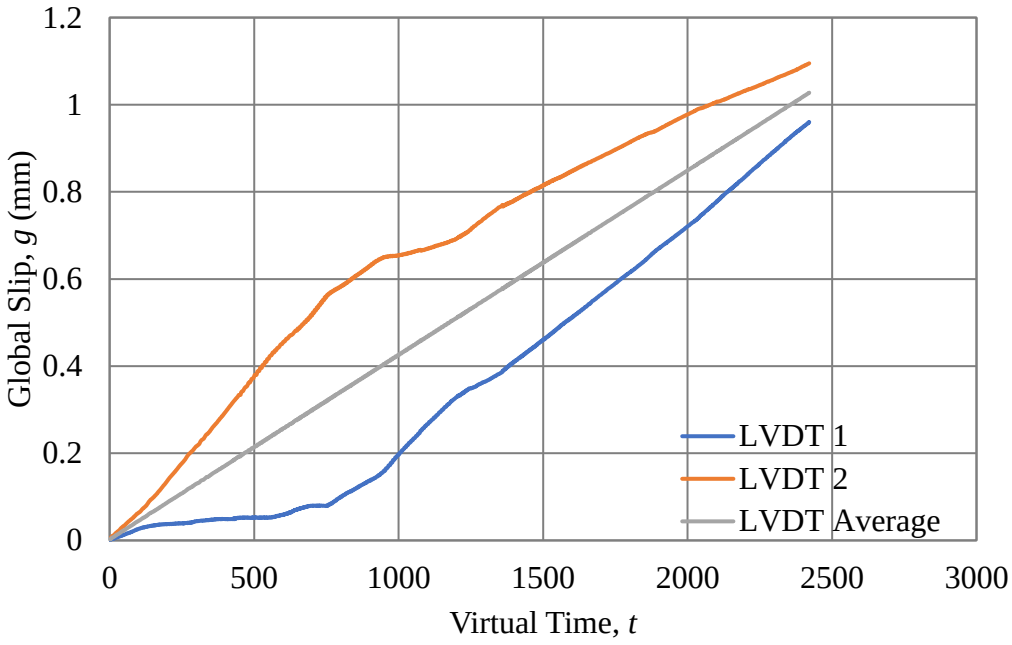

Figure B.21. LVDT response for specimen DS_100_50_E_3S

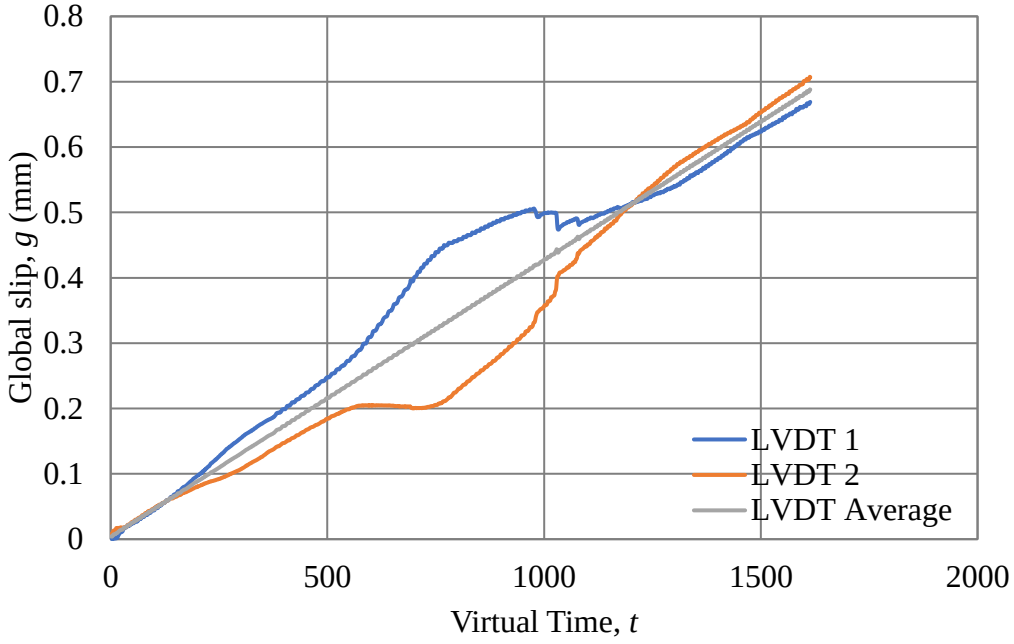

Figure B.22. LVDT response for specimen DS_100_50_E_4S

www.manaraa.com

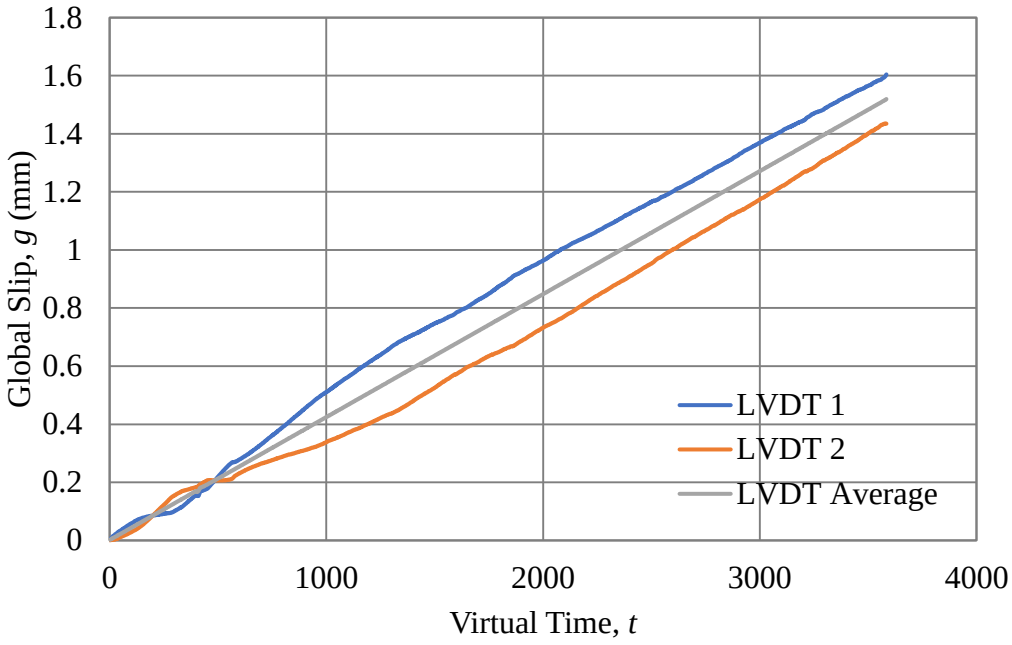

Figure B.23. LVDT response for specimen DS_330_50_M_1

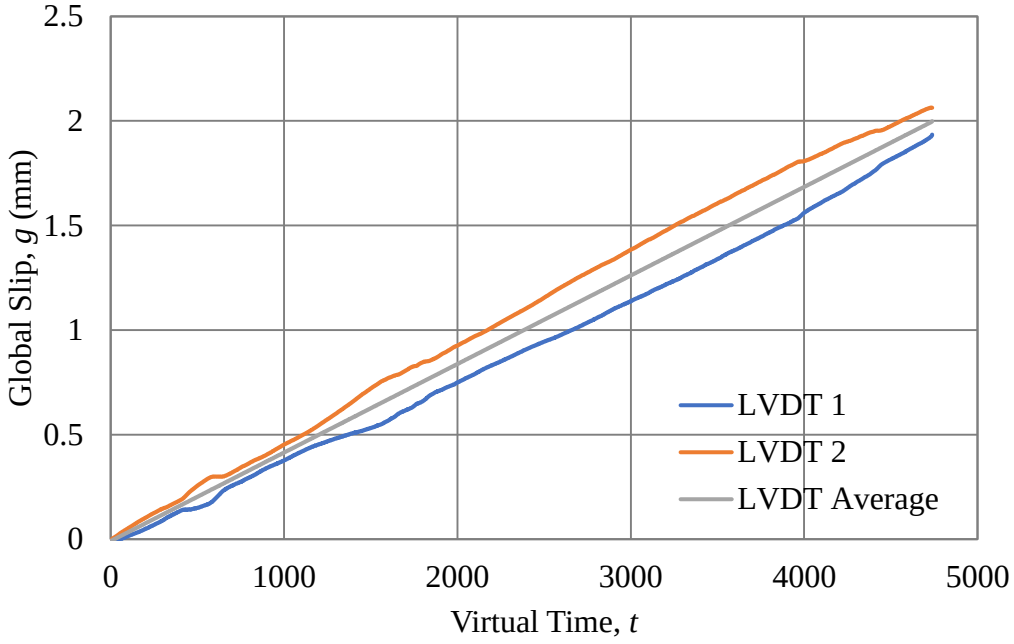

Figure B.24. LVDT response for specimen DS_330_50_M_2

www.manaraa.com

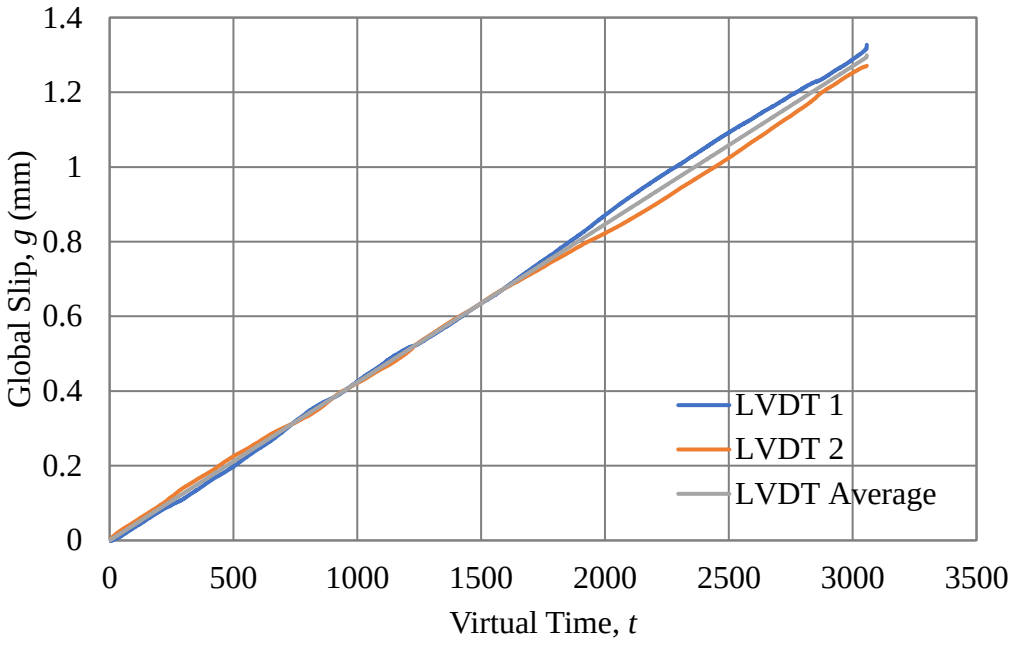

Figure B.25. LVDT response for specimen DS_330_50_M_3

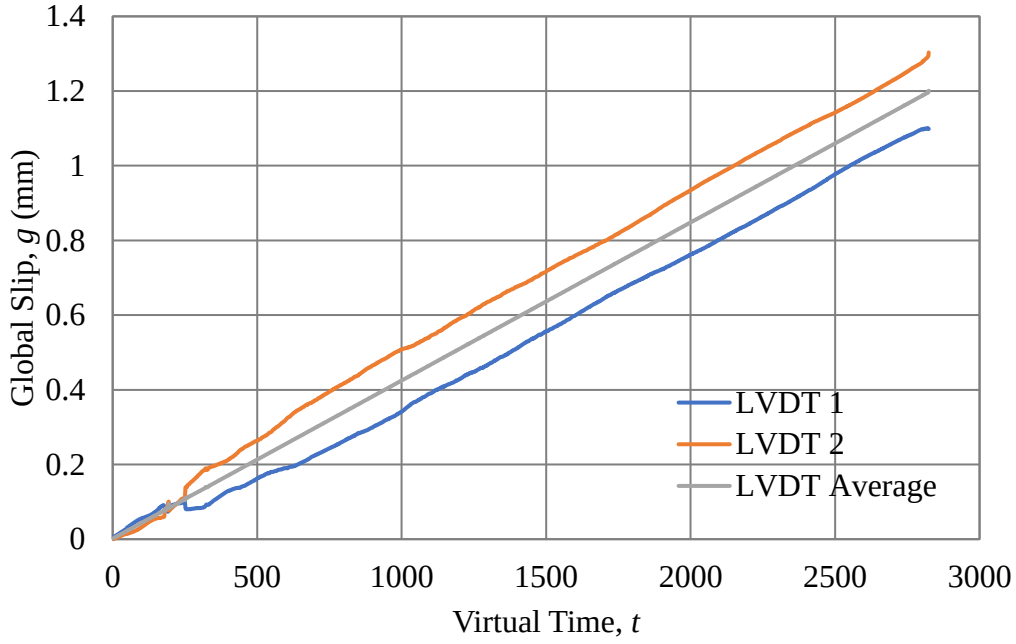

Figure B.26. LVDT response for specimen DS_330_50_M_4

www.manaraa.com

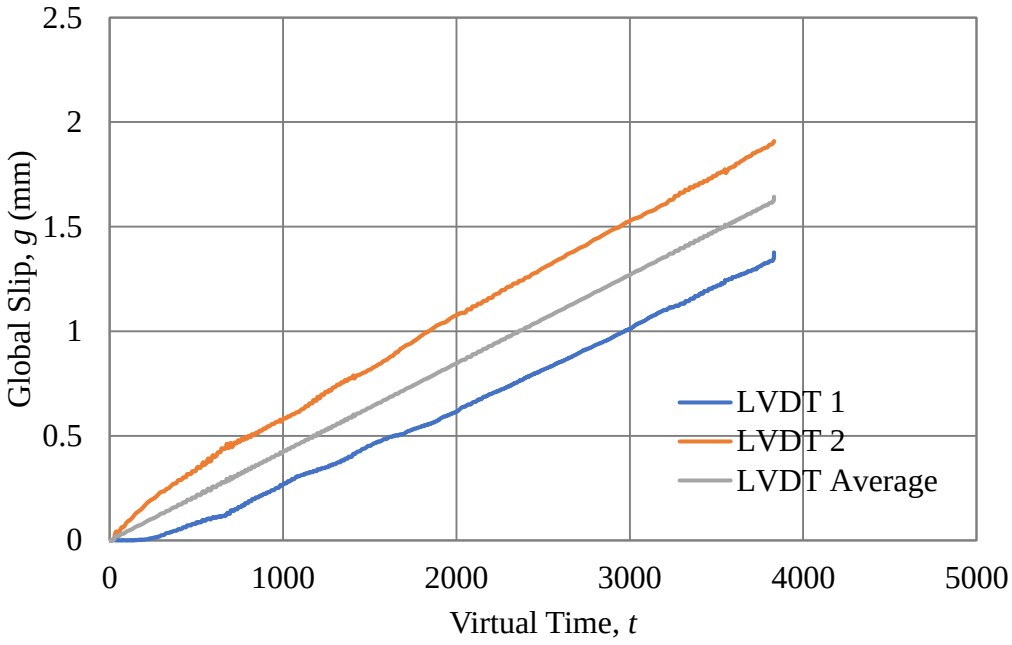

Figure B.27. LVDT response for specimen DS_330_50_M_5

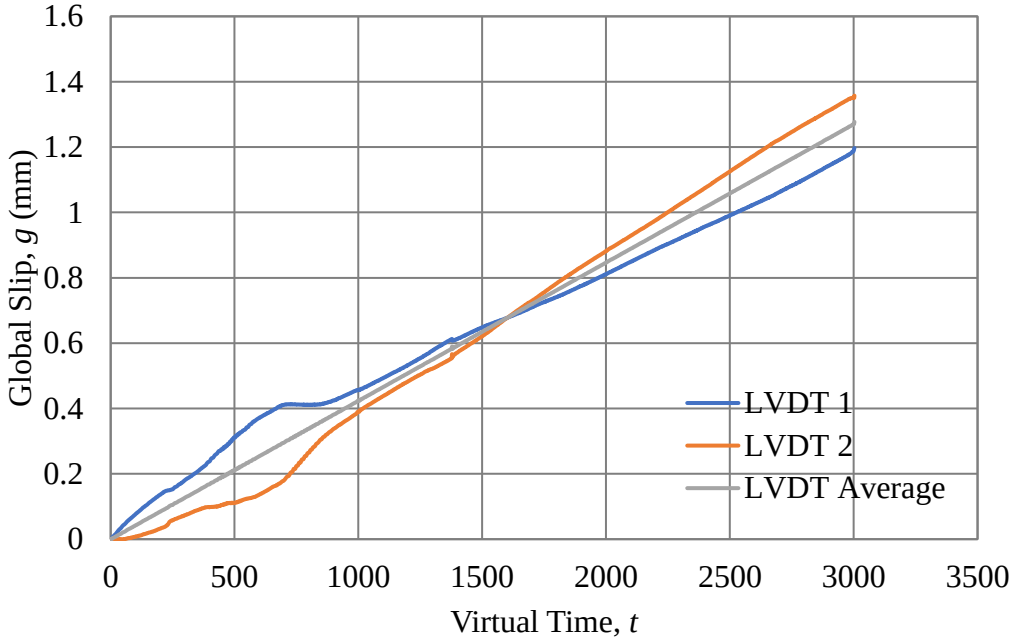

Figure B.28. LVDT response for specimen DS_330_50_C_6S

www.manaraa.com

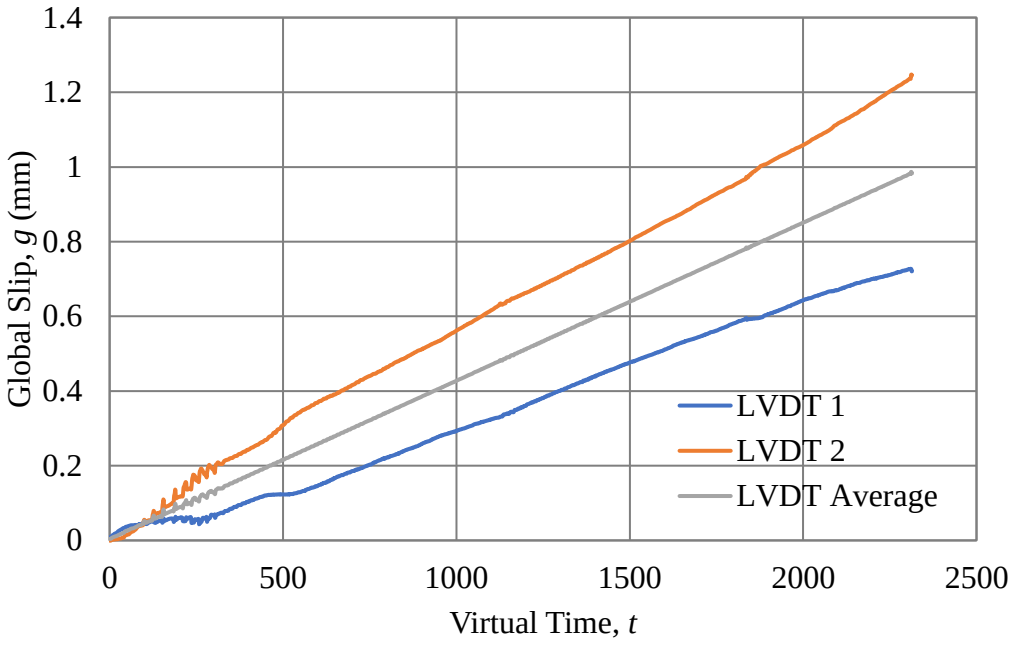

Figure B.29. LVDT response for specimen DS_330_50_M_7S

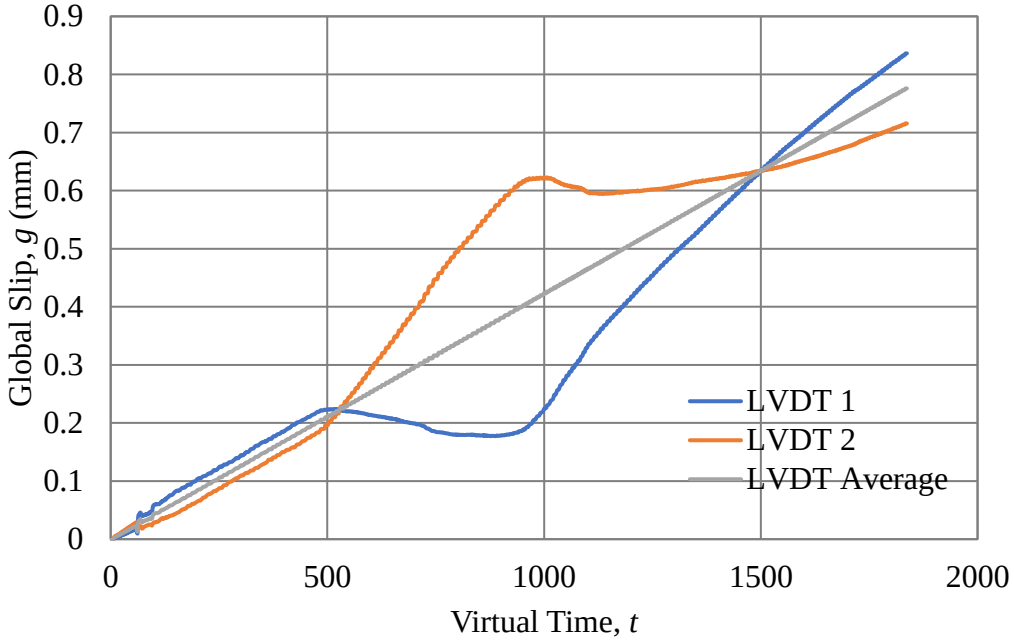

Figure B.30. LVDT response for specimen DS_100_50_M_1

www.manaraa.com

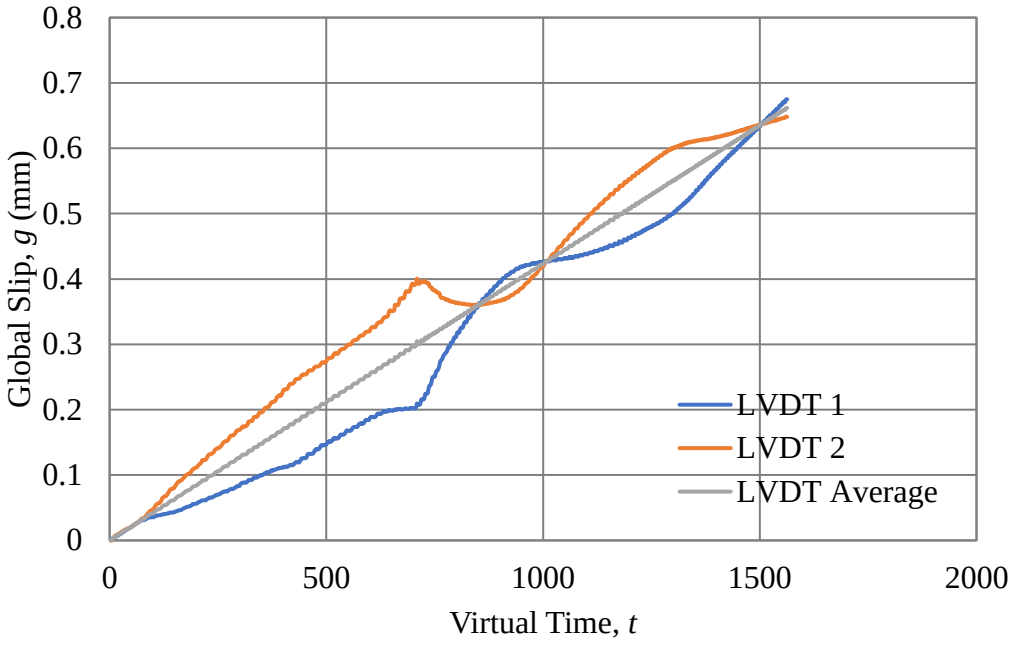

Figure B.31. LVDT response for specimen DS_100_50_M_2

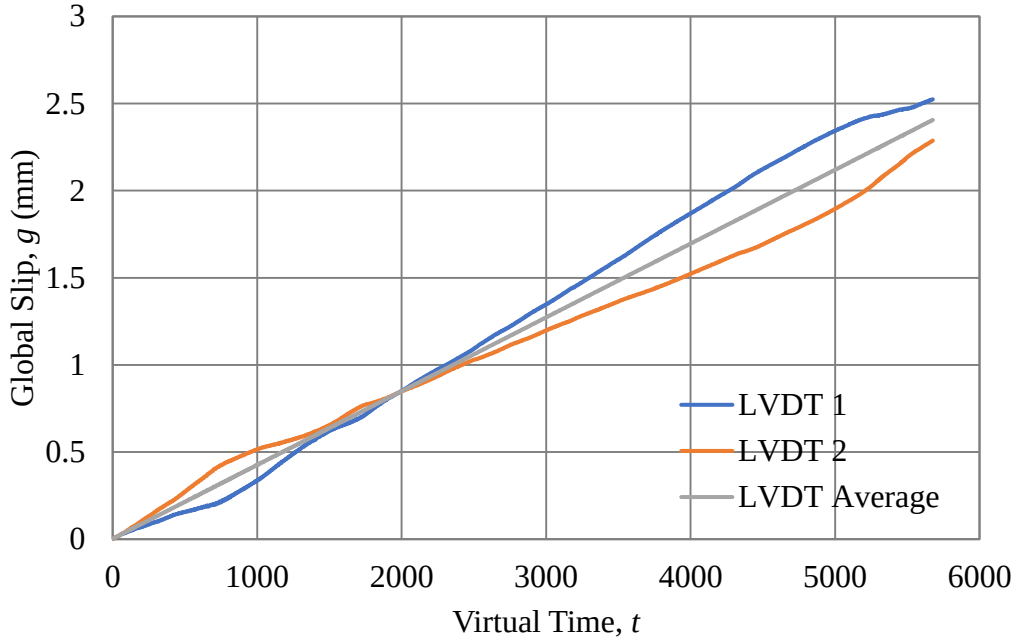

Figure B.32. LVDT response for specimen DS_100_50_M_3S

www.manaraa.com

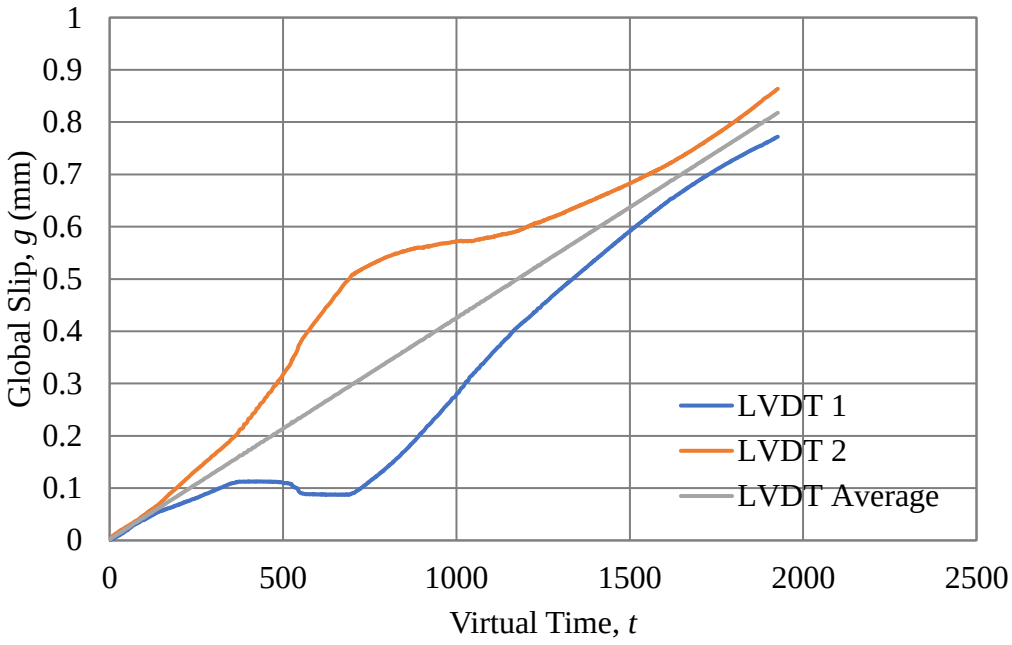

Figure B.33. LVDT response for specimen DS_100_50_M_4S

www.manaraa.com

APPENDIX C.

INDIVIDUAL CURVE FITTING PLOTS

www.manaraa.com

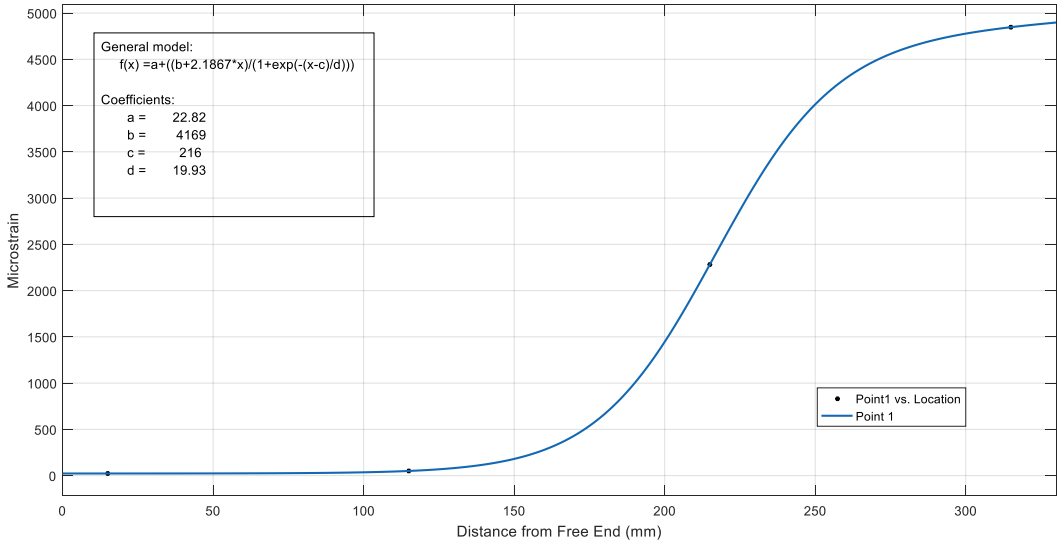

Figure C.1. Curve fitting for Point 1 of specimen DS_330_50_C_6S

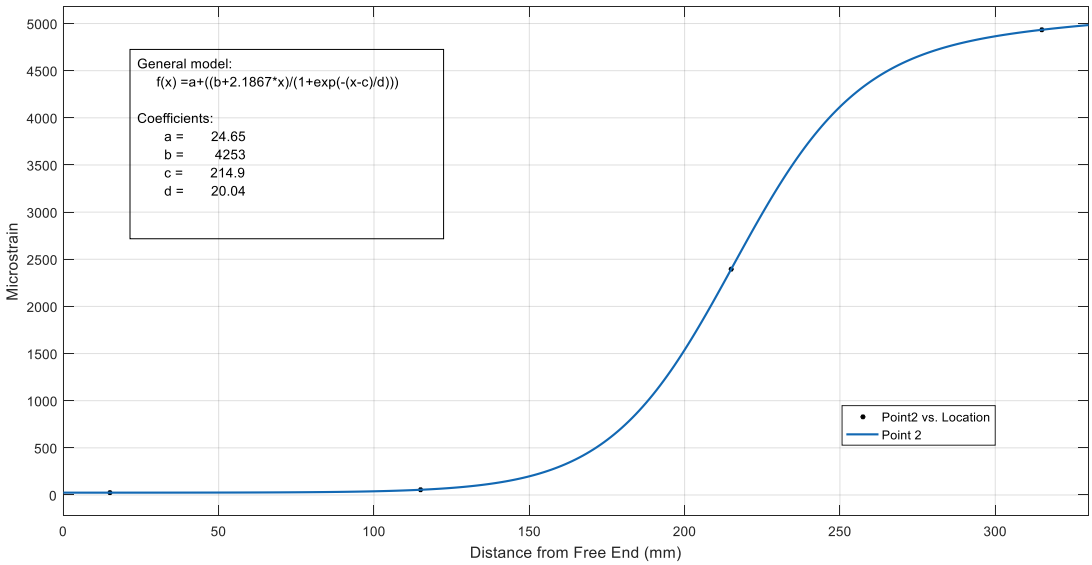

Figure C.2. Curve fitting for Point 2 of specimen DS_330_50_C_6S

www.manaraa.com

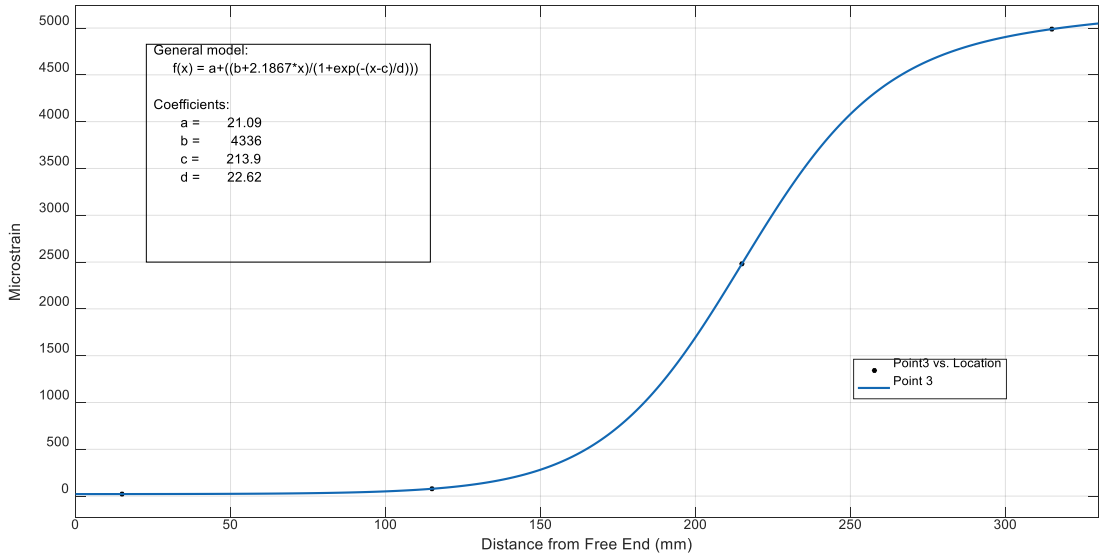

Figure C.3. Curve fitting for Point 3 of specimen DS_330_50_C_6S

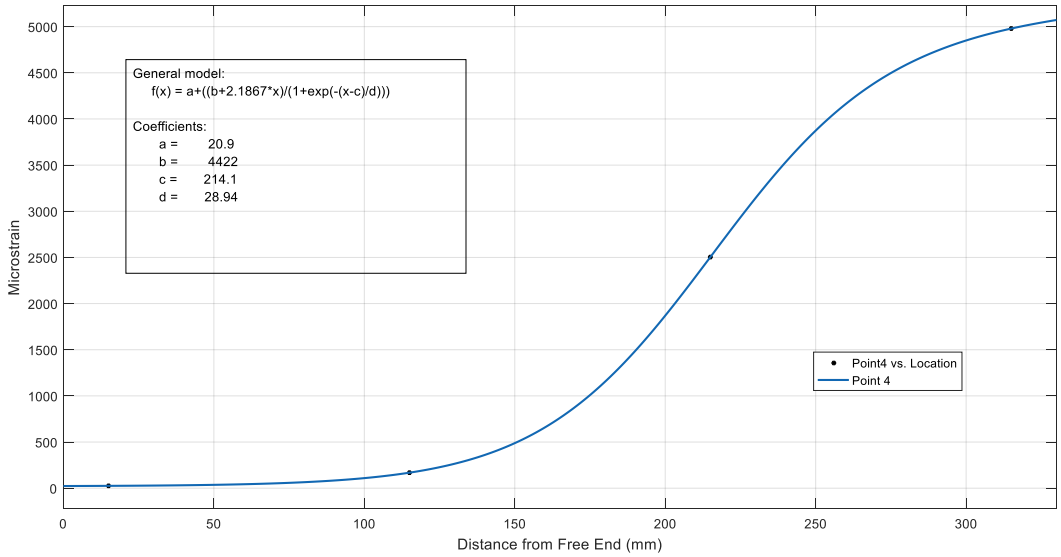

Figure C.4. Curve fitting for Point 4 of specimen DS_330_50_C_6S

www.manaraa.com

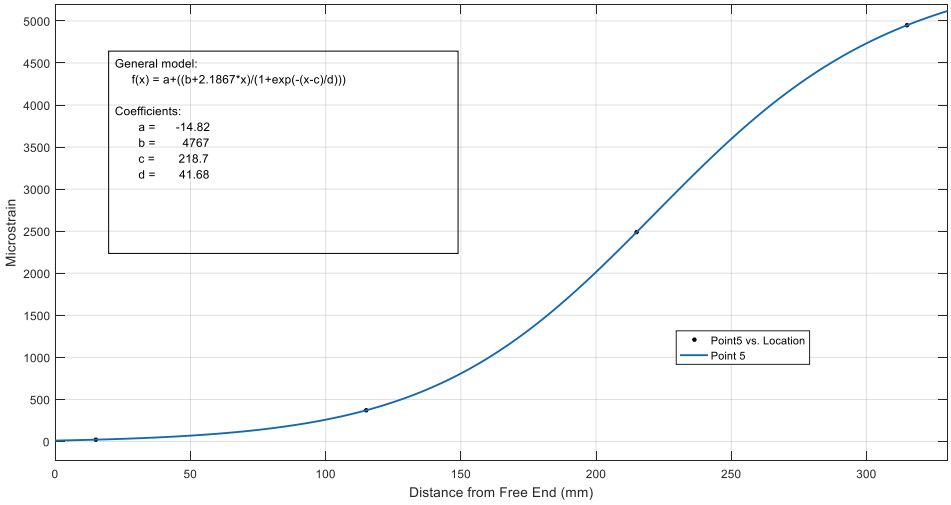

Figure C.5. Curve fitting at Point 5 of specimen DS_330_50_C_6S

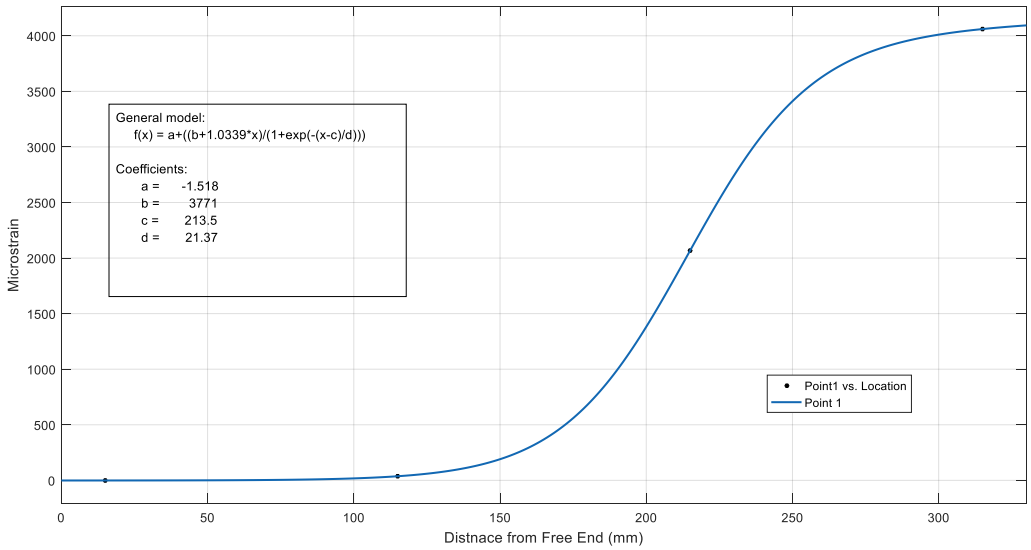

Figure C.6. Curve fitting at Point 1 of specimen DS_330_50_C_7S

www.manaraa.com

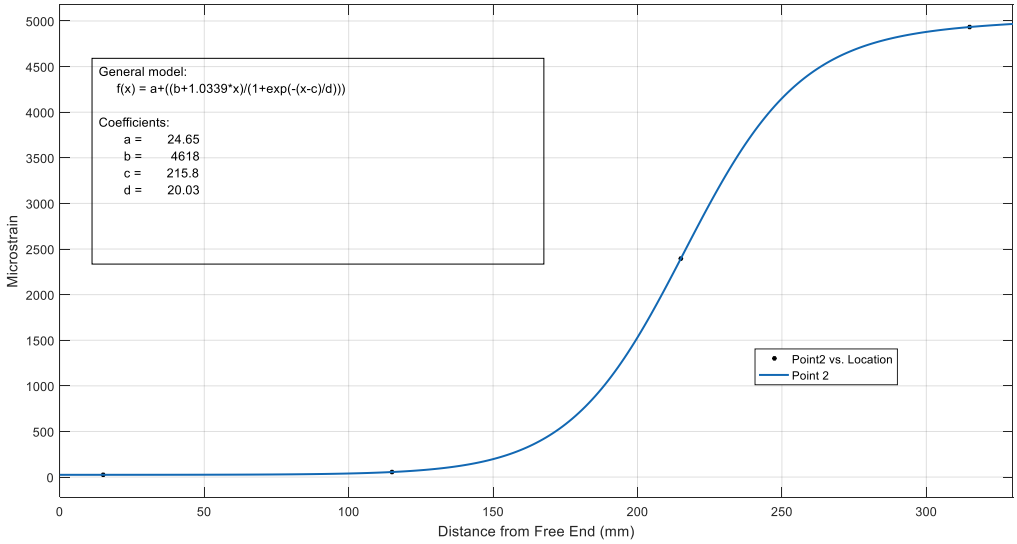

Figure C.7. Curve fitting at Point 2 of specimen DS_330_50_C_7S

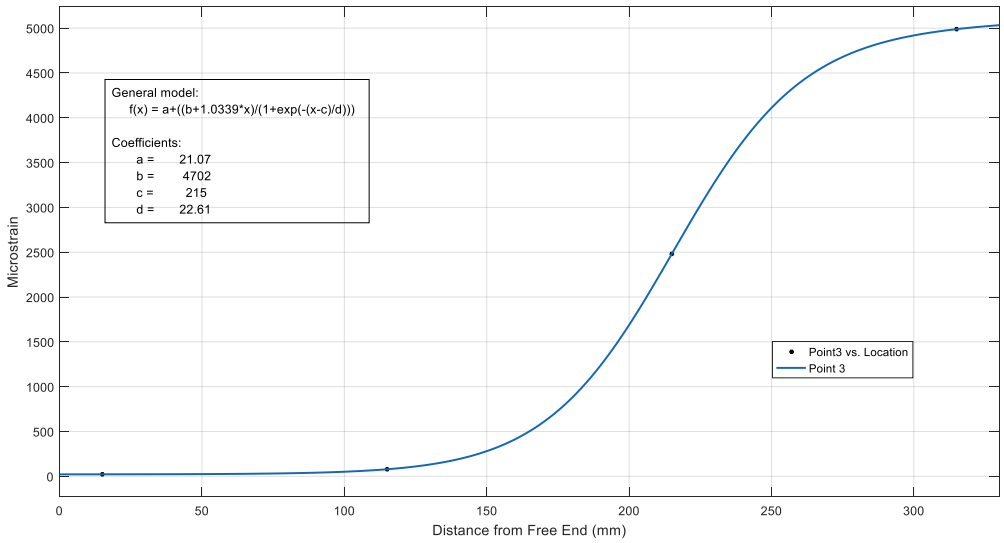

Figure C.8. Curve fitting at Point 3 of specimen DS_330_50_C_7S

www.manaraa.com

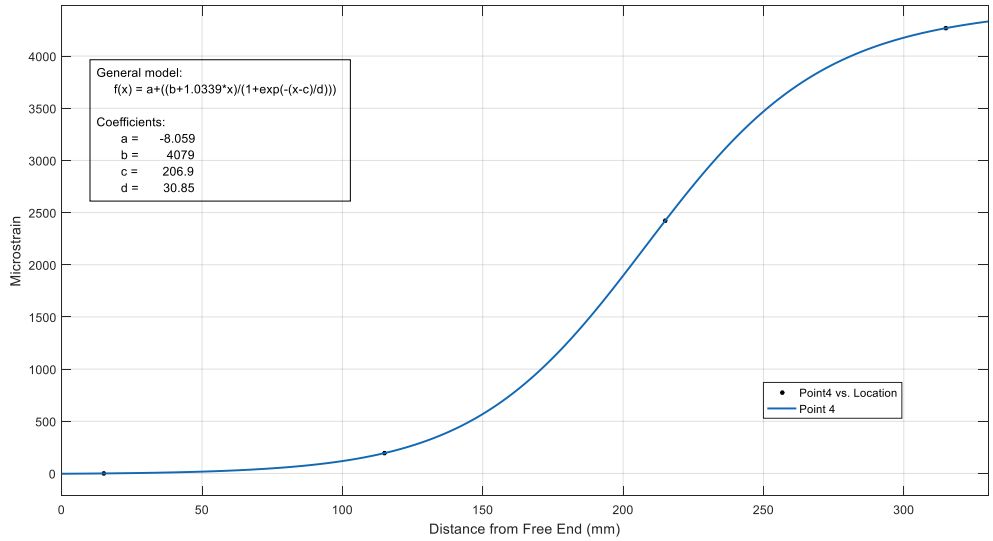

Figure C.9. Curve fitting at Point 4 of specimen DS_330_50_C_7S

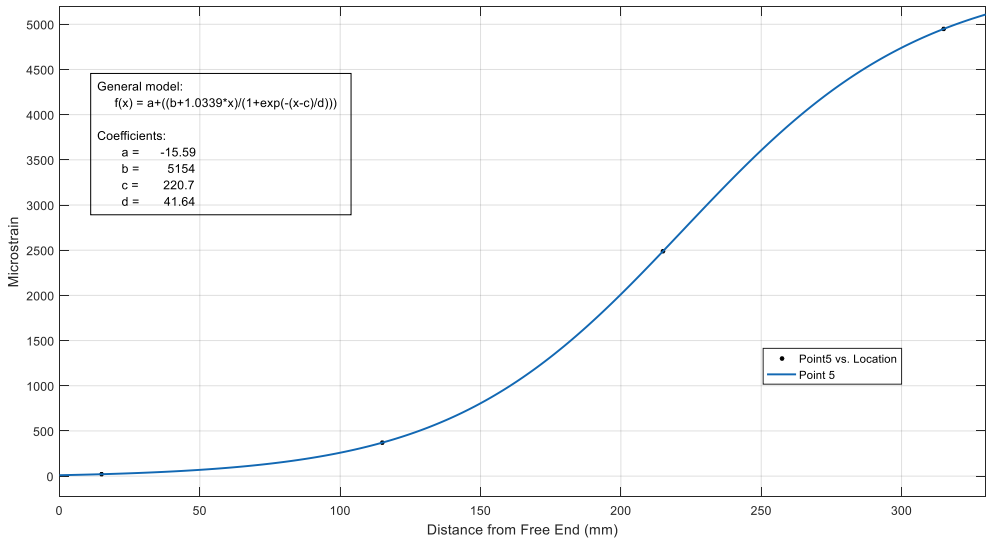

Figure C.10. Curve fitting at Point 5 of specimen DS_330_50_C_7S

www.manaraa.com

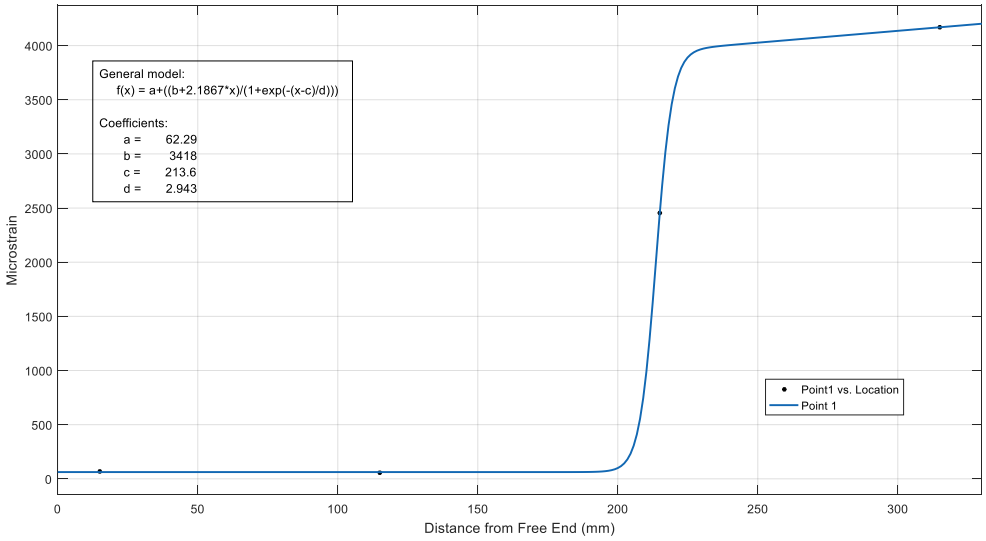

Figure C.11. Curve fitting at Point 1 of specimen DS_330_50_M_6S

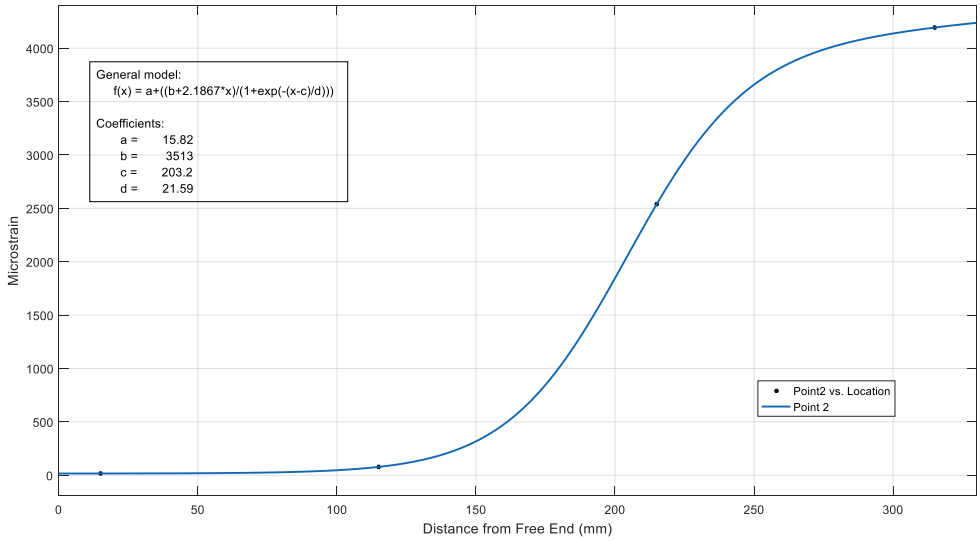

Figure C.12. Curve fitting at Point 2 of specimen DS_330_50_M_6S

www.manaraa.com

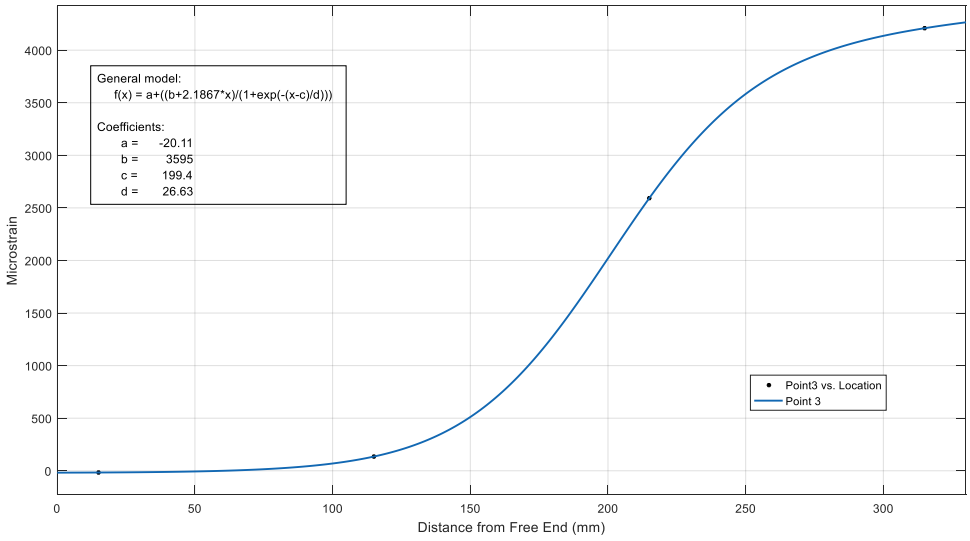

Figure C.13. Curve fitting at Point 3 of specimen DS_330_50_M_6S

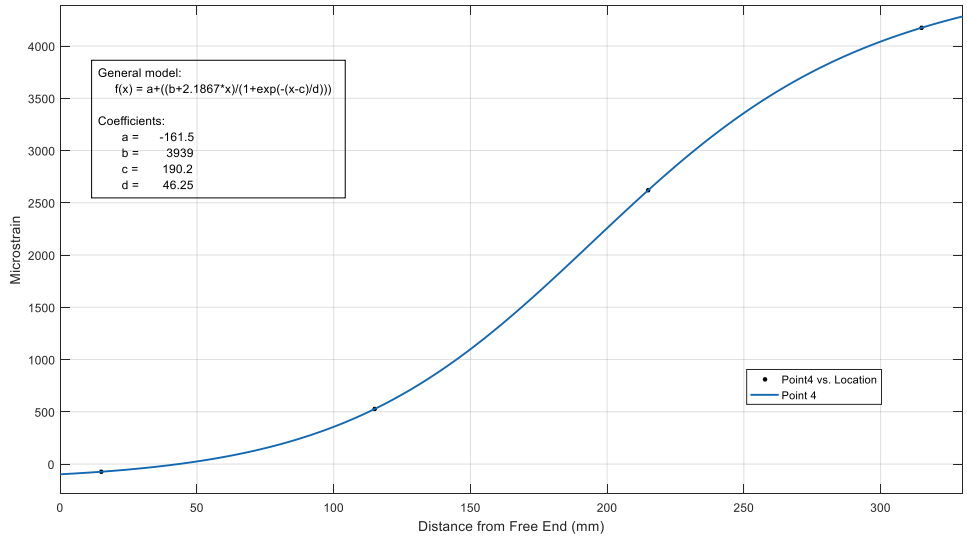

Figure C.14. Curve fitting at Point 4 of specimen DS_330_50_M_6S

www.manaraa.com

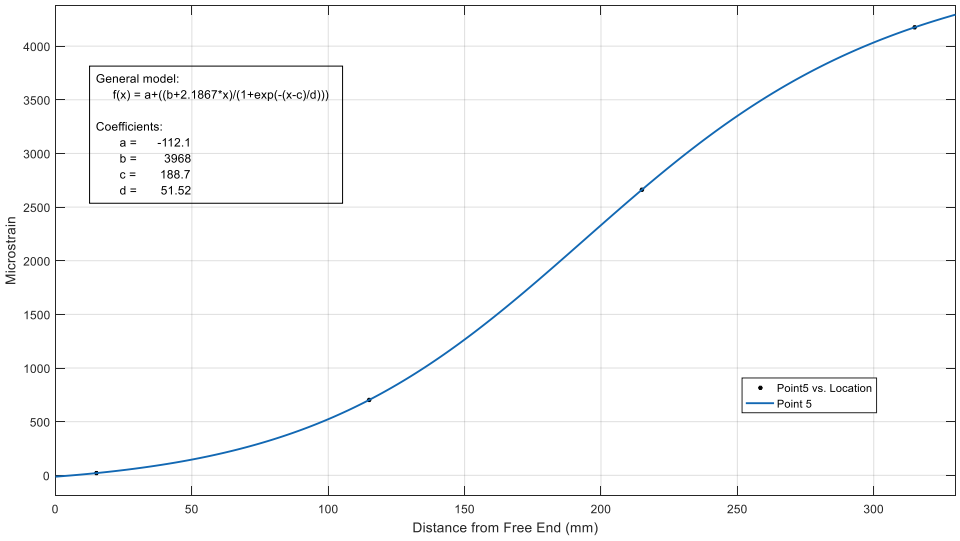

Figure C.15. Curve fitting at Point 5 of specimen DS_330_50_M_6S

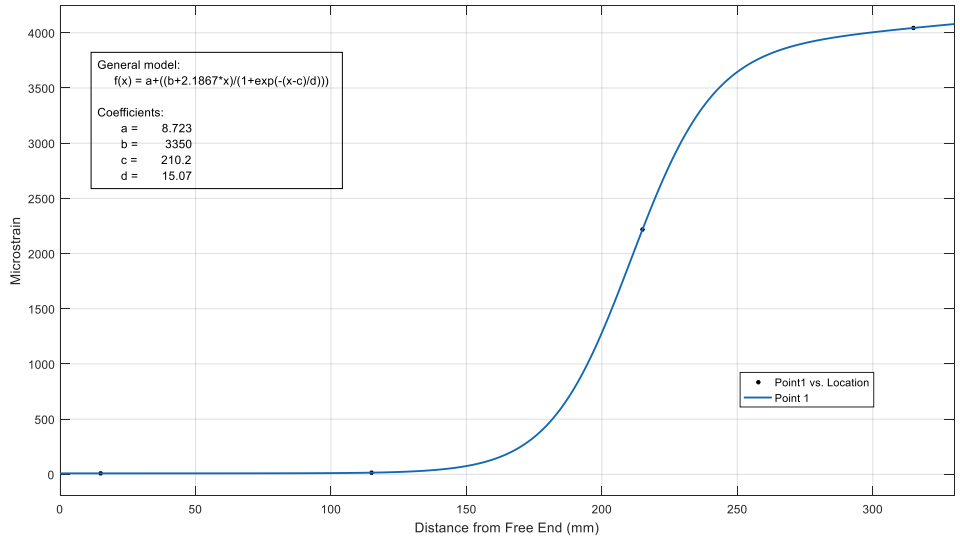

Figure C.16. Curve fitting at Point 1 of specimen DS_330_50_M_7S

www.manaraa.com

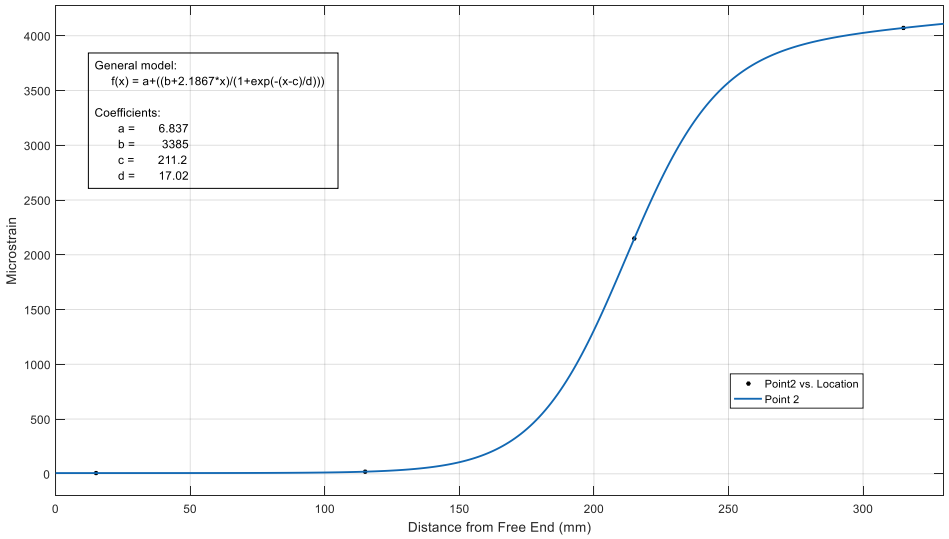

Figure C.17. Curve fitting at Point 2 of specimen DS_330_50_M_7S

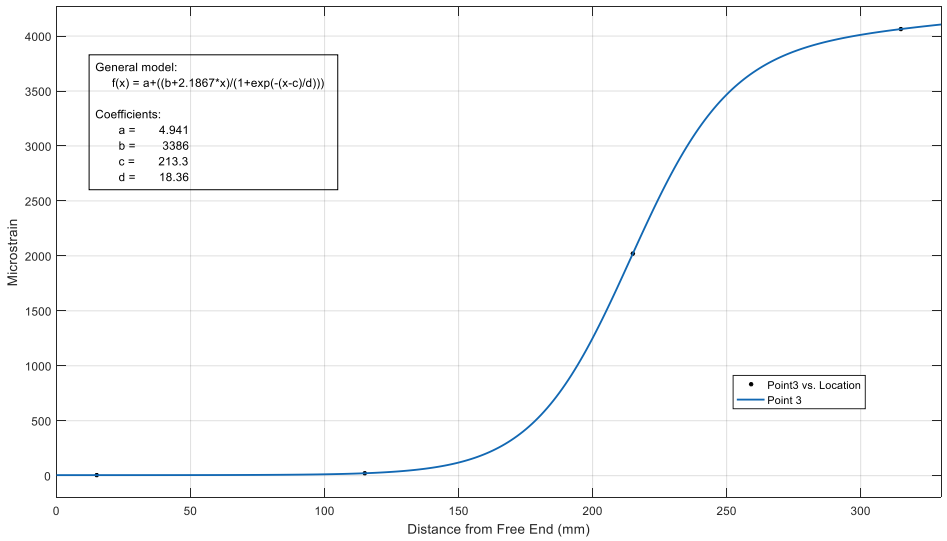

Figure C.18. Curve fitting at Point 3 of specimen DS_330_50_M_7S

www.manaraa.com

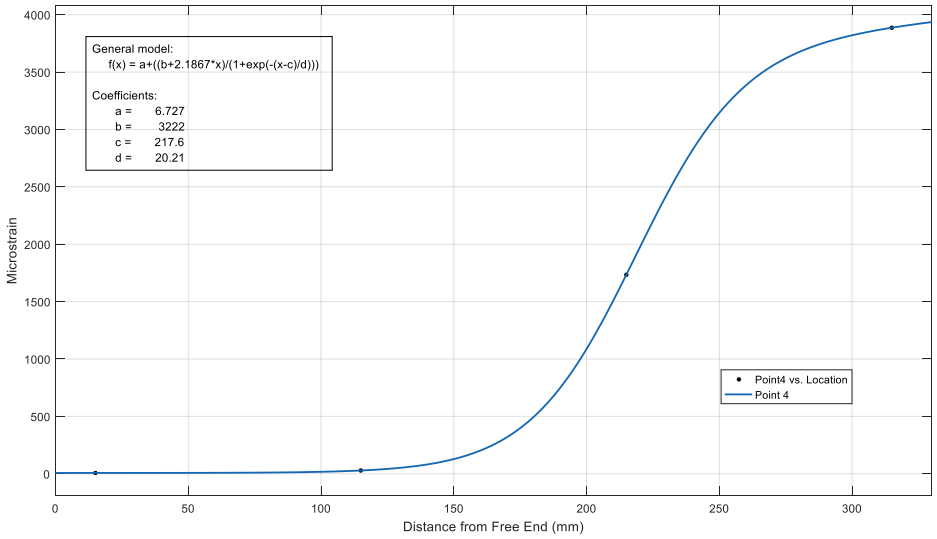

Figure C.19. Curve fitting at Point 4 of specimen DS_330_50_M_7S

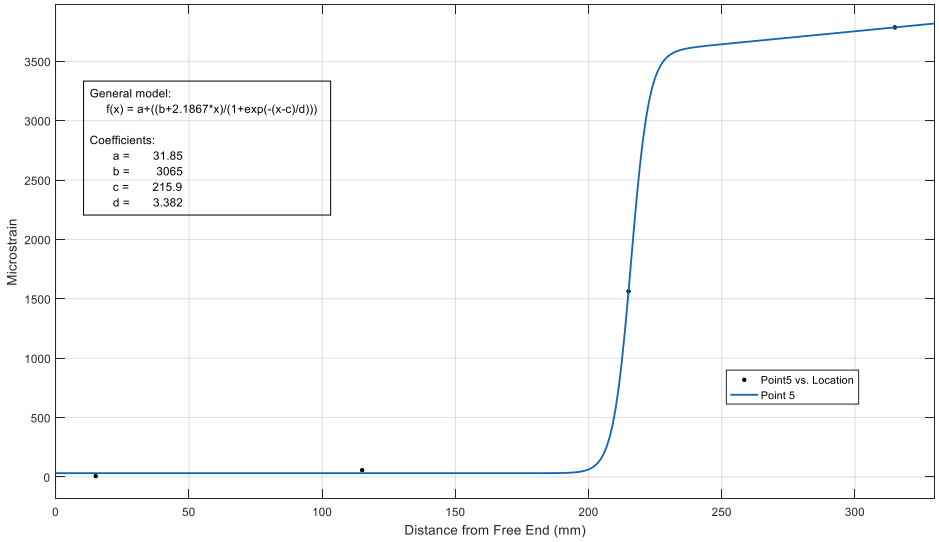

Figure C.20. Curve fitting at Point 5 of specimen DS_330_50_M_7S

www.manaraa.com

BIBLIOGRAPHY

Alabdulhady, M. Y., Sneed, L. H., & Carloni, C. (2017). Torsional behavior of RC beams strengthened with PBO-FRCM composite – An experimental study. *Engineering Structures*, *136*, 393–405. https://doi.org/10.1016/j.engstruct.2017.01.044

Ambrisi, A. D., & Focacci, F. (2011). Flexural Strengthening of RC Beams with Cement-Based Composites. *Journal of Composites for Construction*, *15*(5), 707–720. https://doi.org/10.1061/(ASCE)CC.1943-5614.0000218.

Carloni, C., D'Antino, T., Sneed, L. H., & Pellegrino, C. (2015). Role of the Matrix Layers in the Stress-Transfer Mechanism of FRCM Composites Bonded to a Concrete Substrate. *Journal of Engineering Mechanics*, *141*(6), 04014165. https://doi.org/10.1061/(ASCE)EM.1943-7889.0000883

Carloni, C., & Subramaniam, K. V. (2012). Application of fracture mechanics to debonding of FRP from RC members. *American Concrete Institute, ACI Special Publication*, (286 SP), 1–16.

Ceroni, F., Pecce, M., Matthys, S., & Taerwe, L. (2008). Debonding strength and anchorage devices for reinforced concrete elements strengthened with FRP sheets. *Composites Part B: Engineering*, *39*(3), 429–441. https://doi.org/10.1016/j.compositesb.2007.05.002

D'Ambrisi, A., Feo, L., & Focacci, F. (2012). Bond-slip relations for PBO-FRCM materials externally bonded to concrete. *Composites Part B: Engineering*, *43*(8), 2938–2949. https://doi.org/10.1016/j.compositesb.2012.06.002

D'Antino, T., Carloni, C., Sneed, L. H., & Pellegrino, C. (2014). Matrix-fiber bond behavior in PBO FRCM composites: A fracture mechanics approach. *Engineering Fracture Mechanics*, *117*, 94–111. https://doi.org/10.1016/j.engfracmech.2014.01.011

D'Antino, T., Colombi, P., Carloni, C., & Sneed, L. H. (2018). Estimation of a matrix-fiber interface cohesive material law in FRCM-concrete joints. *Composite Structures*, *193*(February), 103–112. https://doi.org/10.1016/j.compstruct.2018.03.005

D'Antino, T., Pellegrino, C., Carloni, C., Sneed, L. H., & Giacomin, G. (2014). Experimental Analysis of the Bond Behavior of Glass, Carbon, and Steel FRCM Composites. *Key Engineering Materials*, *624*, 371–378. https://doi.org/10.4028/www.scientific.net/KEM.624.371

www.manaraa.com

Donatelli, J. (2016). *Flexural Behavior of RC Beams Strengthened By FRCM with Mechanical Anchorages*.

Focacci, F., D'Antino, T., Carloni, C., Sneed, L. H., & Pellegrino, C. (2017). An indirect method to calibrate the interfacial cohesive material law for FRCM-concrete joints. *Materials and Design*, *128*(April), 206–217. https://doi.org/10.1016/j.matdes.2017.04.038

Grelle, S. V., & Sneed, L. H. (2013). Review of Anchorage Systems for Externally Bonded FRP Laminates. *International Journal of Concrete Structures and Materials*, *7*(1), 17–33. https://doi.org/10.1007/s40069-013-0029-0

Jumaat, M. Z., & Al-Kubaisy, M. (2000). Ferrocement Laminate Strengthens RC Beams. *Concrete International*, 37–43.

Kalfat, R., & Al-Mahaidi, R. (2010). Investigation into bond behaviour of a new CFRP anchorage system for concrete utilising a mechanically strengthened substrate. *Composite Structures*, *92*(11), 2738–2746. https://doi.org/10.1016/j.compstruct.2010.04.004

Loreto, G., Babaeidarabad, S., Leardini, L., & Nanni, A. (2015). RC beams shear-strengthened with fabric-reinforced-cementitious-matrix (FRCM) composite. *International Journal of Advanced Structural Engineering*, *7*(4), 341–352. https://doi.org/10.1007/s40091-015-0102-9

Micelli, F., Annaiah, R. H., & Nanni, A. (2002). Strengthening of Short Shear Span Reinforced Concrete T Joists with Fiber-Reinforced Plasic Composites. *Journal of Composites for Construction*, *6*(4), 264–271. https://doi.org/10.1061/(ASCE)1090-0268(2002)6:4(264)

Mofidi, A., Chaallal, O., Benmokrane, B., & Neale, K. (2012). Performance of End-Anchorage Systems for RC Beams Strengthened in Shear with Epoxy-Bonded FRP. *Journal of Composites for Construction*, *16*(3), 322–331. https://doi.org/10.1061/(ASCE)CC.1943-5614.0000263

Niemitz, C. W., James, R., & Breña, S. F. (2010). Experimental Behavior of Carbon Fiber-Reinforced Polymer (CFRP) Sheets Attached to Concrete Surfaces Using CFRP Anchors. *Journal of Composites for Construction*, *14*(2), 185–194. https://doi.org/10.1061/(ASCE)CC.1943-5614.0000064

Ombres, L. (2014). Concrete confinement with a cement based high strength composite material. *Composite Structures*, *109*(1), 294–304. https://doi.org/10.1016/j.compstruct.2013.10.037

www.manaraa.com

Prota, A., Tan, K. Y., Nanni, A., Pecce, M., & Manfredi, G. (2006). Performance of shallow reinforced concrete beams with externally bonded steel-reinforced polymer. *ACI Structural Journal*, *103*(2), 163–170.

Skuturna, T., & Valivonis, J. (2016). Experimental study on the effect of anchorage systems on RC beams strengthened using FRP. *Composites Part B: Engineering*, *91*, 283–290. https://doi.org/10.1016/j.compositesb.2016.02.001

Sneed, L. H., D'Antino, T., Carloni, C., & Pellegrino, C. (2015). A comparison of the bond behavior of PBO-FRCM composites determined by double-lap and single-lap shear tests. *Cement and Concrete Composites*, *64*, 37–48. https://doi.org/10.1016/j.cemconcomp.2015.07.007

Sneed, L. H., Verre, S., Carloni, C., & Ombres, L. (2016). Flexural behavior of RC beams strengthened with steel-FRCM composite. *Engineering Structures*, *127*, 686–699. https://doi.org/10.1016/j.engstruct.2016.09.006

Trapko, T., Urbanska, D., & Kaminski, M. (2015). Shear strengthening of reinforced concrete beams with PBO-FRCM composites. *Composites Part B: Engineering*, *80*, 63–72. https://doi.org/10.1016/j.compositesb.2015.05.024

Yao, J., Teng, J. G., & Chen, J. F. (2005). Experimental study on FRP-to-concrete bonded joints. *Composites Part B: Engineering*, *36*(2), 99–113. https://doi.org/10.1016/j.compositesb.2004.06.001

Zhang, H. W., & Smith, S. T. (2012). FRP-to-concrete joint assemblages anchored with multiple FRP anchors. *Composite Structures*, *94*(2), 403–414. https://doi.org/10.1016/j.compstruct.2011.07.025

Zhang, H. W., Smith, S. T., & Kim, S. J. (2012). Optimisation of carbon and glass FRP anchor design. *Construction and Building Materials*, *32*, 1–12. https://doi.org/10.1016/j.conbuildmat.2010.11.100

www.manaraa.com

VITA

Christopher Michael Moore was born in Springfield, IL in 1995. His inspiration for pursuing studies in engineering came from his grandfather and uncle, both of whom were engineers.

Christopher graduated from Missouri S&T in May of 2018 with a bachelor's degree in Architectural Engineering and a bachelor's degree in Civil Engineering. He graduated Suma Cum Laude in both degree programs. During his time as an undergraduate student, he became one of five members of the inaugural class of the Greenberg Scholars program, an accelerated master's degree program in the Civil, Architectural, and Environmental Engineering Department at Missouri S&T. He started his Master of Science in Civil Engineering at Missouri University of Science and Technology in August of 2017 by dual enrolling into graduate courses. He received his Master of Science in Civil Engineering from Missouri University of Science and Technology in May 2019.

Christopher began his professional career in January 2019 at Jacobs, a Fortune 500 engineering design firm, in St. Louis, Missouri, working in their bridges and infrastructure group.

www.manaraa.com